Influence des ondes de gravité de montagne sur l'écoulement de grande échelle en présence de niveaux critiques

Armel Martin

THESE de DOCTORAT de
L'UNIVERSITE PIERRE ET MARIE CURIE

Spécialité

Dynamique de l'Atmosphère

présentée par

Armel MARTIN

pour obtenir le grade de

DOCTEUR de L'UNIVERSITE PIERRE ET MARIE CURIE

Sujet de la thèse :

Influence des ondes de gravité de montagne sur l'écoulement de grande échelle en présence de niveaux critiques

Soutenue le 13 juin 2008

devant le jury composé de :

Mme Chantal Staquet	Rapporteuse
M. Eyal Heifetz	Rapporteur
M. Valdimir Tseitline	Président
Mme Evelyne Richard	Examinatrice
M. Riwal Plougonven	Examinateur
M. François Lott	Directeur

Remerciements

Je remercie en premier lieu François Lott, d'abord pour le sujet riche et ouvert qu'il a su me proposer. François a su donner des orientations décisives, poser des questions physiques essentielles, observer mes résultats avec un oeil critique et expérimenté, et me faire profiter de son profond sens physique. François a su aussi me laisser la distance dont j'avais besoin, et parfois résister à mon impatience.

Je remercie Riwal Plougonven, dont la rencontre a été déterminante dans l'orientation qu'a pris mon travail de thèse. Outre l'intérêt que j'ai porté à ses travaux, je le remercie pour sa disponibilité, ses conseils avisés et son objectivité.

Je remercie doublement Bernard Legras. Grâce à lui j'ai pu enseigner pour moitié dans ma discipline, jusqu'au niveau M2, ce qui est un complément fort appréciable au travail de recherche. D'autre part, Bernard a majoritairement sponsorisé ma thèse en me faisant profiter des ressources informatiques qu'il a constituées pour ses propres projets de recherche.

A cet égard, je remercie aussi Fabio D'Andrea, qui a contribué considérablement. Fabio mérite aussi d'être remercié pour sa bonne humeur et sa disponibilité, au même titre qu'Alexandre Stegner.

Parmi les voisins proches, je remercie Guillaume Lapeyre pour sa grande disponibilité, ses tuyaux techniques précieux, ses coups d'gueule, son avidité de savoir et sa curiosité sans bornes. Je remercie aussi Hector Teitelbaum, dont j'ai apprécié la présence et le caractère trempé, avec qui j'ai échangé un peu de science, mais aussi de nombreuses discussions politiques ou philosophiques souvent animées.

Je remercie aussi les "travailleurs de l'ombre" du laboratoire que sont les ingénieurs informatique et calcul, pour leur soutien constant et indispensable : merci à Frédéric Bongat, Virginie Métrot, Mathieu Perrault, et Lionel Guez.

Je remercie Marie-Christine Roos, pour son attention et sa gentillesse, et Marie-Claire Lanceau qui m'a aidé à accéder rapidement à certaines ressources bibliographiques, ainsi qu'à un déguisement de père-Noël.

Je remercie mes collègues de bureau, avec qui j'ai partagé aussi bien de longues heures de silence, parfois tardives, des tuyaux techniques et discussions scientifiques, mais aussi des moments simples et agréables au bureau, autour d'un verre ou sur le chemin du casse-croûte de midi. Notamment dans l'ordre chronologique, Julien Le Sommer, Gilles Belon, Emilie Scherer, Ronan James et Ignacio Pisso, avec qui j'ai passé le plus de temps.

Je remercie profondémment Marion, qui est la plus grande découverte que j'aie pu faire pendant ma thèse. Merci pour son soutien si doux.

Enfin, je remercie tous les musiciens sans qui je n'aurais pu mener à bien cette thèse :

- *Gillespie :* `AMD Opteron(tm) Processor 250 - 2389.274 MHz`
- *Callas :* `Dual-Core AMD Opteron(tm) Processor 270 - 1995.088 MHz`
- *Albeniz :* `AMD Opteron(tm) Processor 244 - 1804.124 MHz`
- *Gluck :* `Dual-Core AMD Opteron(tm) Processor 2216 HE - 2412.388 MHz`
- *Duke :* `AMD Opteron(tm) Processor 252 - 2593.573 MHz`

Mais aussi Bruckner, Debussy, Bach, Pierne, Delibes et Galuppi... Sclavis et Lubat.

Résumé

L'objectif de cette thèse est d'étudier l'effet sur l'écoulement atmosphérique de grande échelle, du déferlement des ondes de gravité de montagne à des niveaux critiques. L'idée sous-jacente est la prise en compte de cet effet dans les paramétrisations des effets montagneux, et notamment l'impact en terme de cyclogénèse de montagne. L'approche est théorique, et repose sur la production de vorticité potentielle dans le cadre du problème de Eady.

D'abord, l'effet sur les échelles synoptiques est évalué dans le cadre d'un modèle semi-géostrophique linéaire, forcé par une force paramétrisée générée par une orographie d'échelle sous-maille isolée, idéalisée ou réaliste. Il est montré que l'influence est cyclolytique dans le cas d'un front froid, et cyclogénétique pour un front chaud.

Ensuite la dynamique 2D complète non linéaire est abordée à l'aide d'un modèle aux équations primitives anélastiques.
La croissance linéaire et non linéaire des modes instables non-géostrophiques, couplant une onde de Eady de surface partiellement équilibrée à une onde d'inertie-gravité de même échelle, est étudiée en tant que point de départ pour la description de la réponse forcée aux échelles sous-synoptiques.
L'effet des ondes de montagne sur ces échelles est ensuite analysé et quantifié à partir d'une paramétrisation, ou d'un forçage direct par une topographie idéalisée. A ces échelles, la réponse non équilibrée est d'amplitude comparable à la partie équilibrée. Elle contient notamment des ondes d'inertie-gravité longues qui sont soit couplées aux ondes de Eady de surface sous forme de modes non-géostrophiques, soit générées spontanément sous forme de trains d'ondes par l'écoulement équilibré associé au dipole de vorticité potentielle. L'étude des mécanismes de saturation non linéaire permet de conclure sur l'amplitude attendue pour ces réponses, qui s'avère relativement faible mais significative.

Abstract

The aim of this thesis is to study the effect of mountain gravity waves breaking at critical levels, upon the atmospheric large scale flow. This question arises in the context of the improvement of the subgrid scale orographic parameterizations, and the need to further understand the phenomenology linked to lee cyclogenesis. The approach is theoretical, and relies on the conceptual framework of potential vorticity production in the Eady problem.

First, the effect upon the synoptic scales is evaluated by forcing a linear semi-geostrophic Eady problem with a parameterized force, which corresponds to an idealized or realistic subgrid scale orography. It is shown that the effect is cyclolytic for a cold front and cyclogenetic for a warm front.

Then, the complete nonlinear 2D dynamics is studied within the anelastic primitive equations framework.
First, the linear and nonlinear growth of unstable non geostrophic modes, which couple a partially balanced surface Eady wave with an inertia-gravity wave of the same scale, is studied as a starting point to describe the sub-synoptic scale response to the forcing. Second, the complete response to the mountain gravity wave forcing is analysed and quantified, by means of a parameterization or a direct forcing by an idealized subgrid scale orography. At these scales, unbalanced and balanced responses have a comparable amplitude. This response notably contains large scale inertia-gravity waves which are either coupled to the surface Eady waves, either spontanously generated in the form of wave trains by the balanced flow associated to the potential vorticity dipole. The study of the nonlinear saturation mechanisms allow to conclude about the expectable amplitude of these responses, which turn out to be rather weak but significant.

Table des matières

1 Introduction **1**
1.1 Météorologie de montagne . . . 1
1.1.1 Les quatre ingrédients de la météorologie de montagne . . . 1
1.1.2 La force exercée par les montagnes . . . 4
1.2 Ondes de montagne . . . 6
1.2.1 Structure des ondes de montagne . . . 6
1.2.2 Niveaux singuliers . . . 8
1.2.3 Effets de la rotation terrestre à plus grande échelle . . . 9
1.2.4 Interaction Ondes de montagne - Ecoulement moyen . . . 10
1.2.5 Ondes de gravité et circulation générale de l'atmosphère . . . 12
1.3 Cyclogénèse de montagne . . . 15
1.3.1 Observations . . . 15
1.3.2 Théories et mécanismes . . . 17
1.3.3 Vers une vision moderne de la cyclogénèse de montagne . . . 20
1.4 Paramétrisation des effets montagneux d'échelle sous-maille . . . 24
1.4.1 Effets montagneux de grande échelle : notion d'orographie enveloppe . . . 25
1.4.2 Effets montagneux de très petite échelle : friction de surface . . . 26
1.4.3 Contrainte des ondes de gravité . . . 26
1.4.4 De l'importance de la portance... et des niveaux critiques directionnels . . . 33
1.4.5 Perspectives pour la paramétrisation des OG de montagne . . . 34
1.5 Questions posées et plan de la thèse . . . 36

2 Synoptic responses to mountain gravity waves breaking at directional critical levels **37**
2.1 Article : Martin and Lott, 2007 . . . 37
2.2 Complementary works . . . 59

3 Linear and nonlinear non-geostrophic unstable Eady modes **63**
3.1 Préliminaires . . . 64
3.2 Introduction . . . 68
3.3 Linear theory and over-reflection for inertia-gravity waves . . . 72
3.3.1 The vertical structure equation . . . 72
3.3.2 The conservation of the angular momentum vertical flux . . . 73
3.3.3 The asymptotic over-reflection criterium . . . 75
3.4 Linear growth of unstable NG Eady modes . . . 78
3.4.1 Numerical simulation of the linear growth - Experiment L . . . 78
3.4.2 The role of the shear Λ, the Rossby and Richardson numbers . . . 84

3.4.3 Other sensitivity studies . . . 86
3.5 Nonlinear growth, saturation, and breakdown . . . 88
3.5.1 Numerical experimental setup - Experiment NL . . . 88
3.5.2 Energy budget : nonlinear saturation and breakdown . . . 88
3.5.3 Saturation mechanisms . . . 89
3.5.4 Instability and breakdown of the inertial critical layer . . . 99
3.6 Conclusion and discussion . . . 102
Appendix . . . 104
A. Model Equations . . . 104
B. Energy budget . . . 105
C. Transformed Eulerian mean equations and Eliassen-Palm flux . . . 105
D. Numerical computation . . . 106
References . . . 108

4 Secondary generation of non-geostrophic unstable modes and inertia-gravity waves by breaking mountain gravity waves 111
4.1 Introduction . . . 112
4.2 Response to a parameterized force . . . 116
4.2.1 Linear response to a weak force in the low-troposphere (P1) . . . 116
4.2.2 Nonlinear response to a strong force in the low-troposphere (P2) 132
4.2.3 Linear response to a weak force in the high-troposphere (P3) . . . 133
4.3 Large scale response to short scale orography . . . 142
4.3.1 Large scale response to a tiny mountain (M1) . . . 142
4.3.2 Nonlinear saturation for higher mountains . . . 149
4.4 Conclusion . . . 151
Apendix . . . 156
A. Model Equations . . . 156
B. Energy budget . . . 157
C. Transformed Eulerian mean equations and Eliassen-Palm flux . . . 158
D. Balanced equations system . . . 158
E. Spontaneous IGW generation forced by the balanced flow . . . 160
F. Numerical scheme . . . 161
References . . . 162

5 Conclusion 165

Bibliographie 169

Chapitre 1

Introduction

1.1 Météorologie de montagne

L'idée que les montagnes peuvent influencer la météorologie et le climat est aussi vieille que la météorologie elle-même. Déjà Aristote, dans son ouvrage *Meteorologica* daté de 340 av. JC, supposait que les montagnes contrôlent la hauteur des nuages. Même si cette vision du nuage naissant à la cime des montagnes peut aujourd'hui paraître naïve, il est cependant exact que de façon générale les montagnes peuvent participer de façon prépondérante à la génération de formations nuageuses et de précipitations de formes multiples, par des mécanismes qui varient selon l'environnement (latitude, position par rapport aux océans, échelles considérées, topographie[1]...). En 1648, Pascal mesurait au Puy-de-Dome la décroissance verticale de la pression atmosphérique dûe à la compressibilité de l'air. Cette expérience a le mérite de nous rappeler que les montagnes ont toutes les chances d'influencer le climat terrestre dans la mesure où les plus grandes d'entre elles (8.8km d'altitude pour l'Himalaya) ont une hauteur comparable à l'échelle caractéristique de variation de densité de l'atmosphère[2] (8.5km). Autrement dit, même si à l'échelle du rayon terrestre la sphéricité de l'enveloppe solide est presque parfaite, l'atmosphère est suffisamment fine pour être considérablement contrainte dans son écoulement par les massifs montagneux, au moins dans sa couche inférieure la plus dense, la troposphère. Cet argument est aussi valable pour les océans, mais nous nous cantonnerons aux effets atmosphériques. En guise d'illustration, la Fig. 1.1 présente une vue ombrée de la surface continentale terrestre, telle qu'elle est vue par les données GLOBE[3] (Global Land One-km Based Elevation), fournies par le NGDC (National Geophysical Data Center) de la NOAA (National Oceanic and Atmospheric Administration, Etats-Unis).

1.1.1 Les quatre ingrédients de la météorologie de montagne

L'effet climatique montagneux le plus évident est sans doute lié à la décroissance des températures avec l'altitude. C'est un point essentiel, qui sous-tend en réalité une

[1] En toute rigueur, le mot *topographie* recouvre tout ce qui caractérise l'état de surface du sol, dont son élévation au dessus du niveau de la mer, alors que le terme *orographie* se réduit strictement à l'élévation, faisant référence à la représentation des montagnes dans les modèles. Par la suite, la distinction ne sera jamais nécessaire dans cette thèse, donc nous utiliserons indifféremment les deux termes, selon l'usage courant.

[2] c'est-à-dire la hauteur qu'elle aurait si sa densité était constante avec l'altitude.

[3] http ://www.ngdc.noaa.gov/mgg/topo/topo.html

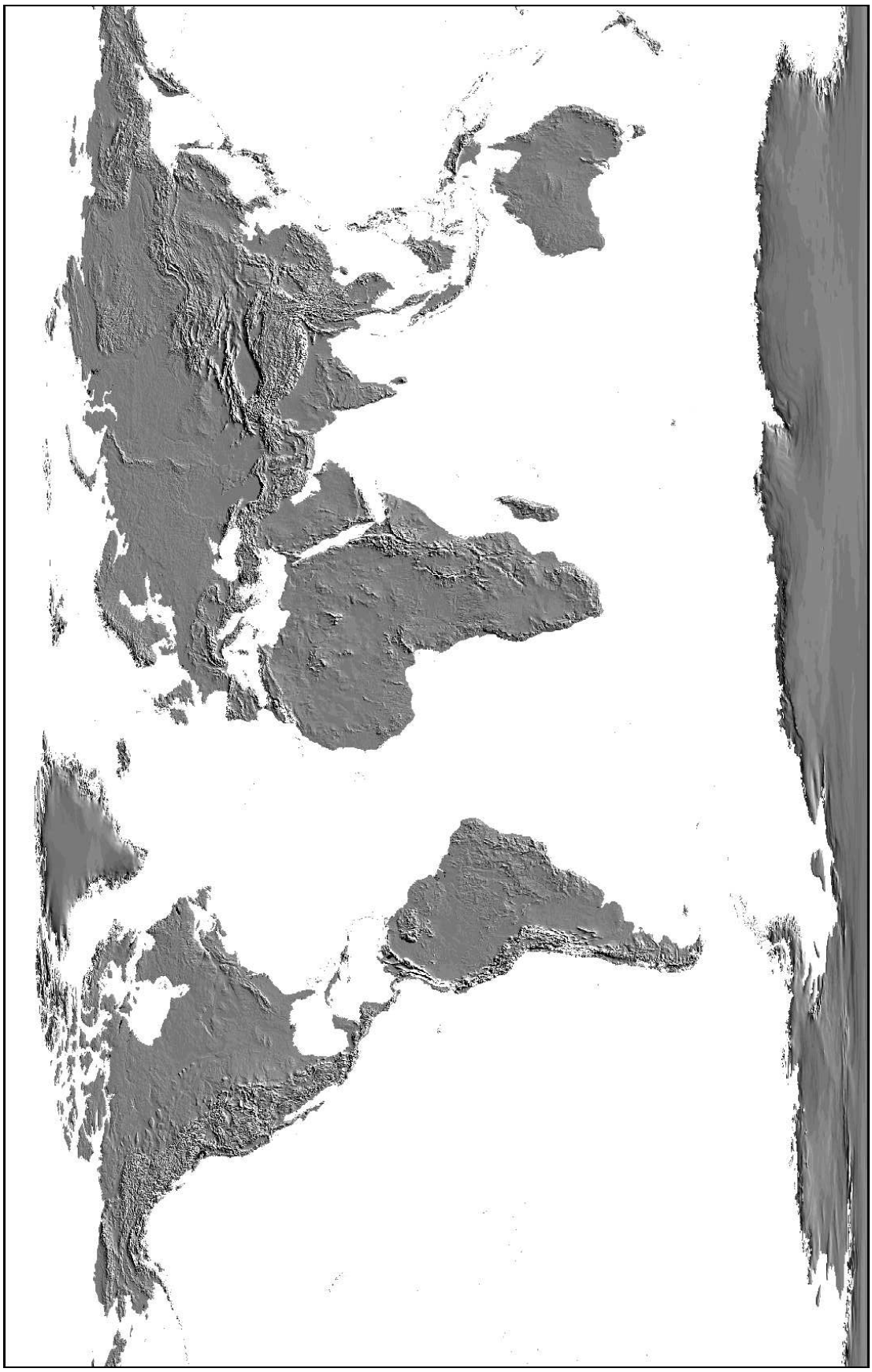

FIG. 1.1 – Vue ombrée des données topographiques GLOBE, fournies par le NGDC.

grande partie des effets montagneux, et pas seulement les effets locaux (on peut penser au rôle des glaciers sur le climat global par exemple). Mais pour comprendre la diversité des phénomènes météorologiques et climatiques liés à la présence des montagnes, et le fait que cette influence se ressent quasiment à toutes les échelles de temps et d'espace sur la planète, on peut appréhender les choses à travers quatre ingrédients physiques de base.

Les deux premiers sont mécaniques, liés aux deux principales forces de rappel qui intéressent le dynamicien des fluides géophysiques : la force de Coriolis et la force d'Archimède.

Aux grandes échelles horizontales, la force de Coriolis peut jouer le rôle de force de rappel grâce à l'existence du gradient méridien de vorticité planétaire, qui lui même est dû à la sphéricité de la Terre. En effet, les montagnes induisent une compression-décompression des colonnes de fluide qui s'écoulent sur elles. Par conservation du tourbillon potentiel (analogue à celle du moment cinétique en physique du solide), cela induit des mouvements horizontaux oscillant latitudinalement, appelés *ondes de Rossby* (Rossby et al. 1939, Rossby 1940, Rossby 1949). Par cet effet notamment, les grandes chaînes montagneuses de l'hémisphère sont connues pour forcer des *ondes planétaires* (5000 à 20000km) stationnaires qui modulent significativement la climatologie régionale aux moyennes latitudes (Charney et Eliassen 1949, Bolin 1950, Hoskins et Karoly 1981), ainsi que des ondes planétaires libres (Salby 1984, Madden 2007). Ces effets ont été revisités plus récemment en introduisant des phénomènes nonlinéaires. Il a ainsi été proposé que les montagnes jouent un rôle important sur la variabilité basse-fréquence aux moyennes et hautes latitudes (Charney et De Vore 1979, Legras et Ghil 1985, Yoden 1985, Lott et al. 2005).
A des échelles un peu plus courtes (1000km) qualifiées de *synoptiques*, nous verrons que les ondes de Eady, qui s'apparentent d'un point de vue dynamique à des ondes de Rossby, jouent aussi un rôle dans la cyclogénèse de montagne (section 1.3).

A des échelles 100 fois plus petites (10km), qualifiées de *méso-échelles*, c'est maintenant la force d'Archimède qui est dominante. Elle intervient parce que l'atmosphère est en moyenne stratifiée en densité de façon stable, le fluide étant d'autant plus léger qu'il est élevé. Ainsi, la force d'Archimède tend à s'opposer aux mouvements verticaux qui conduisent à mélanger du fluide dense à du moins dense, ou inversement. En tant que force de rappel, elle donne alors naissance à des oscillations verticales relativement rapides (période propre de 10 min dans la troposphère, moins dans la stratosphère) et permet la propagation d'ondes. C'est pourquoi la montagne, qui en présence d'un vent horizontal impose un mouvement d'ascension, peut voir son influence se propager verticalement et horizontalement à relativement grande distance, sous la forme d' *ondes de montagne* (Queney 1948, Scorer 1949, Smith 1979a). Nous développerons abondamment ce sujet dans la prochaîne section.

Remarquons toutefois dès maintenant qu'entre les échelles synoptiques précédentes, et les méso-échelles, les mouvements d'échelle sous-synoptiques (100km) combinent naturellement les effets oscillatoires liés à la rotation terrestre et à la stratification. Au cours de cette thèse, nous porterons un intérêt particulier à ce domaine intermédiaire. Par contre, aux très petites échelles, inférieures à 10 km typiquement, les mécanismes ondulatoires précédents ne fonctionnent plus. Certains vents de bas niveau résultent alors prioritairement de l'interaction entre les irrégularités du terrain et la circulation à plus grande échelle (*gaps winds, channel winds*).

Les deux derniers ingrédients de la météorologie de montagne sont thermodyna-

miques, liés pour l'un à la présence de *vapeur d'eau* dans l'air, et l'autre au *rayonnement solaire*.

Puisque la montagne est susceptible de permettre une ascension de l'air, celui-ci se refroidit par détente adiabatique et peut donner lieu à la condensation de la vapeur. Outre l'effet météorologique attendu que sont les précipitations d'origine orographique, l'existence d'un changement de phase de la vapeur d'eau modifie la dynamique "sèche" en jouant sur la densité des parcelles de fluide. Dans cette thèse cependant, nous ne nous intéresserons pas à ces complications. Nous nous cantonnerons ainsi aux effets dynamiques secs, bien que l'influence de la vapeur d'eau soit bien souvent non négligeable. La compréhension des mécanismes de précipitations orographiques est aujourd'hui un domaine à part entière, qui fait l'objet d'intenses recherches (Rotunno et Houze, 2007). Cependant, une compréhension solide et fine de la dynamique sèche est bien souvent un préalable à la compréhension des phénomènes de précipitation orographique.

Enfin, concernant l'insolation, l'inclinaison variable du terrain module localement l'apport d'énergie solaire, ce qui produit des hétérogénéïtés climatiques importantes à petite échelle spatiale (visibles dans la végétation par exemple), ainsi que des variations temporelles diurnes et saisonnières. Plus généralement, une grande partie des phénomènes météorologiques montagneux est imputable au lien intime entre le cycle de l'eau et l'insolation, notamment en présence de couvert neigeux. En effet, les différentiels thermiques engendrent des circulations locales régulières contraintes par le terrain et par le cycle diurne (vents katabatiques, brises diurnes de pente et de vallée), qui modulent éventuellement les précipitations (Smith 1979a, Whiteman 2000). A des échelles de temps et d'espace plus grandes, la présence de glaciers sur les montagnes est un facteur déterminant du climat global et régional de la planète, à travers le rôle joué par l'albédo notamment, mais aussi l'influence sur les régimes de temps ou le piégeage de la vapeur d'eau. En témoignent par exemple les effets du glacier des Laurentides à l'Est du Canada sur le climat nord-américain, ou celui du Groënland sur le climat nord-atlantique (Smith 2003, Whiteman 2000).

1.1.2 La force exercée par les montagnes

Le fait que l'écoulement de l'atmosphère sur les montagnes puisse générer des ondes, qui transportent de la quantité de mouvement, a une conséquence mécanique fondamentale : les montagnes induisent une modification de la quantité de mouvement du fluide. Par principe d'action-réaction, les montagnes exercent donc localement des forces sur l'atmosphère (Eliassen et Palm, 1961), qui résultent globalement en un couple exercé par la Terre solide sur l'atmosphère. Notons que des phénomènes analogues se produisent dans l'océan. Cela peut se comprendre simplement en réalisant que grâce à l'inclinaison du sol, la force de pression de surface admet une composante horizontale. Par ce biais, les montagnes ont donc un moyen d'action sur l'écoulement à des échelles de temps et d'espace variées. Nous développerons largement ce point dans la suite en ce qui concerne l'effet des ondes de montagne (section 1.2), dans la mesure où il sous-tend toute cette thèse.

Signalons toutefois quelques résultats récents illustrant l'effet global des forces exercées par les montagnes aux échelles planétaires, échelles que nous n'étudierons pas dans cette thèse. Des liens ont été d'abord mis en évidence par Lejenäs et Madden (2000) entre les ondes de Rossby, le couple des montagnes et le moment cinétique de l'atmosphère, dans la bande de périodes de 6 à 15 jours. Plus récemment, le couplage du moment cinétique de masse avec le couple des montagnes a été mis en évidence

dans les périodes inférieures à 50 jours. Son rôle est significatif sur la dynamique du signal dominant de la variabilité basse fréquence aux moyennes et hautes latitudes de l'hémisphère nord, à savoir l'Oscillation Arctique (AO) (Lott et al. 2004, Lott et D'Andrea 2005). Enfin, des effets de ce même couple sur les ondes de marée ont récemment été mis en évidence aux fréquences semi-diurne et diurne (Lott et al. 2007).

Dans la suite de cette introduction, nous présenterons d'abord de façon simple les ondes de montagne et les concepts importants qui leurs sont rattachés, puis nous expliquerons comment elles agissent sur la circulation atmosphérique de grande échelle. Ensuite, nous tenteront de définir la problématique de la cyclogénèse de montagne, et son évolution jusqu'à nos jours. Enfin, nous donnerons un aperçu de la paramétrisation des ondes de montagne depuis ses débuts jusqu'à nos jours.

1.2 Ondes de montagne

1.2.1 Structure des ondes de montagne

L'appellation "onde de montagne" fait en réalité référence à une Onde de Gravité (OG) relativement stationnaire générée par l'action du vent sur le relief. La présence de ces ondes se signale parfois par des signatures nuageuses très particulières, telles que des nuages lenticulaires au dessus des pics ou en aval d'une chaîne de montagne, ou des bandes de nuages parallèles en forme de rouleaux. Un premier exemple est montré dans la Fig. 1.2, où les nuages sont observés directement (la photo) et par LIDAR lors d'un vol en altitude (Smith et al. 2002). Les nuages lenticulaires sont détectés par le LIDAR en (z=7.5km ;d=47km) et (z=9km ;d=50km), alors que les couches de cirrostratus (z=9-12km) et de cumulus (z=4-6km) sont manifestement déformées par les oscillations verticales dûes aux ondes. Un deuxième exemple est présenté dans la Fig. 1.3 (Volkert et al., 2003).

La structure d'une OG de montagne est déterminée bien sûr par la taille et la forme de la montagne, mais aussi par les caractéristiques de l'écoulement, notamment le profil vertical de température (ou de température potentielle, caractérisé par la fréquence de Brunt-Vaisälä $N(z)$), celui de l'humidité, et le profil vertical du vent $U(z)$. En première approximation, on peut tirer beaucoup d'informations de la théorie linéaire, qui suppose la longueur d'onde verticale grande devant la hauteur de la montagne. On obtient alors pour une onde monochromatique de nombre d'onde horizontal k et vertical m, en supposant que $N(z)$ et $U(z)$ varient suffisamment lentement (approximation WKB), le lien suivant (voir par exemple Smith 1979, Durran 1986b et 1990, Baines 1995, Salby 1996, Wurtele 1996, Fritts et Alexander 2003) :

$$m^2 = S - k^2 \quad \text{avec} \quad S(z) = \frac{N(z)^2}{U(z)^2}. \tag{1.1}$$

Ceci implique que toute la structure géométrique est contenue dans le paramètre S, appelé *paramètre de Scorer* (Scorer, 1949), et dont l'expression donnée ici est approximative par souci de simplicité. Notamment, on voit que les ondes trop courtes ne pourront se propager verticalement, car leur fréquence intrinsèque Uk est supérieure à N, la fréquence propre de l'atmosphère pour les oscillations verticales dues à la force d'Archimède. Autrement dit, le temps d'advection du fluide le long de la montagne $1/(Uk)$ est plus court que le temps de réaction de l'atmosphère dû à sa stratification, d'où l'absence de propagation de la perturbation dans le milieu. En pratique, c'est pour des échelles orographiques inférieures à 5 à 10km que les ondes de montagne ne sont plus propagatives. Elles participent alors à la formation de la couche limite turbulente de surface, ce sur quoi nous reviendrons.

On voit aussi que pour les ondes très longues, ce qui correspond à l'approximation hydrostatique, la longueur d'onde verticale vaut $\lambda_z = \frac{2\pi U}{N}$. Ceci permet de préciser le critère de linéarité cité plus haut. Pour cela on définit à partir de la hauteur H de la montagne, sa hauteur adimensionnée h, qui est aussi l'inverse du nombre Froude local :

$$h = \frac{NH}{U} = \frac{1}{\mathrm{Fr}}. \tag{1.2}$$

Pour $h > 1$ l'onde devient non linéaire et du déferlement peut se produire là où les isentropes sont si inclinées que du fluide lourd se retrouve au dessus du fluide léger.

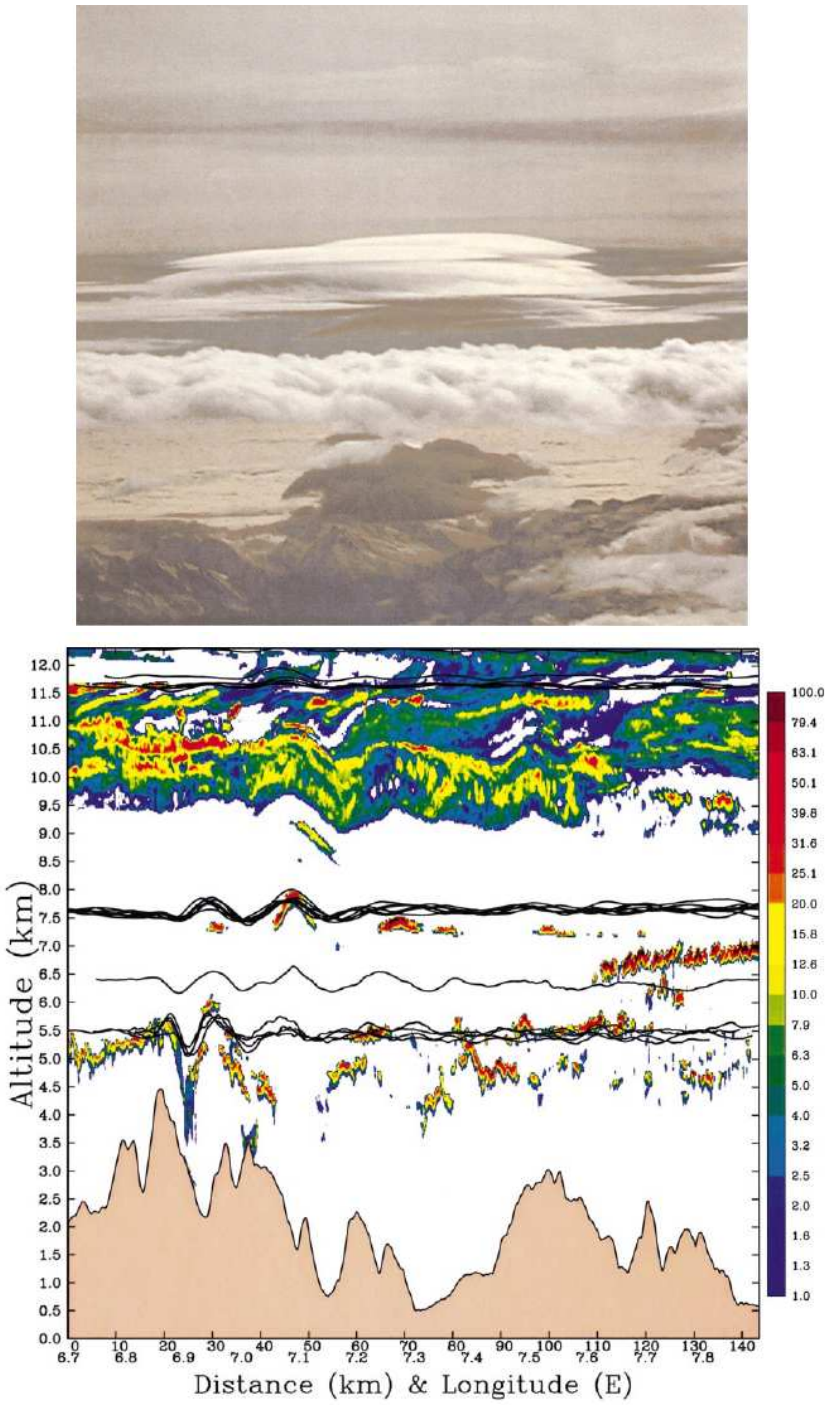

FIG. 1.2 – Ondes de gravité de montagne observées par avion le 2 Novembre 1999 au dessus du Mont Blanc. La photo montre différentes couches de nuages superposées : une couche (sombre) de cirrostratus au dessus, un ensemble de nuages lenticulaires à la hauteur du vol, et des cumulus en dessous. La figure du bas représente les données reccueillies par le LIDAR embarqué sur l'avion, ainsi que le déplacement vertical des parcelles de fluide (traits noirs) déterminé à chaque traversée de l'avion (Smith et al. 2002).

On parle alors d'*instabilité convective*. Cela peut être provoqué localement par une augmentation de stratification et/ou une décroissance du vent, qui fait augmenter $h(z)$, comme c'est le cas à l'entrée dans la basse stratosphère. De façon générale, cela peut se produire pour une amplitude de l'onde suffisamment forte, ce qui arrive notamment

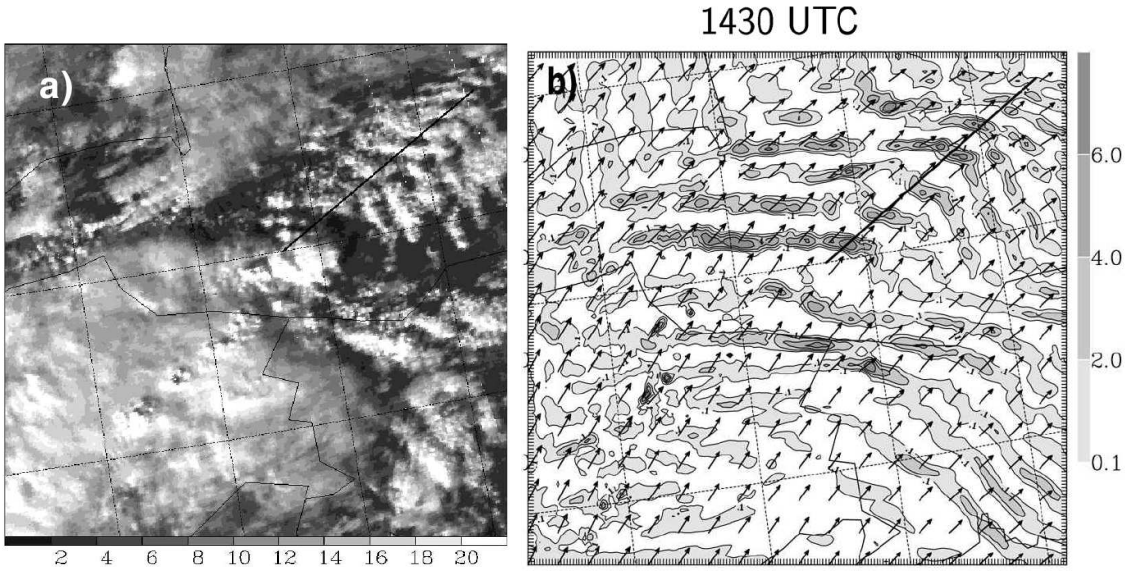

FIG. 1.3 – Ondes de gravité de montagne observées le 25 Octobre 1999 sur la partie Est des Alpes : a) photo satellite prise dans le canal visible (NOAA-14) à 14h22 UTC (radiances en $W.m^{-2}.sr^{-1}$) ; b) section horizontale à 5km d'altitude et à 14h30 UTC de la vitesse verticale (contours et nuances de gris, en $m.s^{-1}$) et du vent horizontal (flèches, vent moyen de 25 $m.s^{-1}$) simulées avec le modèle MESO-NH (Volkert et al. 2003).

à haute altitude parce que la densité décroît, ou à bas niveau simplement parce que la montagne est très haute et le vent suffisamment faible. Dans un tel cas, l'écoulement tend à s'accélérer juste derrière la montagne dans les basses couches, donnant lieu à l'effet de Foehn sec, caractérisé par des vents descendants très forts au pied de la montagne (Lilly 1978, Peltier et Clark 1979, Hoinka 1985, Durran et Klemp 1987, Durran 1990). Si le relief est 3D (montagne isolée), on peut aussi observer la séparation de l'écoulement dans les couches inférieures pour contourner l'obstacle (Miranda et James, 1992). Dans ces conditions, les effets visqueux deviennent non négligeables, et conduisent à la formation d'un sillage. Nous reviendrons en détail sur ces effets dans la section 1.4.

1.2.2 Niveaux singuliers

Notons qu'en réalité, les conditions de variations lentes de N et U nécéssaires à l'étude précédente sont rarement vérifiées, et l'approximation WKB n'est alors, en toute rigueur, plus qu'un support de pensée pour interpréter le comportement de l'onde. Elle est cependant largement utilisée, y compris en pratique, et s'avère relativement efficace. Utilisons-là donc encore pour exploiter davantage la relation (1.1).

On voit qu'à l'approche d'un niveau z tel que $S(z) - k^2$ devient négatif, l'onde ne peut plus se propager verticalement et devient évanescente. L'onde est alors réfléchie, il s'agit d'un *point de rebroussement*. L'onde peut rencontrer un tel niveau si elle entre dans une zone de stratification plus faible (ce qui arrive à l'entrée d'une zone turbulente mélangée, par exemple si l'onde est non linéaire et déferle à ce niveau), ou si le vent augmente suffisament (ce qui peut arriver lors de la traversée du jet des moyennes latitudes, qui est maximal dans la basse stratosphère). Dans ces conditions, l'onde peut subir des réflexions successives et répétées sur le sol puis au point de rebroussement,

jusqu'à constituer une *onde piégée*, contrainte à progresser horizontalement (Scorer 1949, Bretherton 1969). Ce type d'onde peut propager l'effet de la montagne relativement loin en aval, et donner lieu aux formation nuageuses périodiques citées plus haut.

Enfin, l'existence d'un niveau de vent nul implique, toujours par la relation (1.1), que la longueur d'onde verticale doit tendre vers 0. On parle alors de *niveau critique* (Booker et Bretherton, 1967). Si l'onde n'est pas stationnaire, ce niveau intervient là où la vitesse du vent de base rejoint la vitesse de phase de l'onde. A son approche, le mécanisme oscillatoire ne peut plus fonctionner "normalement" puisque le milieu ambiant supportant l'onde se déplace à la même vitesse que celle-ci. Il en résulte que la vitesse verticale est fortement réduite, alors que la vitesse horizontale tend à diverger. La longueur d'onde verticale tend vers zéro, et le vecteur d'onde devient vertical. Comme la vitesse de groupe doit rester perpendiculaire à ce dernier, l'énergie se propage de plus en plus horizontalement. Cette singularité génère localement des gradients importants, qui conduisent aussi au déferlement de l'onde. Celle-ci est alors dissipée dans cette couche critique, qu'elle ne peut traverser sans subir une forte absorption. On parle donc d'*absorption au niveau critique*, du moins pour les ondes de faible amplitude. Il va de soi que la prise en compte des effets non linéaires en cas d'ondes intenses complique le processus, notamment par l'existence de réflexions (ex : Clark et Peltier 1984, Lott et Teitelbaum 1992). Au demeurant, ce qui nous intéresse dans un premier temps est qu'en déferlant, l'onde va être partiellement ou entièrement dissipée à partir d'un certain niveau. Notons enfin, ce qui aura son importance par la suite, qu'en trois dimensions, l'existence d'une composante de vent perpendiculaire au vecteur d'onde ne change pas la nature critique du niveau considéré. En particulier, les ondes stationnaires ($\omega = 0$) rencontrent un niveau critique là où le vent est perpendiculaire à leur vecteur d'onde, car leur pulsation intrinsèque s'annule :

$$\Omega = \omega - \mathbf{k}.\mathbf{U} = 0 - \mathbf{k}.\mathbf{U} = 0. \tag{1.3}$$

Lorsque le vent tourne avec l'altitude, et que plusieurs vecteurs d'onde sont présents, on parle alors de *niveaux critiques directionnels* (Shutts, 1995).

1.2.3 Effets de la rotation terrestre à plus grande échelle

Bien que l'appellation "onde de montagne" soit plutôt réservée à des échelles horizontales suffisamment courtes pour que les effets de la rotation terrestre soient négligeables (le nombre de Rossby $\frac{Uk}{f}$ est grand devant 1), il est utile de comprendre ce qui arrive pour des montagnes de plus en plus larges. La fréquence intrinsèque se réduit, mais ne doit pas être inférieure (en valeur absolue) au paramètre de Coriolis f pour que l'onde reste propagative. La vitesse verticale est proportionnellement plus faible au profit d'un mouvement de plus en plus horizontal. On parle alors d'*Onde d'Inertie-Gravité* (OIG)[4]. Le retour au cas des OG pures correspond donc à l'hypothèse limite $f = 0$. Une conséquence importante de la prise en compte de f est l'apparition de deux nouvelles singularités dans l'équation de propagation verticale dans un vent variable, qu'on appelle *niveaux critiques inertiels*, là où la fréquence intrinsèque vaut $\pm f$ (Jones, 1967).

[4]Dans la suite, on utilisera OG pour l'ensemble du spectre sans distinction, ou alors OIG et OG pure pour distinguer les domaines : avec rotation ou sans.

Si l'on continue à élargir l'échelle horizontale de la montagne, le nombre de Rossby devient inférieur à 1 et la perturbation engendrée par la montagne n'est plus propagative par le biais de la stratification verticale en densité de l'atmosphère. On entre alors dans la catégorie des mouvements lents, qui peuvent être décrits à l'aide d'un formalisme équilibré, tel que le formalisme Quasi-Géostrophique (QG) (Charney, 1948) ou Semi-Géostrophique (SG) (Hoskins, 1975). Cependant, cette perturbation peut maintenant se propager via un mécanisme d'onde de Rossby, grâce à la stratification horizontale de la vorticité planétaire ("l'effet beta", autrement dit grâce à la sphéricité de la Terre), ou grâce à la baroclinicité de l'état de base sous forme d'onde de Rossby de bord, dite onde de Eady (Eady, 1949).

Cela dit, selon le profil du vent et les échelles excitées par la montagne, des niveaux critiques inertiels peuvent exister, séparant des régions où la fréquence intrinsèque est soit supérieure soit inférieure à f. Ainsi, une coexistence est possible entre une onde d'inertie-gravité (propagative) et un mouvement lent équilibré, chacun existant dans des domaines de l'espace séparés par les niveaux critiques inertiels (Nakamura 1988, Wurtele et al. 1996 Shutts 2001, Plougonven et al. 2005). C'est dans ce contexte d'échelles intermédiaires sous-synoptiques, que nous étudierons l'effet des montagnes dans les parties III et IV de cette thèse.

1.2.4 Interaction Ondes de montagne - Ecoulement moyen

Outre le fait que les ondes de montagne peuvent déclencher localement des formations nuageuses et des précipitations, ou mélanger l'air et donc agir sur le transport et sur la chimie atmosphérique, elle peuvent avoir un impact à des échelles bien plus grandes. Cela peut se comprendre de la façon suivante.

La structure classique de l'onde comporte, près de la surface, une surpression sur la pente exposée au vent (montante), et une dépression derrière le sommet, sur l'autre pente (descendante). Cela donne lieu à une force de pression résultante non nulle, exercée sur la topographie dans la direction de l'écoulement moyen. Cette force traduit en fait un transfert de moment cinétique depuis l'atmosphère vers la Terre solide. S'il est relativement bien reconnu que les montagnes se déplacent très peu sous l'effet du vent... (voir De Viron et al. 2005 pour l'influence de l'atmosphère sur le mouvement de la Terre solide), on en déduit que réciproquement l'atmosphère doit être freinée par cette interaction avec la surface. Pour comprendre comment et où la montagne exerce une force sur l'atmosphère, on écrit l'équation du bilan de quantité de mouvement zonale en négligeant la rotation terrestre, en introduisant la vitesse totale $\mathbf{v}$ et sa composante zonale $u = \mathbf{v}.\mathbf{e}_x$, ainsi que la pression p et la masse volumique ρ :

$$\frac{\partial \rho u}{\partial t} + \boldsymbol{\nabla}.(\rho\, u\, \mathbf{v} + p\, \mathbf{e}_x) = 0. \tag{1.4}$$

On l'intègre ensuite sur un volume compris entre la surface $z = h(x)$ (pour une montagne invariante selon y) et une altitude arbitraire z_t, en supposant le domaine périodique selon x, ou en choisissant les parois latérales du volume suffisamment loin pour que les flux à travers elles soient négligeables, ce qui donne :

$$\frac{\partial}{\partial t} \iiint \rho u \,\mathrm{d}x\,\mathrm{d}y\,\mathrm{d}z = - \iint \rho u w \,\mathrm{d}x\,\mathrm{d}y \Big|_{z=z_t} - \iint p\, \frac{\partial h}{\partial x} \,\mathrm{d}x\,\mathrm{d}y \Big|_{z=h}. \tag{1.5}$$

Cette équation signifie que lorsque l'onde de montagne est présente, la force de trainée due à la pression de surface exerce une force de freinage sur le volume de fluide (2ème

terme du second membre), qui peut être compensée par l'existence d'un flux descendant de quantité de mouvement à travers le niveau z_t (1er terme du second membre), qui en l'occurence est porté par l'onde de montagne. Autrement dit, si à partir d'un certain niveau l'onde est partiellement dissipée parce qu'elle déferle, ce flux descendant sera amoindri et donc ne pourra compenser le frein de surface dû à la montagne.

Ainsi, tout se passe comme si la montagne exerçait directement une force là où l'onde est dissipée. Cela peut se comprendre en recourant au formalisme de l'interaction onde - écoulement moyen. Si $\bar{u}$ est la valeur moyenne de u sur un domaine périodique (ou sur un domaine suffisamment grand), et u' l'écart à cette moyenne, on peut établir l'équation d'évolution de la moyenne sous l'effet de la perturbation ondulatoire. Dans le cadre anélastique non tournant, elle s'exprime ainsi (Eliassen et Palm, 1961) :

$$\frac{\partial \rho_0 \bar{u}}{\partial t} = -\frac{\partial}{\partial z}\left(\rho_0 \overline{u'w'}\right). \tag{1.6}$$

Le théorème d'Eliassen-Palm indique par ailleurs que, pour des ondes de faible amplitude linéaires et stationnaires, et lorsque les ondes sont négligeables aux frontières du domaine, le flux $\rho_0\overline{u'w'}$ est constant sur la verticale sauf si l'onde subit localement de la dissipation, ce qui sous l'hypothèse linéaire ne peut arriver qu'en présence d'un niveau critique. Des versions plus générales de ce théorème ont été données par la suite pour différents types d'ondes, introduisant la notion d'*activité d'onde* censée traduire les effets instationnaires, et celle de *circulation résiduelle* pour exprimer plus simplement l'effet des ondes dans le cadre Eulérien transformé (Boyd 1976, Andrews et McIntyre 1976a et b, 1978a, b et c). Nous retiendrons ici simplement que de façon générale, l'onde de montagne transporte une petite partie de la quantité de mouvement de l'écoulement de grande échelle vers le bas, depuis les niveaux où elle subit de la dissipation, c'est-à-dire de façon générale là où elle déferle. Ce flux de quantité de mouvement est transféré à la topographie par la force de trainée due aux forces de pression de surface.

Avant de poursuivre, une précision sémantique s'impose ici. En français, le terme *traînée* correspond à une force de freinage liée à l'écoulement sur un obstacle, opposée à la vitesse du fluide. Or d'une part, les OG peuvent dans certains cas accélérer l'écoulement, et non pas le freiner (cf 1.2.5). D'autre part, un obstacle peut aussi exercer sur le fluide une force perpendiculaire à sa vitesse, verticale et/ou horizontale, qu'on appelle la *portance*. C'est souvent le cas pour les ondes de montagne, et nous y reviendrons. L'ambiguité provient probablement de l'utilisation du terme *drag* en anglais, qui selon les cas signifie la *traînée*, qui est une force s'exerçant sur une surface, ou le *flux de quantité de mouvement* $\rho_0\overline{u'w'}$, qui a la dimension d'une contrainte, et dont découle la force volumique appliquée au fluide en tout point via l'Eq. (1.6). C'est pourquoi dans la suite, nous utiliserons prioritairement le terme *contrainte* lorsque la distinction entre ces significations ne s'impose pas.

Notons que l'existence de cette force localisée n'est pas le seul mode par lequel les ondes de montagne peuvent agir sur l'écoulement moyen. Notamment, en déferlant elles induisent aussi du mélange qui peut se traduire par une diffusivité turbulente. C'est le cas dans la haute mésosphère et la basse thermosphère, où les ondes de gravité sont tenues pour responsables d'un important mélange de l'énergie et des traceurs. Dans une moindre mesure, la dissipation des ondes de gravité peut aussi induire de la diffusion de la quantité de mouvement, et aussi provoquer un chauffage local (Fritts

et Alexander, 2003). D'autre part, d'autres processus d'interaction entre les ondes et l'écoulement moyen ont été récemment mis en évidence, tels que l'effet non dissipatif de *recul à distance* (Bühler et McIntyre 2003) ou l'effet de *capture d'onde* par un écoulement cisaillé (Bühler et McIntyre 2005). Ces effets, liés à la réfraction des OG se propageant dans un écoulement lent et de grande échelle, font appel à une formulation plus subtile des théorèmes de conservation de la quantité de mouvement.

1.2.5 Ondes de gravité et circulation générale de l'atmosphère

On a donc montré que de façon générale, les montagnes peuvent exercer un forçage sur la circulation atmosphérique grâce au déferlement des OG stationnaires, mais aussi des ondes de Rossby (planétaires) qu'elles génèrent (Andrews 1987a, McIntyre 2001). Or d'autres sources importantes d'OG existent, telles que la convection ou les instabilités de jets, qui génèrent plutôt des ondes non stationnaires. Le rôle de ces dernières peut se comprendre de la même façon que précédemment, à condition d'ajouter ce corollaire du théorème d'Eliassen-Palm : une OG non stationnaire qui se dissipe à un niveau de déferlement tend à accélérer l'écoulement moyen dans le sens qui le rapproche de sa propre vitesse de phase. Par conséquent, le rôle des OG ne se réduit pas à exercer un frein sur l'écoulement de grande échelle. Elle peuvent aussi l'accélérer, au sens de l'intensifier.

Le rôle global des OG sur la circulation atmosphérique est schématisé sur les Figs. 1.4 (Kim et al., 2003) et 1.5 (Fritts et Alexander, 2003), qui représentent l'effet des OG sur le profil moyen du vent zonal aux moyennes latitudes en hiver et en été. Les deux diagrammes de la Fig. 1.4 peuvent être vus comme deux sections verticales aux moyennes latitudes de la coupe méridienne de la Fig. 1.5. Les trois principales sources d'OG y sont représentées (orographie, convection, jets), avec les vitesses de phase associées (c), ainsi que leurs niveaux de déferlement par rencontre d'un niveau critique ou par instabilité convective. On voit d'abord que de façon générale, le dépôt de quantité de mouvement dû aux ondes de gravité se produit essentiellement entre la haute troposphère et la basse thermosphère. Les deux courbes grises de la Fig. 1.4 indiquent l'allure qu'aurait le vent zonal en l'absence du forçage par les OG, c'est-à-dire découlant uniquement de l'équilibre radiatif-convectif de grande échelle, qui obéit prioritairement à l'équilibre géostrophique et hydrostatique. Cette représentation est conforme au paradigme classique, et simplificateur, qui présente la troposphère essentiellement comme une région source pour les OG, la stratosphère comme une zone principalement propagative, et la mésosphère et la haute stratosphère comme une région de déferlement important (Kim et al 2003). On voit en particulier que les OG ont un impact essentiel dans la haute stratosphère (40-50km), la mésosphère (entre 50 et 80-90km) et la basse thermosphère (80-90 à 100km) et, où elles freinent considérablement le vent zonal au point d'inverser son gradient. Notamment, le vortex cyclonique de nuit polaire (hiver) est considérablement atténué dans la mésosphère et la thermosphère, par les OG d'origine orographique et convective (de vitesse de phase négative) essentiellement. On y voit aussi, que les OG orographiques imposent une décélération importante dans la basse stratosphère, dont l'effet est plus marqué en hiver. Inversement, on remarque qu'en hiver par exemple, les OG convectives de vitesse de phase positive ainsi que les OG provenant des jets près de la tropopause, tendent à intensifier le jet d'ouest dans la stratosphère.

On comprend donc la représentation simplifiée de la Fig. 1.5, faisant apparaître

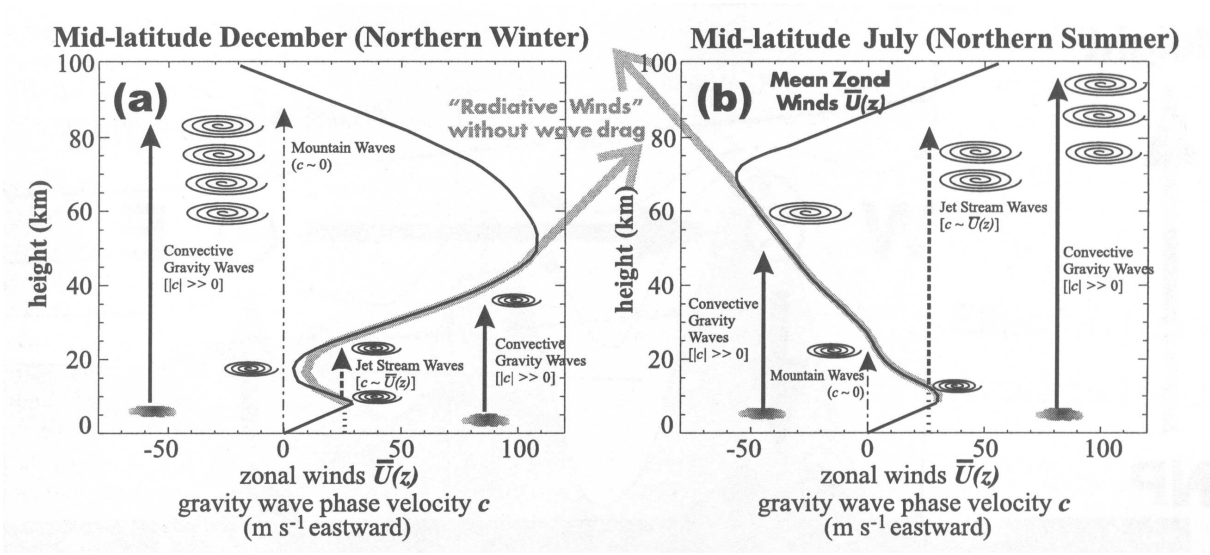

FIG. 1.4 – Schéma illustrant l'action des OG sur les vents zonaux aux moyennes latitudes, dont les profils moyens typiques sont représentés pour l'hiver boréal (a) et l'été boréal (b) (Kim et al. 2003). Les profils de vent attendus en l'absence de forçage par les OG sont représentés par des lignes grises épaisses terminées par des flèches. Les zones de déferlement et dissipation des OG, où celles-ci exercent une force zonale sur le vent moyen, sont indiquées par des spirales. La vitesse de phase des OG est indiquée par c et par la position des sources en abscisse.

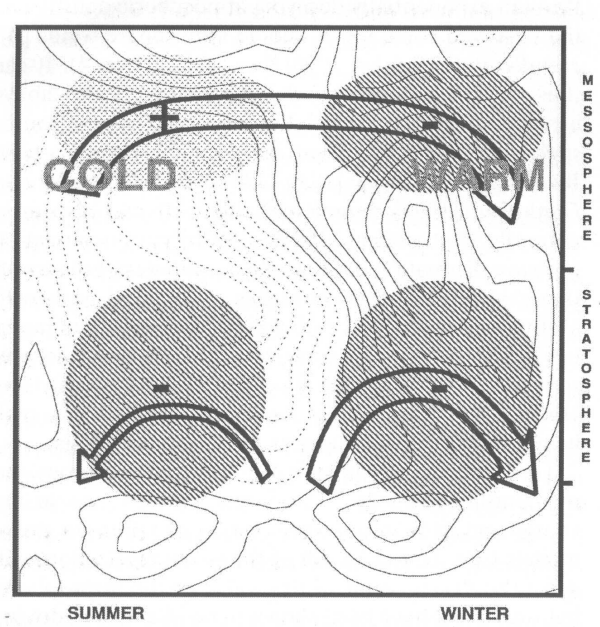

FIG. 1.5 – Schéma illustrant en moyenne zonale le rôle moteur des OG sur la circulation de l'atmosphère moyenne (Fritts et Alexander, 2003). Les zones grisées représentent la force zonale exercée par les OG (orientée vers l'ouest/est pour le signe -/+) sur les vents zonaux (contours pleins pour vent d'ouest, intervalle de 10m.s^{-1}). Le transport induit par les OG sous forme de circulation résiduelle est indiqué par les flèches.

quatre zones de freinage par les OG, deux dans la basse stratosphère et deux dans la mésosphère. Par un effet similaire à la dérive d'Ekman, ce forçage se traduit par une *circulation résiduelle* (représentée par les flèches) essentiellement méridienne, mais aussi verticale par conservation de la masse (Haynes et al. 1991, McLandress 1998). Cette circulation est inter-hémisphérique dans la mésosphère, alors qu'elle est dirigée vers les pôles dans la stratosphère. Cela contraint globalement un mouvement d'ascension dans l'hémisphère d'été, et de subsidence dans l'hémisphère d'hiver. Cette circulation résiduelle tend donc à refroidir la mésosphère d'été et réchauffer la mésosphère d'hiver, jusqu'à inverser localement le gradient thermique méridien imposé par l'insolation à cette altitude. Notons que la circulation résiduelle stratosphérique d'hiver est aussi forcée conjointement par les ondes planétaires dont l'effet est dominant à ce niveau. La découverte de ce mécanisme de couplage entre la troposphère et l'atmosphère moyenne a fait émerger la notion de *contrôle par le haut* (*downward control*), dont on pense aujourd'hui qu'il influence de façon perceptible la dynamique de la troposphère aux grandes échelles de temps, disons supérieures à une semaine (Haynes et al. 1991, Hamilton 1999). Remarquons que d'autres couplages importants impliquant les OG existent, donnant lieu aux Oscillations Quasi Bi-annuelle (QBO, Lindzen et Holton 1968) et Semi-Annuelle (SAO, Dunkerton, 1982).

Cette influence importante des OG sur la Météorologie et le climat, la nécessité de rendre compte de leur présence dans les observations, et de les paramétriser de façon satisfaisante dans les modèles, ont ainsi contribué à replacer les questions théoriques ayant traits aux OG au tout premier plan. En particulier, depuis une vingtaine d'années, des travaux considérables ont été menés pour mieux comprendre et quantifier les différents mécanismes d'une part de génération, et d'autre part de saturation non-linéaire des OG. Nous aborderons ces deux thématiques dans le cadre de cette thèse.

Concernant les sources d'OG, l'une des idées importantes est celle de l'ajustement géostrophique, par lequel un état initial non équilibré de l'écoulement émet des OIG en se relaxant vers un état équilibré correspondant à la distribution initiale de vorticité potentielle (Rossby 1937, Blumen 1972, Fritts et Luo 1992). C'est dans ce cadre qu'a notamment été proposé un mécanisme indirect dû aux montagnes, dit de *génération secondaire*, dans lequel la force générée par des OG de montagne courtes qui déferlent excite des OIG de grande échelle (Scavuzzo et al. 1998, Vadas et al. 2003, Lott 2003). Plus récemment, l'idée s'est progressivement imposée qu'à l'inverse, un écoulement équilibré n'a pas de raison de le rester indéfiniment, et que son évolution peut le conduire à émettre des OIG (Ford et al. 2000, Plougonven et Zeitlin 2002, Vanneste et Yavneh 2004, Viúdez et Dritschel 2006, Plougonven et Snyder 2007, Snyder et al. 2007, Viúdez 2008, Ólafsdóttir et al. 2008). C'est dans ce cadre que nous proposerons un autre mécanisme de génération secondaire lié au déferlement des ondes de gravité de montagne courtes.

1.3 Cyclogénèse de montagne

1.3.1 Observations

L'avènement des observations systématiques des épisodes de cyclogénèse a permis la mise en évidence du rôle significatif joué par les massifs montagneux, qui se révèlent être des régions propices (Pettersen 1956, Whittaker and Horn 1984). Les massifs des Rocheuses et des Alpes ont été particulièrement étudiés, et donnent lieu chacun à un archétype de cyclogénèse de montagne (Pierrehumbert, 1986). D'autres massifs sont cependant répertoriés, comme ceux du Groënland, du plateau tibétain, de l'Atlas algérien, de l'Altaï en Sibérie, ou du Japon, pour ce qui est de l'hémisphère nord. Au sud, les épisodes de cyclogénèse de montagne sont bien sûr beaucoup moins fréquents, mais on cite toutefois les effets du massif andin, ainsi que du massif trans-Antarctique (Schär, 2003).

La notion de cyclogénèse de montagne recouvre une réalité météorologique et climatologique assez vaste, répondant à de multiples critères qui tendent à faire de chaque cas un cas à part. En premier lieu, tout dépend bien sûr des caractéristiques géométriques du massif et du type de régime de vent associé à la région et à la saison. De ce point de vue, la grande diversité morphologique des massifs montagneux cités ci-dessus laisse entrevoir des mécanismes tout aussi divers, comme en témoignent les deux cas relativement différents des Rocheuses et des Alpes (développés ci-après). Tout dépend aussi de l'échelle des phénomènes observés. Littéralement, le terme *cyclogénèse* signifie création de vorticité. Or les vortex de sillage peuvent apparaître à des échelles multiples a priori, depuis les méso-échelles (10km) jusqu'aux échelles synoptiques (1000km). D'ailleurs, historiquement la notion de cyclogénèse était directement rattachée à une chute de pression notable localisée, et le terme anglais *cyclone* désignait une dépression (Pierrehumbert, 1986). Si l'on se focalise sur la production de structures intenses et de grande échelle qui tendent à évoluer vers des dépressions extra-tropicales classiques, alors l'influence des montagnes peut être résumée de façon générale comme suit. Elle consiste souvent à déclencher et/ou moduler un épisode de cyclogénèse extra-tropicale classique[5], qui sans montagne se serait produit probablement à un endroit proche et un peu plus tard (Schär, 2003).

Par exemple, l'effet typique du massif très étendu des Rocheuses consiste globalement à dévier vers le sud et amplifier les systèmes dépressionnaires classiques en provenance du Pacifique, s'approchant des côtes du nord-ouest des Etats-Unis et de l'Alaska (Palmén and Newton 1969, Bannon 1992, Davis 1997). Le centre dépressionnaire est bloqué par l'anticyclone situé sur le massif, il se dirige vers le pôle et s'affaiblit au nord du massif, au profit d'un nouveau centre de basse pression qui apparaît 1000 km plus bas, au sud du massif, débouchant typiquement sur la région du Colorado. Il s'ensuit alors souvent une amplification suite au couplage avec le thalweg stratosphérique[6] qui termine sa traversée du massif. Parfois, la dépression est déviée encore plus loin au sud et rejoint la "storm track" atlantique sur la côte est.

Le cas Alpin est très différent, d'abord parce que les dimensions horizontales du massif sont 5 à 10 fois plus petites pour une hauteur moyenne équivalente (environ 3km), et que le "croissant" Alpin est globalement orienté est-ouest contrairement aux

[5] c'est-à-dire impliquant les ingrédients habituels, à savoir le couplage vertical entre une anomalie thermique basse et une anomalie de vorticité potentielle haute.

[6] ou *thalweg de haut niveau*, traduction pour "upper-level trough".

Rocheuses. Il est caractérisé par un mécanisme en deux phases (Buzzi et Tibaldi, 1978), illustré sur la Fig. 1.6 (Schär, 2003).

Il se produit à l'approche du massif par l'Europe centrale ou du nord, d'un système dépressionnaire classique, c'est-à-dire d'un front froid de bas niveau suivi d'un thalweg de haut niveau (Bleck et Mattocks 1984, Pichler et Steinacker 1987, Tafferner 1990). Cette approche s'accompagne d'un foehn de sud derrière la montagne qui est chaud et humide, et donc qui déstratifie la zone du golfe de Gènes et de l'Italie du nord (Fig. 1.6A). Au contraire, l'air froid arrivant devant la montagne est beaucoup plus stratifié. Cette situation engendre la distortion du front qui se trouve retardé par le massif, le blocage et la séparation de l'écoulement de bas niveau (qui donne lieu respectivement au Mistral au sud et à la Bora au nord), l'amplification de la baroclinicité et d'un gradient de pression important entre l'avant et l'arrière de la montagne (Fig. 1.6B). C'est dans ce contexte dynamique essentiellement sec que la première phase se déroule, consistant alors en la formation rapide d'un noyau dépressionnaire de petite taille en surface, au voisinage du golfe de Gènes. Ce noyau cyclonique est associé à une anomalie thermique chaude. Il s'amplifie ensuite rapidement et peut s'éloigner (Fig. 1.6C). Pendant la deuxième phase, moins rapide, ce précurseur interagit avec le thalweg de haut niveau qui dépasse alors le massif, dans un environnement humide où les effets diabatiques peuvent maintenant avoir un rôle moteur. Si le déphasage est optimal, il se mue en une dépression extra-tropicale intense et dérive vers l'Europe de l'Est ou la côte nord-méditerranéenne. Les forts vents de sud qui le devancent peuvent alors entraîner des orages sur l'Adriatique et de fortes précipitations sur l'Italie du Nord et les Alpes de l'Est (Kljun et al, 2001).

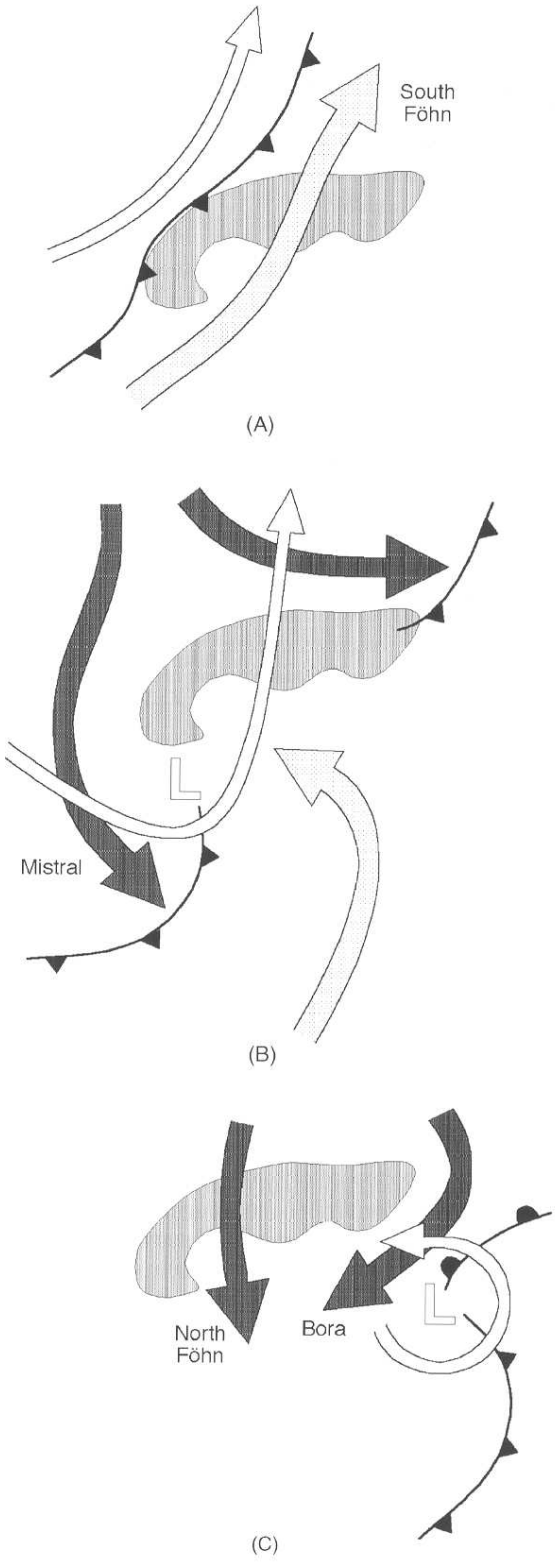

FIG. 1.6 – Réprésentation schématique d'un événement de cyclogénèse alpine classique (Schär, 2003). Les grosses flèches représentent l'écoulement de bas niveau, en face du front froid (flèches blanches) ou derrière (flèches noires). Les flèches fines représentent l'écoulement en altitude.

1.3.2 Théories et mécanismes

De nombreuses théories ont émergé notamment au cours des années 80, pour expliquer les mécanismes dynamiques associés à la cyclogénèse de montagne. Pour les appréhender, il est utile de positionner d'abord le problème à l'aide d'au moins deux nombres sans dimensions. En introduisant des échelles de longueur horizontale L et verticale H caractéristiques du massif, une vitesse U et une fréquence de Brunt-Väisälä N caractéristiques de l'écoulement dans les basses couches, on définit une hauteur adimensionnée h comme précédemment (section 1.2.1), et un nombre de Rossby Ro :

$$h = \frac{NH}{U} \quad \text{and} \quad \mathrm{Ro} = \frac{U}{fL} \tag{1.7}$$

Le nombre de Rossby traduit le caractère équilibré ou non de l'écoulement. Plus il est petit devant 1, plus l'écoulement peut être raisonnablement décrit par le formalisme Quasi-Géostrophique (QG). Quant au nombre h, son interprétation a été est présentée en 1.2.1. L'application d'un modèle QG requiert aussi une condition de faible pente sur l'orographie (Schär et Davies, 1988), qui s'écrit en comparant la hauteur de la montagne H à la hauteur caractéristique de pénétration d'une anomalie de surface associée au rayon de déformation L :

$$\mathrm{Ro}\, h = \frac{NH}{fL} < \frac{1}{2} \quad (\text{ ou} < 1 \text{ en 2D }). \tag{1.8}$$

L'observation des régimes de vents correspondant aux massifs montagneux cités est résumée sur le schéma de la Fig. 1.7 (Schär, 2003), qui montre le résultat important suivant : la plupart des phénomènes de cyclogénèse de montagne réels ne peuvent être décrits correctement par la dynamique QG, et l'on ne peut y négliger les effets non linéaires. De plus, l'utilisation de balances d'ordre supérieur à la balance QG n'est pas de nature à améliorer fondamentalement les choses. Néanmoins, de nombreuses théories ont été proposées dans le cadre QG, linéaire ou non. Celui-ci permet somme toute de comprendre au moins qualitativement des mécanismes essentiels, qui de plus peuvent largement influencer voire contrôler la dynamique méso-échelle. C'est le cas des théories que nous évoquons maintenant.

Une approche courante consiste à considérer la modification par l'orographie de la propagation et de la croissance d'une onde barocline dans un écoulement de base cisaillé, ou autrement dit la *diffusion d'une onde barocline* par le relief. Dans ce cadre, le vent de base n'interagit pas avec la montagne (il est nul en surface), et on considère directement les perturbations secondaires dûes à l'onde barocline. Plusieurs approches sont alors proposées, souvent dans un cadre linéaire. On peut interpréter l'effet en terme d'excitation de modes normaux particuliers par la montagne (Speranza et al 1985, Buzzi et al 1987). On peut aussi considérer l'effet du barrage de l'écoulement méridien à bas niveau par l'orographie (Pierrehumbert, 1985). Ces deux approches peuvent être qualifiées de globales, car elles prennent en compte la modification par la montagne de l'écoulement total de grande échelle.

De façon générale, on peut aussi comprendre l'effet de l'orographie sur une onde barocline aux échelles synoptiques, en raisonnant localement et perturbativement à partir du principe suivant : si l'atmosphère a une stratification stable, et pour une évolution adiabatique, un écoulement de surface qui s'élève (descend) le long de la pente induit localement une anomalie de température potentielle négative (positive).

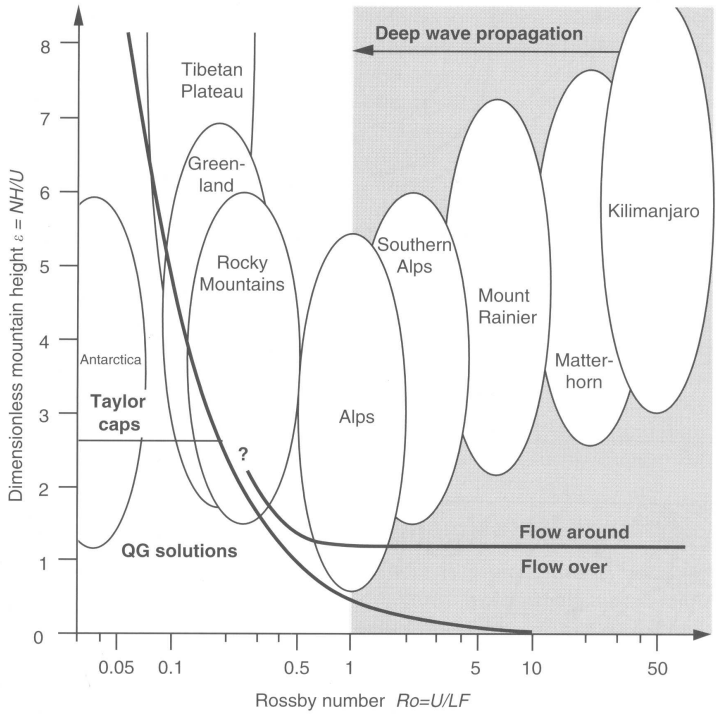

FIG. 1.7 – Diagramme des régimes d'écoulement pour un fluide stratifié sur une montagne idéalisée de hauteur H, de largeur L et de profil $H\,(1+\frac{r^2}{L^2})^{-\frac{3}{2}}$, pour un vent U et une stratification N uniformes. Sont superposés les domaines de paramètres typiques couverts par les principaux massifs montagneux (Schär, 2003).

On peut aussi raisonner par conservation de la vorticité potentielle, et dire qu'une ascension (descente) induit une compression (un étirement) des colonnes de fluide, donc une production locale de vorticité anticyclonique (cyclonique). Ces deux points de vue se rejoignent en fait dans le cadre QG (ou balancé plus généralement), sous la notion d'onde de Rossby de bord, qui se révèlent être un concept unificateur utile pour les effets synoptiques (Davis 1997, Davis et Stoelinga 1999). En effet, à une anomalie de température potentielle de surface positive (négative) correspond une circulation locale cyclonique (anticyclonique). Dans un environnement barocline, ces anomalies se propagent horizontalement selon un mécanisme similaire à celui des ondes de Rossby (Hoskins et al 1985).

Ce concept d'onde de Rossby (ou de Eady) de bord a le mérite de recouvrir aussi une autre théorie importante de cyclogénèse de montagne, locale, dont l'approche pouvait sembler à l'origine très différente de la précédente : celle de la *génération d'onde de montagnes baroclines* (Smith, 1984). Smith propose de modéliser l'environnement barocline qu'est le front incident distordu par le relief, par un vent cisaillé linéairement et tournant. Ce vent n'est pas nul en surface, et génère une onde barocline de bord stationnaire qu'il force à l'endroit de la montagne. Cette onde n'est autre qu'un paquet d'onde de Rossby (Eady) de bord forcé, qui se développe et se propage dans l'environnement barocline en obéissant à la correspondance température-vorticité décrite précédemment. L'intérêt de cette théorie réside notamment dans sa capacité à mieux rendre compte de la première phase (rapide) de la cyclogénèse Alpine, avec un développement rapide d'une dépression de petite échelle au voisinage de la montagne, du côté de la face descendante (pour le vent).

Ces trois théories centrales des années 80 (Speranza et al 1985, Pierrehumbert 1985 et Smith 1984, voir aussi la revue de Mesinger et Pierrehumbert 1986) furent testées par Egger (1988) at Tafferner et Egger (1990) sur des cas réels de cyclogénèse alpine observés pendant la campagne ALPEX (Alpine Experiment, 1982), et simulés par des modèles aux équations primitives. Ces tests montrèrent que les trois théories étaient chacune incapables de rendre compte correctement du phénomène, essentiellement à cause de l'absence de la composante non linéaire de la dynamique du front en présence de relief. Malgré cela, les "théories globales" restent intéressantes d'un point de vue climatologique (Buzzi et Tosi, 1989). Par ailleurs, la pertinence de la théorie de Smith fut soulignée par Schär (1990) dans une étude visant à tester les limites de la cyclogénèse alpine QG non-linéaire. Le mécanisme de Smith intervient dans la première phase et justifie l'échelle horizontale du vortex de sillage observé, mais se trouve amplifié du fait de la taille finie de la zone barocline au voisinage de la montagne, ce qui permet d'atteindre une dépression d'amplitude réaliste.

Plus récemment, la notion de diffusion d'une onde barocline par l'orographie a été revisitée, à la lumière des concepts d'instabilité convective ou absolue (Fantini et Davolio 2001). Un mode neutre de Eady est ajouté à l'état de base classique du problème de Eady, et on étudie les propriétés de stabilité de l'ensemble, c'est-à-dire les modes propres instables des perturbations secondaires à cet état de base. Si l'amplitude initiale de l'onde primaire est suffisamment grande, les modes instables sont de type "frontal" et traduisent une instabilité absolue, qui peut être déclenchée par la présence de l'orographie.

Cependant, comme montré précédemment (Fig. 1.7), les hypothèses de faible nombre de Rossby et de faible pente ne tiennent pas pour la majeure partie des cas réels de cyclogénèse de montagne. A l'approche d'obstacles de pente relativement forte, l'écoulement peut se séparer dans les basses couches pour contourner l'obstacle, ce qui engendre des effets visqueux non négligeables. De plus cela remet en cause l'hypothèse de surface isentrope pour la condition limite inférieure (Schär et Davies, 1988), sur laquelle sont basées toutes les théories précédemment citées. Du coup, dans la première phase de leur développement, les vortex cycloniques orographiques obéissent la plupart du temps à une dynamique largement non géostrophique, et visqueuse. Néanmoins, la seconde phase de leur développement, qui les conduit à maturité, a toutes les chances d'être largement équilibrée.

C'est pourquoi la problématique a progressivement évolué vers une autre question, celle plus générale de l'interaction entre un front et une montagne (Davies 1984, Egger et Hoinka 1992, Blumen 1992, et voir *Meteorology and Atmospheric Physics* vol.48, entièrement consacré à cette question). Cette analyse a notamment bénéficié de l'amélioration des simulations numériques aux équations primitives (Orlanski et Gross 1994, Gross 1994). Un mécanisme particulièrement bien documenté consiste en l'approche d'un front froid, qui se trouve retardé et distordu par le relief, et dans lequel le blocage de l'écoulement dans les basses couches mène à sa séparation. Ce mécanisme correspond particulièrement bien à la cyclogénèse alpine telle qu'elle a été observée pendant la campagne ALPEX (Radinović 1986, Pichler et Steinacker 1987, Kljun et al 2001), ainsi que plus tard lors de la campagne *German Front Experiment* (Hoinka et Volkert 1987, Hoinka et al. 1990, Hoinka et Volkert 1992). D'ailleurs, cet effet de blocage des Alpes était en fait connu depuis Ficker (1920), et Bergeron (1928)

qui en fit la première analyse. Cette distortion s'accompagne de la formation d'une anomalie chaude derrière la montagne, dont la taille peut excéder celle de la montagne elle-même (Kljun et al, 2001).

Par ailleurs, ces campagnes ont aussi permis de confirmer l'importance du second ingrédient typique de la cyclogénèse de motagne, à savoir une perturbation de haute troposphère incidente (correspondant à une anomalie de vorticité potentielle positive), et son rôle dans la seconde phase (Bleck et Mattocks 1984, Pichler et Steinacker 1987, Tafferner 1990), via un mécanisme de croissance barocline classique par couplage et verrouillage de phase avec l'anomalie de bas niveau (Hoskins et al. 1985).

1.3.3 Vers une vision moderne de la cyclogénèse de montagne

Dans ce contexte, la question de l'origine de la vorticité et de la Vorticité Potentielle (VP) dans les sillages montagneux est devenue centrale. En particulier, le cas des montagnes isolées (3D), de petite échelle horizontale (méso-échelle), pour des écoulements non linéaires (nombre de Froude inférieur à 1), a fait l'objet de nombreuses études sur la base de simulations idéalisées. Cette recherche, motivée notamment par l'observation occasionnelle d'allée de Von Karman dans les stratus en aval de certaines îles montagneuses (Chopra 1973), visait d'abord à montrer que la vorticité ne provenait pas d'une éventuelle couche limite de surface turbulente, contrairement aux allées de Von Karman observée en laboratoire à l'aide d'un obstacle cylindrique. Non sans controverse sur l'origine exacte de la vorticité[7] (Smolarkiewicz et Rotunno 1989, Smith 89a et b, Smolarkiewicz et Rotunno 1990, Rotunno et al. 1999), ces études ont permis d'une part d'imposer le point de vue d'anomalie de vorticité potentielle pour décrire la formation des sillages (Schär et Smith 1993, Schär et Durran 1997) grâce à l'élaboration d'un cadre théorique puissant (Pratt 1983, Haynes et McIntyre 1987 et 1990, et Schär 1993), et d'autre part de mieux comprendre les processus dissipatifs qui peuvent engendrer de la VP en l'absence de chauffage diabatique et d'effets frictionnels de surface (Schär et Smith 1993, Schär et Durran 1997, Epifanio et Durran 2002a et b).

Grâce à ces recherches, la question de la cyclogénèse de montagne se formule aujourd'hui à travers une nouvelle problématique. Il s'agit de comprendre *la production orographique d'anomalies de VP à bas niveau*, car cette production est intimement liée à l'établissement des vortex de sillage. Elle est la conséquence de la violation de la conservation de la VP par les divers phénomènes diabatiques et visqueux qui interviennent dans les écoulements réels sur la topographie : les effets de *friction de surface*, mais aussi la *dissipation* qui accompagne le déferlement des ondes de gravité à bas niveau, la recirculation dans le sillage, la séparation de l'écoulement autour de l'obstacle, ou encore le *chauffage diabatique* associé aux précipitations orographiques. Une fois produite dans la zone du sillage, les anomalies sont advectées par l'écoulement, formant des *bannières de VP*.

L'intérêt de la formulation en terme d'anomalie de VP est qu'elle apporte un cadre

[7]Il apparaît que les parcelles acquièrent de la vorticité verticale avant de subir les effets diffusifs, par un mécanisme purement non visqueux : la vorticité horizontale produite par la baroclinicité de l'écoulement au niveau de la pente descendante du relief, est ensuite partiellement transformée en vorticité verticale par cisaillement de la vitesse verticale (*vortex tilting*). Ce mécanisme ne rend toutefois pas compte de l'ampleur des anomalies de vorticité verticale obtenues dans le sillage (Epifanio et Durran 2002b).

conceptuel intermédiaire entre dynamique méso-échelle et synoptique. On sait en effet que c'est par la production d'anomalies de VP que les petites échelles peuvent agir sur les grandes (Raymond, 1992), ce qui de façon générale est potentiellement intéressant dans le contexte de la paramétrisation des effets orographiques sous-maille (voir section 1.4). En tout cas, c'est donc un excellent candidat pour décrire la cyclogénèse alpine qui se déroule en deux phases, dont la première est intrinsèquement non linéaire visqueuse et méso-échelle, alors que la seconde est plus synoptique et conforme à la vision classique de la cyclogénèse (en terme d'interaction entre une anomalie de VP haute et une anomalie de surface). Ainsi, Aebischer et Schär (1998) montrèrent qu'à l'approche d'un front froid précédant un épisode de cyclogénèse, les Alpes peuvent générer des bannières de VP primaires (de taille comparable au massif) ou secondaires (de la taille d'un pic individuel), les bannières primaires ayant toutes les chances de jouer un rôle de précurseur dans la cyclogénèse, en constituant le coeur de la future dépression. L'existence et l'apparente stabilité de ces structures (qui peuvent atteindre 1500 km de longueur) a été ensuite vérifiée par les observations faites en 1999 au cours de la campagne MAP[8], couplées à des simulations méso-échelles à haute résolution (Schär et al 2003, Flammant et al 2004, voir aussi la synthèse MAP à paraître sur ce sujet dans le Quarterly Journal). Ceci est illustré par la Fig. 1.8, qui représente la structure filamenteuse donnée au champ de VP en aval des Alpes par ces bannières secondaires, telle qu'observée lors de l'IOP[9] 15 de MAP (Flammant et al 2004). L'évolution de grande échelle associée est présentée plus loin dans la Fig. 1.9. Notons que les bannières secondaires, qui sont de petite échelle transverse, ont peu de chance d'influencer fortement les échelles synoptiques, mais nous montrerons cependant qu'elles peuvent avoir un rôle dans la génération d'ondes d'inertie-gravité (cf chapitre 4).

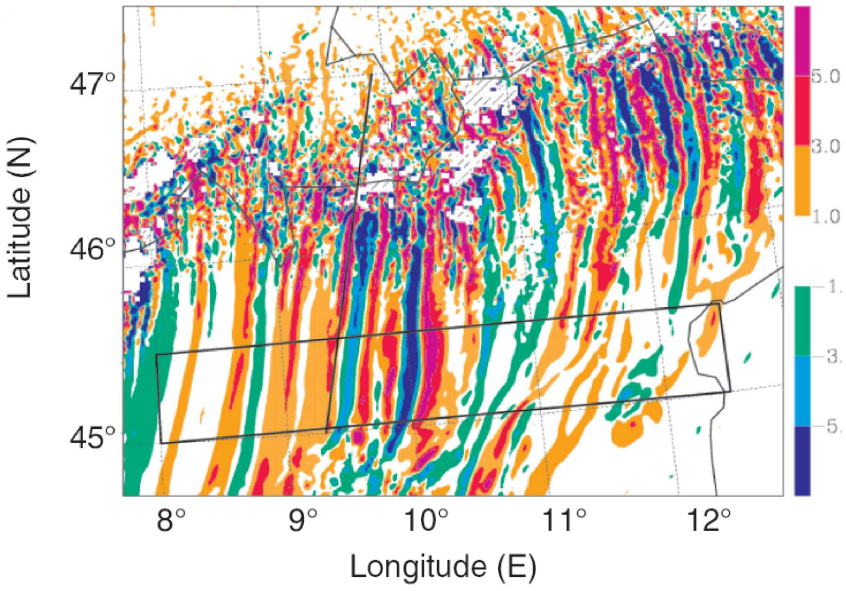

FIG. 1.8 – Champ de vorticité potentielle à 2700 m d'altitude (unité : 1 PVU=10^{-6}K.m^2.kg^{-1}.s^{-1}), à 14h00 UTC le 8 Novembre 1999, simulé par MESO-NH (résolution 2km). Les zones hachées représentent la section de l'orographie, et le rectangle noir les trajectoires de l'avion utilisé (Flammant et al 2004).

[8] *Mesoscale Alpine Program* (Binder et Schär 1996, Bougeault et al. 2001).
[9] *Intense Observation Period.*

A ce stade, si l'on devait retenir une idée simple de la cyclogénèse de montagne, ce serait qu'elle repose le plus souvent sur le blocage plus ou moins intense d'un front froid de bas niveau, associé à l'advection d'une anomalie positive de VP haute. Ce mécanisme a le mérite d'être compatible avec la théorie classique de la cyclogénèse (interaction de deux anomalies de VP), et d'être applicable à de nombreux massifs montagneux, parmi lesquels les Alpes et les Rocheuses. Lors de l'interaction du front froid avec le relief, divers processus peuvent contribuer à l'amplification de l'anomalie de VP basse, parmi lesquel le déferlement des ondes de gravité à bas niveau, qui retiendra notre attention dans cette thèse. Cependant le rôle des ondes de gravité dans la cyclogénèse ne se limite peut-être pas à cela.

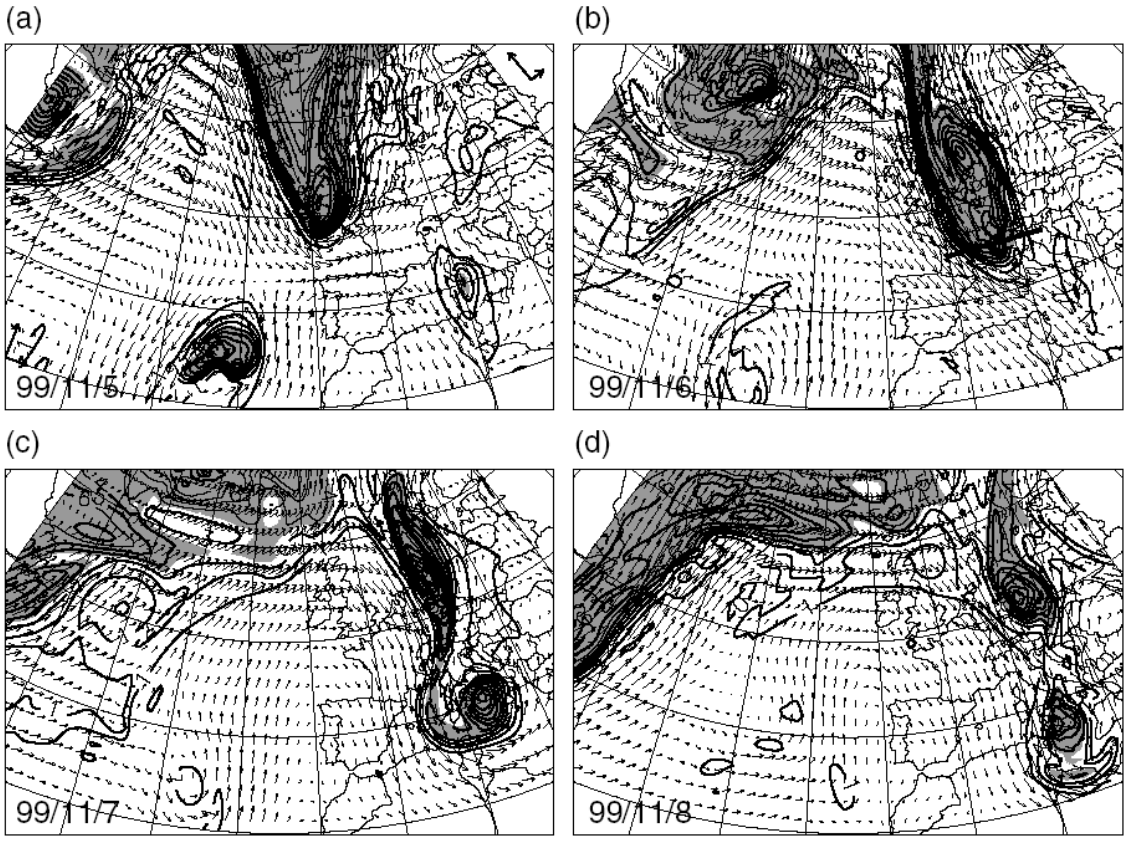

FIG. 1.9 – Analyses du Centre Européen du vent et de la VP (unité : 1 PVU=10^{-6}K.m^2.kg^{-1}.s^{-1}) sur la surface isentrope θ=320K (moyenne troposphère), pendant l'IOP 15 de MAP (5-8 Novembre 1999, 12h00 UTC). Les zones de VP supérieure à 3.5PVU sont grisées. Une flèche de vent est représentée par point de grille, et l'échelle représentative d'un vent de 50m.s^{-1}, qui dépend de la taille de la maille, est représentée dans les coins inférieur gauche et supérieur droit de la carte a) (Hoinka et Davies 2007).

En effet, l'étude de la cyclogénèse (alpine notamment) a aussi contribué à observer les occurences répétées de *panaches de VP* de haut niveau (*PV streamers*) en provenance du réservoir stratosphérique, souvent inclinés nord-sud (voir la revue de Hoinka et Davies 2007 pour MAP). Cette notion de panache de VP s'est imposée, notamment comme une composante souvent associée aux événements de forte précipitation sur les Alpes (Martius et al. 2006, Hoinka et al. 2006). Bon nombre de ces panaches subissent finalement, lors de leur passage au dessus des Alpes, une séparation de leur extrémité sud qui donne naissance à une anomalie positive isolée derrière la montagne, au dessus

du golfe de Gènes (Buzzi et al. 2003, Hoinka et al. 2003, Hoinka et Davies 2007). Ce type d'évolution est semble-t-il souvent associé à un événement de cyclogénèse alpine. C'est le cas de l'IOP 15 de MAP, dont la Fig. 1.9 présente l'évolution du panache de VP, vue par les analyses du Centre Européen (Hoinka et Davies 2007). La compréhension des mécanismes liés à la présence de la montagne et qui conduisent à cette rupture du panache de VP peut constituer un autre angle d'approche de la cyclogénèse de montagne, à travers la recherche de phénomènes capables de redistribuer la VP. A cet égard, le déferlement des ondes de gravité dans la troposphère moyenne est l'un des principaux candidats. Les premières études concernant cette question, pour des cas idéalisés (Morgenstern et Davies 1999) ou à partir de cas réels (Morgenstern et Davies 1999, Buzzi et al. 2003, Hoinka et al. 2003), montrent que les effets orographiques directs (ondes de montagne et déferlement) et les effets diabatiques liés aux précipitations contribuent chacun de façon comparable à ce sectionnement du panache de VP.

1.4 Paramétrisation des effets montagneux d'échelle sous-maille

Après avoir entrevu la diversité et la complexité des phénomènes dynamiques montagneux et leur influence possible sur la météorologie locale ou globale, et la climatologie, la question qui s'impose est de savoir comment en rendre compte correctement dans les Modèles Numériques de Prévision du Temps (MNPT),utilisés en météorologie, et les Modèles de Circulation Générale de l'Atmosphère (MCGA) utilisés dans les modèles climatiques[10].

Par exemple, nous avons vu que les montagnes peuvent générer des ondes de gravité et d'inertie gravité, qui en déferlant peuvent modifier le bilan local d'énergie ou de quantité de mouvement. Or les longueurs d'onde horizontales impliquées varient typiquement de 10 à quelques centaines de kilomètres, alors que la précision des meilleurs MNPT et MCGA actuels ne permet pas de décrire correctement des longueurs d'ondes inférieures respectivement à la cinquantaine et à la centaine de km[11]. Sur la verticale, le cisaillement du vent de base peut faire varier fortement la longueur d'onde. Par exemple, dans la stratosphère, on atteint des longueurs d'ondes verticales de l'ordre du kilomètre. Une résolution encore supérieure serait nécessaire pour décrire les interactions dissipatives de ces ondes avec l'écoulement moyen (déferlement, couches critiques). On touche donc encore la limite actuelle des modèles [12]. Enfin, les ondes de gravité courtes sont des mouvements rapides, dont les périodes peuvent atteindre 5 à 10 minutes, ce qui est inférieur aux pas de temps actuels[13].

Par conséquent, une partie importante du spectre de ces ondes est sous-estimée ou complètement ignorée par les équations dynamiques des modèles. Ceci est indiqué schématiquement dans la Fig. 1.10 (Kim et al. 2003). De ce point de vue, la précision des meilleurs modèles actuels ne doit pas faire illusion. Les ondes les plus courtes ont probablement la plus grande influence dynamique. Il faudrait multiplier environ par 10 la précision des modèles actuels pour résoudre correctement le spectre des ondes de montagne internes, c'est-à-dire propagatives. Ensuite, la résolution directe des processus de saturation demande d'accéder à des échelles encore nettement plus petites. Par exemple, les couches critiques observées dans l'atmosphère peuvent être très fines, de l'ordre de 50 à 200m (Kim et al. 2003).

Pour cette raison, on doit inclure dans les modèles non pas ces ondes, mais leur effets sur l'écoulement de grande échelle (qui lui est résolu), sous forme de *paramétrisations*. Concrêtement, cela signifie qu'on ajoute aux équations du mouvement *une force* locale qui rend compte de l'action sur le bilan de quantité de mouvement, ainsi qu'un terme de *diffusion turbulente verticale* pour les équations de transport de la chaleur ou d'autres traceurs. En ce qui concerne les ondes de montagnes, on parle alors de paramétrisation de l'Orographie d'Echelle Sous-Maille (OESM). Notons que les ondes peuvent induire d'autres effets, tels que la diffusion de la quantité de mouvement, ou un chauffage

[10]Avec l'amélioration progressive de la puissance de calcul, la distinction entre MNPT et MCG tend à se réduire de plus en plus. Néanmoins, de façon générale les MNPT privilégient la finesse de la résolution spatiale et temporelle ainsi que les méthodes d'assimilation, quand les MCG ont des résolution moindres mais une atmosphère plus haute et des schémas de paramétrisation plus riches.

[11]La dernière version déterministe du modèle du centre européen (ECMWF) utilise 799 harmoniques sphériques, soit une résolution de l'ordre de 25km.

[12]ECMWF nouvelle version : 91 niveaux verticaux! soit une quarantaine de niveaux dans la stratosphère.

[13]ECMWF nouvelle version : pas de temps de 12 minutes.

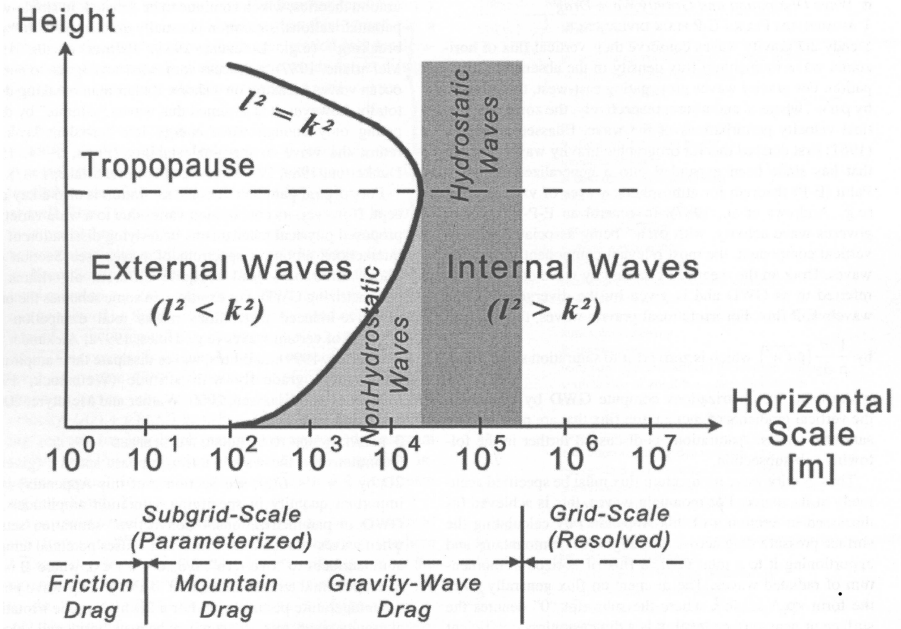

FIG. 1.10 – Schéma général du spectre des OG orographiques en lien avec la résolution des modèles (Kim et al. 2003). Le profil vertical typique du nombre de Scorer $S(z)$ (dénommé ici l^2) est représenté par la ligne continue $l^2 = k^2$ (où k est le nombre d'onde angulaire), séparant les ondes propagatives à droite (*internal waves*) des ondes évanescentes à gauche (*external waves*).

local, qui ont été jusqu'ici négligés dans les paramétrisations. Il semble d'ailleurs que la question du chauffage par les ondes dans la mésosphère redevienne d'actualité (Fritts et Alexander 2003). On remarquera que de façon générale, tous ces effets physiques sont la conséquence de processus dissipatifs d'échelle sous-maille, qui se traduisent notamment par une production de vorticité potentielle. Dans cette thèse nous ne nous intéresserons qu'à l'effet de la force exercée par les ondes de montagne.

1.4.1 Effets montagneux de grande échelle : notion d'orographie enveloppe

Au début des années 80, l'amélioration de la résolution des modèles a fait apparaître des erreurs systématiques sur les vents d'ouest dans le modèle du centre européen. Cela a conduit Wallace et al. (1983) à introduire une *orographie enveloppe* sur les massifs montagneux, qui améliorera les choses. Cette technique tend à rendre compte du fait qu'aux petites échelles du relief, l'écoulement atmosphérique tend à être bloqué dans les vallées, formant une zone de couche limite qui force l'écoulement de grande échelle à s'élever au dessus des plus hauts pics. Le choix d'une orographie moyenne dans le modèle devait donc sous-estimer l'impact des reliefs réels. On lui ajouta donc une enveloppe, dont l'épaisseur est fonction de la variance de l'élevation du sol.

Les progrès obtenus tenaient en fait essentiellement à une meilleure représentation des ondes planétaires (Tibaldi 1986), les ondes de gravité exerçant leur contrainte de façon prédominante à des échelles largement sous-maille à l'époque (résolution horizontale au mieux de 2.5°). Notons qu'aujourd'hui les ondes planétaires sont relativement bien résolues, contrairement aux ondes de gravité (cf Fig. 1.10, à l'extrême droite

du diagramme). Mais cette méthode présente de nombreux inconvénients, à commencer par sa rigidité : elle modifie globalement et définitivement la hauteur de la surface, toutes saisons confondues, ne laissant pas la possibilité de moduler l'effet orographique en fonction des conditions climatiques et encore moins météorologiques, notamment en ce qui concerne le vent de surface et la stratification. D'autre part, à des résolutions aussi grossières elle ne permet toujours pas de rendre compte de la contrainte exercée par les ondes de montagne (cf 1.4.3). Inversement, elle pose des problèmes lorsque la résolution est augmentée (Clark et Miller 1991). Par ailleurs, elle néglige la turbulence qui peut exister au voisinage des sommets importants, elle peut conduire à une surestimation des précipitations, et nuire au bilan radiatif (Lott et Miller, 1997b). Enfin, en supprimant une partie de l'espace réel, cette méthode contraint à se priver des données expérimentales proches de la surface dans le cadre de l'assimilation. Même si le mécanisme qui lui est associé semble pertinent y compris dans un contexte plus moderne (Kim, 1996), elle fut progressivement abandonnée.

1.4.2 Effets montagneux de très petite échelle : friction de surface

Pour des échelles orographiques très petites, inférieures à 5 à 10km (cf Fig. 1.10, à l'extrême gauche du diagramme), les ondes de montagne ne sont plus propagatives, et la réponse de l'atmosphère devient facilement nonlinéaire, son comportement étant contrôlé par la pente de l'orographie. On entre dans le domaine de la couche limite planétaire, et l'écoulement est turbulent (Taylor 1977, Grant et Mason 1990). Dans ce contexte, la force exercée par la montagne sur l'écoulement de grande échelle prend alors la forme d'une force de réaction hydraulique par un obstacle de taille caractéristique l, quadratique en la vitesse (*form drag*).

$$\mathrm{C}\,\rho\,l\,\mathbf{U}^2\,, \tag{1.9}$$

où C est une constante (Taylor 1977, Wood et Mason 1993). La longueur l qui apparaît est alors appelée *échelle de rugosité* de la surface.

C'est pourquoi la première représentation de l'OESM dans les modèles consistait à augmenter cette échelle de rugosité au dessus des montagnes (Tibaldi et Geleyn 1981, Mason 1985, Taylor et al. 1989, Wood et Mason 1993). Ce type de traînée est toujours utilisé aujourd'hui dans cette partie du spectre (Beljaars et al. 2004).

1.4.3 Contrainte des ondes de gravité

On s'intéresse maintenant à l'ensemble des OG internes excitées par la topographie, c'est-à-dire la partie centrale du diagramme de la Fig. 1.10. Suite aux travaux fondateurs de Sawyer (1959, implémentation de l'orographie dans les modèles), de Eliassen et Palm (1961) et Bretherton (1969), l'idée qu'une représentation simple de la contrainte des OG pouvait avoir un impact bénéfique dans les MCGA a d'abord été proposée par Lilly (1972). Aujourd'hui, la question de la paramétrisation des OG s'étend à des sources autres que l'orographie (convection, jets...). Cependant, il est notable que dans toute cette évolution, la question du rôle des montagnes a été le point de départ de cette prise de conscience, puis le point d'ancrage des développements théoriques et appliqués. L'histoire des schémas de paramétrisation des OG est largement dominée, notamment pendant les années 80 et 90, par la prise en compte des ondes de montagne.

En témoigne le premier schéma, implémenté par Boer et al. (1984) dans le GCMA du Centre Canadien du Climat. La paramétrisation des autres sources d'OG en est encore actuellement à ses balbutiements (Fritts et Alexander 2003). Cela tient sans doute essentiellement au fait que la quantification et la localisation des sources d'OG est nettement plus aisée dans le cas orographique que dans les autres mécanismes, même si la suite nous montrera que le problème est déjà très complexe.

a) Généralités : paramétrisation des ondes de gravité

Le développement des schémas de paramétrisation des OG a été fortement marqué par les travaux fondateurs de Lindzen (1981) et Holton (1982) notamment, à tel point que les schémas de première génération sont dits de "type Lindzen", ou dérivés. Plus généralement tous les schémas des années 80 et début 90 ont une approche commune que nous appelerons de type *discrète* (*single wave theory*), et dont le type Lindzen est un cas particulier. Cette catégorie est encore largement dominante actuellement. Mais on a vu naître dans les années 90 un autre type d'approche qualifié de *spectrale*.

Méthode discrète :
La méthode discrète considère l'émission dans l'espace physique d'une ou plusieurs OG monochromatique(s) d'amplitude prescrite, à partir d'une source localisée sur un point de grille (en surface pour l'orographie, en altitude pour la convection). Il s'agit ensuite de déterminer le profil vertical du flux de quantité de mouvement $\rho_0\overline{u'w'}$ pour en déduire celui de la force par l'Eq. (1.6), ainsi que le profil de la diffusivité turbulente verticale K_{zz}, le tout en fonction de l'écoulement de grande échelle à l'instant t et dans la même colonne, notamment les profils de vent et de stratification.

Par exemple, Lindzen (1981) se place dans le cadre 2D linéaire, sous l'approximation WKB (milieu lentement variable), et détermine la hauteur de déferlement z_b d'une OG pure stationnaire et monochromatique à partir du critère d'instabilité convective. Il suppose ensuite qu'au delà de ce niveau, l'onde reste nonlinéaire et saturée, marginalement instable, et la turbulence qu'elle induit s'oppose à sa croissance exponentielle naturelle dûe à la décroissance verticale en densité. Cette *hypothèse de saturation* par diffusion turbulente fourni l'évolution du flux de quantité de mouvement avec l'altitude entre le premier niveau de déferlement z_b, et un éventuel niveau critique z_c situé à haute altitude, au-delà duquel le flux doit être en principe nul.

Il est notable que malgré les hypothèses extrêmement simplificatrices de cette approche, elle est relativement efficace, et toujours d'actualité. Notamment, toutes les paramétrisations d'OG sont monodimensionnelles, au sens où elles supposent une propagation uniquement verticale des OG et négligent les effets liés aux variations horizontales du milieu, ainsi que les effets de dispersion lors de l'émission par un relief 3D, dans un vent éventuellement 3D lui aussi (Shutts, 1998). La plupart reposent aussi sur l'hypothèse hydrostatique (sauf pour les ondes piégées), l'approximation d'OG pure (rotation négligée), et l'hypothèse de milieu lentement variable nécessaire à l'approximation de l'optique géométrique (ou WKB), qui sous-tend la théorie des rayons (Whitham 1974, Lighthill 1978). Sachant que les ondes de montagnes typiques ont une longueur d'onde verticale de plusieurs kilomètres, l'approximation WKB paraît grossière. On ne sait toutefois pas faire grand chose d'autre qui puisse rester simple dans un contexte atmosphérique réel.

Méthode spectrale :
Dans les méthodes spectrales, on se place dans l'espace de Fourier et on considère le spectre des OG existantes. Ceci permet notamment de traiter individuellement la saturation onde par onde. On peut plutôt les rattacher, dans une certaine mesure, aux travaux de Lindzen et Holton (1968), démontrant l'origine de l'oscillation quasi bi-annuelle (QBO) dans le forçage du vent zonal par les OG générées par la convection tropicale. Elles sont donc naturellement dédiées à la paramétrisation des OG dont les sources sont plus difficilement quantifiables et/ou localisables que l'orographie, telles que la convection, ou les instabilités de jet. Elles sont aussi plus adaptées au traitement des ondes non stationnaires. On introduit alors des spectres qui sont représentatifs des spectres observés (ex : Hines 1997a et b, Medvedev et Klaassen 2000, Warner et McIntyre 2001) ou des spectres arbitraires (Alexander et Dunkerton 1999).

b) Schémas de première génération : la contrainte linéaire

Dans les années 80, la plupart des schémas de paramétrisation des OG dûes à l'OESM s'inspiraient alors fortement des travaux de Lindzen (1981). On évalue la trainée au niveau de la surface d'un ensemble fini d'OG pures d'échelle sous-maille (souvent une seule), dans le cadre 2D linéaire hydrostatique. On obtient une loi du type

$$-\rho_0 \, N_0 \, U_0 \, H^2 \, \mathbf{e}_x \tag{1.10}$$

pour un obstacle de hauteur H soumis à un vent moyen $U_0 \, \mathbf{e}_x$ de stratification N_0 uniformes selon z. La quantité de mouvement est alors déposée dans la même direction que la contrainte de surface au delà d'un niveau de déferlement déterminé à partir d'un critère d'instabilité convective, et en suivant une hypothèse de saturation non linéaire sur le flux.

Suite au premier schéma implémenté par Boer et al. (1984), sans hypothèse de saturation (profil linéaire), Chouinard et al. (1986) présentèrent un schéma utilisant la variance de l'OESM pour évaluer l'amplitude initiale de l'onde, et dans lequel le nombre de Froude inverse local est cette fois utilisé pour mesurer la nonlinéarité des ondes et distribuer verticalement la contrainte. Puis Palmer et al. (1986) et McFarlane (1987) développèrent indépendemment deux schémas ressemblants, en utilisant l'hypothèse de saturation de Lindzen (1981), schémas qui inspirèrent de multiples études par la suite. Il est notable qu'à l'époque, on essayait déjà de prendre en compte les effets de blocage des basses couches de l'écoulement à bas nombre de Froude, soit en définissant un critière limitant la déviation standard de l'orographie sous-maille utilisée (Palmer et al. 1986., Miller et Palmer 1986, McFarlane 1987, McFarlane et al. 1987), soit en introduisant une fonction de modulation du flux pour représenter la transition en fonction du nombre de Froude (Pierrehumbert 1986, Stern et al. 1987, Stern et Pierrehumbert 1988, Alpert et al. 1988). En outre, Palmer et Miller (1986) et Miller et al. (1989) introduisirent une variance de l'OESM dépendant de l'azimuth, c'est-à-dire une première représentation de l'anisotropie du relief.

L'introduction de ces paramétrisations prenant en compte la contrainte des OG de montagne s'avèra alors efficace pour corriger des défauts qui survenaient avec l'amélioration de la résolution des modèles dans la fin des années 70 et début 80. A l'époque en effet, on observe une durée de vie des dépressions synoptiques trop longue sur les continents (Palmer et al. 86). D'un point de vue climatologique, cela se traduit par des vents d'ouest troposphériques trop forts aux moyennes et hautes latitudes pendant les hivers de l'hémisphère nord, associés à un biais froid dans la

basse stratosphère à haute latitude. D'un point de vue dynamique, on interprète alors cette dégradation par le fait que le flux méridien de moment cinétique vers les poles, porté par les tourbillons baroclines de grande échelle, se trouve mieux représenté et de fait intensifié, alors que le transfert de moment cinétique entre l'atmosphère et la Terre solide par les ondes de gravité est toujours absent du bilan. Les deux erreurs ne peuvent donc plus se compenser comme c'était le cas dans les anciens modèles à faible résolution. En passant, c'est aussi dans ce contexte que l'on essaya d'abord infructueusement d'augmenter la force de friction des montagnes (Swinbank, 1985) (cf 1.4.2), et qu'on introduisit une orographie enveloppe (cf 1.4.1).

L'application d'une contrainte par les OG permet de déplacer le jet vers les basses latitudes, tout en le séparant du vortex polaire, qui se trouve freiné dans la basse stratosphère (Palmer et al. 1986, McFarlane 1987). Cette contrainte induit, par un mécanisme de type dérive d'Ekman, une circulation résiduelle méridienne vers le pôle (cf Fig. 1.5), à laquelle sont associés un échauffement dans la basse stratosphère polaire. Tous ces effets sont visibles dans la Fig. 1.11, extraite de Palmer et al. 1986.

c) Prise en compte des effets orographiques nonlinéaires et 3D

Comme nous l'avons vu, l'écoulement au dessus d'un obstacle devient non linéaire au delà d'un nombre de Froude inverse 1/Fr de l'ordre de 1 (Eq. (1.2)). Dans ces conditions, l'application de la formule de l'Eq. (1.10) n'est plus vérifiée. En réalité, le comportement des fluides en écoulement sur un obstacle à faible nombre de Froude donne lieu à des régimes variés, et souvent très sensibles aux divers paramètres de l'orographie ou de l'écoulement. Par exemple, l'apparition à bas niveau et en aval d'une zone de déferlement de l'onde de montagne dépend fortement de la géométrie de l'obstacle. Une montagne 3D a tendance à disperser l'énergie rayonnée dans plusieurs directions, alors qu'une montagne 2D concentre le rayonnement qui a lieu le long de son axe (Hines, 1988). D'autre part, la possibilité ou non de contourner l'obstacle influence aussi l'apparition du déferlement. Enfin, pour une montagne 3D anisotrope, le rapport d'aspect horizontal reste un paramètre sensible (Smith, 1989a).

Les observations issues des campagnes de mesure des années 80 (ex : PYREX, Bougeault et al. 1997) et l'apparition des simulations non linéaires numériques à mésoéchelle (ex : Stein 1992, Miranda et James 1992, Ólafsson et Bougeault 1996, 1997, Schär et Durran 1997), ont toutefois fait considérablement avancer cette question, tout au moins en ce qui concerne les écoulements à vent et stratification uniformes. On peut en tirer un comportement générique simplifié, constitué de trois régimes distincts pour la force de pression de surface en fonction du nombre de Froude inverse, schématisé sur la Fig. 1.12 par Scinocca et McFarlane (2000). Pour le comprendre, il est utile de remarquer que $\frac{1}{\mathrm{Fr}}$ représente non seulement la hauteur adimensionnée de la montagne, mais aussi l'importance effective de la stratification sur l'écoulement.

Régime 1 ("libre") : En régime linéaire (Fr grand), le phénomène physique dominant est le transport vertical de quantité de mouvement horizontale par l'onde, dont le flux contre-balance exactement la force de pression de surface. D'après l'Eq. (1.10), cette force est proportionnelle à

$$\frac{U_0^3}{N_0 \mathrm{Fr}^2}. \tag{1.11}$$

Régime 2 ("déferlement") : Mais lorsque Fr passe en dessous d'une valeur

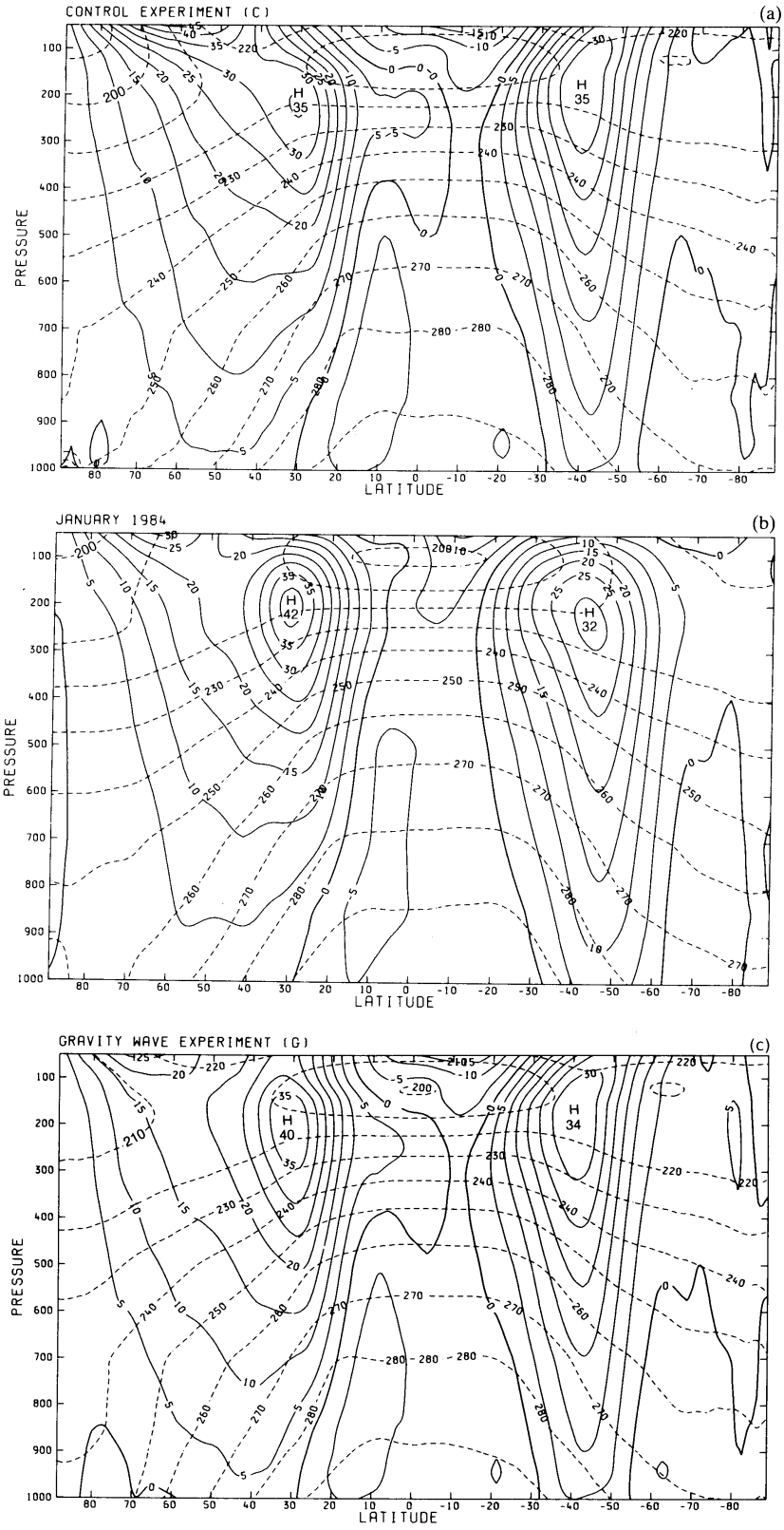

FIG. 1.11 – Climatologies des moyennes zonales du vent zonal et de la température, pour le mois de Janvier (Palmer et al. 1986) : a) simulée avec le GCM du Meteorological Office (UK) sans paramétrisation des OG, b) issue des réanalyses du Met Office (Janvier 1984), c) simulée avec le GCM du Met Office avec paramétrisation des OG.

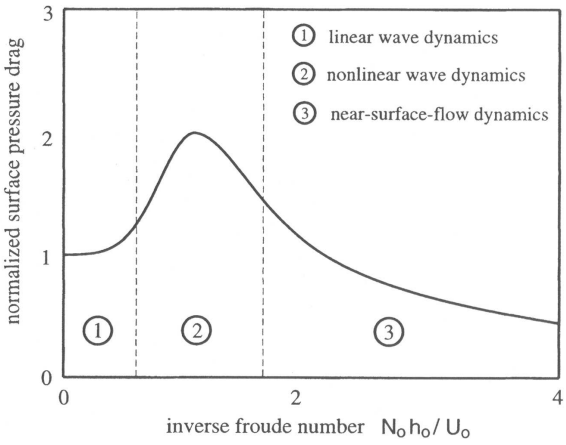

FIG. 1.12 – Evolution schématique de la force de pression de surface en fonction du nombre de Froude inverse, pour des écoulement à profils de vent U et de stratification N uniformes forcés par une montagne (Scinocca et McFarlane, 2000). Ce diagramme fait apparaître qualitativement trois régimes distincts d'écoulement. La valeur de la force de pression est adimensionnalisée par sa valeur théorique pour le même obstacle dans le cadre linéaire de propagation libre des OG, c'est-à-dire $\alpha N_0 U_0 H^2 = U_0^3/(N_0 \mathrm{Fr}^2)$, avec $\mathrm{Fr} = U_0/(N_0 H)$.

critique Fr_c (de l'ordre de 1), alors l'onde commence à déferler dans sa première longueur d'onde verticale, ce qui induit une redistribution de la quantité de mouvement horizontale en dessous de la couche mélangée ainsi créée (cela peut se comprendre qualitativement en terme de réflexion dans le cadre de la théorie des rayons). Dans ces conditions, souvent associées à l'effet de Foehn sec comme cité plus haut (1.2.1), la force de pression de surface peut augmenter fortement par *piégeage* et *amplification résonnante* de l'onde (Peltier et Clark 1979, Durran et Klemp 1987, Bacmeister et Pierrehumbert 1988). Il en résulte qu'une partie importante de la quantité de mouvement est alors déposée dans les basses couches, notamment à travers l'émission éventuelle d'*ondes piégées* en aval (Bretherton 1969, Durran 1995b, Lott 1998, Georgelin et Lott 2001), ne laissant s'échapper au dessus de la zone de déferlement qu'un *flux résiduel* que l'on peut évaluer par (Peltier et Clark 1984, Ólafsson et Bougeault 1996)

$$\frac{U_0^3}{N_0 \mathrm{Fr}_c^2}. \tag{1.12}$$

Régime 3 ("blocage") : Une nouvelle transition se produit pour une montagne encore plus haute ou une stratification encore plus forte (Fr très petit), vers un régime caractérisé par une dynamique concentrée au voisinage de la surface, offrant une analogie forte avec les écoulements hydrauliques dans le cas des fluides peu profonds (Durran, 1986a). Notamment, le fluide dans les basses couches ne peut plus s'élever au dessus de l'obstacle, donc se sépare et s'écoule autour (Fig. 1.13). Son comportement est alors dominé par les phénomènes de *blocage en amont* (Pierrehumbert et Wyman, 1985), l'apparition d'une paire de *vortex de sillage*, et éventuellement l'*émission périodique de vortex* (Schär et Smith 1993a et b, Ólafsson et Bougeault 1996, Schär et Durran 1997). La contrainte au sol est alors représentée par une force de blocage (Eq. (1.9)), et la quantité de mouvement transportée verticalement est très faible. Notons que dans le cas 2D, les régimes 2 et 3 peuvent cohabiter (Pierrehumbert et Wyman, 1985).

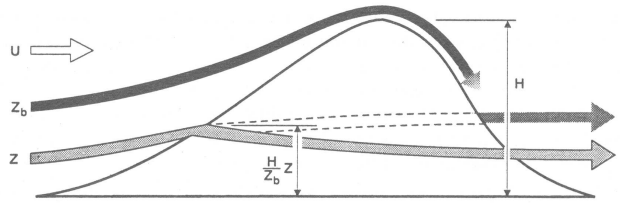

FIG. 1.13 – Représentation schématique du comportement de l'écoulement en cas de blocage de bas niveau (régime 3), dans le cadre du schéma de Lott et Miller (1997). La plus basse couche isentrope à ne pas subir de séparation de l'écoulement par le relief est repérée par l'altitude z_b.

Cette décomposition en trois régimes forme l'ossature de l'actuel schéma de paramétrisation de l'OESM du GCMA de troisième génération du Centre Canadien du Climat (Scinocca et McFarlane, 2000). Ce schéma décompose donc la contrainte de surface en trois composantes. La première représente le flux vertical de quantité de mouvement par l'OG, qui sature pour Fr<Fr_c en un flux résiduel. La seconde paramétrise la résonnance et l'effet des ondes piégées dans le régime 2. La troisième représente l'effet de blocage apparaissant à petit Fr. Cet aboutissement a bien sûr profité des avancées successives des schémas des années 90, qui ont progressivement amélioré la prise en compte de tous ces effets.

Bacmeister (1993) est le premier à prendre en compte le fait qu'un relief anisotrope génère une contrainte linéaire de surface qui n'est pas forcément parallèle au vent de surface, et contient donc une portance. Il se limite cependant à prendre en compte l'axe de bi-dimensionnalité de l'OESM.

Kim et Arakawa (1995) remarquent l'occurence fréquente du régime de déferlement (2) dans les cas réels, via des simulations 2D. Ils proposent une amélioration en prenant en compte, en plus du nombre de Froude, l'anisotropie et la convexité des pics dans la représentation statistique de l'OESM, de façon à augmenter si besoin le drag dans les basses couches. En effet, le seul nombre de Froude ne permet pas de distinguer entre un effet de blocage en amont, qui réduit la contrainte de l'onde, et du déferlement en aval, qui l'augmente.

Le schéma de Lott et Miller (1997) propose deux avancées importantes. D'une part, sur la base des travaux de Miller et al. (1989) et Baines et Palmer (1990), il améliore la représentation des effets de l'anisotropie de l'OESM sur le flux vertical de quantité de mouvement. Pour cela, on ajuste les propriétés statistiques de l'OESM associée à chaque point de grille sur un modèle d'obstacle ellipsoïdal, pour lequel on sait calculer la contrainte de surface linéaire d'après Philipps (1984). L'amplitude et la direction de la contrainte dépendent donc de l'orientation du vent de surface par rapport aux axes caractéristiques de l'éllipsoïde. De plus, comme pour Bacmeister (1993), elle contient une portance. D'autre part, en s'inspirant de Baines et Palmer (1990), il introduit une force de profil (Eq. (1.9)) pour rendre compte du blocage des basses couches à faible Fr, avec une évaluation dynamique de la hauteur de fluide bloqué (Fig. 1.13), et une prise en compte de la variation du profil de l'obstacle en fonction de l'inclinaison du vent de surface. De plus, le réglage des paramètres est ajusté à partir des données de la campagne PYREX. La perte de flux de quantité de mouvement à bas niveau dûe aux ondes piégées sera aussi représentée de façon simple plus tard (Lott 1999).

Le schéma de Gregory et al. (1998) prend aussi en compte les effets cités plus

haut, grâce à une dépendance simple de la contrainte de surface en Fr. Malheureusement, la contrainte y est partout parallèle au vent de surface. Par contre, un modèle à deux couches est introduit pour déterminer et quantifier plus précisément le rôle des ondes piégées. L'originalité de ce schéma réside aussi dans le traitement spectral des propriétés statistiques de l'OESM. Leur approche, qui est néanmoins aussi de type discrète (on applique une condition de déferlement sur le flux total), ouvre ainsi le champ à des méthodes de paramétrisation spectrales ou mixtes, comme Alexander et Dunkerton (1999).

En plus de sa structure en trois composantes, le schéma de Scinocca et McFarlane (2000) comporte plusieurs avancées importantes. D'abord la représentation ellipsoïdale de l'OESM est conservée, mais appliquée à un jeu de données topographiques 2 fois plus précises que Lott et Miller (1997) (ETOPO5, 5' de précision). Plus important, on ajoute deux paramètres qui caractérisent la bi-dimensionnalité de l'OESM à chaque point de grille. Cela va servir ensuite à décomposer la force de profil (régime "blocage") en deux composantes indépendantes, et ainsi d'introduire une portance à très bas niveau, causée par le blocage. Enfin, le flux vertical de quantité de mouvement horizontale porté par l'OG est décomposé en deux ondes représentant chacune l'effet d'une moitié de l'espace sous-maille du point de grille. En traitant indépendemment l'évolution verticale de ces deux composantes, on rend mieux compte de l'effet d'un vent 3D tournant avec l'altitude. En effet, dans tous les schémas précédents, la contrainte était portée par un unique vecteur parallèle à la contrainte au sol. Une extinction brutale à un niveau critique, où le vent est perpendiculaire à la contrainte, est donc possible, causant un dépôt de quantité de mouvement excessif sur une couche trop fine. L'existence de deux ondes permet ainsi de mieux distribuer verticalement la force.

1.4.4 De l'importance de la portance... et des niveaux critiques directionnels

Nous avons vu que, parmi l'ensemble des améliorations récentes de la paramétrisation de l'OESM, la prise en compte progressive du fait que la force exercée par la topographie n'est pas systématiquement parallèle au vent de surface tient une place importante. Précisémment, c'est la prise en compte de l'anisotropie du relief qui a introduit un angle entre le vent et la contrainte.

Lott (1999) a insisté sur l'utilité de bien équilibrer la répartition entre traînée et portance, en introduisant si besoin des forces de portance supplémentaires dans les paramétrisations. Il montre en effet, à l'aide du GCMA du LMD[14] qu'aux grandes échelles, l'application d'une portance explicite sur un sol plat à la place des montagnes rend compte relativement bien de l'effet des grandes chaînes de montagnes sur les ondes planétaires, qui est lié à la compression des colonnes de fluide. Il confirme en cela le théorème proposé par Smith (1979c), qui stipule que dans la limite quasi-géostrophique et sous l'approximation "eau peu profonde", l'application d'un forçage par une élévation de l'orographie a, au premier ordre, un effet rigoureusement équivalent à celui d'une force perpendiculaire au vent.

A plus petite échelle, l'existence d'un vent tournant avec l'altitude donne lieu, en présence d'un spectre polychromatique d'OG orographiques, à des niveaux critiques directionnels. Ceux-ci ont la particularité d'induire, dans la zone où ils se concentrent,

[14]LMDz. Laboratoire de Météorologie Dynamique, France.

une force perpendiculaire au vent à toute altitude, par *sélection azymuthale* du flux vertical de quantité de mouvement (Shutts 1995, Broad 1995). Autrement dit, dans ces conditions on obtient une portance qui non seulement est située en altitude au dessus de la montagne, mais qui de plus tourne avec le vent. Or, toute montagne isolée ou toute portion d'OESM génère un spectre polychromatique d'OG plus ou moins riche. Et on observe relativement fréquemment des situations de vent tournant avec l'altitude, notamment dans la troposphère à l'approche d'un front généré par une perturbation synoptique. Comme nous l'avons évoqué, ce phénomène de sélection azymuthale est encore très mal représenté dans les schémas actuels, même dans celui de Scinocca et McFarlane (2000) qui comporte seulement deux ondes. C'est pourquoi l'étude des impacts de ce phénomène est un des principaux objectifs de cette thèse.

1.4.5 Perspectives pour la paramétrisation des OG de montagne

Si la sélection azymuthale est mal représentée, c'est probablement parce que c'est typiquement un phénomène qui gagne à être traité par une méthode spectrale. Cela dit, des améliorations des schémas discrets présentés ci-dessus sont toujours possibles. En témoignent par exemple les récents efforts pour corriger le modèle de trainée linéaire de Philipps (1984) en y introduisant les effets du cisaillement vertical du vent (Teixeira et Miranda, 2006), ou encore la prise en compte des effets de la rotation sur le blocage à bas niveau (Shutts, 1998b). D'autres raisons sont cependant en faveur des méthodes spectrales. Par exemple, on considère souvent les OG de montagne stationnaires, mais parfois l'orographie peut générer des ondes non stationnaires (Lott et Teitelbaum 1993, Nance et Durran 1997), qui sont beaucoup plus faciles à introduire de façon spectrale (Alexander et Dunkerton, 1999). D'autre part, dans l'approche discrète le traitement indépendant d'un nombre fini d'ondes monochromatiques néglige l'interaction possible des ondes entre elles. Notamment, le schéma peut sous-évaluer le déferlement si les grandes ondes modifient significativement l'état de base vu par les courtes, de façon à les rendre plus instables (Palmer et al. 1986). Certaines méthodes spectrales tentent de rendre compte de certaines interactions ondes-ondes (Hines 1997a et b, Medvedev et Klaassen 2000), mais pas encore de cette dernière malheureusement (Kim et al. 2003).

Une autre piste possible pour l'amélioration est de réussir à coupler des schémas qui sont pour l'instant distincts, alors que les processus physiques associés ne le sont pas en réalité. On peut remarquer par exemple le lien intime entre la force de friction de surface et celle des montagnes (Eq. (1.9)) : d'une part l'existence d'une couche limite turbulente tend à modifier (réduire semble-t-il) l'amplitude des ondes (Oláfson et Bougeault 1997, Doyle et al. 2000, Smith et al 2002), et d'autre part le comportement nonlinéaire des ondes de gravité d'échelle sous-maille très courte (< 10km) peut inciter à augmenter artificiellement l'échelle caractéristique de rugosité dans la traînée turbulente de surface (section 1.4.2). Cela laisse penser qu'il serait judicieux de coupler ces deux forces à l'avenir. De même, le couplage des schémas de paramétrisation des OGs de source orographique et convective commence à être d'actualité, tant les processus de précipitation et de propagation sont interdépendants (Kim et al. 2003).

Comme nous l'avons remarqué plus haut, la paramétrisation des OG n'est pas près de disparaître avec l'amélioration des performances numériques. A moyen terme

c'est d'ailleurs plutôt le contraire, car le fait que les modèles résolvent une partie croissante du spectre des OGs ne simplifie pas forcément le problème. D'abord cela peut contraindre à un nouveau réglage des paramètres d'ajustage des schémas de paramétrisation. Ensuite, l'importance récemment accordée au mécanisme de contrôle par le haut dans l'atmosphère (cf section 1.2.5) dans les efforts pour prévoir le temps à long-terme (plus d'une semaine), conduit à la nécessité de réhausser le toit des modèles, d'améliorer la résolution verticale, et de mieux paramétriser le rôle des OG dans cette région. Cela induit automatiquement une diminution du pas de temps car les vents sont plus intenses en altitude. Dans ces conditions, l'hypothèse de staticité de l'écoulement de base dans toute la colonne du modèle, qui est toujours employée pour propager les OG, devient de moins en moins valable. Un pas de temps trop court contribue aussi à l'augmentation de la variabilité temporelle de la contrainte des OG dans les modèles, notamment parce que certaines ondes sont maintenant résolues. Cela ne rend cependant pas compte de façon correcte des interactions ondes-ondes citées plus haut (Kim et al. 2003). Donc nul doute que cette thématique nous fournisse de nouveaux défis théoriques pour les années à venir.

Par exemple, la nature monodimensionnelle verticale de tous les schémas de paramétrisation des OG (orographiques ou non) dans les modèles représente une limite sérieuse, toutes méthodes confondues (discrètes ou spectrales). En ce qui nous concerne, la dispersion latérale anisotrope des OG forcées par un relief 3D, en présence de rotation ou non (Smith 1979b, Shutts 1998a), est susceptible de réduire la contrainte en altitude par rapport à celle proposée par les schémas actuels (Shutts 1998a, Broad 1999, Broutman et al. 2001). Cela justifie la poursuite des efforts théoriques pour comprendre l'influence des OG de montagne sur les grandes échelles, notamment en présence de niveaux critiques puisque ceux-ci tendent à accentuer la dispersion latérale. Dans ce contexte, l'approche en terme de source de vorticité potentielle semble être un outil pertinent, d'abord pour comprendre, et peut-être pour paramétriser. Ce sera donc l'objet de cette thèse.

1.5 Questions posées et plan de la thèse

Rappelons donc succintement les questions posées, auxqelles nous nous intéresserons au cours de cette thèse. S'agissant de la force exercée par les OG de montagne rencontrant des niveaux critiques :

- quelle est l'influence qualitative et quantitative relative à la cyclogénèse de montagne ?
- plus généralement, en lien avec la question de la paramétrisation, quelle est l'influence sur les grandes échelles et sur la partie balancée ?
- peut-on qualifier et quantifier la répartition entre réponse balancée et non balancée ?
- concernant la partie non balancée, quels sont les mécanismes possibles de génération secondaire d'OIG par les montagnes via cette force, et peut-on les quantifier ?

Le travail présenté dans cette thèse est constitué de trois parties. Toutes ces parties sont des études idéalisées dans le cadre du problème de Eady. Dans la première (chapitre 2), nous analyserons et quantifirons les effets d'une force générée par des OG à des niveaux critiques directionnels, dans le cadre semi-géostrophique linéarisé. Ce travail constitue une sorte de première approche physique de la paramétrisation des niveaux critiques directionnels, dans le cadre des grandes échelles. Dans la suite, nous compléterons cette première approche grâce à des simulations 2D aux équations primitives, qui nous permettrons d'accéder aux échelles sous-synoptiques et méso-échelles. Le chapitre 3 sera l'occasion d'étudier les modes normaux instables du problème de Eady aux échelles sous-synoptiques, pour comprendre leur mécanisme d'instabilité et leur mécanisme de saturation nonlinéaire. Enfin le chapitre 4 reprendra la problématique du chapitre 2 dans le cadre de ce modèle 2D, et donnera lieu à une évaluation directe de l'effet des OGs courtes sur l'écoulement de grande échelle.

Chapitre 2

Synoptic responses to mountain gravity waves breaking at directional critical levels

Résumé

Dans cette partie, nous étudions dans le cadre d'un modèle simple, l'effet sur les échelles synoptiques des ondes de gravité (OG) de montagne en présence de niveaux critiques directionnels. Nous utilisons une version semi-géostrophique linéaire du modèle de Eady avec ou sans tropopause, en adaptant le cadre conceptuel de la théorie de la cyclogénèse de montagne proposé par Smith (1984). Nous ajoutons donc une force paramétrisée dans la moyenne troposphère, représentant l'action des OGs sur l'écoulement de grande échelle, en présence d'un massif montagneux isolé. Cette force produit un dipole de Vorticité Potentielle (VP) incliné, qui est progressivement advecté et étiré par l'écoulement de base cisaillé.

Tout d'abord, on considère le cas d'un relief idéalisé comprenant une variance orographique de petite échelle. En l'absence de tropopause, la réponse au sol induite par la VP est comparable à la réponse dûe à l'enveloppe de l'orographie. Dans le cas d'un front froid, la force des OG produit une légère dépression au dessus de la montagne et une crête anticyclonique plus intense, qui s'étend dans la direction du sillage de la VP. L'effet s'opposant partiellement à celui de l'enveloppe orographique, il est jugé cyclolytique. Dans le cas d'un front chaud, le motif forcé à la surface est différent. La force induit aussi une grande crête anticyclonique sous le dipole de VP, mais qui s'étend au dessus de la montagne, et une dépression substantielle dans le sillage de surface. L'effet amplifie donc celui des grandes échelles, et notamment il est donc cyclogénétique.

Dans la suite, on vérifie la robustesse des précédents résultats par une série de tests de sensibilité. Nous changeons la configuration du relief et de l'écoulement de base. Puis nous montrons que l'approximation quasi-géostrophique n'est pas suffisante pour évaluer correctement les réponses en surface, du fait de l'importance de la structure verticale particulière du dipole de VP. Ensuite nous introduisons une tropopause et donc des modes baroclines instables. Enfin, nous considérons le cas d'un spectre orographique plus réaliste, représentatif du massif alpin. S'en suit une discussion sur l'intérêt théorique et pratique de cette étude.

Après l'article, on présente certains résultats complémentaires concernant les simulations avec tropopause, ouvrant sur la nécessité d'une approche basée non plus sur les modes normaux mais sur les modes optimaux.

2.1 Article : Martin and Lott, 2007

Synoptic Responses to Mountain Gravity Waves Encountering Directional Critical Levels

ARMEL MARTIN AND FRANÇOIS LOTT

Laboratoire de Météorologie Dynamique du CNRS, Ecole Normale Supérieure, Paris, France

(Manuscript received 28 November 2005, in final form 26 June 2006)

ABSTRACT

A heuristic model is used to study the synoptic response to mountain gravity waves (GWs) absorbed at directional critical levels. The model is a semigeostrophic version of the Eady model for baroclinic instability adapted by Smith to study lee cyclogenesis. The GWs exert a force on the large-scale flow where they encounter directional critical levels. This force is taken into account in the model herein and produces potential vorticity (PV) anomalies in the midtroposphere.

First, the authors consider the case of an idealized mountain range such that the orographic variance is well separated between small- and large-scale contributions. In the absence of tropopause, the PV produced by the GW force has a surface impact that is significant compared to the surface response due to the large scales. For a cold front, the GW force produces a trough over the mountain and a larger-amplitude ridge immediately downstream. It opposes somehow to the response due to the large scales of the mountain range, which is anticyclonic aloft and cyclonic downstream. For a warm front, the GW force produces a ridge over the mountain and a trough downstream; hence it reinforces the response due to the large scales.

Second, the robustness of the previous results is verified by a series of sensitivity tests. The authors change the specifications of the mountain range and of the background flow. They also repeat some experiments by including baroclinic instabilities, or by using the quasigeostrophic approximation. Finally, they consider the case of a small-scale orographic spectrum representative of the Alps.

The significance of the results is discussed in the context of GW parameterization in the general circulation models. The results may also help to interpret the complex PV structures occurring when mountain gravity waves break in a baroclinic environment.

1. Introduction

The large-scale flow response to the breaking of vertically propagating gravity waves (GWs) has been the subject of many studies during the last 40 years. They follow the seminal works of Eliassen and Palm (1961) and Bretherton (1969), which have shown that mountain GWs induce a net transfer of momentum from the ground toward the atmosphere. The importance of mountain GWs for the atmospheric circulation is now well established. The parameterization of mountain GWs in general circulation models (GCMs) reduces the cold bias these models present near the tropopause in the Northern Hemisphere midlatitudes (Boer et al. 1984; Palmer et al. 1986; McFarlane 1987). More recent parameterizations of subgrid-scale orography (SSO) include trapped lee waves (Miller et al. 1989) and nonlinear low-level flow blocking (Lott and Miller 1997; Scinocca and McFarlane 2000), which both reduce biases in the low-level winds.

Although SSO parameterizations are often evaluated by looking at systematic errors on the zonal mean flow, they also influence nonzonal planetary-scale patterns. For these patterns, it is noteworthy that the SSO parameterizations are not necessarily helpful, unless they permit that the SSO force has a substantial component in the direction perpendicular to the low-level flow (Lott 1999; Webster et al. 2003). This component can have three origins: (i) the anisotropy of the mountains (Phillips 1984; Scinocca and McFarlane 2000; Webster et al. 2003); (ii) the fact that the mean orography in large-scale models does not produce enough vortex compression (Smith 1979; Lott 1999); and (iii) the presence of directional critical levels encountered by the

Corresponding author address: Dr. Armel Martin, Laboratoire de Météorologie Dynamique du CNRS, Ecole Normale Supérieure, 24, rue Lhomond, 75235 Paris CEDEX 05, France.
E-mail: martin@lmd.ens.fr

DOI: 10.1175/JAS3873.1

GWs (Shutts 1995). In this last circumstance, the orientation of the force with respect to the background flow is a consequence of the fact that a monochromatic GW encounters a critical level where the background wind is perpendicular to its horizontal wave vector. The GW is then absorbed, provided that the background flow Richardson number is larger than 0.25 at this altitude (Booker and Bretherton 1967). Since the momentum flux associated with a monochromatic GW is parallel to its horizontal wave vector, aloft an isolated mountain the selective absorption of one GW at each level results in a force perpendicular to the wind at the same altitude. Note that this effect is the result of a vertical shear and is distinct from the effects of horizontal variations in the background flow, which can modify the horizontal wave vector itself (Bühler and McIntyre 2005).

Another large-scale process related to mountains is lee cyclogenesis, for which various dynamical mechanisms were proposed. The local triggering of standing or transient Eady or Rossby edge waves (Smith 1984, 1986; Davis 1997), the low-level modification of preexisting large-scale unstable baroclinic mode (Pierrehumbert 1985; Speranza et al. 1985; Fantini and Davolio 2001), or the cold front distortion by low-level blocking (Messinger and Pierrehumbert 1986; Schär 1990; Gross 1994) are some of these processes. Actually, they are not exclusive, and this variety of theories illustrates the complexity of this problem. Accordingly, few studies have addressed the role of small-scale orography on it.

Nevertheless, as the resolution of regional models increases, the synoptic scales are nowadays rather accurately represented. Besides, quite recently the forecast models began to solve together the synoptic scales and the mesoscale dynamics, including the upper-level GWs and the low-level potential vorticity (PV) banners appearing downstream of the individual mountain peaks (Hoinka et al. 2003; Liniger and Davies 2003; Schär et al. 2003; Flamant et al. 2004; Jiang and Doyle 2004). This recent progress in numerical modeling appeals for a better understanding of the impact of the small-scale dynamics onto the synoptic flow, which is incidentally one of the central objectives of the Mesoscale Alpine Program (MAP; Binder and Schär 1996; Bougeault et al. 2001). It is also in this context that Aebischer and Schär (1998) have suggested that the low-level cyclonic PV generated along the southwestern flank of the Alps could help to trigger lee cyclogenesis.

Although the interaction between mesoscale and synoptic-scale dynamics has been addressed during MAP, by means of either direct field measurements or numerical simulations, relatively few theoretical studies address this problem. It is nevertheless challenging for at least three reasons. First, the net force due to the breaking GWs acts over a domain where horizontal scales correspond to Rossby numbers of order 1 or larger. In this case, the large-scale response to the GWs is not entirely balanced but also contains reemitted inertio-gravity waves (Scavuzzo et al. 1998; Lott 2003). Second, in the midtroposphere the mountain GWs have little chance to break if the wind increases unidirectionally, because the stationary waves' vertical wavenumber decreases with altitude. Nevertheless, in the presence of fronts, many GWs can be absorbed at directional critical levels in the midtroposphere (Shutts 1995) and break thereafter (Broad 1999). The effect of this process on the large-scale flow has never been evaluated. Third, a force that is everywhere perpendicular to the background wind can produce dipolar PV banners with an unusual structure.

This paper presents a theoretical model of the large-scale effect of the GWs generated by an idealized front passing over a mountain range. This model accounts for the GWs through the large-scale momentum deposit they induce where they encounter critical levels, in the midtroposphere. For this purpose, we adopt a semigeostrophic (SG) version of Smith's (1984) model of lee cyclogenesis in which we include a GW force following Shutts (1995). The use of a balanced formalism here is supported by Lott (2003), which has shown by direct 2D simulations that after 12 h typically the balanced part dominates the inertio-gravity waves' part in the total response to GW absorption at a critical level. In this framework, we analyze the surface response associated with the PV anomaly produced by the GW force and compare this response with that due to the smooth large-scale mean orography.

The paper is organized as follows. In section 2 we present the model. In section 3 we analyze the case of a cold front interacting with an idealized complex mountain range in the absence of tropopause. In section 4 we describe the warm front case. In section 5 we compare the quasigeostrophic (QG) response with the SG response, we present some sensitivity tests to the altitude at which the gravity waves interact with the background flow, and we analyze the influence of the tropopause (which introduces unstable baroclinic modes). In section 6 we present the results for orographic spectra representative of the Alps. Section 7 is a summary and a discussion of the implications of our results to the parameterization of mountain GWs in GCMs, or to the interpretation of the PV patterns produced in the midtroposphere when a front crosses a mountain range.

2. Model

a. Equations for the large-scale flow

A central assumption of our model is that the power spectrum of orography shows a clear separation between the large scales and the small scales. This permits us to study separately the synoptic dynamics and the GW dynamics. Although this separation is not valid in reality, it is implicitly assumed in SSO parameterization schemes. For this assumption to be valid, we adopt in sections 3, 4, and 5 an idealized mountain range profile given by

$$h(\mathbf{x}) = H_0 e^{-(x^2+y^2/2L^2)}\,[1 + \cos(\mathbf{k}_w\mathbf{x})] = \mathcal{H}(\mathbf{x})\,[1 + \cos(\mathbf{k}_w\mathbf{x})], \quad (1)$$

where $\mathbf{k}_w = k_w\mathbf{e}_x + l_w\mathbf{e}_y$. In Eq. (1), L is the characteristic large scale, $\mathbf{k}_w$ is the dominant horizontal wavenumber associated with the small scales, $2H_0$ is the maximum altitude of the mountain range, and $\mathcal{H}(\mathbf{x})$ is the large-scale orography profile, that is, the envelope of the ridges (Figs. 1a,b).

In the linear context, and in the absence of critical levels, the large-scale effect of the GWs forced by $h' = \mathcal{H}(\mathbf{x})\cos(\mathbf{k}_w\mathbf{x})$ is very small if $k_wL \gg 1$. Nevertheless, if the GWs encounter directional critical levels (Fig. 1c), they are absorbed and can deposit the momentum they transport. For the large-scale flow, this effect can be translated into a force per unit mass (see section 2c and the appendix),

$$\mathcal{F}(\mathbf{x}, z) = \mathcal{F}(\mathbf{x}, z)\mathbf{e}_x + \mathcal{G}(\mathbf{x}, z)\mathbf{e}_y, \quad (2)$$

whose impact adds to that of the large-scale orography profile $\mathcal{H}(\mathbf{x})$.

To study the response to $\mathcal{F}$ and $\mathcal{H}$, we adopt the Boussinesq approximation and consider an idealized front such that the background wind $\mathbf{U}$ and the potential temperature Θ_b have uniform shears,

$$\mathbf{U}(z) = U(z)\mathbf{e}_x + V_0\mathbf{e}_y = (U_0 + \Lambda z)\mathbf{e}_x + V_0\mathbf{e}_y, \quad (3)$$

$$\Theta_b(y, z, t) = \theta_r + \theta_{0z}z + \Theta_y y + \theta_{\mathrm{ad}}(t). \quad (4)$$

In Eqs. (3)–(4), V_0 is the surface wind, Λ is the vertical wind shear, θ_r is a constant reference temperature, θ_{0z} is the vertical stratification, Θ_y is the cross-front potential temperature gradient, and $\theta_{\mathrm{ad}}(t)$ is the uniform change in potential temperature associated with the advance of the front. In this framework, the constant Brunt–Väisälä frequency N, Θ_y, and $\theta_{\mathrm{ad}}(t)$ can be written

$$N^2 = \frac{g\theta_{0z}}{\theta_r}, \quad \Theta_y = -\frac{\Lambda f\theta_r}{g}, \quad \text{and} \quad \theta_{\mathrm{ad}}(t) = -V_0\Theta_y t. \quad (5)$$

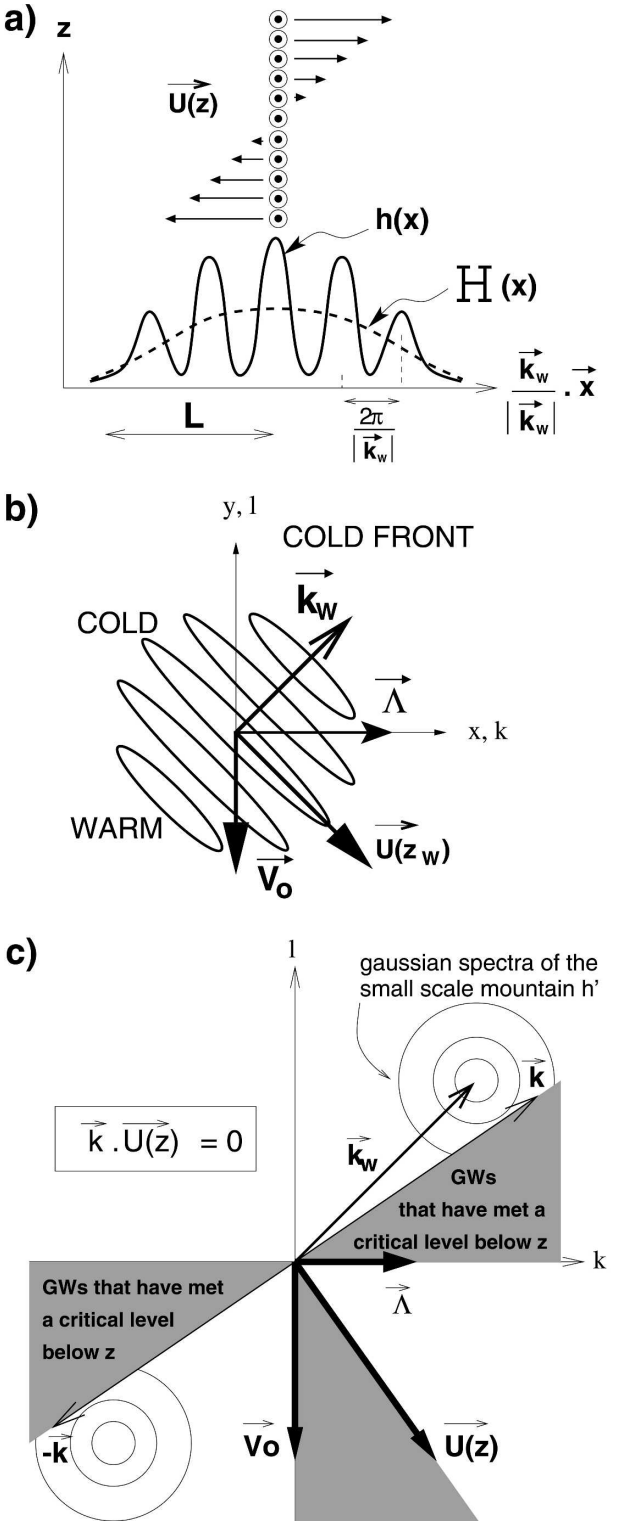

FIG. 1. Schematic representation of the idealized mountain range and of the background flow used to derive the model equations in the cold front case: (a) vertical section with horizontal axis along $\mathbf{k}_w$, (b) view from top, and (c) spectrum of the small-scale orography $h' = \mathcal{H}(\mathbf{x})\cos(\mathbf{k}_w\mathbf{x})$.

In Eq. (5), the thermal wind balance relates Θ_y to Λ, f is a constant Coriolis parameter, and g is the gravity constant.

If we assume that the forcings $\mathcal{F}$, $\mathcal{G}$, and $\mathcal{H}$ are of small amplitude and have a characteristic horizontal scale L such that the large-scale Rossby number V_0/fL is near or below 1, the response of the flow can be evaluated using a forced and linearized version of the hydrostatic SG equations given in Hoskins (1975):

$$\begin{aligned}
(\partial_t + \mathbf{U}\boldsymbol{\nabla})u_g + w\Lambda - fv + \partial_x\phi &= \mathcal{F}, && \text{(a)}\\
(\partial_t + \mathbf{U}\boldsymbol{\nabla})v_g + fu + \partial_y\phi &= \mathcal{G}, && \text{(b)}\\
\partial_z\phi &= g\theta/\theta_r, && \text{(c)}\\
(\partial_t + \mathbf{U}\boldsymbol{\nabla})\theta + v\Theta_y + w\theta_{0z} &= 0, && \text{(d)}\\
\partial_x u + \partial_y v + \partial_z w &= 0. && \text{(e)}
\end{aligned} \tag{6}$$

In Eq. (6), (u, v, w) are the components of the wind perturbation, $\phi = p/\rho_r$ is the geopotential perturbation, p is the perturbation pressure, and ρ_r is a constant reference density. Still in Eq. (6) $u_g = \partial_y\phi/f$ and $v_g = \partial_x\phi/f$ are the geostrophic components of the wind perturbation. From the system of Eq. (6), we form the linearized budget of the PV disturbance q. For this, we calculate $\{\boldsymbol{\nabla} \times [(6a), (6b), (6c)]\} \cdot \boldsymbol{\nabla}\Theta_b + \Lambda\partial_y(6d) - \theta_{0z}R_i^{-1}\partial_x(6b)$, and use Eq. (5), which yields

$$(\partial_t + \mathbf{U}\boldsymbol{\nabla})\rho_r q + \boldsymbol{\nabla} \cdot \mathbf{J}_N = 0, \quad \text{where} \tag{7}$$

$$\begin{aligned}
\rho_r q(\mathbf{x}, z, t) = {} & \theta_{0z}[(1 - \mathrm{Ri}^{-1})\partial_x v_g - \partial_y u_g]\\
& + \Lambda\partial_y\theta + \Theta_y\partial_z u_g + f\partial_z\theta, \quad \text{and}
\end{aligned} \tag{8}$$

$$\begin{aligned}
\mathbf{J}_N = {} & -\theta_{0z}(1 - \mathrm{Ri}^{-1})\mathcal{G}\mathbf{e}_x + \theta_{0z}\mathcal{F}\mathbf{e}_y\\
& - \Theta_y\mathcal{F}\mathbf{e}_z.
\end{aligned} \tag{9}$$

In Eqs. (7) and (9), $\mathbf{J}_N$ is the nonadvective PV flux, and $\mathrm{Ri} = N^2/\Lambda^2$ is the background flow Richardson number. Note that Eqs. (7)–(9) are the linearized version of Hoskins (1975) SG PV budget, with $\mathcal{F}$ added. Notably, $\mathbf{J}_N$ is everywhere parallel to the background isentropes ($\mathbf{J}_N \cdot \boldsymbol{\nabla}\Theta_b = 0$). And since these isentropes are advected by the background flow, the global PV flux $\rho_r q\mathbf{U}(z) + \mathbf{J}_N$ never crosses them, which is consistent with the "PV impermeability theorem" (Haynes and McIntyre 1987).

Then, to determine the surface response from the PV, we also consider the two linearized free-slip adiabatic boundary conditions

$$[\partial_t + \mathbf{U}(0)\boldsymbol{\nabla}]\theta + v\Theta_y = -\theta_{0z}\mathbf{U}(0)\boldsymbol{\nabla}\mathcal{H} \quad \text{at} \quad z = 0, \tag{10}$$

$$[\partial_t + \mathbf{U}(D)\boldsymbol{\nabla}]\theta + v\Theta_y = 0 \quad \text{at} \quad z = D. \tag{11}$$

b. Inversion of the PV perturbation

If the forcings $\mathcal{F}$, $\mathcal{G}$, and $\mathcal{H}$ are specified, it is convenient to solve the Eqs. (7)–(11) in the Fourier space.[1] In this space, the PV perturbation in Eq. (7) is then

$$\rho_r\hat{q} = i\frac{1 - e^{i(\mathbf{k}\cdot\mathbf{U})t}}{\mathbf{k} \cdot \mathbf{U}}\{\Theta_y\partial_z\hat{\mathcal{F}} + \theta_{0z}[-ik(1 - \mathrm{Ri}^{-1})\hat{\mathcal{G}} + il\hat{\mathcal{F}}]\}, \tag{12}$$

provided that $\hat{q}(t = 0) = 0$. Introducing the geostrophic balance and the hydrostatic relation Eq. (6c), we can invert the PV in terms of geopotential via the elliptic equation

$$\frac{\partial^2\hat{\phi}}{\partial z^2} - 2i\lambda_i\frac{\partial\hat{\phi}}{\partial z} - (\lambda_r^2 + \lambda_i^2)\hat{\phi} = \frac{g}{f\theta_r}\rho_r\hat{q}, \quad \text{where} \tag{13}$$

$$\lambda_r = \frac{N}{f}\sqrt{1 - \mathrm{Ri}^{-1}}|\mathbf{k}| \quad \text{and} \quad \lambda_i = l\frac{\Lambda}{f}. \tag{14}$$

First, we form a particular solution that contains the whole PV $\hat{q}$ and vanishes at $z = 0$:

$$\hat{\phi}_p(\mathbf{k}, z, t) = e^{-\lambda z}\int_0^z e^{2\lambda_r z'}\int_{z'}^D -\frac{g\rho_r}{f\theta_r}\hat{q}e^{-\lambda^* z''}\,dz''\,dz', \tag{15}$$

$$\text{where} \quad \lambda = \lambda_r - i\lambda_i \quad \text{and} \quad \lambda^* = \lambda_r + i\lambda_i. \tag{16}$$

Then, to satisfy the boundary conditions, we add to this particular solution two boundary waves

$$\hat{\phi}(\mathbf{k}, z, t) = \hat{\phi}_p(\mathbf{k}, z, t) + \hat{\phi}_u(\mathbf{k}, t)e^{-\lambda z} + \hat{\phi}_d(\mathbf{k}, t)e^{+\lambda^*(z-D)}. \tag{17}$$

In this formalism, the boundary conditions Eqs. (10)–(11) become

$$\begin{aligned}
\lambda_r[\partial_t - i\mathbf{k} \cdot \mathbf{U}(0)](\hat{\phi}_u - \hat{\phi}_d e^{-\lambda^* D}) - ik\Lambda(\hat{\phi}_u + \hat{\phi}_d e^{-\lambda^* D})&\\
= \{[\partial_t - i\mathbf{k} \cdot \mathbf{U}(0)]\partial_z\hat{\phi}_p(0) + \Lambda\hat{\mathcal{F}}(0)\}_W&\\
- \{i\mathbf{k} \cdot \mathbf{U}(0)N^2(1 - \mathrm{Ri}^{-1})\hat{\mathcal{H}}(\mathbf{k})\}_E&
\end{aligned} \tag{18}$$

$$\begin{aligned}
\lambda_r[\partial_t - i\mathbf{k} \cdot \mathbf{U}(D)](\hat{\phi}_u e^{-\lambda D} - \hat{\phi}_d) - ik\Lambda(\hat{\phi}_u e^{-\lambda D} + \hat{\phi}_d)&\\
= \{-\lambda_r[\partial_t - i\mathbf{k} \cdot \mathbf{U}(D)]\hat{\phi}_p(D)&\\
+ ik\Lambda\hat{\phi}_p(D) + \Lambda\hat{\mathcal{F}}(D)\}_W,&
\end{aligned} \tag{19}$$

[1] Convention: $\phi(\mathbf{x}) = \int_{-\infty}^{\infty}\int_{-\infty}^{\infty}\hat{\phi}(\mathbf{k})e^{-i\mathbf{k}\mathbf{x}}\,dk\,dl$, where $\hat{\phi}(\mathbf{k}) = (1/4\pi^2)\int_{-\infty}^{\infty}\int_{-\infty}^{\infty}\phi(\mathbf{x})e^{i\mathbf{k}\mathbf{x}}\,dx\,dy$.

at $z = 0$ and $z = D$, respectively. In the right-hand side of Eqs. (18)–(19) we have separated the forcings due to the GWs (W), and to the envelope $\hat{\mathcal{H}}(E)$. In the following, the response is always described at the ground, where $\hat{\phi} = \hat{\phi}_W + \hat{\phi}_E$ because $\hat{\phi}_p(z = 0) = 0$.

c. Evaluation of $\mathcal{F}(x, z)$

To evaluate the force $\mathcal{F}(\mathbf{x}, z)$, we first calculate a net force $\overline{\mathcal{F}}(z)$ using the linear theory of GWs in a linear background shear flow (Shutts 1995 and the appendix):

$$\overline{\mathcal{F}}(z) = -\frac{d}{dz}\overline{\mathbf{u}'w'}, \quad \text{where}$$

$$\overline{\mathbf{u}'w'} \equiv \frac{1}{\pi L^2}\int_{-\infty}^{+\infty}\int_{-\infty}^{+\infty}\mathbf{u}'w'\,dx\,dy. \tag{20}$$

In Eq. (20), $\mathbf{u}'$ and w' are the small-scale velocities associated with h'. Then, we consider that the horizontal distribution of $\mathcal{F}(\mathbf{x}, z)$ resembles the envelope profile $\mathcal{H}(\mathbf{x})$:

$$\mathcal{F}(\mathbf{x}, z) = \overline{\mathcal{F}}(z)e^{-(x^2+y^2)/L^2}. \tag{21}$$

Although in Eq. (21), $\mathcal{F}(\mathbf{x}, z)$ results in a net force equal to $\overline{\mathcal{F}}(z)$, Eq. (21) assumes that the GW field stays confined over the mountain range $\mathcal{H}$. This assumption is only valid for hydrostatic waves in the absence of shear, while for the background flow we consider here, Shutts and Gadian (1999) have shown for an isolated mountain that the GW field is spread downstream over a distance that can reach a few times the horizontal scale of the mountain. Nevertheless, we adopt this assumption for several reasons. First, the drag $\overline{\mathbf{u}'w'}$ is less widely spread because it is quadratic. Second, Lott (2003) have shown in 2D that the spread of the drag is reduced if we increase the vertical resolution and add a small amount of dissipation to take account of the breaking. Third, since we consider here the combined effect of several different anisotropic individual ridges, a possible local shift of the force over a distance comparable to $2\pi/|\mathbf{k}_w|$ can be reasonably neglected in respect to L, the scale of the global mountain.

As our GWs have horizontal wavenumber $\mathbf{k} \sim \pm\mathbf{k}_w$ [Eq. (1) and Figs. 1b,c], the forcing $\mathcal{F}$ is only significant if there exists a critical level z_w for $\mathbf{k}_w$: $\mathbf{U}(z_w)\cdot\mathbf{k}_w = 0$. In other words, the background wind has to pass from one side of the ridges to the other when z increases (Fig. 1b). For a cold front in the Northern Hemisphere, for example, $V_0 < 0$ and $\Lambda > 0$, this only occurs if $k_w.l_w > 0$ (Figs. 1b,c). For a warm front ($V_0 > 0$ and $\Lambda > 0$) this only occurs if $k_w.l_w < 0$. In both cases, the total force is well approximated by

$$\overline{\mathcal{F}}(z) \approx \frac{1}{2\sqrt{\pi}}N\Lambda L H_0^2 k_0(z)^2 e^{-L^2\|\mathbf{k}_w\|^2 + L'^2k_0^2}\frac{\Lambda z|V_0|}{\|\mathbf{U}(z)\|^2} \times \left(\mathbf{e}_x - \frac{U(z)}{V_0}\mathbf{e}_y\right), \tag{22}$$

where

$$k_0 = \left[k_w - l_w\frac{U(z)}{V_0}\right]\Big/\left[1 + \frac{U(z)^2}{V_0^2}\right], \quad \text{and}$$

$$L'^2 = \left[1 + \frac{U(z)^2}{V_0^2}\right]L^2. \tag{23}$$

Coherently, $\mathcal{F}(z)$ is everywhere orthogonal to the background flow $\mathbf{U}(z)$ (see the appendix).

d. Computation

To solve this problem numerically, we consider a horizontally periodic domain of size 20 000 km × 20 000 km × 10 km. The fields are represented by 512 × 512 harmonics and 81 vertical levels, yielding a resolution of 40 km × 40 km × 125 m. First, we compute analytically the PV anomaly using the diagnostic Eq. (12) and integrate it vertically by a trapezoidal approximation to evaluate $\hat{\phi}_p$ in Eq. (15). Then, we solve the first-order differential Eqs. (18)–(19), treating separately the parts "W" and "E." This yields temporal integrals that converge for a time step of 2 h.

3. Cold front with no tropopause

In this section, we place the tropopause altitude at $D = \infty$. And we consider an idealized cold front moving toward the south in the Northern Hemisphere midlatitudes, across an idealized mountain range. The flow and orography parameters are, respectively,

$$\begin{aligned} &\theta_r = 300\ \text{K}, \quad \rho_r = 1\ \text{kg m}^{-3}, \quad f = 10^{-4}\ \text{s}^{-1}, \\ &N = 10^{-2}\ \text{s}^{-1}, \quad \Lambda = 4.10^{-3}\ \text{s}^{-1}, \\ &U_0 = 0\ \text{m s}^{-1}, \quad V_0 = -20\ \text{m s}^{-1}. \\ &H_0 = 800\ \text{m}, \quad L = 200\ \text{km}, \end{aligned} \tag{24}$$

$$|\mathbf{k}_W| = \frac{2\pi}{70\,000}\,\text{m}^{-1}, \quad \text{with} \quad k_w = l_w. \tag{25}$$

The mountain range half-height width is $2L\sqrt{\ln 2} \approx$ 330 km. It is typically constituted of five to seven ridges, which are 70 km wide and oriented southeast–northwest (Fig. 1b). The dimensionless mountain heights $NH_0/fL = 0.4 < 1$ for the large-scale orography $\mathcal{H}$, and $N2H_0/V_0 = 0.8 < 1$ for the small-scale orography h', justify a linear treatment for both. The large-scale Rossby number is $V_0/fL \approx 1$, and the ratio between the

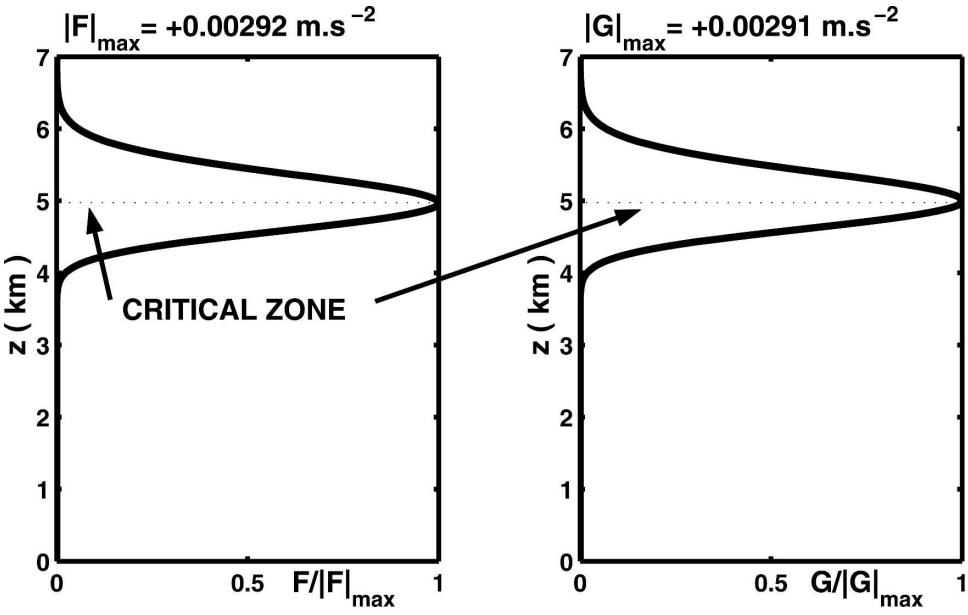

FIG. 2. Vertical profile of the force $\overline{\mathcal{F}}(z)$ in the idealized cold front case in section 3: $\theta_r = 300$ K, $f = 10^{-4}\ \mathrm{s}^{-1}$, $N = 10^{-2}\ \mathrm{s}^{-1}$, $\Lambda = 4.10^{-3}\ \mathrm{s}^{-1}$, $U_0 = 0\ \mathrm{m\ s}^{-1}$, $V_0 = -20\ \mathrm{m\ s}^{-1}$, $H_0 = 800$ m, $L = 200$ km, $|\mathbf{k}_W| = 2\pi/70\,000\ \mathrm{m}^{-1}$, and $k_w = l_w$.

large and the short scales is $2L|\mathbf{k}_w|/2\pi \approx 6 > 1$. Note that we could arbitrarily choose to have a bigger number of thinner ridges in the same envelope as here. But, therefore, we should have also reduced the height of these ridges to conserve a reasonable orographic variance and force.

a. PV anomaly due to the absorbed GW forcing $\mathcal{F}$

The vertical profile of the net force $\overline{\mathcal{F}}(z)$ in Eq. (22) is displayed in Fig. 2. Each component reaches a maximum near $z_w = 5$ km and is only substantial over a vertical depth of 1 or 2 km around z_w. In the rest of the paper we will refer to this area as the critical zone.

Figures 3a–c show three horizontal sections of the PV anomaly due to $\mathcal{F}$ in the critical zone at $t = 12$ h. At the three levels, the PV amplitude is between 0.4 and 0.8 potential vorticity units (PVU; where 1 PVU $= 1.0 \times 10^{-6}\ \mathrm{m^2\ s^{-1}\ K\ kg^{-1}}$), and the PV patterns are predominantly oriented in the direction of the background wind $\mathbf{U}(z_w)$. As we explain further hereafter, the PV patterns have this structure because first the PV is produced by $\mathcal{F}$ aloft the mountain, and then the PV is advected by the background flow. To interpret the differences between those three levels, one visualizes schematically the nonadvective PV flux $\mathbf{J}_N$ in Fig. 4. Figure 4a shows that $\mathbf{J}_N$ is pointing upward to be parallel to the isentropes. In the (y, z) plane, J_{Nz} essentially takes the PV from below z_w to put it above (Fig. 4a), yielding the predominantly positive PV lobe above z_w (Fig. 3a) and the predominantly negative one below (Fig. 3c). Near the altitude z_w, the divergence of the vertical component of the nonadvective PV flux is null,

$$\partial_z J_{Nz} = \Theta_y \partial_z \mathcal{F} = 0; \tag{26}$$

therefore the PV is only due to the vector $\mathbf{J}_{Nxy} = J_{Nx}\,\mathbf{e}_x + J_{Ny}\,\mathbf{e}_y$, which is nearly opposite to the wind, the force $\mathcal{F}(z_w)$ being perpendicular to it (Fig. 4b). Hence, near z_w, $\mathbf{J}_{Nxy}$ tends to take PV from downstream to put it upstream, according to the direction of $\mathbf{U}(z_w)$. At small times, it results in a positive PV anomaly along the upstream flank of the mountain and a negative one downstream (Fig. 4b). Afterward, the negative PV anomaly produced aloft of the mountain is advected downstream at the velocity $\mathbf{U}(z_w)$, yielding the midtropospheric start-up anticyclone in Fig. 3b. Still near z_w but over the mountain, the long-term response is a steady-state cyclonic PV anomaly (Fig. 3b). There, the PV due to $\mathbf{J}_{Nxy}$ is exactly balanced by the advection term

$$(\mathbf{U} \cdot \boldsymbol{\nabla})\rho_r q + \boldsymbol{\nabla} \cdot \mathbf{J}_{Nxy} = 0. \tag{27}$$

The PV structure in Fig. 3 essentially represents a PV banner, whose characteristic horizontal width and depth are fixed by the width and depth of the critical zone, around $2L = 400$ and 2 km, respectively (see Figs. 2 and 4), while its length is controlled by the advection [i.e., around $|\mathbf{U}(z_w)|\,t$]. This PV banner has a 3D structure that is very different from the PV banners occurring in barotropic flows when the low-level flow passes

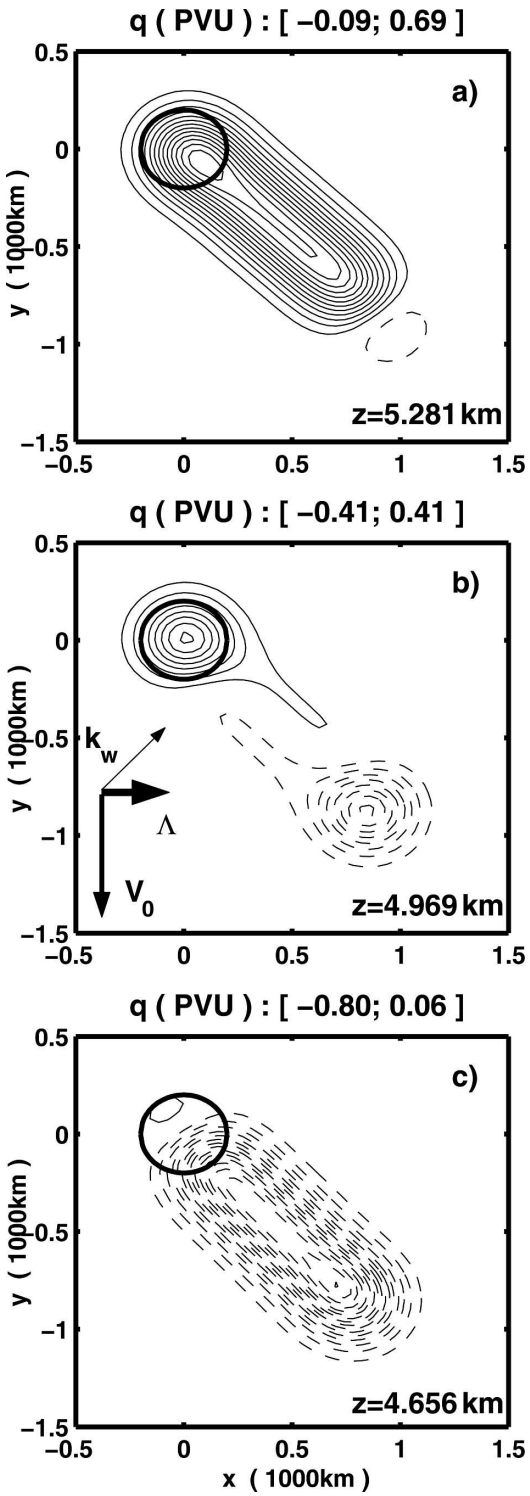

FIG. 3. Horizontal sections of the PV anomaly in the critical zone, at $t = 12$ h and for different heights: (a) $z = 5.281$ km, (b) $z = 4.969$ km, and (c) $z = 4.656$ km. Same parameters as in Fig. 2. Contour interval (CI) = 0.05 PVU. Negative values are dashed. The minimum and maximum values of q are indicated above each panel. The location and half-height width of the mountain range is indicated by the circle.

around individual mountain peaks or when mountain GWs break in the absence of critical levels. In these cases, the effect of the mountain can still be modeled by a nonadvective PV flux $\mathbf{J}_N$. It is nevertheless perpendicular to the background wind rather than parallel to it, resulting in PV lobes of opposite signs localized one next to the other in the horizontal (Schär and Durrän 1997).

b. *Surface pressure ϕ_W due to the forcing $\mathcal{F}$*

Figures 5a–c show the surface pressure perturbation induced by the GW momentum deposit. At small times (Fig. 5a), it presents a small-amplitude (approximately −0.1 mb) trough over the mountain and a ridge downstream of it [toward $\mathbf{U}(z_w)$]; its amplitude is around 0.2 mb. Over a longer time (Figs. 5b,c), the trough over the mountain near disappears, while the downstream ridge extends along the direction of $\mathbf{U}(z_w)$. To the west of this extending ridge, a second trough is developing (Figs. 5b,c). At 36 h, the maximum amplitude of the surface signal is 1.1 mb.

To interpret this response, Fig. 6 shows the surface temperature anomaly $(\theta_r/g)\partial_z\phi_p(0)$ associated with the particular solution ϕ_p. This term is central because it translates the PV into Eady waves forcing [see Eq. (18)] via the weighted average (in the Fourier space):

$$\frac{\theta_r}{g}\,\partial_z\hat{\phi}_p(\mathbf{k}, z = 0, t) = -\int_0^D \frac{\hat{q}}{f}\,e^{-\lambda^* z}\,dz. \qquad (28)$$

At $t = 12$ h, $(\theta_r/g)\partial_z\phi_p(0)$ is negative over the mountain and positive downstream of it. This follows that the midtroposphere PV in Fig. 3 is predominantly positive over the mountain and negative downstream of it. Note also that the positive lobe in surface temperature exceeds in amplitude the negative one, because the negative PV in Fig. 3c has a stronger influence at the surface than the positive one in Fig. 3a. Note also that the pattern of $(\theta_r/g)\partial_z\phi_p(0)$ is substantially larger in horizontal size than the PV pattern. Again, this is due to the weight $e^{-\lambda_r z}$ in Eq. (28), which favors the large scales, a general property of PV inversion operators (Hoskins et al. 1985). Still at $t = 12$ h, the surface trough over the mountain and the downstream ridge in Fig. 5a are essentially needed for the surface temperature $(\theta_r/g)\partial_z\phi_W(0)$ to oppose $(\theta_r/g)\partial_z\phi_p(0)$.

At later stages ($t = 24$ h, 36 h), the temperature pattern $(\theta_r/g)\partial_z\phi_p(0)$ is more complex (Figs. 6b,c), with an elongated negative anomaly appearing along the northeast flank of the extending downstream positive anomaly. This negative anomaly is the surface signature of the upper-level positive PV (the one shown in Fig. 3a at $t = 12$ h). At these times, it is no longer masked by

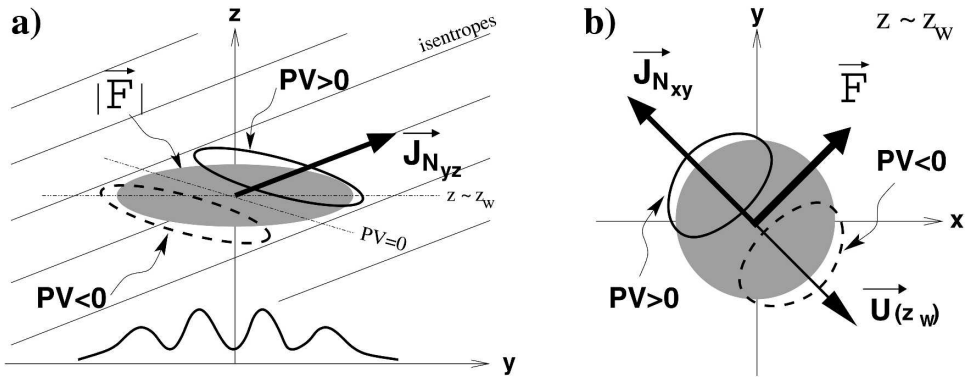

FIG. 4. Schematic representation of the nonadvective PV flux $\mathbf{J}_N$ and of its effects on the PV. The PV lobes are schematized by the thick solid and dashed closed lines. The gray area represents the critical zone; that is, the zone where the GWs force $\mathcal{F}$ is substantial. (a) Vertical section at $x = 0$; the tilted isentropes are also schematized by thin solid lines, and (b) horizontal section at $z = z_w$.

the lower-level negative anomaly (the one in Fig. 3c at $t = 12$ h), because the wind is turning clockwise with altitude.

As a result, the surface response ϕ_W is predominantly anticyclonic along the axis of $\mathbf{U}(z_w)$ (Figs. 5b,c). Nevertheless, it presents a trough along the southeastern flank of this ridge, to the opposite of the place where the elongated negative surface anomaly of $(\theta_r/g)\partial_z\phi_p(0)$ is located in Figs. 6b,c. This bears witness to the fact that boundary Eady waves start to modulate the surface response via the meridional thermal advection in Eq. (18) and make it differ from the simple mirror image of the PV deposit.

To support this last statement, we note that the Eady wave forcing $(\theta_r/g)\partial_z\phi_p(0)$ (Fig. 6) has a quite stationary structure upstream of the advected start-up anticyclone. In terms of Eady wave dispersion relationships, this translates into

$$\omega = \mathbf{k}\cdot\mathbf{U}\left(z = \frac{1}{\lambda_r}\right) = k\frac{\Lambda}{\lambda_r} + lV_0 = 0. \qquad (29)$$

As the shape of $(\theta_r/g)\partial_z\phi_p(0)$ also imposes $k \sim l$, Eq. (29) yields $\lambda_r \sim \Lambda/-V_0 = 2\times10^{-4}\ \mathrm{m}^{-1}$ and a dominant wavelength $2\pi/|\mathbf{k}| \sim 3000$ km rather consistent with Fig. 5c. For these scales, the group velocity points toward the south-southwest:

$$\mathbf{C}_g = \left(\frac{\Lambda}{\lambda_r}\frac{l^2}{|\mathbf{k}|^2}, \frac{\Lambda}{\lambda_r}\frac{l^2}{|\mathbf{k}|^2}\right) \sim \left(-\frac{V_0}{2}, \frac{3V_0}{2}\right), \qquad (30)$$

whereas $\mathbf{U}(z_w)$ is southwest. Accordingly, we observe the development of a trough at the west of the extending ridge.

c. Surface pressure ϕ_E due to $\mathcal{H}(x)$

The time evolution of ϕ_E is shown in Figs. 5d–f at $t = 12$, 24, and 36 h, respectively. A boundary Eady lee wave is developing and extending downwind according to $\mathbf{U}(0) = V_0\mathbf{e}_y$. The wave is bounded downstream by the start-up cyclone due to the warm potential temperature anomaly θ_{0z} $\mathcal{H}$ present over the mountain range when $t < 0$ and swept away by $\mathbf{U}(0)$ when $t > 0$. It is bounded over the mountain by an anticyclonic pattern due to vortex compression. The corresponding high keeps almost constant after 12 h and reaches 1.2 mb at 36 h. Immediately downstream of the mountain a trough, whose amplitude reaches -1.3 mb at 36 h is settling. The amplitudes obtained are significantly smaller than in Smith (1984, 1986) because our mountain is substantially smaller in width and height.

As in section 3b this surface response can also be interpreted in terms of stationary boundary Eady wave dynamics. In this case the large-scale orography induces a steady forcing with dominant wavenumbers $|\mathbf{k}| \approx 1/L$, and Eq. (29) implies

$$l/k = -\Lambda/(\lambda_r V_0) \sim 0.5 > 0. \qquad (31)$$

Accordingly, the troughs and ridges are oriented from northwest to southeast and are strongly inclined along the y axis. Likewise, Eq. (31) permits us to predict $2\pi/l \approx 4\pi L = 2400$ km, which roughly corresponds to the crest-to-crest distance along the y axis in Fig. 5f. These values yield a dominant group velocity consistent with the Eady lee wave extension along the y axis in Fig. 5f:

$$\mathbf{C}_g \approx (6, -20)\ \mathrm{m\ s}^{-1}. \qquad (32)$$

d. Total response at the surface $\phi = \phi_W + \phi_E$

The total response $\phi = \phi_W + \phi_E$ is displayed in Figs. 5g–i. Although the GW effect is rather small,

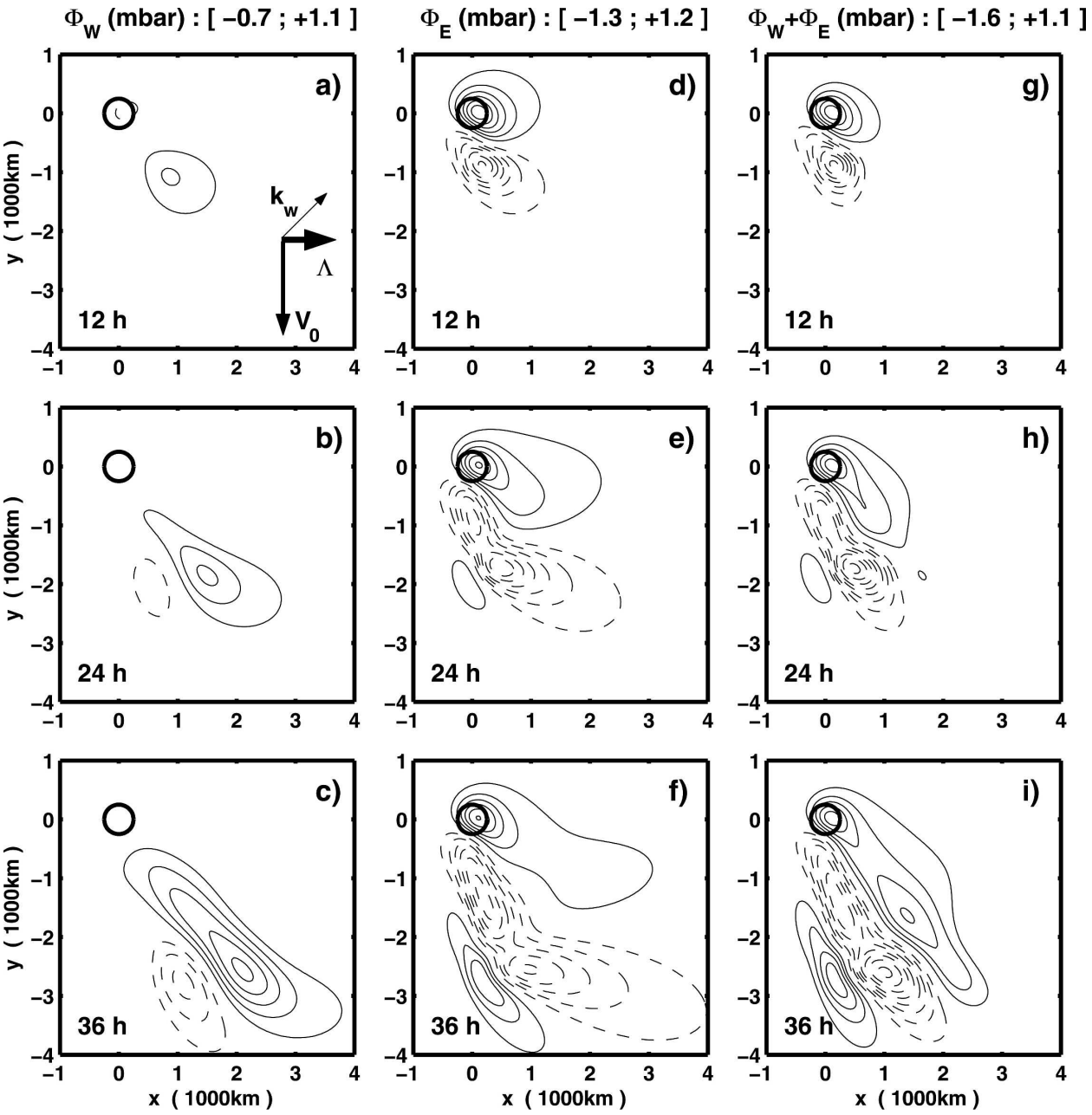

FIG. 5. Evolution of the surface geopotentials at $t = 12$, 24, and 36 h. Same parameters as in Fig. 2. (a)–(c) Geopotential due to the GWs (ϕ_W); (d)–(f) geopotential due to the large-scale orography profile $\mathcal{H}(\mathbf{x})$ (ϕ_E); (g)–(i) total perturbation ($\phi_W + \phi_E$). The magnitude is indicated as a pressure in millibars because $\rho_r = 1$ kg m^{-3}. Negative values are dashed and CI = 0.2 mb. The minimum and maximum values reached at $t = 36$ h are indicated at the top of each column. The configuration of the background front with regards to the orientation of the ridges is schematized in (a).

they reduce by near 20% the ridge produced by the large-scale orography over the mountain, as well as the downstream trough. More pronounced effects occur farther downstream. In particular the ridge produced by the GWs and, which extends below the PV banner in Fig. 5b, substantially affects the surface response in the far field.

4. Warm front with no tropopause

In this part, we consider the case of a warm front by taking $V_0 = 20$ m s^{-1} in our model. To obtain a significant force $\mathcal{F}$ we also rotate the small-scale ridges and take $k_w = -l_w$ (see appendix). All the other parameters are the same as in section 3.

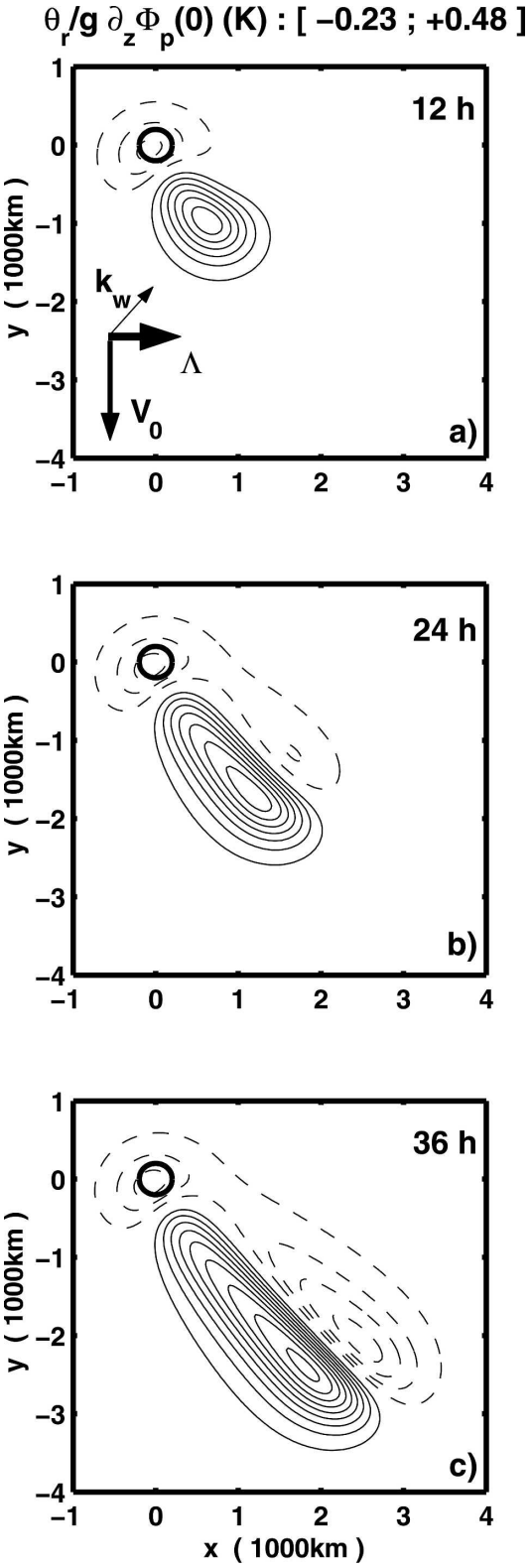

FIG. 6. Evolution of the potential temperature anomaly at the surface $(\theta_r/g)\partial_z\phi_p(0)$, same parameters as in Fig. 2; (a) $t = 12$ h, (b) $t = 24$ h, and (c) $t = 36$ h. Negative values are dashed and CI = 0.5 K.

As in the cold front case, the PV anomaly on both flanks of the critical zone has an elongated structure. It is predominantly positive above z_w and negative below (Figs. 7a,c). This is almost as in the cold front case in Figs. 3a,c. Near the altitude z_w nevertheless (Fig. 7b), the PV anomaly over the mountain is negative, and an opposing pattern of positive PV is advected downstream at the velocity $\mathbf{U}(z_w)$, the opposite to what occurs in the cold front case in Fig. 3b.

This last difference between the cold front case and the warm front case is an important result that has a simple dynamical origin. The necessity that there exist critical levels in the troposphere for the GWs to affect the large-scale flow imposes that the GW force has one component in the direction of the shear Λ (the x component in our case, see Fig. 4b). Its other component is opposed to the low-level wind, which is natural for a gravity wave drag. Where this force acts, $\mathcal{F}$ makes an angle with $\mathbf{U}(z_w)$ equal to $\pi/2$ in the cold front case and equal to $-\pi/2$ in the warm front case. From this, it follows that the horizontal component of the PV flux $\mathbf{J}_{Nxy}$ is such that $\mathbf{J}_{Nxy} \cdot \mathbf{U}(z_w) < 0$ in the cold front case, whereas $\mathbf{J}_{Nxy} \cdot \mathbf{U}(z_w) > 0$ in the warm front case. Because of this difference, the surface response to the GWs in the warm front case (Figs. 8a–c) presents no symmetry with that in the cold front case (Figs. 5a–c). On the other hand, the response to the large-scale orography ϕ_E is the symmetric of the cold front response, in respect to the x axis (Figs. 5d–f and 8d–f).

In response to the PV pattern in Fig. 7, the surface response ϕ_W is dominated by a strong anticyclonic lobe, which stays attached to the mountain (Figs. 8a–c). Immediately downstream, according to $\mathbf{U}(0)$ a substantial trough develops. Note also that the magnitude of the response is stronger than in the cold front case (between 1.8 and -1.2 mb at $t = 36$ h). It follows that the anticyclonic PV anomalies over the mountain and extending below z_w downstream of it in Figs. 7b,c reinforce each other to produce a strong surface response near the mountain. By summing the two responses, it is apparent in Figs. 8g–i that in this case the absorbed GWs reinforce the anticyclone over the mountain, as well as the downslope trough.

5. Sensitivity experiments

a. Quasigeostrophic simulations

The fundamental reason for choosing the SG formalism rather than the QG formalism is that we obtain a more accurate PV budget, closer to the primitive equation PV budget. More precisely, in our case, the nonadvective PV flux $\mathbf{J}_N$ has a vertical component J_{Nz} that keeps $\mathbf{J}$ parallel to the tilted isentropes (Haynes and

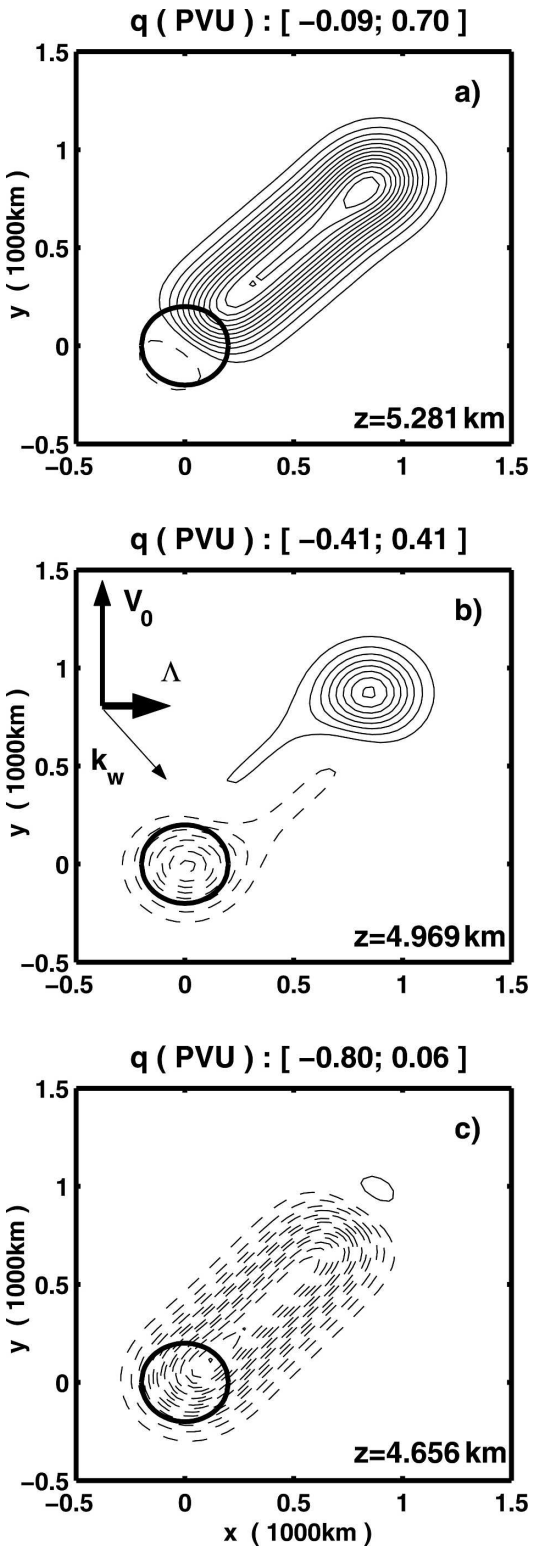

FIG. 7. Horizontal sections of the PV anomaly in the critical zone at $t = 12$ h and for different heights, for the warm front case in section 4: (a) $z = 5.281$ km, (b) $z = 4.969$ km, and (c) $z = 4.656$ km. Same parameters as in Fig. 2 except $V_0 = 20$ m s^{-1} and $k_w = -l_w$. Negative values are dashed and CI = 0.05 PVU.

McIntyre 1987). This vertical component is neglected in the QG formalism. To evaluate its significance, we have repeated the cold and warm front experiments in sections 3 and 4 using a QG version of the model of section 2. To do it, we take $\Theta_y \mathcal{F}_z = \mathrm{Ri}^{-1} = 0$ in the PV Eq. (12) and $\mathrm{Ri}^{-1} = \lambda_i = 0$ in the definition of the vertical decay length λ Eq. (14).

The most noticeable difference is that the warm front response is exactly antisymmetric with the cold front response according to the x axis (Fig. 9). Because of the neglect of J_{Nz}, at all altitudes the PV is due to a horizontal flux $\mathbf{J}_{Nxy}$ that is aligned with the wind (not shown), so it resembles that at z_w in the SG simulations (Figs. 3b and 7b). The QG simulations fail in simulating the substantial, sign-definite, and elongated PV anomaly located on the lower flank of the critical zone (Figs. 3c and 7c). That is the reason why the surface signal in the QG cases is much smaller than in the corresponding SG cases.

Nevertheless, we can notice that downstream of the mountain the GWs remain cyclolitic for a cold front case and cyclogenetic for a warm front. Over the mountain, the GWs still produce a low for the cold front case and a high for the warm front.

b. Front, orography, and critical zone altitude

The numerical simplicity of our model permits us to analyze many different flow and orography configurations. For example, increasing only H_0 favors the GW forcing [varying in H_0^2, Eq. (22)] relative to the large-scale orography forcing [in H_0, Eq. (18)]. Increasing the number of ridges in our mountain (i.e., increasing $|\mathbf{k}_w|L$) results in the same effect, even if L is fixed, and although the critical zone becomes thinner. Changing the orientation of the ridges [i.e., the angle $(\widehat{\mathbf{e}_x, \mathbf{k}_w})$] has a more subtle effect. In the cold front case, for $0 < (\widehat{\mathbf{e}_x, \mathbf{k}_w}) < (\pi/4)$, the GWs meet critical levels nearer the ground. It results in three effects: (i) the PV anomaly is nearer the ground, (ii) the advection of PV is slower, and (iii) the axis of the PV anomaly is closer to the surface wind $V_0\mathbf{e}_y$. As illustrated in Figs. 10a–c, this makes the surface response (i) thinner in width, (ii) shorter in length, and (iii) oriented closer to the surface wind $V_0\mathbf{e}_y$. The same results hold for the warm front case and for $-(\pi/4) < (\widehat{\mathbf{e}_x, \mathbf{k}_w}) < 0$ (not shown). The compromise of those different processes is summarized in Fig. 11, where the extrema of ϕ_W at $t = 36$ h are plotted versus $(\widehat{\mathbf{e}_x, \mathbf{k}_w})$ in the cold and warm front cases. Notably, in both cases, the maximum amplitude is obtained for an intermediate value of $|(\widehat{\mathbf{e}_x, \mathbf{k}_w})|$, and not for $|(\widehat{\mathbf{e}_x, \mathbf{k}_w})| \approx 0$ for which z_w is nearer the ground. The reason is that $z_w \approx 0$ requires $\mathbf{k}_w \cdot \mathbf{U}_0 \approx 0$, that is, a

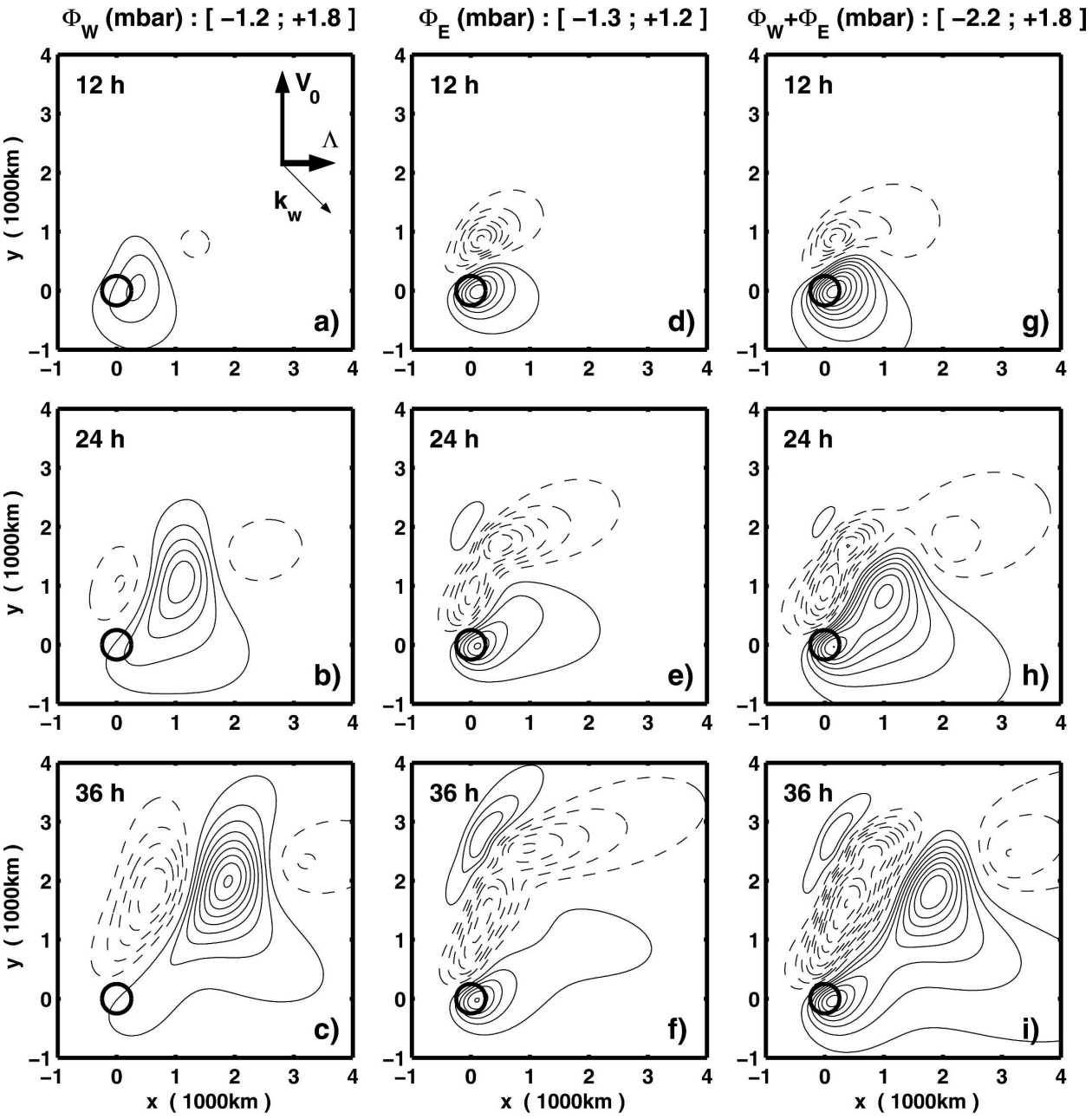

FIG. 8. Same as in Fig. 5 but in the warm front case (same parameters as in Fig. 7).

quasi-null cross-ridge velocity, and therefore a weak GW drag [see Eq. (A5) in the appendix]. The amplifying effect of the descent of the critical zone by decreasing $|(\widehat{\mathbf{e}_x, \mathbf{k}_w})|$ is thus balanced by a decrease of the total force amplitude.

c. Influence of the tropopause

To study the impact of the geostrophic baroclinic instability on our results, we place a rigid lid at the altitude $D = 10$ km. A conventional linear stability analysis for our model shows that unstable baroclinic modes have wavelengths exceeding $2\pi/(2.6 \times f/ND) \sim 2400$ km, and that the most unstable mode is oriented in the alongfront direction ($\mathbf{\Lambda} = \Lambda \mathbf{e}_x$) with a wavelength near 3700 km [$\mathbf{k} = 1.7 \times f/(ND)\mathbf{e}_x$].

As shown in Figs. 12a–c for the cold front case in section 3, in the short term (12 h; Fig. 12a) the instability essentially has a slight quantitative effect on the surface pressure pattern, compared to the case with no

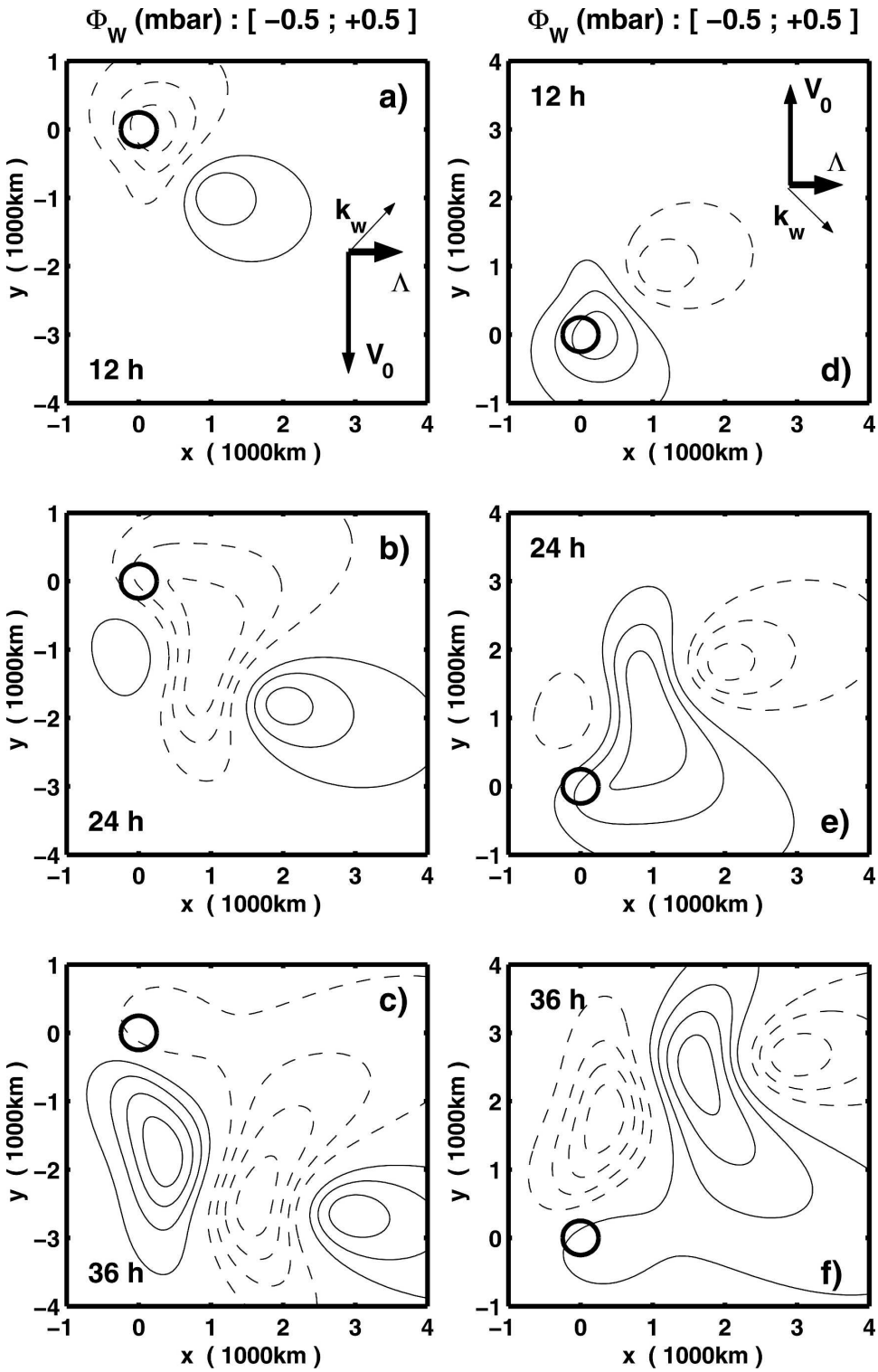

FIG. 9. Quasigeostrophic response to the GWs force. (a)–(c) Cold front; same parameters as in Fig. 5. (d)–(f) Warm front; same parameters as in Fig. 8. Negative values are dashed and CI = 0.1 mb.

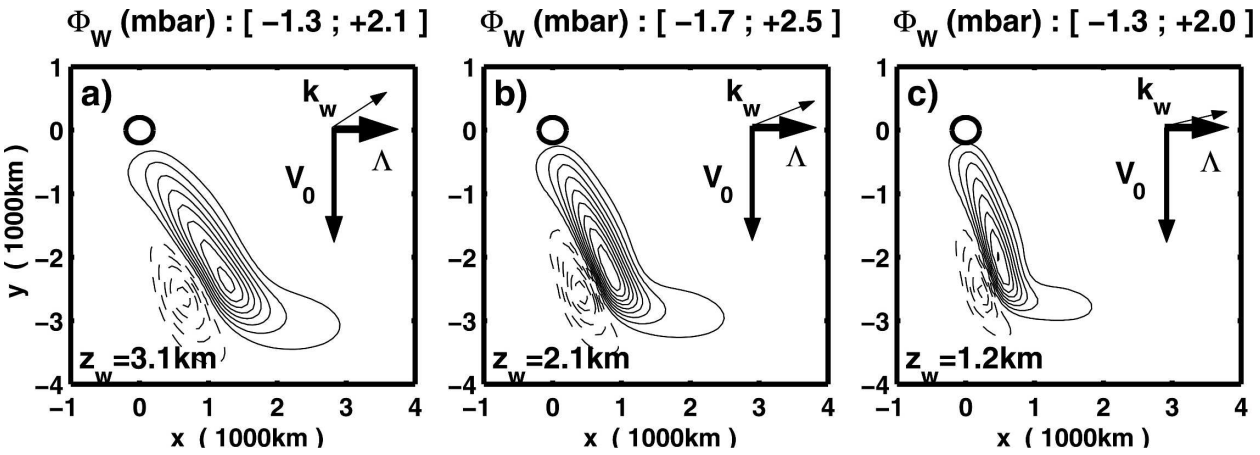

FIG. 10. Surface geopotential ϕ_W induced by the GWs at $t = 36$ h for three different orientations $(\widehat{\mathbf{e}_x, \mathbf{k}_w})$, and for the cold front in section 3. Same background flow and orography parameters as in Fig. 2 except: (a) $(\widehat{\mathbf{e}_x, \mathbf{k}_w}) = 0.7 \times \pi/4$, (b) $(\widehat{\mathbf{e}_x, \mathbf{k}_w}) = 0.5 \times \pi/4$, and (c) $(\widehat{\mathbf{e}_x, \mathbf{k}_w}) = 0.3 \times \pi/4$. The corresponding altitude of the critical zone is also indicated; CI = 0.25 mb.

tropopause in Fig. 5a. At $t = 24$ h (Fig. 12b), the presence of long unstable modes starts to modulate the response substantially. In particular, near and over the mountain the trough is more intense (see Fig. 5b), and its horizontal scale exceeds 2000 km along $\mathbf{\Lambda}$. Later ($t =$ 36 h; Fig. 12c), the long modes' influence is even stronger. Nevertheless, they do not much affect the maximum amplitude of the signal but rather spread it toward $\mathbf{\Lambda}$. A qualitatively comparable behavior occurs in the warm front case of section 4 (Figs. 12d–f), except that it is quantitatively less pronounced.

6. Extension to more realistic mountains

The near monochromatic nature of the small-scale orography used until now results in a rather thin critical zone. In reality, however, mountains have broadband spectra and the GWs can interact with critical levels almost everywhere over the entire troposphere depth. To account for this, we follow Gregory et al. (1998) and represent the real orography spectrum over square domains of size $X \times Y$ by a spectral density function $A(\mathbf{k})$ that captures exactly the orographic variance

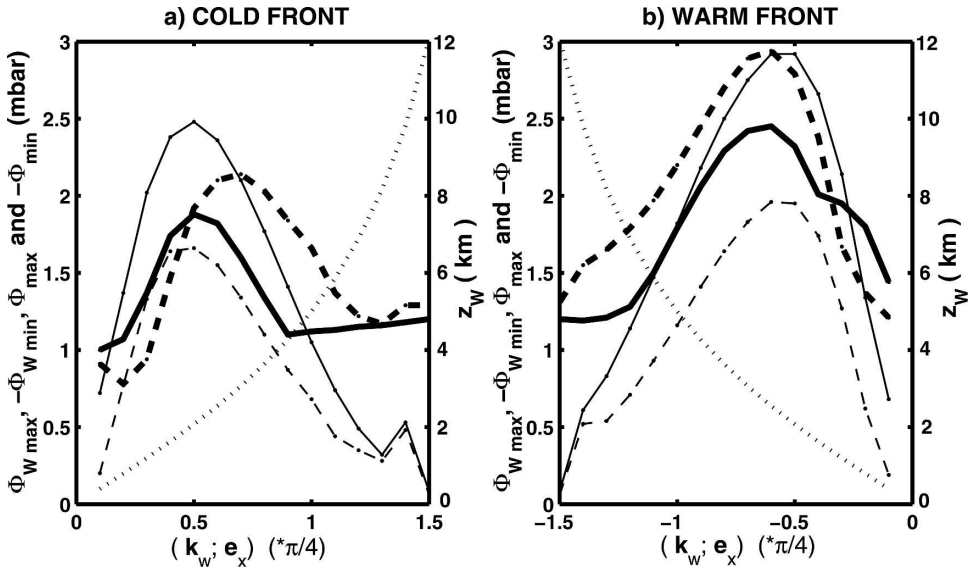

FIG. 11. Extrema in the surface geopotential due to the GWs at $t = 36$ h and for various angles $(\widehat{\mathbf{e}_x, \mathbf{k}_w})$: (a) cold front and (b) warm front. In both (a) and (b), $\max(\phi_W)$ is the thin solid line, $-\min(\phi_W)$ is thin dashed, $\max(\phi_W + \phi_E)$ is thick solid, $-\min(\phi_W + \phi_E)$ is thick dashed, and z_w is dotted.

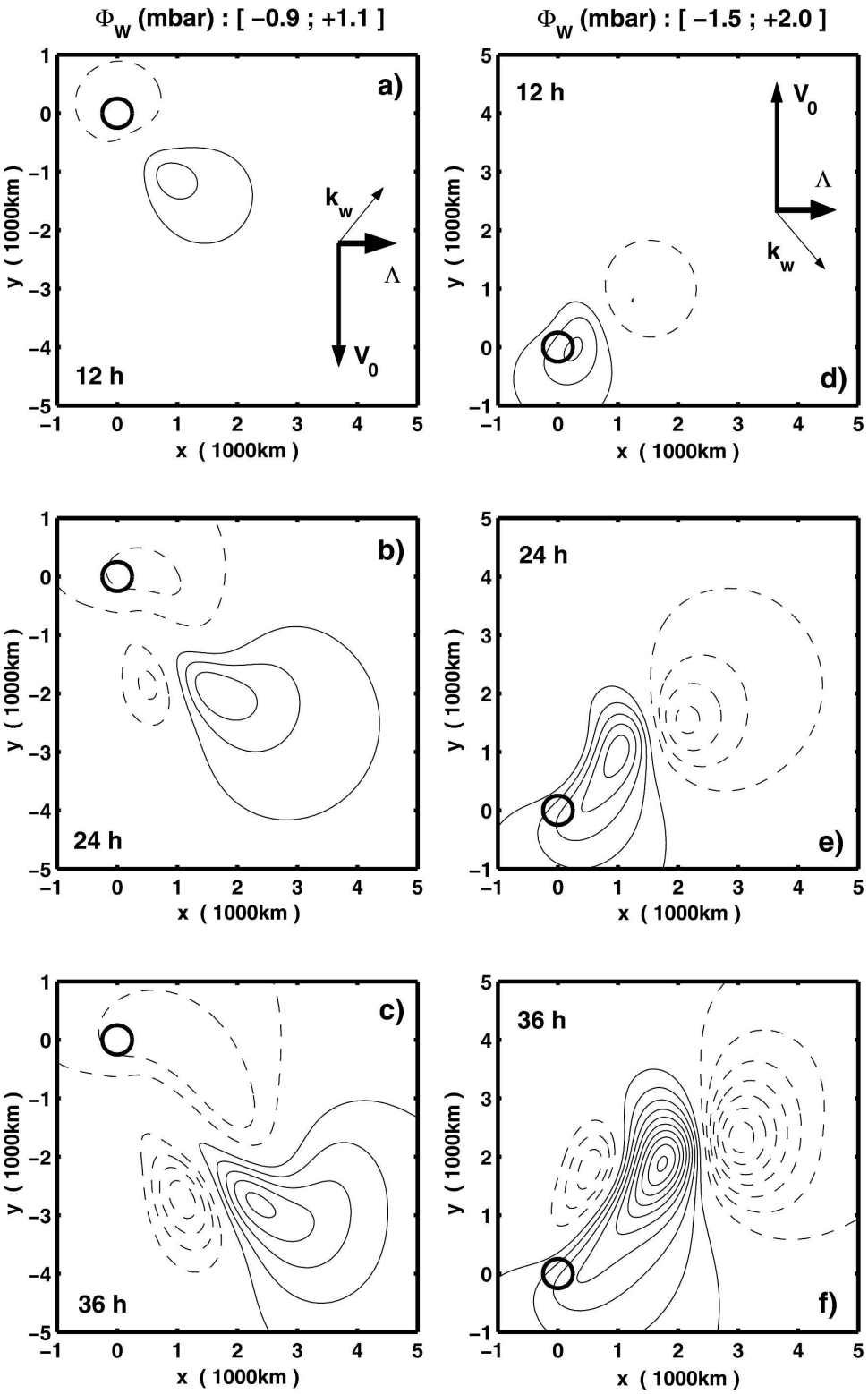

FIG. 12. Simulations with a tropopause at $D = 10$ km. Cold front with the same parameters as in Fig. 5: (a) $t = 12$ h, (b) $t = 24$ h, and (c) $t = 36$ h. Warm front with the same parameters as in Fig. 8: (d) $t = 12$ h, (e) $t = 24$ h, and (f) $t = 36$ h. Negative values are dashed and CI = 0.2 mb.

$$\frac{1}{XY}\int_0^X\int_0^Y h'^2\,dx\,dy = \int_0^{+\infty}\int_0^{2\pi}\frac{4\pi^2}{XY}|\hat{h}(K,\alpha)|^2 K\,dK\,d\alpha = \int_0^{+\infty}\int_0^{2\pi} A(K,\alpha)K\,dK\,d\alpha. \quad (33)$$

In Eq. (33) K and α are the polar coordinates of $\mathbf{k}$, and $\hat{h}(K, \alpha)$ is the Fourier transform of h' inside of the domain $X \times Y$, which can be estimated for real data by the FFT coefficient $\tilde{h}$ calculated from the discrete series of h'. We then assume an isotropic spectral density in the wavenumber band relevant for gravity waves

$$KA(\mathbf{k}) = a\left(\frac{K_0}{K}\right)^{\gamma}, \quad \text{for} \quad K_L < \|\mathbf{k}\| < K_U. \quad (34)$$

In Eq. (34) K_0 and γ are constants that vary regionally, and $a = 1\ \text{m}^3$ is introduced for dimension consistency. We take $K_U = 2\pi/(10\ \text{km}) \approx N/V_0$ because disturbances with shorter wavelength do not propagate vertically, and $K_L = 2\pi/\sqrt{X^2 + Y^2}$, that is, approximately the longest harmonic the domain $X \times Y$ can represent. Note that we could have defined K_L as the lower cutoff of the stationary inertia GWs, $K_L = f/V_0 \approx 1200$ km. This is larger than the size of our domain, and hence is not represented in our spectrum analysis. Nevertheless, we have checked that the following analyses are not sensitive to K_L; for such low values of γ, the orographic variance concentrates on the small scales.

To evaluate the effect of this spectrum in the context of our model, we consider the effect of the small-scale mountains located in a domain of size $\pi L^2 = XY$ and use the method in the appendix to evaluate the net force due to $A(\mathbf{k})$:

$$\overline{\mathcal{F}} = \frac{2N\Lambda a}{2-\gamma}\left[\left(\frac{K_0}{K_U}\right)^{\gamma}K_U^2 - \left(\frac{K_0}{K_L}\right)^{\gamma}K_L^2\right]\frac{\Lambda z|V_0|^3}{\|\mathbf{U}(z)\|^4} \times \left[\mathbf{e}_x - \frac{U(z)}{V_0}\mathbf{e}_y\right]. \quad (35)$$

We then distribute this force regionally as in section 2, $\mathcal{F}(\mathbf{x}, z) = \overline{\mathcal{F}}(z)e^{-(x^2+y^2/L^2)}$.

To give realistic values to the parameters K_0 and γ, we have considered the Alpine sector (43°–48°N, 5°–16°E) and used the 2-Minute Gridded Global Relief Data (ETOPO2; around 2-km horizontal resolution; see the National Geophysical Data Center 2006). In this sector, we define 30 partially overlapping square domains, each of size $XY = 352\ \text{km}^2 = \pi L^2$, giving $L =$ 200 km as in sections 3, 4, and 5 (Fig. 13a). For each of these domains, we estimate $[\gamma, \ln(K_0^{\gamma})]$ by a best square fit between $A(\mathbf{k})$ and the azimuthal mean of the orography periodogram $\tilde{h}\tilde{h}^*$. An example for one particular box (43°48′N, 46°58′N) × (5°26′E, 9°58′E) is shown in Fig. 13. For this box, the best fit is $\gamma = 0.96$ and $\ln(K_0^{\gamma}) = 10.2$ (Fig. 13b). For other boxes, the results are summarized in Fig. 13c; even if the parameters γ and $\ln(K_0^{\gamma})$ have significant variations (the range obtained for γ is from 0.56 to 1.02), the resulting force for each box has a rather stable magnitude around $2 \times 10^{-4}\ \text{kg m}^{-2}\ \text{s}^{-2}$. Therefore, in our simulations we can use, for the force, the mean values

$$\gamma = 0.76; \quad \ln(K_0^{\gamma}) = 13.5. \quad (36)$$

Note that our γ is smaller than in Gregory et al. (1998; who found $\gamma > 1$), probably because the Alps are sharper than the mountains studied by these authors.

Figures 14a,b present the vertical profiles of $\mathcal{F}$ obtained with Eqs. (35)–(36) and for the cold front of section 3. As expected, the critical zone is deeper than in Fig. 2 and covers the entire troposphere. The surface response to this force in the absence of tropopause is shown in Fig. 14c at $t = 36$ h. It resembles very much that of the idealized case in Fig. 5c. A predominant ridge is followed by a weaker trough, both being embedded in the south-southeast sector. The dominant wave vector is very similar to that of section 3b, although not so well defined. The reason is that the critical zone is deep, giving no precise horizontal axis to the PV pattern.

7. Discussion and conclusions

This paper gives a heuristic evaluation of the significance of mountain GWs for the synoptic-scale dynamics near large mountain ranges, in the presence of directional critical levels. The model used is an extension of the model of Smith (1984) for lee cyclogenesis. It includes a representation of the GWs adapted from Shutts (1995). The interaction between the GWs and the large-scale flow occurs via the PV anomaly, which is produced by the force due to the GWs, which encounter critical levels in the troposphere.

Section 3 details this interaction for a cold front, in the case where there is a good separation between the small-scale dynamics and the large-scale dynamics. In a configuration such that almost all the GWs encounter critical levels, they induce a force in a thin critical zone centered around a well-defined altitude z_w. The level z_w depends on the configuration of the front relative to the orientation of the anisotropic small-scale orography. This force is everywhere perpendicular to the background flow and produces a PV anomaly around z_w that is advected and steered by the background wind.

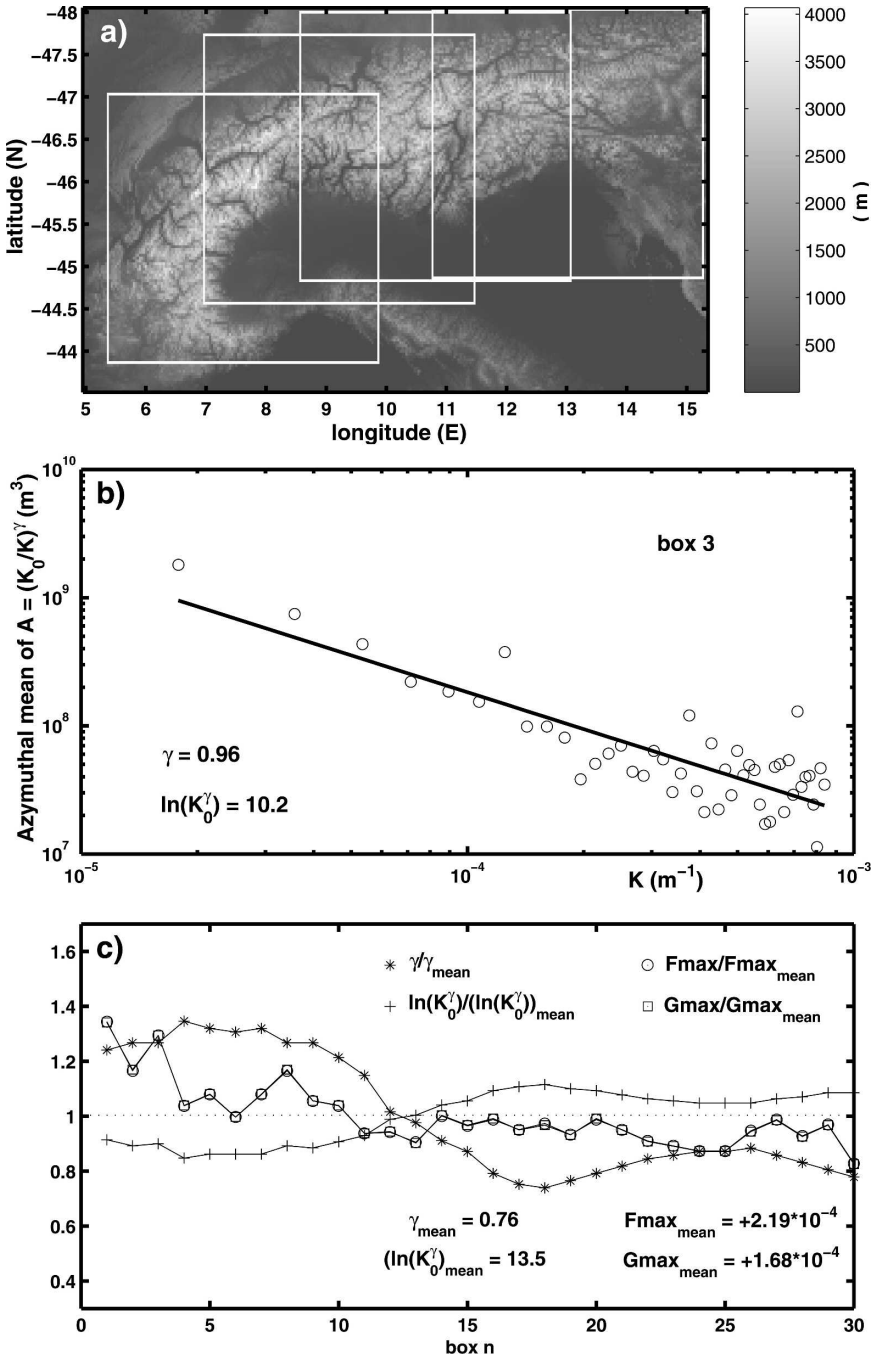

FIG. 13. Spectral analysis of the Alps. (a) Elevation from ETOPO2. Five among the 30 boxes used to evaluate the mean spectrum are indicated for illustration. (b) Azimuthal mean of the periodigram (circles) and best square linear fit (thick solid) for box 3 shown in the lower left of (a). (c) Best fit values for the 30 boxes: γ (solid and star), $\ln(K_0^{\gamma})$ (solid and plus), $\mathcal{F}_{\max}$ (solid and circles), and $\mathcal{G}_{\max}$ (solid and square). All values in (c) are divided by their mean value over the 30 boxes.

Near z_w, the PV anomaly is predominantly cyclonic aloft of the mountain, and it presents a start-up anticyclone that travels at the velocity $\mathbf{U}(z_w)$ away from the mountain (Fig. 3). Below z_w the PV anomaly is predominantly anticyclonic, whereas above z_w it is predominantly cyclonic. Accordingly, the surface response at small times (12 h in Fig. 5a) presents a trough over the mountain and a ridge downstream. Over a longer

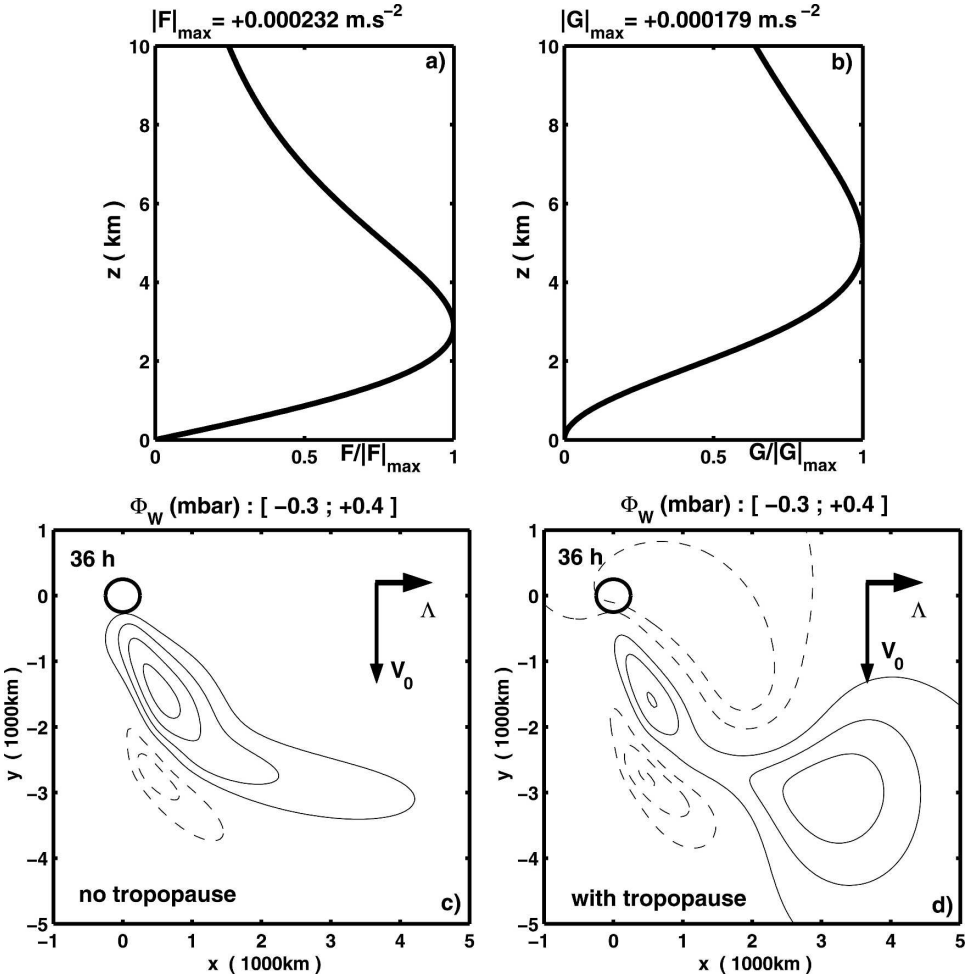

FIG. 14. Cold front simulations with an orographic spectrum representative of the Alps. (a) Vertical profile of $\overline{\mathcal{F}}(z)$, (b) vertical profile of $\overline{\mathcal{G}}(z)$, (c) ϕ_W at $t = 36$ h with no tropopause, and (d) ϕ_W at $t = 36$ h with tropopause at $D = 10$ km. Negative values are dashed and CI = 0.1 mb.

term, this response is modulated by Eady waves (Figs. 5b,c); the trough over the mountain becomes quite small, and an elongated ridge builds up immediately downstream toward $\mathbf{U}(z_w)$. The GWs thus tend to slightly reduce the amplitude of the response to the large-scale orography, notably the ridge over the mountain and the lee trough (Figs. 5d–f). As the lee trough is associated with lee-cyclone initiation in Smith (1984), we can argue that the GWs are cyclolytic in the cold front case.

In section 4 we repeat the same study in the warm front case (Figs. 7 and 8), after rotating by 90° the orientation of the mountain ridges in order that the GWs exert a substantial force. In this case, the PV anomaly produced by the GWs is predominantly anticyclonic over the mountain and cyclonic downstream (Fig. 7). It is also predominantly anticyclonic below z_w and cyclonic above. Hence, the surface response presents a large-scale ridge attached to the mountain (Figs. 8a–c), and extending below the PV anomaly, toward $\mathbf{U}(z_w)$ (Fig. 7). Eady wave dynamics produce a trough downstream of the mountain, toward the surface wind $\mathbf{U}(0)$ (Figs. 8b,c). In this case, and contrary to the cold front case, the GWs reinforce the ridge over the mountain and the downstream trough (Figs. 8d–f).

The rest of the paper consists of doing tests of the robustness of these results. They indeed seem to be linked to geometrical properties of the GW directional critical levels, indicating that they are rather systematic. In section 5a, we adopt the QG framework. This illustrates the important role of the vertical component of the PV flux in baroclinic environments. In section 5b, we change the orientation of $\mathbf{k}_w$, and other crucial parameters. Even if those changes have some quantitative effects on the amplitude or the horizontal scale of the surface response, the cyclolytic nature of the GWs in

the cold front case stays unchanged. The same is true in the warm front case, where the interaction remains cyclogenetic. The introduction of a tropopause in section 5c is more significant qualitatively, even if in our model, the baroclinic instabilities can only modulate the GW response at horizontal scales much larger than discussed up to now. The effect is particularly pronounced in the cold front case (Figs. 12a–c), where, compared to the same case without a tropopause (Figs. 5a–c), the trough over the ridge becomes rather large in the long term (Fig. 12c) instead of becoming small (Fig. 5c), while the ridge downstream becomes rather small instead of being large. In the warm front case (not shown) the effect of the GWs aloft of the mountain and immediately downstream of it stays the same as that without a tropopause. It is only in the far field and at large scales that the influence of the baroclinic instabilities becomes substantial.

In section 6 we present an extension of our model to more realistic small-scale orographic spectra. We use for this a method presented in Gregory et al. (1998) in the context of the parameterization of mountain GWs via a spectral method in the Met Office (UKMO) model. This method consists again of evaluating the GW force exactly but using a realistic spectral density function for the orography. For the case of the Alps (Fig. 13), the GW force is more broadly distributed over the troposphere. Nevertheless, the surface responses to the GWs (Fig. 14) share many properties with the responses for the idealized orography profiles used in sections 3, 4, and 5.

Despite the attractive simplicity of our model, these results should be interpreted with some caution. For instance, the neglect of unbalanced effect can be inaccurate for shears larger than here; the inertio-gravity waves generated during the interaction (Lott 2003; Vadas et al. 2003; Shutts 2003) or the nongeostrophic unstable baroclinic modes (Plougonven et al. 2005) may have a substantial influence at the surface. More seriously, by representing the fronts by uniform shears we do not consider the barotropic growth of unstable modes that the smooth mountain and the GWs may trigger. This may result in effects rather different from those discussed here, in particular because the horizontal scale of the unstable modes may be much closer to the horizontal scale of the mountain.

Nevertheless, we believe that the structure of the PV anomalies we discuss here is of some interest. They are produced by PV fluxes that are everywhere parallel to the background wind, a situation rarely discussed in the literature. As a result, they do not resemble the horizontal PV banners that are often discussed. These PV anomalies are also strongly affected by the inclination of the isentropes. For these reasons, they may reflect some aspects of the mesoscale and synoptic-scale PV patterns found in the observations. For example, Hoinka et al. (2003) have carried out an analysis of the MAP intensive observation period 15 (IOP-15) in which a PV streamer from the low stratosphere passes above the Alps, triggering lee cyclogenesis. They mention the importance of the breaking GWs in the cutoff process and the presence of enhanced shear. Since the order of magnitude of our PV anomalies is comparable to theirs, the process we have studied here might have some relevance in their case.

Another interest of this study is to give a theoretical approach to the problem of mountain GW parameterization in large-scale models. In this respect, the fact that the response to the GWs is generally smaller than the response to the large-scale orography is reasonable. The SSO parameterizations are intended for correcting errors, not for producing the dominant signal. In this context, it gives two messages.

First, a rather systematic error of large-scale models is that they underestimate, at least in winter, the anticyclonic circulation that occurs over the large-scale mountains. These errors have been corrected in the past either by introducing an envelope orography, or by introducing lift forces oriented perpendicularly to the geostrophic flow and toward the right (in the Northern Hemisphere). The two approaches are in good part equivalent (Lott 1999). Although the GW force is also perpendicular to the flow, our results show that it does not systematically help the building up of anticyclones over mountains. Indeed, it is probably the other way around because cold fronts are stronger than warm fronts in a climatological sense. Second, our results show that absorbed GWs have little chance to help lee cyclogenesis and seem to have a rather cyclolytic influence, if we again assume that cold fronts are more frequent.

APPENDIX

Evaluation of the GW Force $\overline{\mathcal{F}}$

We use the linear Boussinesq theory of hydrostatic stationary mountain GWs in uniform background shears (Shutts 1995). The vertical velocity for each monochromatic wave satisfies

$$\frac{\partial^2 \hat{w}'}{\partial z^2} + \frac{N^2}{[\mathbf{k}\cdot\mathbf{U}(z)]^2}(k^2 + l^2)\hat{w}' = 0, \quad \text{with}$$

$$\hat{w}'(0) = -i\mathbf{k}\mathbf{U}_0\hat{h}'. \qquad \text{(A1)}$$

The waves that present a critical level at $z_c = -\mathbf{k}\mathbf{U}_0/k\Lambda > 0$ can be written

$$\hat{w}'(z) = -i\mathbf{k}\mathbf{U}_0\hat{h}'\left(1 - \frac{z}{z_c}\right)^{1/2+\epsilon i\alpha}, \quad \epsilon = \pm 1, \quad \text{for} \quad z < z_c \tag{A2}$$

$$\approx 0 \qquad \text{for} \quad z > z_c, \tag{A3}$$

where $\alpha = \sqrt{\mathrm{Ri}(k^2 + l^2/k^2) - \frac{1}{4}}$. We take $\epsilon\mathbf{k}\mathbf{U}_0 > 0$ to impose an upward group velocity. In Eqs. (A2)–(A3) the GWs reflected or transmitted at z_c have been neglected because $\mathrm{Ri} \approx 6 \gg 0.25$ (Booker and Bretherton 1967). Note that Eq. (A2) is an exact solution of Eq. (A1) for the entire domain under z_c. Besides, the mean stress satisfies

$$\overline{\mathbf{u}'w'} \equiv \frac{1}{\pi L^2}\int_{-\infty}^{+\infty}\int_{-\infty}^{+\infty}\mathbf{u}'w'\,dx\,dy = \frac{4\pi^2}{\pi L^2}\int_{k=0}^{+\infty}\int_{l=-\infty}^{+\infty}(\hat{\mathbf{u}}\hat{w}^* + \hat{\mathbf{u}}^*\hat{w})\,dl\,dk. \tag{A4}$$

We take the background wind of Eq. (3) for a cold front ($V_0 < 0$, $\Lambda > 0$), and use Eqs. (A2)–(A3) and the dispersion relationships for the GWs, which yields

$$\overline{\mathbf{u}'w'}(z) = \frac{8\pi^2}{\pi L^2}\int_{k=0}^{+\infty}\int_{l=-\frac{kU(z)}{V_0}}^{+\infty} -\frac{\mathbf{k}}{\|\mathbf{k}\|}(\mathbf{k}\mathbf{U}_0)N|\hat{h}'|^2\,dl\,dk + \ldots, \tag{A5}$$

where the dots are for the z-independent part of the flux carried by the GWs that do not encounter critical levels. Then, the associated force is

$$\overline{\mathcal{F}}(z) = -\frac{d}{dz}\overline{\mathbf{u}'w'} = \frac{8\pi^2}{\pi L^2}N\Lambda \times \int_0^{+\infty} k^2\left|\hat{h}'\left[k, l = -k\frac{U(z)}{V_0}\right]\right|^2 dk \times \frac{\Lambda z}{\|\mathbf{U}(z)\|}\left[\mathbf{e}_x - \frac{U(z)}{V_0}\mathbf{e}_y\right]. \tag{A6}$$

This last formula is valid for any kind of front of the form of Eq. (3), cold or warm. For the idealized orography profile of Eq. (1), $h' = \mathcal{H}(\mathbf{x})\cos(\mathbf{k}_w\mathbf{x})$, which leads to

$$\hat{h}' = \frac{H_0L^2}{4\pi}(e^{-(\mathbf{k}-\mathbf{k}_w)^2(L^2/2)} + e^{-(\mathbf{k}+\mathbf{k}_w)^2(L^2/2)}). \tag{A7}$$

To simplify the analytical treatment under the assumption that the horizontal scales are clearly separable ($\|\mathbf{k}_w\|\,L \gg 1$), we neglect the second Gaussian term of Eq. (A7), because it is centered around $-\mathbf{k}_w$ and the integral in Eq. (A6) is for $k > 0$. The steepest descent estimate of the integral of the remaining Gaussian term in Eq. (A6) yields the Eqs. (22)–(23) in section 2c. Note that if $k_w\,l_w < 0$ for the cold front case, we obtain $\overline{\mathcal{F}} \approx 0$, because the waves that encounter a critical level have a very small amplitude in this case. On the opposite, in the warm front case, $\overline{\mathcal{F}} \approx 0$ if $k_w\,l_w > 0$.

REFERENCES

Aebischer, U., and C. Schär, 1998: Low-level potential vorticity and cyclogenesis to the lee of the Alps. *J. Atmos. Sci.,* **55,** 186–207.

Binder, P., and C. Schär, 1996: MAP design proprosal. Meteo Swiss, 77 pp. [Available online at http://www.map.meteoswiss.ch/map-doc/prop/MDP.pdf.]

Boer, G. J., N. A. McFarlane, R. Laprise, J. D. Henderson, and J.-P. Blanchet, 1984: The Canadian Climate Center spectral atmospheric general circulation model. *Atmos.–Ocean,* **22,** 397–429.

Booker, J. R., and F. P. Bretherton, 1967: The critical layer for internal gravity waves in a shear flow. *J. Fluid Mech.,* **27,** 513–539.

Bougeault, P., and Coauthors, 2001: The MAP special observing period. *Bull. Amer. Meteor. Soc.,* **82,** 433–462.

Bretherton, F. P., 1969: Momentum transport by gravity waves. *Quart. J. Roy. Meteor. Soc.,* **95,** 213–243.

Broad, A. S., 1999: Do orographic gravity waves break in flows with uniform wind direction turning with height? *Quart. J. Roy. Meteor. Soc.,* **125,** 1695–1714.

Bühler, O., and M. E. McIntyre, 2005: Wave capture and wave-vortex duality. *J. Fluid Mech.,* **534,** 67–95.

Davis, C. A., 1997: The modification of baroclinic waves by the Rocky Mountains. *J. Atmos. Sci.,* **54,** 848–868.

Eliassen, A., and E. Palm, 1961: On the transfer of energy in the stationary mountain waves. *Geofys. Publ.,* **22,** 1–23.

Fantini, M., and S. Davolio, 2001: Instability of neutral Eady waves and orography. *J. Atmos. Sci.,* **58,** 1146–1154.

Flamant, C., E. Richard, C. Schär, R. Rotunno, L. Nance, M. Sprenger, and R. Benoit, 2004: The wake south of the Alps: Dynamics and structure of the lee-side flow and secondary potential vorticity banners. *Quart. J. Roy. Meteor. Soc.,* **130,** 1275–1303.

Gregory, D., G. J. Shutts, and J. R. Mitchell, 1998: A new gravity-wave-drag scheme incorporating anisotropic orography and low-level wave-breaking: Impact upon the climate of the UK Meteorological Office unified model. *Quart. J. Roy. Meteor. Soc.,* **124,** 463–493.

Gross, B. D., 1994: Frontal interaction with isolated orography. *J. Atmos. Sci.,* **51,** 1480–1496.

Haynes, P. H., and M. E. McIntyre, 1987: On the evolution of vorticity and potential vorticity in the presence of diabatic heating and frictional or other forces. *J. Atmos. Sci.,* **44,** 828–841.

Hoinka, K. P., E. Richard, G. Poberaj, R. Busen, J.-L. Caccia, A. Fix, and H. Mannstein, 2003: Analysis of a potential-vorticity streamer crossing the Alps during MAP IOP-15 on 6 November 1999. *Quart. J. Roy. Meteor. Soc.,* **129,** 609–632.

Hoskins, B. J., 1975: The geostrophic momentum approximation

and the semi-geostrophic equations. *J. Atmos. Sci.,* **32,** 233–242.

——, M. E. McIntyre, and A. W. Robertson, 1985: On the use and significance of isentropic potential vorticity maps. *Quart. J. Roy. Meteor. Soc.,* **111,** 877–946.

Jiang, Q., and J. D. Doyle, 2004: Gravity wave breaking over the central Alps: Role of complex terrain. *J. Atmos. Sci.,* **61,** 2249–2266.

Liniger, M. A., and H. C. Davies, 2003: Substructure of a map streamer. *Quart. J. Roy. Meteor. Soc.,* **129,** 633–651.

Lott, F., 1999: Alleviation of stationary biases in a GCM through a mountain drag parameterization scheme and a simple representation of mountain lift forces. *Mon. Wea. Rev.,* **127,** 788–801.

——, 2003: Large scale flow response to short gravity waves breaking in a rotating shear flow. *J. Atmos. Sci.,* **60,** 1691–1704.

——, and M. J. Miller, 1997: A new subgrid-scale orographic parametrization: Its formulation and testing. *Quart. J. Roy. Meteor. Soc.,* **123,** 101–127.

McFarlane, N. A., 1987: The effect of orographically excited gravity wave drag on the general circulation of the lower stratosphere and troposphere. *J. Atmos. Sci.,* **44,** 1775–1800.

Messinger, M., and R. Pierrehumbert, 1986: Alpine lee cyclogenesis: Numerical simulation and theory. *Scientific Results of the Alpine Experiment,* GARP Publications Series 27, Vol. I, WMO/International Council of Scientific Unions, 141–165.

Miller, M. J., T. N. Palmer, and R. Swinbank, 1989: Parametrization and influence of subgridscale orography in general circulation and numerical weather prediction models. *Meteor. Atmos. Phys.,* **40,** 84–109.

National Geophysical Data Center, cited 2006: 2-Minute Gridded Global Relief Data (ETOPO2v2). NOAA/NESDIS/NGCD. [Available online at http://www.ngdc.noaa.gov/mgg/fliers/06mgg01.html.]

Palmer, T. N., G. J. Shutts, and R. Swinbank, 1986: Alleviation of a systematic westerly bias in general circulation and numerical weather prediction models through an orographic gravity wave drag parametrization. *Quart. J. Roy. Meteor. Soc.,* **112,** 1001–1039.

Phillips, D. S., 1984: Analytical surface pressure and drag for linear hydrostatic flow over three-dimensional elliptical mountains. *J. Atmos. Sci.,* **41,** 1073–1084.

Pierrehumbert, R. T., 1985: A theoretical model of orographically modified cyclogenesis. *J. Atmos. Sci.,* **42,** 1244–1258.

Plougonven, R., D. J. Muraki, and C. Snyder, 2005: A baroclinic instability that couples balanced motions and gravity waves. *J. Atmos. Sci.,* **62,** 1545–1559.

Scavuzzo, C. M., M. A. Lamfri, H. Teitelbaum, and F. Lott, 1998: A study of the low frequency inertio-gravity waves observed during PYREX. *J. Geophys. Res.,* **103** (D2), 1747–1758.

Schär, C., 1990: Quasi-geostrophic lee cyclogenesis. *J. Atmos. Sci.,* **47,** 3044–3066.

——, and D. R. Durran, 1997: Vortex formation and vortex shedding in continuously stratified flows past isolated topography. *J. Atmos. Sci.,* **54,** 533–554.

——, M. Sprenger, D. Lüthi, Q. Jiang, R. B. Smith, and R. Benoit, 2003: Structure and dynamics of an Alpine potential-vorticity banner. *Quart. J. Roy. Meteor. Soc.,* **129,** 825–855.

Scinocca, J. F., and N. A. McFarlane, 2000: The parametrization of drag induced by stratitified flow over anisotropic orography. *Quart. J. Roy. Meteor. Soc.,* **126,** 2353–2393.

Shutts, G. J., 1995: Gravity-wave drag parametrization over complex terrain: The effect of critical-level absorption in directional wind-shear. *Quart J. Roy. Meteor. Soc.,* **121,** 1005–1021.

——, 2003: Inertia-gravity wave and neutral Eady wave trains forced by directionally sheared flow over isolated hills. *J. Atmos. Sci.,* **60,** 593–606.

——, and A. Gadian, 1999: Numerical simulations of orographic gravity waves in flows which back with height. *Quart. J. Roy. Meteor. Soc.,* **125,** 2743–2765.

Smith, R. B., 1979: Some aspects of the quasi-geostrophic flow over mountains. *J. Atmos. Sci.,* **36,** 2385–2393.

——, 1984: A theory of lee cyclogenesis. *J. Atmos. Sci.,* **41,** 1159–1168.

——, 1986: Further development of a theory of lee cyclogenesis. *J. Atmos. Sci.,* **43,** 1582–1602.

Speranza, A., A. Buzzi, A. Trevisan, and P. Malguzzi, 1985: A theory of deep cyclogenesis in the lee of the Alps. Part I: Modifications of baroclinic instability by localized topography. *J. Atmos. Sci.,* **42,** 1521–1535.

Vadas, S. L., D. C. Fritts, and M. J. Alexander, 2003: Mechanism for the generation of secondary waves in wave breaking regions. *J. Atmos. Sci.,* **60,** 194–214.

Webster, S., A. R. Brown, D. R. Cameron, and C. P. Jones, 2003: Improvements to the representation of orography in the Met Office unified model. *Quart. J. Roy. Meteor. Soc.,* **129,** 1989–2010.

2.2 Complementary works

In the following, we add interesting results that we could not introduce in the article, and which probably need further investigation. All these results are based on variations from the experiments described in the sections 4 and 5.c of the previous article, that is the warm front case. But we systematically compare the results with and without a rigid upper boundary localized at a height D=10km. The same can be done in the cold front case but the behaviour is different.

In the Fig. 2.1, three simulations with the upper boundary are presented in each column, in which the height of the dominant critical level z_w is lowered from 5km (Figs. 2.1a,b, c) to 3.1km (Figs. 2.1d,e,f) and then to 1.2km (Figs. 2.1g,h,i). In each column, the first two pictures present the response at t=36h and 72h respectively in terms of the surface geopotential perturbation, and the last one presents the time evolution of the maximum and minimum values of the surface geopotential (red) in comparison with the same experiment with no upper boundary (black). In particular, the Fig. 2.1a presents the same response as the Fig. 12f of the article, but with a different contour interval. The first thing to note is that, from the Figs. 2.1b,e,h, the presence of the most unstable baroclinic Eady mode is reduced when the force and the PV are lowered so that they are closer to the surface than the upper boundary. This is confirmed by the Figs. 2.1c,f,i, which show that the baroclinic growth is more efficient when the PV is localized near the steering level of the two boundaries Eady problem. In comparison, the simulations with no upper boundary give very similar results. Qualitatively, this result follows that in the presence of two boundaries, when the PV is produced near the steering level its zonal advection velocity equals the phase velocity of the baroclinic normal modes. This way, the PV can follow these modes and impose a continuous and efficient forcing. This situation is actually the counterpart of the resonant forcing that occurs in the problem with no tropopause, and leads to the linear growth of the surface resonant mode (black curves in Figs. 2.1c,f,i). Moreover, the growth is not exponential anymore in the Figs. 2.1f,i, and show different regimes with enhanced growth in the first ten hours and reduced growth later. The blatant assymetry between negative and positive values also suggests that the growth mechanism is not reduced to normal mode instability.

In our highly idealized model, the background shear is uniform with infinite extension. This is of course highly unrealistic. A way to account roughly for the finite size of the front in our model, is to cut the forcing by the GWs at a certain date. It means that there is no more directional wind shear aloft the mountain from this date, and hence the mountain GWs do not break anymore. But the existing PV anomalies produced before are still present in the front area, and are advected by the directional windshear following with the same process described before. This experiment allows to measure the efficiency by which the dipolar PV anomly can sustain the growth of the surface perturbation. The results of such experiments are presented for two heights z_w=5km or 3.1km, in the Figs. 2.2a,e respectively (surface response at t=72h) and the Figs. 2.2c,f (time evolution of the surface minimum and maximum in blue diamonds, in comparison with the run without cut in red circles). The force is cut after 12h in the first experiment, and after 24h in the second. The Figs. 2.2a,e show that the perturbation even more ressembles the most unstable Eady mode after several days, because the PV anomalies are no more attached to the mountain. The Figs. 2.2c,f show that

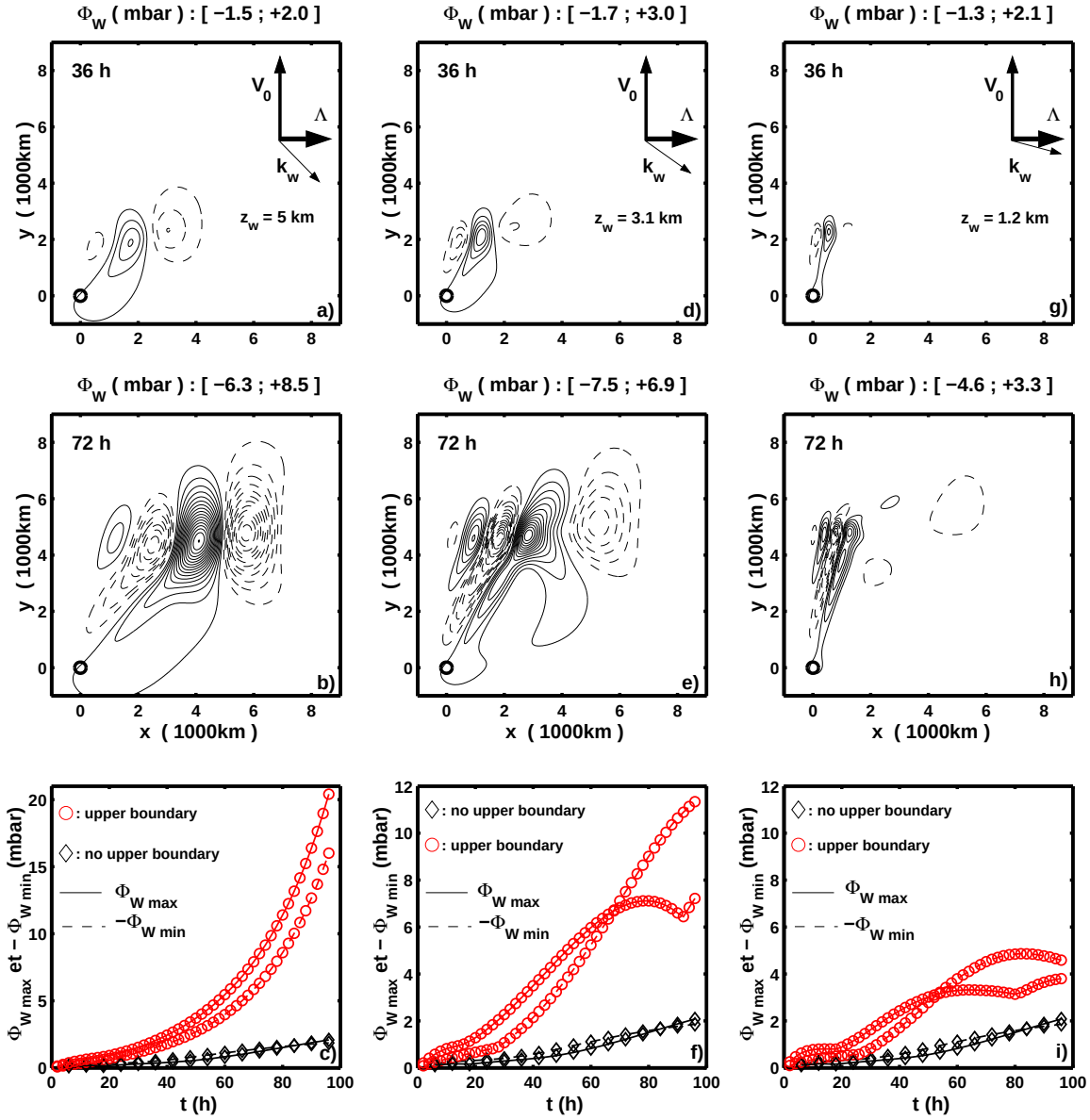

FIG. 2.1 – Surface geopotential perturbation at t=36h and 72h in the warm front case with an upper boundary (D=10km) : z_w=5km in a) and b), z_w=3.1km in d) and e), z_w=1.2km in g) and h). Negative values are dashed and CI = 0.5 mb. The time evolution of maximum (solid) and minimum (dashed) values is summarized in c), f) and i) for the corresponding column experiments (red), with the associated experiments with no upper boundary for comparison (black).

the growth is almost not affected by the removal of the force, or even slightly enhanced. This result is related to the fact that, as soon as the initial transient growth of the PV magnitude is terminated, that is after the first ten hours, then the lifetime of the forcing by the GWs can change the form of the advected PV dipole, but not the magnitude of the PV anomalies. The slight differences that appear in the time evolution only relies on the different form (length) of the moving PV anomalies, which implies the forcing of slightly different wavenumbers.

One last experiment is presented in the Figs. 2.2b,e and c,f (green squares), which differs by the two previous ones in the fact that the PV anomaly is also abruptly turned to zero after t=36h. This is expected to account very crudely for the disappearance of PV anomalies due to dissipation, and to measure the growth efficiency of the interaction of the remaining surface and tropopause Eady waves. As our model is balanced, no spurious transient effect is produced by this brutal change. The Figs. 2.2c,f show that the growth is seriously reduced by this modification, which gives rise to a transient adaptation stage in the case of a low forcing (Fig. 2.2f).

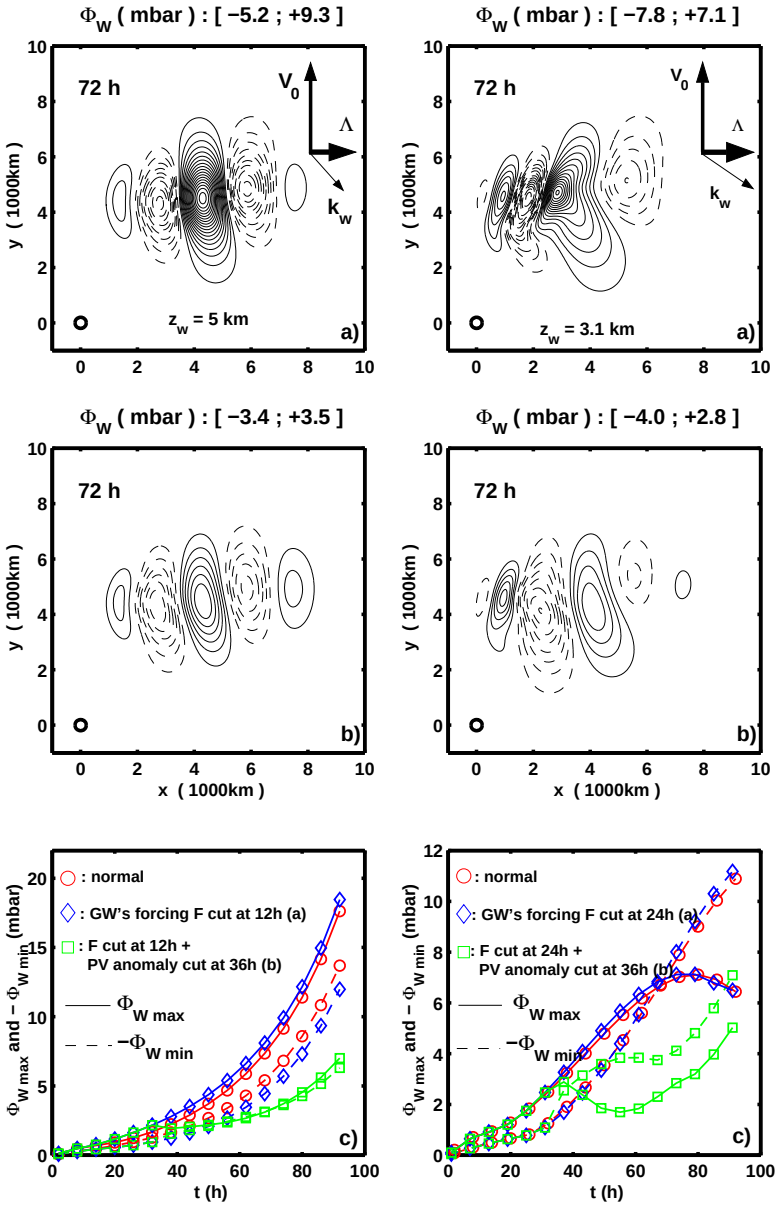

FIG. 2.2 – Surface geopotential perturbation at t=72h in the warm front case with an upper boundary (D=10km) : in a) and b) z_w=5km and the force is cut at t=12h ; in d) and e) z_w=3.1km and the force is cut at t=24h. The PV is also cut at t=36h in b) and e). Negative values are dashed and CI = 0.5 mb. The time evolution of maximum (solid) and minimum (dashed) values is summarized in c) and f) for the corresponding column experiments, with the reference standard experiments in red for comparison.

These results appeal for a better understanding of the influence of some parameters of our problem in terms of finite time growth (Orr 1907, Farrell 1982, Heifetz and Methven 2005). Thus, we might refine the discussion about lee cyclogenesis impacts by analysing the different growth mechanisms in the context of finite time growth, notably in the first days, and finding optimal configurations. To do so, the recent works of De Vries and Opsteegh (2005, 2007a) constitute a good starting point. These authors have analysed and quantified the different growth mechanisms and optimal perturbations for finite time growth in the 2D linear quasi-geostrophic Eady problem, with and without troposphere. In this aim, they consider the total solution of the Eady problem as constituted not only of the normal modes, which are pairs of mutually interacting Eady edge waves (potential temperature anomalies with zero inflow PV), but also of the continuous modes, each inverted from a sheet of inflow PV perturbation localized at a given height. In this framework, if the continuous modes are decomposed into two contributions, one carrying the inflow PV anomaly but no boundary Potential Temperature (PT), and the other carrying the boundary PT anomaly but no inflow PV, then the finite time growth is the result of all the mutual interactions between pairs of PV or PT anomalies. Thus, three different growth mechanisms can be identified. The more classical is the exponential growth corresponding to normal mode instability, namely the mutual amplification of counter-propagating edge waves, which is only possible in the presence of a tropopause. But more generally, the two other mechanisms can act with or without tropopause, and are usually dominant in the first stages of the growth. One is called *resonance*, and corresponds to the amplification of an edge wave by an inflow PV anomaly moving at the same phase velocity. It leads to linear growth if the PV is localized at the steering level of the edge wave (Thorncroft and Hoskins 1990, Bishop and Heifetz 2000). And the other is called *PV unshielding*, or *PV/PT unshielding*, which represents a generalization of the Orr (1907) mechanism, namely the streamfunction growth resulting from the difference between the instantanous phase velocity of all the PV and PT anomalies.

To adapt this theoretical framework to our problem, we should first try to extend the results of De Vries and Opsteegh (2005, 2007a) to our 3D linear semi-geostrophic framework. This means that we must change our current perturbation decomposition to use the one described above, separating completely the inflow PV anomaly fields from the edge PT anomaly fields. We shall also have to choose a norm as regards to which the singular vector will be searched, and which is relevant for cyclogenesis. Notably, the use of a semi-norm like the surface kinetic energy is not possible as soon as several PV anomalies are present (Ve Vries and Opsteegh 2005). But also, we might choose a norm for the initial state that is different from the one used for the final state, because our point is to determine the best place to deposit a given fixed amount of PV to get optimal cyclogenesis. Then, we will have to extend these results to continuous spectrum perturbations, by adding the contributions of each wavenumber to represent PV anomalies and perturbations localized in the horizontal space.

Chapitre 3

Linear and nonlinear non-geostrophic unstable Eady modes

Résumé

Dans cette partie, nous étudions la dynamique des modes instables de Eady non-géostrophiques aux échelles sous-synoptiques. A ces échelles, les modes instables de Eady sont issus du couplage entre une onde de Eady de bord et une onde d'inertie-gravité au voisinage d'un niveau critique inertiel. Leurs taux de croissance sont plus faibles que ceux des modes géostrophiques d'un ordre de grandeur. On commence par étudier la croissance linéaire par le biais de calculs analytiques, puis à l'aide de simulations numériques, dans le cadre de l'approximation anélastique d'une atmosphère bi-dimensionnelle non hydrostatique(2D). Puis on étudie la croissance non linéaire à l'aide du même modèle.

L'approche analytique permet de donner un cadre conceptuel pour l'interprétation des résultats numériques. En particulier, elle permet d'anticiper et comprendre l'influence de certains paramètres, comme le nombre de Richardson Ri à travers le phénomène de surréflection. Les simulations linéaires sont analysées en comparaison avec les études précédentes, qui furent réalisées dans le cadre de l'approximation de Boussinesq non visqueuse. Elles permettent ainsi d'une part de valider le modèle concernant sa capacité à résoudre la dynamique au voisinage des niveaux critiques, aux échelles sous-synoptiques, par la reproduction de taux de croissance très faibles. D'autre part elles permettent d'évaluer les corrections induites par la prise en compte de la compressibilité et de la non hydrostaticité de l'atmosphère. Enfin, les simulations non linéaires sont réalisées dans le but d'identifier les mécanismes de saturation qui interviennent à ces échelles, et de mesurer le niveau de saturation du mode.

On montre ainsi dans le cadre linéaire, que les modes anélastiques sont plus (resp. moins) instables que les modes de Boussinesq si $\mathrm{Ri} > 1$ (resp. $\mathrm{Ri} < 1$).
Dans le cadre non linéaire, on montre que les modes saturent à un niveau plus faible que les modes géostrophiques d'environ un ordre de grandeur. Ce couplage est donc potentiellement observable même s'il est faiblement instable. Le mécanisme de saturation est double, et essentiellement dû à la dynamique au voisinage du niveau critique. L'écoulement très cisaillé et statiquement instable induit un transfert d'énergie vers les petites échelles via les instabilités de cisaillement et convectives. De plus, une boucle de rétro-action positive se met en place entre le mode instable et l'écoulement moyen, qui mène à l'amplification d'une oscillation inertielle qui déstabilise la couche critique. Cette déstabilisation se traduit par la génération d'ondes de gravité courtes et intenses.

3.1 Préliminaires

Comme nous l'avons vu en introduction, la dynamique des effets montagneux ne saurait se réduire aux effets équilibrés d'échelle planétaire ou synoptique. Il est donc nécessaire de réduire notre échelle horizontale d'étude. Dans la suite, nous nous placerons donc dans le domaine des échelles dites *sous-synoptiques*, c'est-à-dire intermédiaires entre les échelles synoptiques et les méso-échelles, correspondant typiquement à la centaine de km. Nous garderons le cadre idéalisé du problème de Eady pour étudier l'effet des montagnes sur l'atmosphère, de façon à rendre compte des instabilités baroclines. Avant d'envisager de forcer l'atmosphère à des échelles sous-synoptiques, il est utile de connaître les modes propres, instables ou non, du problème de Eady à ces échelles. C'est en effet sur ces structures que va se projetter la réponse à notre forçage. Nous aurons donc le soucis de bien comprendre leur dynamique linéaire, mais aussi nonlinéaire. En particulier, il s'agit de quantifier le niveau de saturation nonlinéaire de ces structures, et ainsi le niveau d'impact physique que l'on peut réellement en attendre. Avant d'aborder cette étude proprement dite, faisons quelques rappels sur les singularités dans le problème de Eady, et sur leur traitement mathématique.

Instabilités dans les écoulements cisaillés

Ce domaine d'échelles intermédiaires est précisémment là où se fait la transition entre deux domaines extrêmes : d'une part la dynamique de grande échelle des mouvements vorticaux, généralement rassemblés sous le concept unificateur des ondes de Rossby, et d'autre part la dynamique de petite échelle des ondes de gravité pour lesquelles l'écoulement est divergent sur l'horizontale. Il se trouve que la complexité mathématique du problème augmente assez brutalement lorsque l'on se propose de travailler dans cette zone intermédiaire, où l'on doit notamment tenir compte de la rotation terrestre pour les ondes d'inertie-gravité. D'un point de vue physique, on pouvait s'y attendre puisque l'on fait maintenant coexister deux mécanismes ondulatoires fondamentalement différents.

Ainsi, de par leur abord plus simple, les deux domaines extrêmes ont fait l'objet d'études largement plus nombreuses, et donné lieu à des développement conceptuels approfondis et fructueux de façon plus ou moins parallèle. Par exemple, la vision en termes d'anomalies de vorticité potentielle et d'interaction à distance de modes de Rossby contra-rotatifs (Bretherton, 1966) a fait considérablement progresser notre compréhension des instabilités barocline et barotrope géostrophiques. Ce faisant, les efforts consacrés à la question générale des instabilités des écoulements cisaillés ont néanmoins permis de bâtir des ponts conceptuels importants entre les deux domaines. Ainsi, l'instabilité de Kelvin-Helmholtz peut être vue comme un cas particulier d'instabilité barotrope, en terme d'interaction à distance d'anomalies de vorticité (Drazin et Reid, 1981). Dans cet esprit, un autre concept fort est celui de *sur-réflection*, qui permet d'appréhender les instabilités d'écoulements cisaillés à toutes les échelles (voir par exemple Lindzen 1988, pour une revue). Cependant, cette approche n'est pas toujours la plus adaptée, et c'est ce qui justifie les efforts actuels pour élargir le champ d'application de la vision en terme d'interaction à distance (Harnik et Heifetz 2007, Harnik et al 2008, Umurhan et al 2008).

Différentes facettes du problème de Eady et ses singularités

Revenons donc au problème de Eady 2D ou assimilé. Nous considérons un vent de base cisaillé linéairement $\mathbf{U}(z) = U(z)\,\mathbf{e}_x = (U_0 + \Lambda z)\,\mathbf{e}_x$, et nous cherchons les modes propres des perturbations sous la forme $w(x,z,t) = \Re\{\hat{w}\}$ ($\Re$ pour la partie réelle), avec $\hat{w} = W(z)\,.\,e^{\frac{z}{2H_\rho}}\,.\,e^{i(kx-\omega t)}$, où $H_\rho = (-\frac{d}{dz}\ln\rho_0)^{-1}$ est la hauteur caractéristique de l'atmosphère. De façon générale, on peut toujours écrire une équation dite de *structure verticale* pour la vitesse verticale w (Inverarity et Shutts, 2000).

Aux petites échelles, cette équation décrit la dynamique des ondes de gravité, et prend la forme :

$$\frac{\mathrm{d}^2\,\hat{w}}{\mathrm{d}z^2} - \frac{1}{H_\rho}\frac{\mathrm{d}\,\hat{w}}{\mathrm{d}z} + \left[\frac{N^2k^2}{\Omega^2} - k^2\right]\,\hat{w} = 0\,,$$

où $\Omega = \omega - kU(z)$ est la pulsation intrinsèque. Le terme du milieu n'apparaît pas dans l'approximation de Boussinesq. De même le terme $-k^2\hat{w}$ disparaît dans l'approximation hydrostatique. La particularité essentielle de cette équation est donc l'existence d'un niveau critique là où Ω s'annule.

Au contraire, aux très grandes échelles cette équation peut par exemple prendre la forme proposée par Eady (1949) dans le cadre de l'approximation de Boussinesq :

$$\frac{\mathrm{d}^2\,\hat{w}}{\mathrm{d}z^2} - 2\Lambda k\,\frac{f^2}{\Omega(\Omega^2 - f^2)}\,\frac{\mathrm{d}\,\hat{w}}{\mathrm{d}z} + \frac{N^2k^2}{\Omega^2 - f^2}\,\hat{w} = 0\,.$$

Cette fois l'équation admet deux singularités supplémentaires, les niveaux critiques inertiels, où $\Omega = \pm f$. Mais si les échelles sont très grandes et/ou le cisaillement Λ faible, ces niveaux critiques sont très éloignés les uns des autres. Ainsi, dans la configuration classique du problème de Eady avec toit, on peut aux grandes échelles négliger la présence des niveaux critiques inertiels, en supposant que $\Omega \ll f$. Ceci revient à s'intéresser à des mouvements à faible nombre de Rossby. L'équation précédente prend alors la forme simplifiée suivante ans le cadre de l'approximation Boussinesq :

$$\frac{\mathrm{d}^2\,\hat{w}}{\mathrm{d}z^2} + 2\,\frac{\Lambda k}{\Omega}\,\frac{\mathrm{d}\,\hat{w}}{\mathrm{d}z} - \frac{N^2k^2}{f^2}\,\hat{w} = 0\,,$$

qui n'est autre que l'*équation Omega* (Holton, 1992). Le remplacement du terme en w_z par la vitesse méridienne v dans cette équation, en utilisant par exemple les équilibres géostrophique et hydrostatique, fait alors disparaître la singularité en $\Omega = 0$. Dans cette formulation, le niveau critique devient en fait un niveau non singulier appelé *niveau directionnel* (en anglais "steering level"). Son rôle est alors mis en évidence dans le cadre de la vision de Bretherton (1966) de l'instabilité barocline. Cependant son caractère critique réapparaît en présence d'un gradient méridien de vorticité planétaire ("effet β") ou plus généralement d'un gradient méridien de vorticité potentielle de l'état de base, comme le montre la théorie de la sur-réflection de l'instabilité barocline. Il réapparaît aussi à cause de la compressibilité du fluide dans le cadre anélastique. Pour le voir, on s'intéresse plutôt à l'équation géostrophique du géopotentiel ϕ (Charney, 1947) :

$$\frac{\mathrm{d}^2\,\hat{\phi}}{\mathrm{d}z^2} - \left[\frac{\beta + \Lambda k/H_\rho}{\Omega} + \frac{N^2k^2}{f^2} + \frac{1}{4H_\rho^2}\right]\,\hat{\phi} = 0.$$

Traitement mathématique des singularités

Dans le cas qui nous intéresse, nous seront donc obligés de prendre en compte a priori les trois niveaux critiques. Illustrons la méthode générale sur une équation différentielle du type de celle que nous aurons à traiter, c'est-à-dire d'ordre 2 et de la forme :

$$W''(z) + p(z).W'(z) + q(z).W(z) = 0$$

où la variable z peut être complexe. Cette équation admet un point z_0 dit *singulier* si la fonction p ou q est singulière en z_0, c'est-à-dire non analytique en z_0. La plupart du temps, cela induit un comportement singulier des solutions en z_0, mais pas toujours. D'autre part, parmi les singularités possibles d'une solution, il y en a de plus "fortes" que d'autres. Pour cela on distingue les points singuliers *réguliers* des *irréguliers*. En l'occurence, le point singulier est régulier si $(z - z_0).p(z)$ et $(z - z_0)^2.q(z)$ sont analytiques en z_0. Par contre, il est irrégulier si ce n'est pas le cas. S'ouvre alors toute la zoologie des solutions à singularité irrégulière ou *essentielle*, pour laquelle il n'existe pas de théorie générale.

Dans le cas d'un point singulier régulier, il existe heureusement une théorie. On sait qu'il existe toujours au moins une solution de la forme

$$W(z) = (z - z_0)^\alpha \, A(z),$$

où $A(z)$ est analytique en z_0 et développable en série de Taylor sur un domaine allant au moins jusqu'au prochain point singulier (Bender et Orszag, 1978). Le nombre α peut être complexe, et il est appelé *exposant indiciel*. On peut donc chercher W sous la forme d'un développement en série de Frobenius valable jusqu'au prochain point singulier,

$$W(z) = (z - z_0)^\alpha \sum_{n=0}^{+\infty} a_n \, (z - z_0)^n$$

ce qui mène à une équation du second ordre vérifiée par α :

$$\alpha^2 + (p(0) - 1)\, \alpha + q(0) = 0\,.$$

La plupart du temps, cela mène alors à deux solutions linéairement indépendantes, avec des exposants différents α_1 et α_2. On voit donc que si par chance α_1 et α_2 sont des entiers naturels, alors en fait la solution générale n'est pas singulière. On parle alors de singularité *apparente*. Si l'un des exposants est entier négatif, on a donc une singularité classique de type *pole*. Enfin, dans le cas général les exposants sont complexes, et on parle alors de *point de branchement*. Dans ce cas il est alors nécessaire de couper le plan complexe, car la fonction puissance d'un complexe $(z-z_0)^\alpha$ peut être multivaluée, tout comme la fonction logarithme. Ce point est essentiel pour l'étude des niveaux critiques, comme nous le verrons, car l'effet du niveau critique sur W dépend du côté par lequel la singularité est contournée dans le plan complexe. C'est un raisonnement de ce type qui a permis à Booker et Bretherton (1967) de quantifier pour la première fois l'effet d'absorption d'une onde de gravité par un niveau critique.

Parfois cependant, on obtient pas deux solutions indépendantes sous forme de développement de Frobenius, mais une seule, l'autre faisant apparaître en plus une fonction logarithme. Cela dit la singularité logarithmique est en quelque sorte une version dégénérée du point de branchement, et reste une singularité régulière. Dans

le cadre de la théorie des niveaux critiques, les singularités sont des points de branchement classiques en 3D, mais deviennent logarithmiques en 2D (voir par exemple Yamanaka et Tanaka, 1984). C'est dans ce cadre que nous nous placerons, et nous verrons notamment l'influence de la compressibilité de l'atmosphère dans sa formulation anélastique.

3.2 Introduction

It is now recognized that gravity waves (GWs) and inertia gravity waves (IGWs) are relatively ubiquitous in the atmosphere, and that they influence the large scale circulation, notably in the middle atmosphere (Fritts and Alexander, 2003). Nevertheless, our ability to parameterize them correctly in the general circulation models is currently limited by our lack of knowledge about their sources (Kim et al 2003, McLandress and Scinocca 2005). Notably, the processes that link balanced flow to IGWs are still poorly understood (see for example Plougonven and Snyder 2007, and ref therein). One of these mechanisms is the unstable coupling between a partially balanced surface Eady wave and an IGW of the same wavelength, through a critical level (Plougonven et al, 2005).

A stationary wave perturbation of wavenumber $\mathbf{k}$ and frequency ω superimposed on a background windshear $\mathbf{U}(z)$ will meet critical levels where its intrinsic frequency $\Omega = \omega - \mathbf{kU}(z)$ is equal to 0 (Booker and Bretherton 1967, called thereafter *Classical critical Level*, or CL), or equal to the inertial frequency $\Omega = \pm f$ (Jones 1967, called thereafter *Inertial critical Levels*, or IL). In a uniform two-dimensional (2D) background windshear, one CL z_{CL} is surrounded by two ILs $z_{IL}^{\pm}$, as schematized in Fig. 3.1 for the general 2D Eady problem. In two dimensions, the IGWs cannot propagate inside of the layer between z_{IL}^{+} and z_{IL}^{-}, because the intrinsic frequency is smaller than f, whereas they can propagate outside. In 3D, the there exist also a pair of turning levels between the two ILs (Yamanaka and Tanaka, 1984). Thus, the layer between these two turning levels will thereafter be called the *evanescence layer*.
If we consider different horizontal scales $1/|\mathbf{k}|$ for the perturbation, decreasing from the synoptic scales to the mesoscales, the corresponding ILs become closer to each other as $1/|\mathbf{k}|$ decreases. Meanwhile, the associated dynamics also changes, from the classical Quasi-Geostrophic (QG) dynamics of the Eady problem to the short GWs dynamics. In the former, there is a unique CL in the flow domain between the two boundaries. In the latter, the critical levels become so close to each other in comparison with the height of the upper boundary that they collapse into a unique CL. For intermediary subsynoptic scales, the dynamics is that of IGWs, for which we cannot neglect the the role of the ILs.

Unstable modes have been proved to exist these three domains of scales, when there are one, two or three critical levels in the flow domain (Charney 1947, Eady 1949, Stone 1970, Tokioka 1970, Tai 1983, Rosenthal and Lindzen 1983, Nakamura 1988)[1] Actually, the existence of such unstable modes in a baroclinic shear can generally be related to conditions leading to over-reflection, as shown by Lindzen et al. (1980) for the geostrophic baroclinic instability, Rosenthal and Lindzen (1983) for GWs, and Tai (1983) for IGWs. Historically, the over-reflection process was used to interpret other kinds of shear instabilities in the presence of boundaries, like the Kelvin-Helmoltz one (Lindzen and Rosenthal 1976) and the barotropic one (Lindzen and Tung, 1978). In this over-reflection process, the existence of a critical layer inside of which the waves are evanescent, and which is separating two propagation areas, was shown to be necessary for the instability to appear, in addition to rigid boundaries or turning levels at both ends of the domain (Lindzen et al. 1980, Miller and Lindzen 1988). In these instabilities,

[1]Note that a critical level is not systematically really singular, depending on the model approximations used. For example, the Charney (1947) model in the f plane is singular in the anelastic framework but not within the Boussinesq approximation.

the mechanism by which the unstable mode draws some energy from the background shear flow is often presented as reminiscent of the Orr (1907) mechanism, involving the wave fields vertical tilt as regards to the shear.

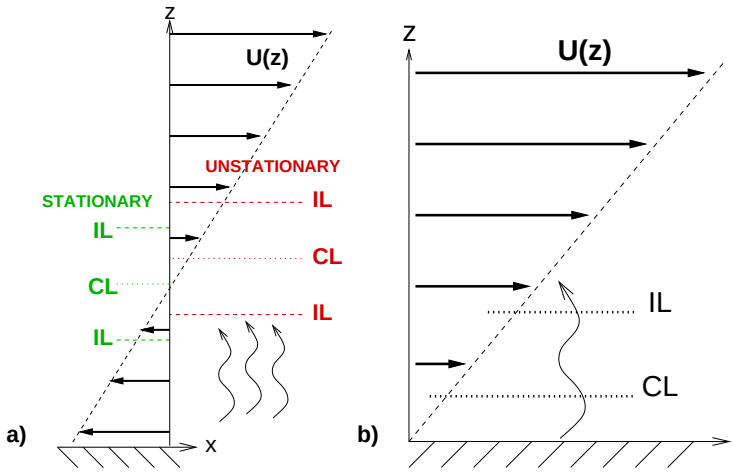

FIG. 3.1 – Wave perturbation on a uniform background windshear Λ, in the classical Eady problem for subsynoptic scales : a) general case, b) with no surface wind, as in PMS (CL : Classical critical Level, IL : Inertial critical Level). For 2D unstationary modes, the CL is not localized where the wind vanishes.

In the present study, we concentrate on the unstable modes that have only two critical levels in the flow domain, the lower IL being under the surface (Fig. 3.1b). These modes appear for subsynoptic scales (Stone 1970, his Fig. (2) and following), and have a structure different from the geostrophic unstable modes. Thus, hereafter they will be called *unstable Non-Geostrophic (NG) Eady modes*. In particular, the evanescence layer between the surface and the IL bears the propagation of a subsynoptic scale baroclinic Eady edge wave, which can be highly non-geostrophic, whereas above the IL an IGW can propagate at the same phase velocity. This structure was first described by Tokioka (1970), and later by Nakamura (1988) who introduced the idea of a baroclinic interaction between an Eady edge wave and an inertial critical layer to interpret the dynamics of these unstable modes. Yamazaki and Peltier (2001a and b) extended this study for meridional wavenumbers. This supports the earlier of Tai (1983), who have shown within the hydrostatic Boussinesq approximation, that in this configuration over-reflection will always occur, giving rise possibly to the growth of an unstable mode growth. Later, Wurtele et al (1996, 1999, 2000) examined the forcing of such modes by analytical and nonlinear simulations, and showed that a stationary response cannot be expected for some oscillatory modes. In the same time, Shutts (2001) identified such structures, coupling surface baroclinic Eady waves and upper IGWs trains, in the polychromatic response to the forcing by an isolated mesoscale mountain. Shutts (2003) extended this study for 3D linear wind shears.

More recently, Plougonven et al. (2005) (hereafter PMS) have shed new lights on the structure of these modes by analytical and numerical calculations in the linear hydrostatic Boussinesq framework. Particularly, they have quantified analytically and numerically the amplitude of the coupling, computed by different means their growth rate and phase velocity, and the dependance on Rossby number and height of the upper rigid lid z_{top}. They also confirmed that unstable modes also exist with no upper rigid lid ($z_{top} \to \infty$) but a radiation upper boundary condition. An example of such a

mode, calculated by the method of PMS, is shown in Fig. 3.2a and will be discussed in subsection 3.4.1. The growth rates found are significantly smaller than those obtained for the longer geostrophic baroclinic unstable modes, as found earlier by Stone in the case of Richardson numbers typically higher than 1. Note nevertheless that for small Richardson numbers, both kinds of unstable modes have comparable growth rates, especially for strong meridional wavenumbers (Stone, 1970).

The present study is motivated by the need to understand and quantify the processes of secondary generation of IGWs linked to the orography forcing, as a consequence of short mountain GWs breaking. The next chapter is devoted explicitly to this aim. In this respect, the main objectives of the present chapter are (i) to check that we are able to simulate correctly the linear and nonlinear interaction between balanced motion and IGWs near critical levels, in the NG Eady problem, and (ii) to characterize the linear and nonlinear dynamics of these unstable modes in our viscid anelastic and non hydrostatic framework. In particular, to measure the very low growth rates we needed high vertical resolution and low diffusivity parameters (viscosity and conductivity). Consequently, the numerical cost restrains the study, for the moment, to the 2D modes ($\mathbf{k} = k.\mathbf{e}_x$). Also, this study will allow to evaluate the effects of compressibility (anelastic) and non hydrostasy on the unstable modes. Indeed, as shown first by Teitelbaum et al (1987), the nature of the approximations used must change the nature of the singularities of the problem, which can modify at least quantitatively the over-reflection process. Finally, we need to understand the nonlinear saturation of these modes, and to assess their saturation amplitude, in order to decide wheither this mechanism that couples balanced motion to IGWs is significant or not.

To our knowledge, the nonlinear saturation of these unstable NG modes was never adressed. Their hybrid structure make think that the nonlinear saturation process will be a combination of those that were described respectively for large scale 2D Eady waves (Nakamura and Held, 1989), and for IGWs (Lelong and Dunkerton, 1998a and b). For the large scale 2D Eady waves in the absence of IL, Nakamura and Held (1989) have shown that the saturation results from a *n*onlinear equilibration : the background stratification is modified by the advection of the Potential Vorticity (PV) produced near the surface fronts. For IGWs, the breaking process was characterized by Dunkerton (1997) and Lelong and Dunkerton (1998a,b). They have extended respectively by linear stability analyses and numerical simulations the earlier studies of breaking GWs (Winters and D'Asaro 1989, Winters and Riley 1992, Winters and D'Asaro 1994, Fritts et al. 1994, Fritts et al. 1996a). They confirmed notably the importance of three dimensionnal (3D) effects in the acceleration and complexity of the breakdown, but also the predominance of Shear Instability (SI) over Convective Instability (CI) during the early stages of the breakdown. Indeed, Winters and D'Asaro (1994) shown that a 2D simulation can over-estimate the lifetime of the elongated unstable shear layers which appear in a breaking background GW. Nevertheless, we show in this study that a 2D nonlinear simulation of the NG modes saturation might be relevant to measure at least an upper bound of the level of saturation, and to characterize the mechanism during the early stages of the breakdown. Finally, the fact that these NG modes present elongated sheared and overturned tongues in the flow is also challenging because of the amount of potential energy stored in it. During the breakdown, this can result in the generation of smaller scale IGWs through linear mechanisms (Sutherland et al. 1994), as well as nonlinear mechanisms, like the *enveloppe radiation* (Scinocca and Ford, 2000) or the *mixed-layer collapse* (Bhüler et al., 1999).

The outline of the chapter is as follows. The section 3.3 presents the linear theory of the unstable NG Eady modes in relation with the over-reflection of IGWs, in the framework of the nonhydrostatic anelastic 2D equations. The section 3.4 is dedicated to the results of the linear numerical simulations, which are compared to the results obtained by PMS in the hydrostatic Boussinesq framework. In section 3.5, we describe the nonlinear saturation mechanism for the most unstable mode. The model equations, definitions and notations, and numerical details are presented in the appendix, or in the body of the text when needed.

3.3 Linear theory and over-reflection for inertia-gravity waves

3.3.1 The vertical structure equation

Following Inverarity and Shutts (2000, Eq.(24)), the linear vertical structure equation of the first order 2D perturbation to a uniformly sheared background flow $U(z).\mathbf{e}_x = (U_0 + \Lambda z).\mathbf{e}_x$ can be derived from the inviscid nonhydrostatic anelastic equations, for an inviscid and adiabatic fluid with constant background stratification N^2 and on the f-plane. Searching an eigenmode vertical velocity of the form $w(x,z,t) = \Re\{\hat{w}\}$ ($\Re$ for real part), and taking

$$\hat{w} = W(z)\,.\,e^{\frac{z}{2H_\rho}}\,.\,e^{i(kx-\omega t)}, \tag{3.1}$$

where $H_\rho = (-\frac{d}{dz}\ln\rho_0)^{-1}$ is the characteristic height of the atmosphere, we obtain

$$\xi(\xi^2-1)\frac{\mathrm{d}^2W}{\mathrm{d}\xi^2}+2\frac{\mathrm{d}W}{\mathrm{d}\xi}+\left[\mathrm{Ri}\,\xi-\alpha\sqrt{\frac{\mathrm{Ri}}{\mathrm{Bu}}}\,(\xi^2+1)-\frac{\alpha^2}{4}\frac{\mathrm{Ri}}{\mathrm{Bu}}\,\xi(\xi^2-1)-\delta^2\frac{\mathrm{Ri}}{\mathrm{Bu}}\,\xi^3\right]\,W=0, \tag{3.2}$$

which is written in terms of the reduced variable $\xi = -\frac{\Omega}{f}$, where $\Omega = \omega - kU(z)$ is the intrinsic frequency. In Eq. (3.2), we have introduced the Richardson and Burger numbers Ri and Bu, defined and related to the Rossby number Ro by

$$\mathrm{Ri} = \frac{N^2}{\Lambda^2}\,,\ \mathrm{Bu} = \left(\frac{NH}{fL}\right)^2 \quad \text{, and} \quad \mathrm{Ro} = \frac{\Lambda H}{fL} = \sqrt{\frac{\mathrm{Bu}}{\mathrm{Ri}}}, \tag{3.3}$$

where $L = \frac{1}{k}$ and H are respectively the horizontal and vertical scales of the motion. We have also introduced

$$\alpha = \frac{H}{H_\rho} \quad \text{, and} \quad \delta = \frac{H}{L} = \frac{f}{N}\sqrt{\mathrm{Bu}}, \tag{3.4}$$

which characterize respectively the importance of the compressibility in the anelastic equations, and of the nonhydrostaticity. The hydrostatic Boussinesq version can be retrieved taking $\alpha = \delta = 0$.

The Eq. (3.2) has four singular points in $\xi = 0, \pm 1$ and ∞ (Bender and Orzag 1978, Olver 1974). In the hydrostatic Boussinesq case, these singularities are all regular, and the point $\xi = 0$ is an apparent singularity. By contrast, we see that the anelastic terms introduce two important modifications. First, the singularity in ∞ become irregular because of the terms of order higher than 2 in ξ. Incidentally, we note that the non-hydrostatic term has the same impact. Second, the singularity in 0 is still regular, but the calculations show that it is no more apparent, except if $\mathrm{Ri} = 1$.

The eigenmode's frequency is the eigenvalue of Eq. (3.2) constrained by given boundary conditions, and must be considered complex in the general case : $\omega = \omega_r + i\omega_i$. The growth rate is ω_i, and the mode is unstable if $\omega_i > 0$. Because of that, the singularities of Eq. (3.2) are slightly moved into the complex plane out of the real axis of the altitudes z. Nevertheless, as we generally obtain very small growth rates, $|\omega_i| \ll f$ and we can still define the critical levels by reasonning on the real part of Ω :

$$z_{CL} = \frac{1}{\Lambda}\left(\frac{\omega_r}{k} - U_0\right) \quad \text{and} \quad z^{\pm}_{IL} = \frac{1}{\Lambda}\left(\frac{\omega_r \mp f}{k} - U_0\right), \tag{3.5}$$

even if they are not strictly singular.

3.3.2 The conservation of the angular momentum vertical flux

Following Jones (1967), we first consider a parcel of fluid that is oscillating with the wave perturbation velocity $\mathbf{u} = (u, v, w)$, around a reference position $\mathbf{x}_0 = (X_0, Y_0, Z_0)$ which is moving with the background flow at the velocity $\mathbf{U} = U.\mathbf{e}_x$. We define the eulerian field of the parcel displacement $\boldsymbol{\nu}(\mathbf{x}_0, t) = (\nu_1, \nu_2, \nu_3)$ from the rest position $\mathbf{x}_0$, which satisfies

$$\mathbf{u}(\mathbf{x}_0, t) = (\partial_t + U\partial_x)\,\boldsymbol{\nu}(\mathbf{x}_0, t) \tag{3.6}$$

The vertical component of the angular momentum of this parcel (per unit volume), in the f-plane terrestrial referential, is

$$\begin{aligned}\rho_0.(X_0+\nu_1).(v+f/2(X_0+\nu_1)) - \rho_0.(Y_0+\nu_2).(U+u-f/2(Y_0+\nu_2)) = \\ \rho_0.f/2(X_0^2+Y_0^2) - Y_0U + \rho_0.X_0(v+f\nu_1) - \rho_0.Y_0(u-f\nu_2) + \rho_0.(v\nu_1 - u\nu_2)\end{aligned} \tag{3.7}$$

After neglecting the last wave quadratic terms by considering that the position $\mathbf{x}_0$ can be chosen arbitrarily far from the origin, the mean vertical flux of angular momentum carried by the wave is obtained :

$$\rho_0.X_0\,\overline{(v+f\nu_1)w} - \rho_0.Y_0\,\overline{(u-f\nu_2)w} = \frac{\rho_0}{2}.X_0\,\Re\{\hat{w}^*(\hat{v}+f\hat{\nu_1})\} - \frac{\rho_0}{2}.Y_0\,\Re\{\hat{w}^*(\hat{u}-f\hat{\nu_2})\}\,. \tag{3.8}$$

In Eq. (3.8) we have moved in the complex plane by assuming a wave mode $\mathbf{u} = \Re\{(\hat{u}, \hat{v}, \hat{w})\}$ of the form of Eq. (3.1). Reminding the 2D inviscid linear polarization relations for the wave perturbation of Eq. (3.1), which were used to obtain Eq. (3.2),

$$\begin{aligned}
-i\Omega\,\hat{u} + \Lambda\,\hat{w} - f\,\hat{v} + ik\,\hat{\phi} &= 0 && (3.9)\\
-i\Omega\,\hat{v} + f\,\hat{u} &= 0 && (3.10)\\
-i\Omega\,\hat{w} + \partial_z\hat{\phi} - \frac{g}{\theta_0}\,\hat{\theta} &= 0 && (3.11)\\
ik\,\hat{u} + (\partial_z - \frac{1}{H_\rho})\,\hat{w} &= 0 && (3.12)\\
-i\Omega\,\hat{\theta} + \Theta_y\,\hat{v} + \theta_{0z}\,\hat{w} &= 0\,, && (3.13)
\end{aligned}$$

we then formulate the angular momentum flux only in terms of $\hat{w}$, by using the Eqs. (3.10), (3.12), and (3.6) :

$$\begin{aligned}
\Re\{\hat{w}^*(\hat{u}-f\hat{\nu_2})\} &= \frac{1}{k}\,\Re\left\{i\left(\frac{f^2}{\Omega^2}-1\right)\left(-\frac{1}{H_\rho}|\hat{w}|^2 + \hat{w}^*\frac{\mathrm{d}\hat{w}}{\mathrm{d}z}\right)\right\} && (3.14)\\
\Re\{\hat{w}^*(\hat{v}+f\hat{\nu_1})\} &= 0 \quad (\text{ in 2D only})\,.
\end{aligned}$$

Asymptotic equations :

In the following, we adapt the method of Tai (1983) to the present nonhydrostatic anelastic 2D equations. Note that some of the following equations are written with the sign $\approx$ instead of $=$. This means that they are written under the assumption that the imaginary part of ξ, $\Im\{\xi\} = -\frac{\omega_i}{f}$, is small enough to be neglected in front of the real part $\Re\{\xi\}$ and $\Re\{\xi\} - 1$, except when ξ is very close to the singular points 0 and 1 respectively. This is strictly valid for a neutral mode in inviscid conditions, in which case $\omega_i = 0$. But it is only approximate for an unstable mode, even if inviscid. Consequently, these equations with $\approx$ must be read as *asymptotic* relations in the case of

vanishing growth rate and viscosity. The smaller the growth rate is, the more accurate is this approximation. This fact must be stressed, since this asymptotic approach is largely used in the litterature, but not often discussed.

Under this asymptotic approach ($\left|\frac{\omega_i}{f}\right| \ll 1$), the Eq. (3.14) can be simplified by considering that Ω (or ξ) is near real :

$$\frac{\rho_0}{2}\,\Re\{\hat{w}^*(\hat{u}-f\hat{\nu_2})\} \approx -\frac{\rho_0}{2k}\,\Im\left\{\left(\frac{1}{\xi^2}-1\right)\hat{w}^*\frac{\mathrm{d}\hat{w}}{\mathrm{d}z}\right\} \equiv -\,G(z) \tag{3.15}$$

Thus, in the following, the function $G(z)$ will represent the asymptotic vertical profile of the opposite of the vertical flux of angular momentum (by unit length).

Now, the Eq. (3.2) is rewritten by introducing the polynoms $\tilde{p}(\xi)$ and $\tilde{q}(\xi)$,

$$\tilde{p}(\xi)\,\frac{\mathrm{d}^2W}{\mathrm{d}\xi^2}+2\,\frac{\mathrm{d}W}{\mathrm{d}\xi}+\tilde{q}(\xi)\,W=0\,, \tag{3.16}$$

and by introducing $\Psi(z)=e^{\int\frac{d\xi}{\xi(\xi^2-1)}}.W(z)$ we obtain the canonical form of the vertical structure equation,

$$\frac{\mathrm{d}^2\Psi}{\mathrm{d}\xi^2}+Q(\xi)\,\Psi=0, \quad \text{where} \quad Q(\xi)=\frac{\tilde{p}\tilde{q}-1+\tilde{p}'}{p^2} \tag{3.17}$$

is a function singular in 0 and ±1. From this last equation we deduce that

$$\frac{\mathrm{d}}{\mathrm{d}\xi}\left(\Im\left\{\Psi^*\frac{\mathrm{d}\Psi}{\mathrm{d}\xi}\right\}\right)=-\Im\{Q\}|\Psi|^2\approx 0\,, \tag{3.18}$$

and by using the definition of Ψ and the one of $G(z)$ in Eq. (3.15), we also obtain

$$\frac{\mathrm{d}}{\mathrm{d}\xi}\left(\Im\left\{\Psi^*\frac{\mathrm{d}\Psi}{\mathrm{d}\xi}\right\}\right)\approx\frac{2f}{\Lambda}\,e^{2\int\frac{d\xi}{\xi(\xi^2-1)}}.\frac{\xi^2}{1-\xi^2}\,\frac{\mathrm{d}G}{\mathrm{d}\xi}. \tag{3.19}$$

Finally, the Eqs. (3.18)-(3.19) imply the following simple property between the critical levels :

$$\frac{\mathrm{d}G}{\mathrm{d}\xi}\approx 0. \tag{3.20}$$

This means that $G(z)$, or the vertical flux of vertical angular momentum, is a constant between the critical levels under the previous asymptotic assumptions, that is for an inviscid and neutral mode. Nevertheless, G can have discontinuities at the critical levels. Actually, since $\omega_i \neq 0$ for an unsteady and viscid mode, G will undergo abrupt but continuous variations near the critical levels.

Note that this asymptotic result is equivalent to the Eliassen-Palm (EP) theorem for small amplitude IGWs. Indeed, as shown in appendix C, in our context the zonal mean vertical EP flux can be defined as

$$F^z=\rho_0\left[\frac{f}{\theta_{0z}}\,\overline{v\theta}-\overline{uw}\right]. \tag{3.21}$$

Straightforward manipulations of Eqs. (3.10), (3.12) and (3.13) show that

$$\overline{uw} \;=\; -\frac{1}{2k}\Im\left\{\hat{w}^*\frac{\mathrm{d}\hat{w}}{\mathrm{d}z}\right\} \quad \text{and} \tag{3.22}$$

$$\frac{f}{\theta_{0z}}\overline{v\theta} \;=\; -\frac{1}{2k}\,\frac{1}{|\xi|^2}\,\Im\left\{(\frac{\mathrm{d}}{\mathrm{d}z}-\frac{1}{H_\rho})\hat{w}\left[-\frac{H}{\sqrt{\mathrm{Bu}\,\mathrm{Ri}}}\frac{1}{\xi}(\frac{\mathrm{d}}{\mathrm{d}z}-\frac{1}{H_\rho})\hat{w}^*+\hat{w}^*\right]\right\}. \tag{3.23}$$

The asymptotic form of the last equation leads to the well known relationship

$$\frac{f}{\theta_{0z}}\overline{v\theta} \approx \frac{f^2}{|\Omega|^2}\,\overline{uw}, \tag{3.24}$$

which yields

$$F^z \approx \frac{\rho_0}{2k}\left(1-\frac{1}{|\xi|^2}\right)\Im\left\{\hat{w}^*\frac{\mathrm{d}\hat{w}}{\mathrm{d}z}\right\} \approx -\,G(z) \tag{3.25}$$

Thus, in the asymptotic limit, that is for a neutral and inviscid perturbation, we retreive the common result that the vertical EP flux is equal to the vertical flux of angular momentum.

3.3.3 The asymptotic over-reflection criterium

Now we form the vertical energy flux $\overline{pw}$ by the combination $\frac{iw^*}{2\Omega k^2}\,[\,-\Omega k\,(3.9) - ifk\,(3.10) + (f^2-\Omega^2)\,(3.12)\,]$, which yields :

$$\overline{pw} = \frac{\rho_0}{2}\,\Re\left\{\frac{i}{\Omega k^2}\left[[\Lambda\Omega k - \frac{\Omega^2-f^2}{H_\rho}]\,.\,|\hat{w}|^2 + (\Omega^2-f^2)\,\hat{w}^*\partial_z\hat{w}\right]\right\}, \tag{3.26}$$

where $p=\rho_0\phi$ is the pressure perturbation, and $*$ denotes the complex conjugate. Simplifying this formula by considering again that Ω is real, under the same asymptotic limit as previously, we obtain :

$$\overline{pw} \approx \frac{\Re\{\Omega\}}{k}\,\frac{\rho_0}{2k}\,\Im\left\{\left(\frac{1}{\xi^2}-1\right)\hat{w}^*\frac{\mathrm{d}\hat{w}}{\mathrm{d}z}\right\} \equiv \frac{1}{k}\,\Re\{\Omega\}\,G(z). \tag{3.27}$$

Given that $G(z)$ is nearly constant between the critical levels, the asymptotic vertical energy flux will therefore essentially follow the variations of Ω between the singularities.

To know the impact of the singularities on the energy flux, we need to calculate explicitely the jumps of $G(z)$. Because of the anelastic and hydrostatic correction terms, the Eq. (3.2) cannot be transformed into the hypergeometric equation, as it is the case in the Boussinesq framework. Nevertheless, its solutions can still be developped in more general Frobenius series around the singularities (Olver, 1974). As said before, the eigenmodes we study here appear in the presence of only 2 critical levels ($\xi=0$ and $\xi=-1$), the lower IL ($\xi=1$) being under the surface. Around $\xi=0$ we find

$$W(\xi) = A_0\,\left[\gamma\,\xi^3\,w_0^B(\xi)\,\log(\xi) + w_0^A(\xi)\right] + B_0\,\xi^3\,w_0^B(\xi) \tag{3.28}$$

where

$$\gamma = \frac{\alpha}{3}\sqrt{\frac{\mathrm{Ri}}{\mathrm{Bu}}}\,(\mathrm{Ri}-1)\,, \tag{3.29}$$

and around $\xi=1$,

$$W(\xi) = A_1\,\left[w_1^B(\xi)\,\log(\xi-1) + w_1^A(\xi)\right] + B_1\,w_1^B(\xi)\,. \tag{3.30}$$

In Eqs. (3.28) and (3.30), A_0, B_0, A_1 and B_1 are constants. The functions w_0^A and w_0^B are analytical in 0, satisfying $w_0^A(0)=w_0^B(0)=1$, and are expandable in Taylor series around 0 on a domain of radius larger than 1. The functions w_1^A and w_1^B are analytical in 1, satisfying $w_1^A(1)=0$ and $w_1^B(1)=1$, and are expandable in Taylor series around 1 on a domain of radius larger than 1. Now we use the Eqs. (3.28)-(3.30) to calculate

the jumps of G across the two critical levels, taking into account that $\omega_i > 0$ for an unstable mode when choosing the branch cuts in the complex plane. We find that across z_{IL},

$$G_1^+ - G_1^- = \rho_0(0)\,\frac{|\Lambda|}{2f}\,2\pi\,|A_1|^2\,, \tag{3.31}$$

which is always positive. And across z_{CL},

$$G_0^+ - G_0^- = \gamma\,\rho_0(0)\,\frac{|\Lambda|}{2f}\,3\pi\,|A_0|^2\,, \tag{3.32}$$

which is of the sign of $\mathrm{Ri}-1$, according to Eq. (3.29). Note that the Eqs. (3.31)-(3.32) are valid for a positive or negative shear Λ, under the convention that the labels $^+$ and $^-$ refer to the z-axis oriented upward.

Now we consider an IGW excited from the region under the CL by an Eady edge wave, which corresponds to the numerical experiments described in the next sections. If there is no upper rigid boundary but a radiation condition, the vertical flux of energy must be upward far above the IL because the source is under the CL. Hence from Eq. (3.27), $G_1^+ \approx G_\infty < 0$ because $\Omega < 0$ in this region. If there is a rigid upper boundary, nevertheless G_1^+ will not be strictly positive. Let us first consider the hydrostatic Boussinesq case, by taking $\alpha = 0$, and hence $G_0^+ = G_0^- = G_1^-$. From Eq. (3.31) we deduce that $G_0^- < 0$, hence $\overline{pw} < 0$ under the CL where $\Omega > 0$. So, we retrieve the result of Tai, that for a uniform shear Λ and a constant stratification N^2, and in the presence of only one CL and one IL above the CL, there will always be over-reflection.

Now, adding the nonhydrostatic term in Eq. (3.2) will not change qualitatively this result, except that a very high upper rigid boundary might modify slightly the values of A_0 and A_1. By contrast, the anelastic corrections introduce a jump in $\xi = 0$ (Eq. (3.32)) which can change significantly this result, depending notably on the value of γ and the sign of $\mathrm{Ri}-1$ through Eq. (3.29). This will be discussed further in the context of our numerical simulations, in subsection 3.4.2. Note that it was already noticed by Teitelbaum et al (1987) that the different approximations of the rotating fluid equations can generally influence quantitatively the over-reflection amplitude.

We shall stress again here that the previous analysis leading to the over-reflection criterium is asymptotic. This means that the jump expressions in Eqs. (3.31)-(3.32) are certainly qualitatively true, but quantitatively erronous. As we shall see in the numerical simulations, the existence of a non negligeable growth rate and viscosity will affect the shape of what was called a discontinuity. It means also that in practice, it is not possible to localize precisely the level at which the wave will be over-reflected. Actually, this is related to a more fundamental remark. Namely, for the present Eady mode, it is not strictly correct to state that the Eady edge wave is over-reflected at the IL or the CL, as it is not a vertically propagating wave, and as the area between the surface and the IL is evanescent for IGWs. Rigorous interpretation in terms of over-reflection in this Eady problem context requires to remind that in reality, viscosity will establish continuously the uniform shear Λ from 0 within a thin surface layer (Bretherton, 1966). Inside of this layer, the shear is not uniform, and the previous Eady edge waves are now Rossby waves that can propagate vertically. These Rossby waves can be over-reflected by the global evanescence layer that is above (Lindzen et al., 1980), in which are localized the singular levels. In such a background wind, the

over-reflection would be diagnosed by a negative energy flux $\overline{pw}$ inside of this sheared boundary layer. In this chapter nevertheless, we do not carry on over-reflection calculations and keep the windshear uniform in the entire domain. Thus, we will quantify the instability exclusively in terms of interaction with the mean flow near the IL, and more generally inside of the whole evanescence layer.

3.4 Linear growth of unstable NG Eady modes

3.4.1 Numerical simulation of the linear growth - Experiment L

i) Numerical experimental setup

We define a reference numerical experiment called L (Linear), from which we will start a series of sensitivity tests. From now and until the end of this study,

$$U_0 = 0, \tag{3.33}$$

since a non zero surface wind does not change the following results in the linear context. The set of the other physical parameters is :

$$f = 10^{-4}\,\mathrm{s}^{-1},\ N = 10^{-2}\,\mathrm{s}^{-1},\ L = 100\,\mathrm{km},\ H = 1\,\mathrm{km},\ \Lambda = 10^{-2}\,\mathrm{s}^{-1},\ z_{top} = 20\,\mathrm{km}, \tag{3.34}$$

which satisfies

$$\mathrm{Ri} = \mathrm{Ro} = \mathrm{Bu} = 1. \tag{3.35}$$

The described computation was made after turning off the nonlinear terms in the model, with a vertical resolution of $\Delta z = 10m$, with 64 horizontal wavenumbers, with a diffusivity constant $\mu = \kappa = 0.004\ \mathrm{m}^2.\mathrm{s}^{-1}$ (see also the details about the numerical model in appendix D). In such conditions, the viscous scale l_μ defined by Hazel (1967) for GWs encountering a CL is

$$l_\mu = \left[\frac{\mu L}{\rho_0 \Lambda}\right]^{1/3} \sim 34\mathrm{m}. \tag{3.36}$$

This gives an indication for the vertical resolution needed to compute accurately the structure of the inertial critical layer.
The growth of the NG mode is triggered by initializing the flow perturbation fields by a QG balanced Eady edge wave of the same wave number, and same characteristic height H. This method introduces an inertial oscillation whose amplitude ratio can be reduced by performing a series of subsequent very long growth simulations.

The choice of these physical parameters is motivated by several arguments. The wavelength of the first mode is $2\pi L \sim 628$km, which corresponds to subsynoptic scales, in which we are interested. The value of H is then chosen to satisfy Bu=1, in reference to the quasi-geostrophic (QG) balanced flow case. Taking account of the previous results from PMS, we chose the values of Λ and z_{top} in order to obtain a maximum growth rate, which makes the sensitivity studies easier. Finally, chosing Ro=Ri=1 allows to compare our anelastic numerical simulation with the Boussinesq one of PMS, in virtue of the result of section 2 that for Ri=1, the anelastic (and hydrostatic) corrections only alter the far upper field near the upper boundary but do not change the dynamics near the singularities. Note that in this 2-D context no symmetric instability can occur in this linear problem.

Note that as shown by PMS, the existence of a rigid upper boundary condition is not necessary to obtain unstable modes. We exemplify this in Fig. 3.2, where the vertical velocity structure obtained by the same experiment as L, but with a 40km sponge layer added, is shown (b) and compared to the corresponding PMS calculation (a). Nevertheless, in order to minimize the numerical cost and for simplicity, in the following we chose to impose a rigid upper boundary at $z = z_{top}$ rather than a thick sponge layer or a radiation condition.

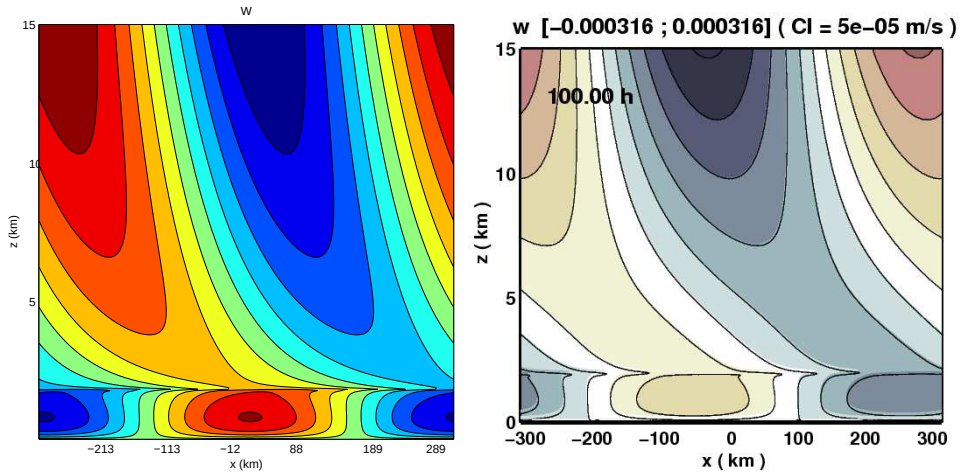

FIG. 3.2 – Vertical velocity of the unstable NG mode : a) computed by PMS, and b) obtained by the same anelastic numerical simulation as experiment L except that a 40km sponge layer was added.

ii) Analysis of experiment L

a. Normal mode's eigenvalue : growth rate and critical levels

The growth rate ω_i is measured from the perturbation energy growth presented in the Figs. 3.3a,b (equations in appendix B), and compared to the result of PMS after non-dimensionalization by the Eady model characteristic time scale $\frac{N}{f\Lambda}$. In this case, we found

$$\sigma = \omega_i \frac{N}{f\Lambda} = 0.0211 \pm 1\%, \tag{3.37}$$

which is close to the result obtained by PMS2005 ($\sigma_{\rm PMS}$=0.0198). The tendencies shown in Fig. 3.3c will be discussed in a subsequent paragraph, in relation with the Eliassen-Palm flux profile.

The four wave fields u, v, w and θ are shown in Fig. 3.4, and the geopotential perturbation ϕ in Fig. 3.5. In all these fields, the singularity at the IL appears near z=2km, at the place of the transition between an Eady edge wave and an IGW. This is particularly clear in the the vertical velocity field in Fig. 3.4c. Note that the CL, which must be located under the IL at a distance $\frac{fL}{\Lambda}$=1km (Eq. (3.5)), appears near z=1km as a very smooth maximum of vertical velocity amplitude. Hence, its behaviour is not singular, consistently with the fact that the CL singularity is apparent for Ri=1. To corroborate this general observation more precisely, we measure the phase velocity in the Hofmuller diagram of the vertical velocity at the height z=1km, shown in Fig. 3.6. We obtain

$$c_\Phi = 8.55 \text{ m.s}^{-1} \pm 0.2\%, \tag{3.38}$$

which indicates a CL localized near z_{CL}=855m in virtue of Eq. (3.5). This is above the PMS value ($z_{CL\,(\rm PMS)}$=790m) by around 8%. It is also close to the steering level of the corresponding QG Eady edge wave $\frac{fL}{N}$ = 1km, but lower. This will be discussed more generally in section 3.4.2. Now from z_{CL}, the height of the IL can be deduced more precisely than above :

$$z_{IL} = z_{CL} + \frac{fL}{\Lambda} = 1855\text{m}. \tag{3.39}$$

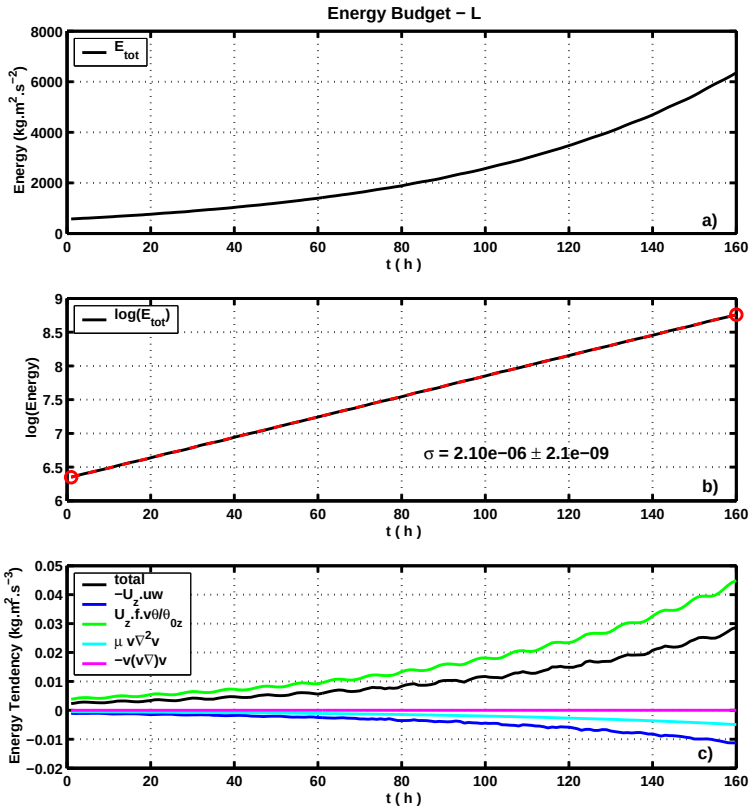

FIG. 3.3 – Energy budget versus time, in experiment L (section 3.4.1) : a) total energy, b) Logarithm of the total energy to measure the growth rate, c) tendency terms of the energy budget (see appendix B). In the legend, the diffusive tendency term $\frac{\mu}{\rho_0}(\mathbf{v}\nabla^2\mathbf{v} + \frac{g^2}{\theta_0^2 N^2}\,\theta\nabla^2\theta)$ and the advective tendency term $-\mathbf{u}(\mathbf{u}\nabla)\mathbf{u} - \frac{g^2}{\theta_0^2 N^2}\,\theta(\mathbf{u}\nabla)\theta$ are indicated schematically by $\mu\, v\nabla^2 v$ and $-v(v\nabla v)$ respectively. In b), the red dashed line between two red circles is the linear fit.

b. Wave fields

The three fields u, v, and θ (Fig. 3.4a,b,d) have their amplitude increasing when approaching the IL. More precisely, we can check that the pictures of Fig. 3.4 satisfy qualitatively the linear wave equations for one eigenmode $\mathbf{u}(x,z,t) = \Re\left\{\hat{\mathbf{u}}(z)\ \exp^{i(kx-\omega t)}\right\}$, and that the behaviour corresponds to an Eady edge wave under the IL and an IGW above.

This can be seen by writing the approximate forms of the polarization relationships Eqs. (3.9)-(3.10) at different levels (we neglect the anelastic correction in $1/H_\rho$), remembering that $\Omega(z) = \omega_r + i\omega_i - k\Lambda z$ and $\omega_i \ll f$. Near the surface, $\Omega \sim f$, and the approximate relations

$$\hat{u} \sim i\hat{v} \quad ; \quad \Lambda\hat{w} \sim 2\hat{v} - ik\hat{\phi} \quad ; \quad \hat{w}_z \sim k\hat{v} \quad ; \quad \frac{g}{\theta_0}\hat{\theta} \sim \Lambda\hat{u} \tag{3.40}$$

account correctly for the Eady edge wave phase relationships observed in Fig. 3.4 under the CL. Near the IL, $\Omega \sim -f$. This changes the phase relationships to

$$\hat{u} \sim -i\hat{v} \quad ; \quad \Lambda\hat{w} \sim -ik\hat{\phi} \quad ; \quad \hat{w}_z \sim -k\hat{v} \quad ; \quad \frac{g}{\theta_0}\hat{\theta} \sim \Lambda\hat{u} \tag{3.41}$$

which also corresponds to the structures observed in the critical zone. The fields $\hat{u}$ and $\hat{\theta}$ are still in phase, but now the phase difference between $\hat{u}$ and $\hat{v}$ is of opposite sign. In

addition, the quasi horizontal tilt of the phase lines is coherent with the fact that for linear propagating IGWs approaching an IL, the ratio between horizontal and vertical wavenumbers vanishes. Note nevertheless that the structure of the mode above the IL reveals the existence of two IGWs superimposed, propagating respectively upward and downward because of the rigid upper boundary. By comparison, in the NG mode grown with a sponge layer (Fig. 3.2b), this tilting of the phase lines is more progressive, because there is no downward propagative IGW in this case. Finally, near the CL we have $\Omega \sim i\omega_i$, and the relationships are

$$\hat{u} \sim -\frac{\omega_i}{f}\hat{v} \sim -2.10^{-2}\hat{v} \quad ; \quad \hat{w}_z \sim -ik\hat{u} \quad ; \quad \frac{gk}{\theta_r}\hat{\theta} \sim -if\hat{v}_z \tag{3.42}$$

which explains respectively that at this level : $\hat{u}$ and $\hat{v}$ are in phase opposition, the vertical divergence of $\hat{w}$ is weaker, and the phase lines of $\hat{u}$ and $\hat{\theta}$ do not tilt in the same direction.

The geopotential ϕ (Fig. 3.5) is a direct picture of the pressure p because for small pressure perturbations $\phi \approx \frac{p}{\rho_0}$, which is always the case in this study. Comparison of the total pressure to its hydrostatic contribution shows a difference smaller than 1% in amplitude (not shown). Hence, the map of ϕ can be interpreted through $\phi_z = \frac{g}{\theta_r}\theta$ from the map of θ (Fig. 3.4d), starting from the Eady edge wave pressure perturbation at the surface. The main feature to note is that ϕ has extrema at the IL, which are localized in phase with v.

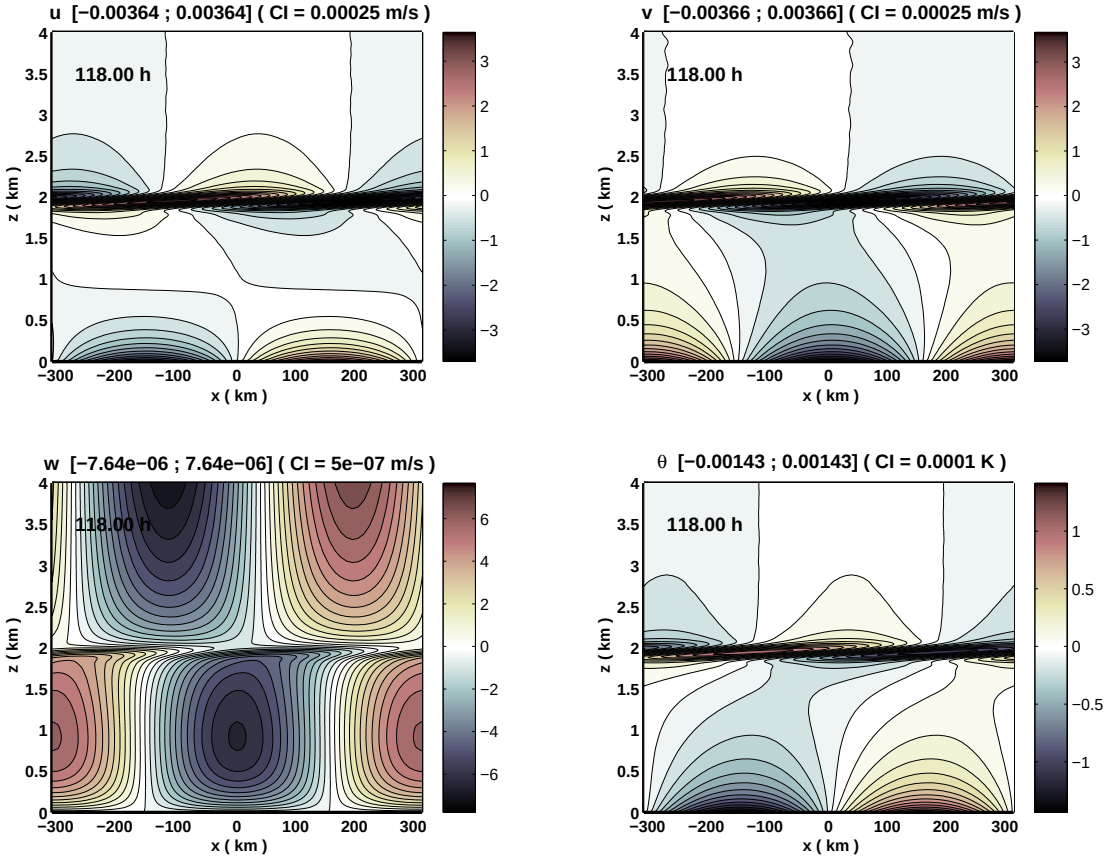

FIG. 3.4 – Velocity and potential temperature fields of the NG mode of experiment L, at t=118h. a) zonal velocity u, b) meridonal velocity v, c) vertical velocity w, and d) potential temperature θ.

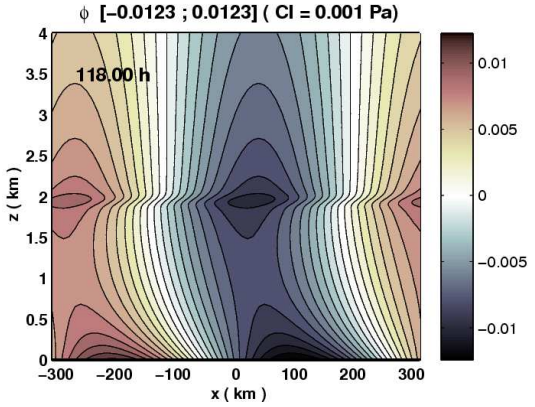

FIG. 3.5 – Geopotential perturbation ϕ of the NG mode in experiment L, at t=118h.

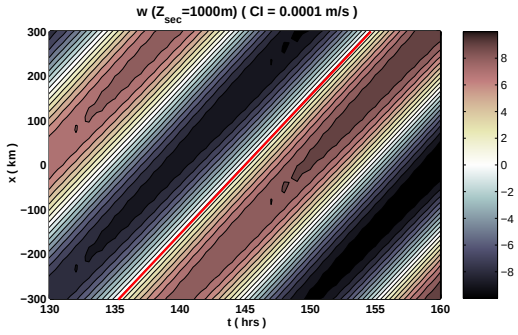

FIG. 3.6 – Hofmuller diagram of the vertical velocity at 1000m above the surface, to measure the phase velocity, for the NG mode of experiment L in section 3.4.1.

c. Energy budget and vertical Eliassen-Palm flux

The energy budget equations used here can be found in appendix B. The phase tilt under the IL is upshear for v and downshear for θ (Figs. 3.4b,d), which is reminiscent of the classical baroclinic instability. More generally, this phase tilt allows the unstable mode to extract potential energy from the baroclinic background flow, by making the global mean meridional heat flux positive, as shown in the energy tendencies in Fig. 3.3c (term in $v\theta$, green curve). Conversely, the global mean of the vertical flux of horizontal momentum is negative, which means that the unstable mode is providing some horizontal kinetic energy to the background flow (term in $-uw$, blue curve). This contribution is nevertheless dominated by the previous one, which makes the perturbation grow.

More precisely, as explained in Appendix C, we can obtain the vertical distribution of the previous energy tendencies by calculating the vertical Eliassen-Palm (EP) flux of this system

$$F^z = \rho_0 \left[\frac{f}{\theta_{0z}} \overline{v\theta} - \overline{uw} \right]. \tag{3.43}$$

The vertical profile of F^z and its two components are shown in Fig. 3.7a. In this figure, the profile is averaged in time over the entire experiment to remove the influence of the spurious inertial oscillation, and normalized by the maximum of $\rho_0 \frac{f}{\theta_{0z}} \overline{v'\theta'}$. Consistently with Fig. 3.3c, the meridional heat flux $\rho_0 \frac{f}{\theta_{0z}} \overline{v\theta}$ and the vertical flux of horizontal momentum $-\rho_0 \overline{uw}$ have respectively positive and negative values, and their sum is positive (black curve) which makes the mode grow. Each of these two flux components has an extremum in the vicinity of the IL (z_{IL} =1.855km) because of the singularity, and the energy is provided by the background flow to the unstable NG mode predominantly at this level. It is also essentially near this inertial singular level that the wave action exchange is concentrated, as found earlier by Lindzen et al (1980) concerning the large scale baroclinic instability[2]. Note also that the flux does not vanish near the

[2]In our case, the study in terms of action budget did not reveal fruitfull for the following reason. The derivation of the small amplitude formulation of the action budget, given by Andrews (1987) for example, requires a first order development of the PV budget for small perturbations. It yields a relation of the form $\partial_t \overline{\mathcal{A}} + \partial_z \overline{F^z} = \overline{D}$, where $\overline{D}$ is a source term linked to all the diffusive effects and forcings. But in our linear anelastic system, the mean and background PV is $\overline{P} = \frac{1}{\rho_0} f\theta_{0z}[1 - \mathrm{Ri}^{-1}]$, which it is close to zero when Ri is close to 1. Because of that, the small perturbation approximation

surface as it would do in the QG case. Actually, it increases a little. This was also observed by PMS (personal communication).

Note that this typical EP flux profile, associated with the fields structure described in Fig. 3.4, allow us to interpet the structure of this unstable NG mode in analogy with the classical counter-propagating Rossby wave perspective for the QG Eady problem. Namely, as proposed by Nakamura (1988), it can be seen as the result of the interaction between a boundary Eady wave and an inertial critical layer.

Finally, we note that this profile of the total EP flux F^z is consistent with the previous asymptotic analysis in section 3.3.3. Indeed, F^z is everywhere constant except in the vicinity of the IL where it undergoes a globally negative jump, and near the lower IL (which is slightly under the surface). The fact that the mode is unstable induces a discrepancy with the asymptotic profile (section 3.3), which is a strict Heaviside profile. Instead of that, the flux increases significantly before falling to 0. The Fig. 3.7b will be described in the next section.

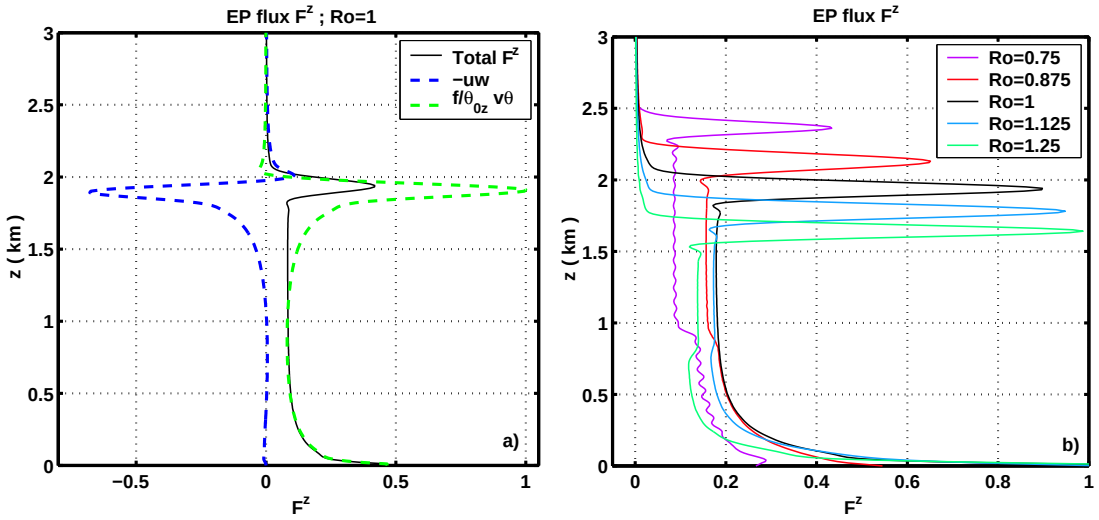

FIG. 3.7 – a) Vertical Eliassen-Palm (EP) flux F^z (black) and its two components $\rho_0 \frac{f}{\theta_{0z}} \overline{v'\theta'}$ (green) and $(-\rho_0 \overline{u'w'}$ (blue) averaged in time in experiment. The profiles are normalized by the maximum of $\rho_0 \frac{f}{\theta_{0z}} \overline{v'\theta'}$. b) Vertical Eliassen-Palm (EP) flux F^z in experiment L but for different values of Ro. All the profiles are normalized by the maximum of F^z for Ro=1, which is localized at the surface.

breaks down and the diffusive source terms in $\overline{D}$ become strongly dominant in the action budget, as regards to the action tendency $\partial_t \overline{\mathcal{A}}$ and the EP flux divergence $\partial_z \overline{F^z}$. Nevertheless, we found that $\partial_t \overline{\mathcal{A}} + \partial_z \overline{F^z} \approx 0$, thus F^z can still be interpreted as an action flux in our context. But using the complete lagrangian mean formulation of the action budget might be more relevant here.

3.4.2 The role of the shear Λ, the Rossby and Richardson numbers

The sensitivity of the eigenvalues to Ro was studied by PMS. We have carried on the same sensitivity experiment, and the results are shown in the Fig. 3.8 for comparison. Note that here, changing Ro is equivalent to change the shear Λ or the Richardson number Ri, because the constants N, f, L and Bu are fixed (see Eq. (4.10) with Bu=1). We keep this in mind for the following discussion.

The Fig. 3.8a presents the phase velocity c_ϕ of the NG mode after normalization by ΛH, which is also the height of the CL normalized by H (Eq. (3.5)). The curve follow well the results of PMS, except a constant offset that was not elucidated[3], indicating that the CL falls slowly with Ro but keeps close to the QG steering level ($\frac{fL}{N} = 1$km). More precisely, PMS have shown that the CL keeps but close to (but higher than) the steering level of the asymptotically balanced Eady edge wave which also falls with Ro (see their Fig. (4)a for radiating modes). This means that the dynamics of the upward and downwward IGWs is slaved to the dynamics of the edge wave, even when the Rossby number Ro is of order 1. In other words, the partially balanced surface Eady wave strongly controls the dynamics of the NG mode by imposing a CL close to $\frac{fL}{N}$. Indeed, this determines the localization of the IL, and then the growth rate σ only depends on the two boundary conditions.
The fact that z_{CL} falls with Ro can be seen as a consequence of the non geostrophic contribution to the dynamics, which makes decrease the effective Burger number $\frac{Nz_{CL}}{fL}$. This was first interpreted by Nakamura (1988), by introducing a modified Rossby radius $L_R = \frac{\sqrt{N^2+\Lambda^2}\,H}{f}$ which depends on the shear. Conversely, we can use it to derive an approximate law for z_{CL}, namely

$$z_{CL} \sim \frac{fL}{\sqrt{N^2+\Lambda^2}} = \frac{H}{\sqrt{1+\mathrm{Ri}^{-1}}} = \frac{H}{\sqrt{1+\mathrm{Ro}^2}}, \tag{3.44}$$

which is relatively well followed by the present results and PMS ones (dash-dotted line in Fig. 3.8a).

Concerning the growth rates (Fig. 3.8b), the bell shape of the curve found by PMS is retrieved, but shifted and inclined differently. We first discuss this general bell shape, and then the discrepancy between our anelastic growth rates and the PMS ones.

As said previously, increasing the shear Λ will make fall z_{CL}. But it will also make fall even faster the distance $z_{IL} - z_{CL} = \frac{f}{k\Lambda} = H\sqrt{\mathrm{Ri}} = H/\mathrm{Ro}$. For small values of Ro, this is expected to enhance the growth rate because the inertial layer is getting closer to surface Eady wave, making it easier their mutual interaction in order to extract energy from the background flow. In other words, the vertical integral of F^z must first increase when lowering the inertial layer. But when Ro$\sim$1 or larger, z_{CL} and z_{IL} are so close to the surface that the surface Eady wave and the inertial layer merge together. It gives a very shallow perturbation that cannot extract some energy. Note that coming back to the over-reflection point-of-vue (section 3.3.3), it is rather natural to expect that a resonant height of the inertial layer will be achieved, that maximizes the growth rate, as it is the case in any resonant cavity.

[3] *This difference is systematic, and might be attributed to the use of the Asselin filtered leap-frog temporal scheme, which is known to accelerate the waves (Durran, 1999), and to the numerical and physical diffusive terms in the model.*

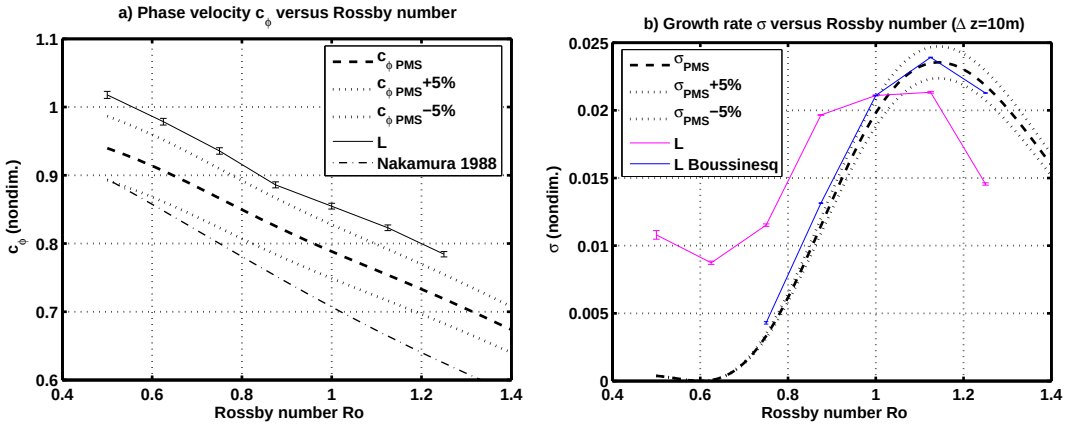

FIG. 3.8 – Evolution of the nondimensional phase velocity (normalized by ΛH) (a) and nondimensional growth rate (normalized by $\frac{f\Lambda}{N}$)(b) versus the Rossby number $\mathrm{Ro} = \frac{\Lambda H}{fL}$. All other parameters are the same as in experiment L in section 3.4.1. The Boussinesq growth rates obtained by PMS and its $\pm 5\%$ interval are respectively indicated by the dash-line and the dotted-lines. The dash-dotted line presents the law from Nakamura (1988) in Eq.(3.44).

Now, the discrepancy between PMS results and ours, observed for $\mathrm{Ro} \neq 1$ in Fig. 3.8a, can be understood qualitatively by using the asymptotic results obtained in section 3.3.3. Notably the Eqs. (3.29), (3.28) and (3.32) quantify, in the asymptotic limit, the influence of the regular singularity appearing at the CL for $\mathrm{Ri} \neq 1$ upon the energy transfer between the background flow and the perturbation. These theoretical jumps at the CL have also been observed on the EP flux profiles in our numerical simulations. This is summarized in the Fig. 3.7b, in which each profile have been normalized by the maximum of the EP flux in the case Ro=1 (black curve) for easy comparison[4]. As expected from the calculations in section 3.3.3, the profiles for $\mathrm{Ro} \neq 1$ show a jump at the CL which increases roughly as $\mathrm{Ro} - 1$ (the corresponding jump of G increases as $\mathrm{Ri} - 1$), accounting for the more and more significant singularity that arises far from Ro=Ri=1.

Thus, the influence upon the growth rates can be analysed as follows. First, in the domain $\mathrm{Ro} < 1$ ($\mathrm{Ri} > 1$) we have $G_0^- < G_0^+ < 0$. This means that the over-reflection should be reinforced at the CL, by a supplementary amount of energy provided by the background flow to the unstable mode. Consequently the growth rate must be larger than in the Boussinesq framework of PMS. That is what we observe in Fig. 3.8a. By contrast, if $\mathrm{Ro} > 1$ ($\mathrm{Ri} < 1$) we have $G_0^- > G_0^+ < 0$, and hence the unstable mode leaves a part of its energy to the background flow near the CL, which should reduce the growth rate. This is also observed in Fig. 3.8a. Moreover, γ is actually proportional to $\sqrt{\mathrm{Ri}}\,(\mathrm{Ri} - 1)$, which probably explains that the discrepancy is more pronounced for $\mathrm{Ro} < 1$ than for $\mathrm{Ro} > 1$. Finally, the fact that we still find unstable growth rates for $\mathrm{Ro} > 1$ prooves that this second singularity at the CL is not strong enough to prevent the growth thanks to over-reflection. This was actually expectable because this singularity is somewhat less fundamental than the one at the IL, disappearing progressively when Ri gets closer to 1.

[4]Note that this maximum in the black curve is localized at the surface, and not at the IL.

3.4.3 Other sensitivity studies

In this section, we present some supplementary results to complete the benchmark of the present anelastic model on the Boussinesq results from PMS.

i) Vertical resolution and diffusivity

The Fig. 3.9 shows the sensitivity of the growth rate with the vertical resolution The uncertainty of the measure is only linked to the presence of the spurious IGW, hence it can be reduced by longer simulations, which is more difficult with very high resolutions. This figure shows a posteriori that we need a minimum resolution of order $\Delta z = 10m$ to resolve correctly the critical level interaction. Consistently, the resolution need to be sufficiently lower than the viscous scale l_μ defined for non-rotating conditions in Eq. (4.24). For bad resolutions, the growth rate is artificially increased. By contrast, the phase velocity is very weakly sensitive to the vertical resolution (not shown), consistently with the idea previously explained that it is essentially controled by the Eady edge wave dynamics, which can be resolved with lower resolutions.

Increasing the diffusivity $\mu = \kappa$ was found to reduce the growth rate. The proportionality ratio is around 0.03 for Ro=1. This means for example that taking $\mu = 0.1$ will give a difference of around 17% with the inviscid growth rate. Values between 0.004 and 0.01 have been found to yield a correct growth rate for the case Ro=1.

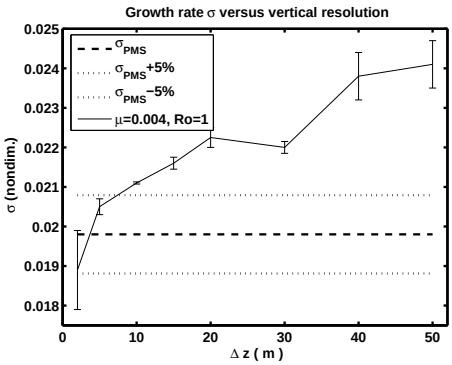

FIG. 3.9 – Evolution of the nondimensional growth rate (normalized by $\frac{f\Lambda}{N}$), versus the vertical resolution Δz. All other parameters are the same as in experiment L. The Boussinesq growth rates obtained by PMS and its $\pm 5\%$ boundaries are respectively indicated by the dash-line and the dotted-lines.

ii) Height of the rigid upper boundary

The constants A_0, B_0, A_{-1} and B_{-1} in Eqs. (3.28)-(3.30) depend on the height of the rigid upper boundary. The Fig. 3.10 illustrates the results obtained by changing z_{top} in experiment L, in comparison with PMS results. The growth rate is monotonously increasing with z_{top} in the range studied, contrary to the PMS results which account for an optimal height around 20km. As Ri=1, the anelastic singularity at the CL is apparent and hence cannot influence the growth rate, through A_0 in Eq. (3.32). Therefore the discrepancy with PMS results appearing for a higher upper boundary ($z_{top} > 20$km) can only be attributed to the irregular singularity in $z \to \infty$, because of the anelastic and nonhydrostatic terms in Eq. (3.2). Incidentally, this shows also that these corrections are likely neglectable until z_{top}=20km.

iii) Horizontal wave-number

To understand the effect of changing the horizontal scale from L to $L' = \frac{L}{\tilde{k}}$, where $\tilde{k}$ is a non-dimensionalized wavenumber, we write the new characteristic numbers using

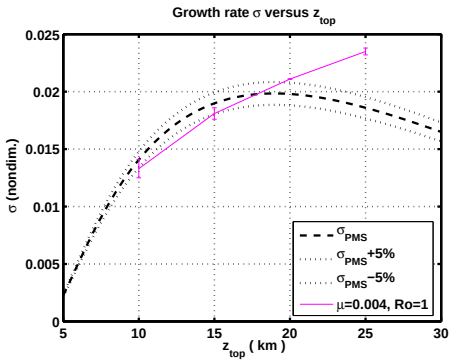

FIG. 3.10 – Evolution of the nondimensional growth rate (normalized by $\frac{f\Lambda}{N}$), versus the height of the rigid upper boundary. All other parameters are the same as in experiment L in section 3.4.1. The Boussinesq growth rates obtained by PMS and its ±5% interval are respectively indicated by the dash-line and the dotted-lines.

a vertical height H' a priori different from H :

$$\text{Ro'} = \frac{\Lambda H'}{fL'} = 1\,, \quad \text{Bu'} = \frac{NH'}{fL'}\,, \text{ and Ri'} = \frac{N^2}{\Lambda^2} = \frac{\text{Bu'}}{\text{Ro'}^2} = \text{Ri} = 1 \tag{3.45}$$

The experiments show that the most unstable mode observed in each case still corresponds to $\text{Bu}' \sim 1$, which means that $H' \sim \frac{H}{\tilde{k}}$. This is again a consequence of the fact that z_{CL} is essentially controled by the surface dynamics, as explained previously. Consequently, the new CL and IL are $z'_{CL} = z_{CL}/\tilde{k}$ and $z'_{IL} = z_{IL}/\tilde{k}$, and Ro and Ri remain unchanged. Therefore, this new system is equivalent to experiment L after increasing the height of the upper boundary to $z'_{top} = \tilde{k} z_{top}$. According to the sensitivity to z_{top} presented in Fig. 3.10, our anelastic and nonhydrostatic growth rates must be larger than PMS ones for $\tilde{k} > 1$. This is indeed observed in Fig. 3.11a. Conversely, the phase velocity (or z_{CL}) shown in Fig. 3.11b follows a curve in $1/\tilde{k}$ because $c'_\Phi = \Lambda z'_{CL}$, exactly as in PMS, being insensitive to the upper boundary.

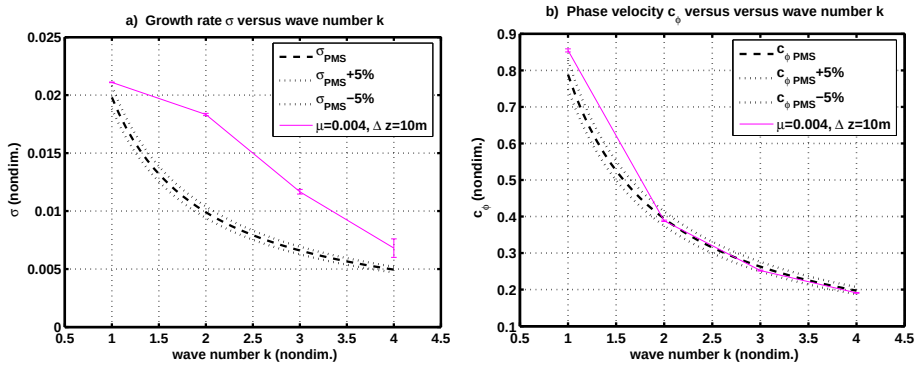

FIG. 3.11 – Evolution of the nondimensional growth rate (normalized by $\frac{f\Lambda}{N}$) (a) and nondimensional phase velocity (normalized by ΛH) (b), versus the horizontal wave-number k. All other parameters are the same as in experiment L in section 3.4.1. The Boussinesq growth rates and phase velocities obtained by PMS and its ±5% interval are respectively indicated by the dash-line and the dotted-lines.

3.5 Nonlinear growth, saturation, and breakdown

3.5.1 Numerical experimental setup - Experiment NL

In this experiment called NL, we initialize a nonlinear simulation with the linear NG mode studied in L (subsection 3.4.1). But now we use a set of 256 horizontal wavenumbers to resolve as accurately as possible the small scales produced by the nonlinearities. The strong vertical resolution (Δz=10m) and large height of the domain does not allow us to increase further the horizontal resolution. The initial amplitude is small in order that the nonlinear terms are neglectable at the begining.

The nonlinear growth of the mode will naturally increase the energy stored in the small scales, through mechanisms that we analyse in section 3.5.3. We found it impossible to use more than 128 harmonics in the horizontal with the conventional laplacian diffusive terms introduced in appendix A, because of numerical instabilities. To double the horizontal resolution, we needed to change the parametrization of the energy cascade to the small horizontal scales. More specifically, we needed to make the diffusivities μ and κ increase with the wavenumber k, for k larger than a cut-off wavenumber k_c which is imposed arbitrarily from numerical considerations. One way to do that is to increase artificially the order of the diffusive terms from the initial order 2 (laplacian) to the order p (hyperlapacian) (Winters & D'Asaro 1989, Lelong and Dunkerton 1998). Thus, in experiment NL we impose[5]

$$\mu = \kappa = \mu_0 \left(1 + \left(\frac{k}{k_c} \right)^{p-2} \right) \quad \text{with} \quad k_c = 90 \quad \text{and} \quad p = 4. \tag{3.46}$$

The value of μ_0 is imposed by the linear experiment L, in which we found a value that lead to an accurate growth rate : $\mu_0 = 0.004\text{m}^2.\text{s}^{-1}$.

3.5.2 Energy budget : nonlinear saturation and breakdown

The energy budget is presented in Fig. 3.12 for the whole experiment, and should be compared to Fig. 3.3. From these curves, we can divide the experiment NL into 3 stages.

During the **first stage**, which will be arbitrarily said to end near t=160h, the energy growth is exponential, with a growth rate very close to the linear one measured in section 3.4.1, slightly smaller.

During the **second stage**, which ends near t=197h when a breakdown occurs, a slight inertial oscillation becomes visible in the energy. This is much more clearly visible in the tendencies (Fig. 3.3c), which show the inertial oscillation of period around 17h amplifying strongly before the breakdown, modulating strongly the growth at this stage. We will investigate further the origin of this inertial oscillation in the section 3.5.3. Beforehand we take it for given in the following analysis. In the same time, the dissipation tendency (cyan) intensifies. Actually, more precisely the breakdown begins near t=194 hrs, when the total tendency (black) peaks sharply and starts to decrease abruptly to reach negative values near t=198h. The next minimum is reached, only 10-12h after the previous one near t=199h, in advance compared to the inertial oscillation period. Actually, one can see that the total tendency is geared by the advection

[5]In the following spectra, the value of p was increased to 8 at the very end of the simulation, after the global breakdown.

tendency term (pink), which is the signature of the nonlinear dynamics of the perturbation flow. This term starts to be negative at t=193h and falls down abruptly to an intense negative minimum reached at t=199h, testifying of a strong transfer of energy towards the background flow at this moment.

After this breakdown the **third stage** begins : the tendency curves show a rather chaotic evolution, nevertheless underlied by the still remaining inertial oscillation. The dissipation comes back to a smaller magnitude, and the energy oscillates around a stationary value.

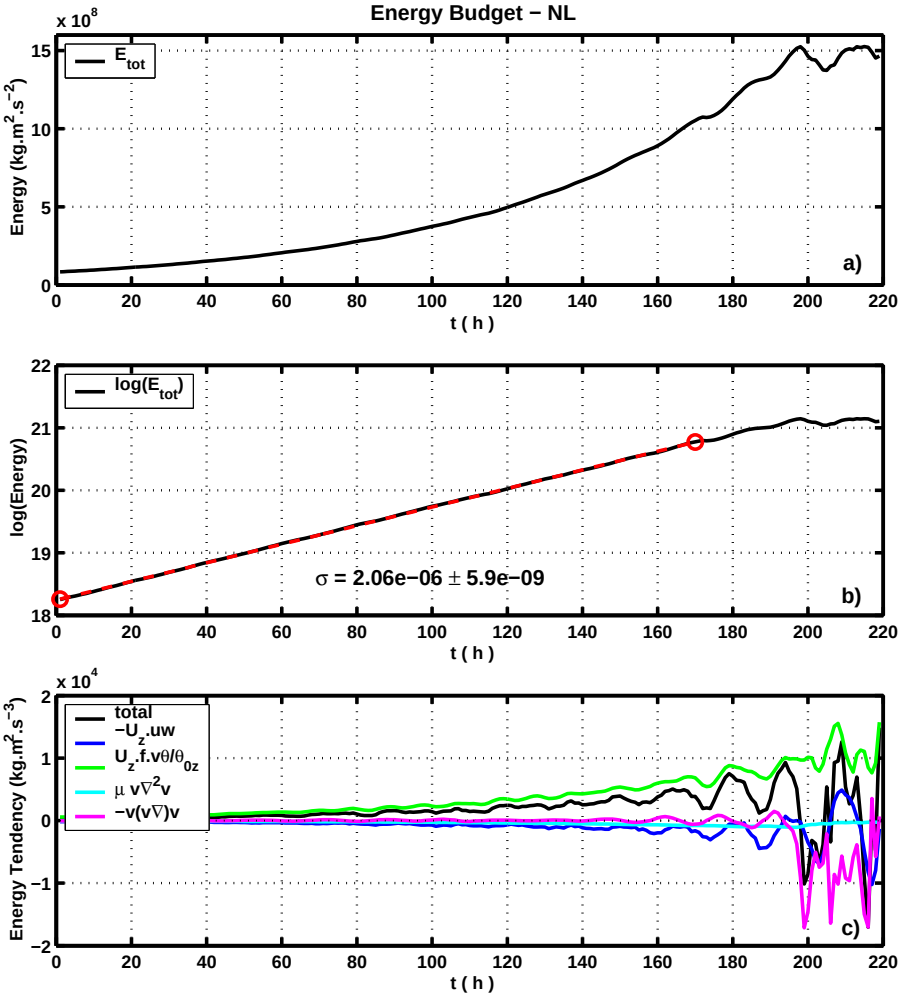

FIG. 3.12 – Energy budget versus time for experiment NL. Same conventions as in Fig.3.3.

3.5.3 Saturation mechanisms

In this subsection, we analyse carefully what happens during the second stage of NL. We illustrate the analysis with the situation near the date t=178h, that is at a crest of the total energy tendency (black in Fig. 3.12c). We examine successively the different mechanisms that might enter into account, namely :
(i) the small scale instabilities of the inertial critical layer,
(ii) the feedback of the mean flow on the global unstable NG mode, and
(iii) the nonlinear equilibration of the surface Eady wave.

Stability diagnosis of the nonlinear mode

The Fig. 3.13 shows the wave fields at t=178h. In the same time, we present various diagnostics at t=178h in the Fig. 3.14, to interprete the stability of this flow : the total potential temperature $\tilde{\theta}$ (a), the total local Brunt Vaïsalla frequency $N^2_{tot} = \frac{g}{\bar{\theta}}\partial_z\tilde{\theta}$ (b), the total horizontal mean zonal wind $\Lambda.z + \bar{u}$ (c), the total local zonal shear $\Lambda + u_z$ (d), and the quantity $\frac{2\alpha}{\pi}$ (e) where α is related to the total local zonal Richardson number Ri_{tot} as follows :

$$\alpha = \arctan\left[4\mathrm{Ri}_{tot}\right] = \arctan\left[\frac{4N^2_{tot}}{(\Lambda + u_z)^2}\right]. \tag{3.47}$$

Indeed, as the inertial critical layer is strongly sheared and overturned, it is likely to give rise to the Kelvin-Helmholtz instability or Shear Instability (SI)[6] and the Convective Instability (CI). These instabilities all occur under specific necessary conditions on the value of Ri_{tot}. Namely the stratified SI is expected for $0 \ll \mathrm{Ri}_{tot} < 0.25$ ($\alpha < 0.5$), the unstratified SI for $\mathrm{Ri}_{tot} \approx 0$ or $-0.25 < \mathrm{Ri}_{tot} < 0$ ($-0.5 < \alpha < 0$), and more generally the CI for $\mathrm{Ri}_{tot} < 0$ ($\alpha < 0$). Plotting α instead of Ri_{tot} provides a smoother visualization of local stability. Note that the strongly sheared meridional velocity v should also give rise to transverse shear instability in a 3D context, but this cannot arise in the present 2D framework. For this reason we do not care about the meridional vertical shear v_z. Note also that the symmetric instability is precluded in this 2D problem.

The nonlinear mode presented in Fig. 3.13 should be compared to the linear one in the first 3km of Fig. 3.4. A clear distortion of the wave fields by the nonlinear terms appears through two features. First, a slight assymmetry between positive and negative anomalies appears in each field, notably near the surface. As the nonlinear terms become non neglectable at the surface, the ageostrophic circulation makes the streamlines of meridional wind v tighten in the cyclonic region near x=175km (Fig. 3.13b), and move away from each other in the anticyclonic region near x=-150km (Hoskins, 1975). As a consequence, the warm surface potential temperature anomaly θ concentrates on a smaller region and intensifies, whereas the cold one is becoming wider (Fig. 3.13d). For this reason, the mean stratification is becoming negative at the place of the warm surface anomaly of θ (Fig. 3.14b), as well as the Richardson number (Fig. 3.14f). The second feature is the emergence of small scale waves in the vertical velocity (Fig. 3.14c), notably in the negative lobe. These waves and their source will be analysed in the following.

In terms of stability, the structure of the inertial critical layer appears clearly in the Fig. 3.14a, b and d, as a succession of elongated tongues, alternatively positively sheared and stratified and then negatively sheared and stratified. Here the positive-negative assymmetry is also visible, with the negative tongues lying above the positive ones on the major part of the domain. In these tongues, the amplitude of the wave fields u, v and θ reach around 2m.s^{-1} and 0.7K respectively (Fig. 3.13a,b,d). In spite of this rather weak amplitude, these tongues are so thin that the stratification (Fig. 3.14b) and zonal shear (Fig. 3.14d) reach very intense negative values (respectively $-2.3\,10^{-4}$ s^{-1} and -0.022 s^{-1}). They reach even more intense positive values because the background flow is positively sheared and stratified (respectively $4.2\,10^{-4}$ s^{-1} and 0.035 s^{-1}). This intense overturning is also clearly visible in the total potential temperature

[6]Given the large horizontal scales of the present instabilities, we will prefer the more general Shear Instability to Kelvin-Helmholtz instability.

field in Fig. 3.14a. Consequently, in the presence of nonlinear terms in the dynamics, the tongues positively sheared and stratified are likely unstable through the stratified SI, whereas the tongues negatively sheared and stratified should bear a mixed SI and CI. These properties are summarized by the local Richardson number in the Fig. 3.14f. Note that in this last picture, around the negative tongues, α (Ri_{tot}) reaches alternatively very high and very low values in a very narrow area, and the contours are very concentrated. The reason is that the transition between positive and negative stratification occurs nearly at the same place than the transition between positive and negative zonal shear. This similarity between the two fields is a general consequence of the fact that u and θ are nearly in phase in the inertial critical layer, as shown previously by the aid of Eq. (3.41). This argument also stands at the surface (Eq. (3.40)).

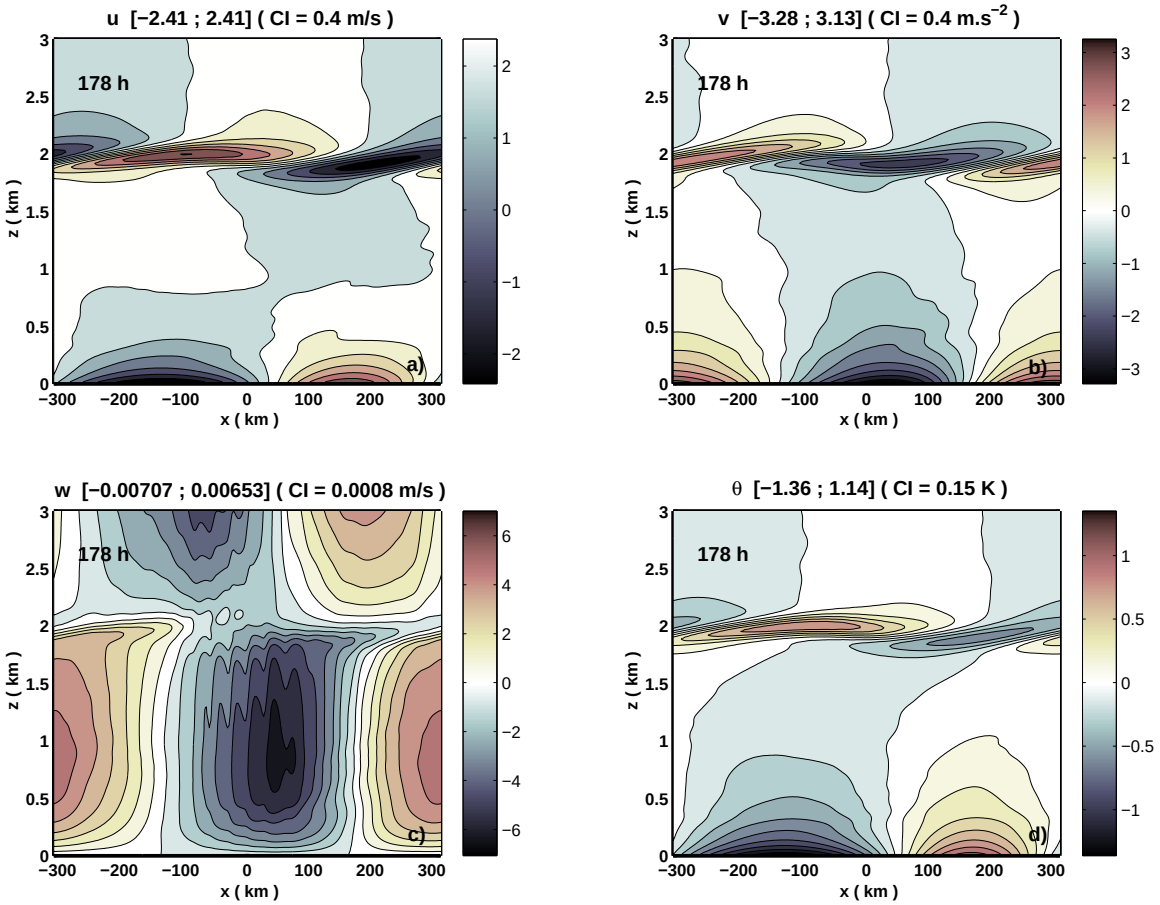

FIG. 3.13 – Velocity and potential temperature fields of the NG mode of experiment NL at $t = 178$hrs.

(i) Small scale instabilities and GWs generation

a. In the spectra

The Fig. 3.15a shows the evolution of the total energy of each wavenumber of the disturbance for the period t=171h to 180h, after normalization by the maximum at t=171h. The spectra for the dates t=210h to 215h have been also represented for subsequent discussion, and are gathered in the upper part of the graph (E(k)$> 10^{-5}$). Consistently, the maximum is for k=1 and corresponds to the linear unstable NG

mode. Only the wavenumbers lower than 100 are shown because the hyperlaplacian cuts every $k > k_c = 90$.

The energy spectra in Fig. 3.15a clearly show a rapid and nearly exponential energy production around the wavenumber $k_{KH} = 22$ and the corresponding harmonics $2k_{KH} = 44$ and $3k_{KH} = 66$, testifying of the rise of small scale instabilities. This reveals a rapid transfer of energy from the large scale flow to the small scale $\frac{L}{k_{KH}}$, and the associated nonlinear propagation to the algebraic multiples of k_{KH}. The wavelength corresponding to k_{KH} is 28.5km, which is in agreement with the wavelength of the short scale waves observed in Fig. 3.13c.
To elucidate further the nature of these instabilities, we present in the Figs. 3.15b,c,d,e the evolution between t=171h and 180h of the partition between potential and kinetic energy components E_{pot} and E_{kin}, integrated over the bands k=1 (b), k=20-24 (c), k=40-48 (d) and k=60-72 (d). Conventionally, the shear instability (SI) is associated with a flux of kinetic energy from the large scales towards the short scale instabilities, whereas the convective instability (CI) is associated with a supply of potential energy to the short scales (Lelong and Dunkerton 1998a). The Fig. 3.15b indicates that the total energy of the linear NG mode in k=1 decreases during the observed period, essentially because of a decrease of the kinetic energy. This is also observed for the mean pertubation in k=0 (not shown). Moreover, the observation of the spectra of the tendencies $-\Lambda < uw >$ and $\Lambda \frac{f}{\theta_{0z}} < v\theta >$ for the same period indicate that, the background flow $\mathbf{U}(z)$ also supplies predominantly some kinetic energy to the short scales (not shown).
Concerning the short scales, the Figs. 3.15c,d,e are in agreement with these observations. They show that E_{kin} is always larger than E_{pot}, and that the tendencies $\mathrm{d}(\ln E_{kin})/\mathrm{d}t$ and $\mathrm{d}(\ln E_{pot})/\mathrm{d}t$ are of the same order. This means that the tendency $\mathrm{d}E_{kin}/\mathrm{d}t$ is larger than $\mathrm{d}E_{pot}/\mathrm{d}t$. For example, the ratio is about 60% for E_{kin} and 40% for E_{pot} in the band k=20-24, and it is even more advantageous for E_{kin} in the other bands. This indicates that the SI mechanism is dominant during the first stages of the inertial critical layer instability, but more or less mixed to the CI mechanism nevertheless.

b. In the fields

At this stage, these small scale instabilities do not emerge in the total horizontal wind and potential temperature of the NG mode, but only in the vertical velocity (Fig. 3.13). Nevertheless, it is possible to observe them directly in the wave fields by removing the wavenumbers $k < 15$ from the total fields. The Fig. 3.16 shows the detailed structure of the small scale meridional vorticity $u_z - w_x$ at t=178h in the center of the inertial critical layer, and the Fig. 3.17 shows the associated small-scale wave fields. In each of these pictures, we have removed the zero contour for clarity. In the Fig. 3.16, to give a reference in space, we have superimposed the contours $[-1, 0, 2, 4] * 10^{-4}$ of N^2_{tot} in red, and the contours $[-1, 0, 1, 2, 3] * 10^{-2}\mathrm{m.s}^{-1}$ of the total zonal shear in green. This figure shows a dominant series of billows ressembling those observed in the KH instability. They are horizontally centered around x=0km, that is at the middle of the positively stratified and sheared tongue previously shown in the Figs. 3.14b,d,e, and at the left of the warm surface anomaly. In the vertical, these billows are localized along the transition between positive and negative stratification (red curves) or zonal shear (green curves), that is where the Richardson number varies abruply. A secondary series of billows is developping on the lower flank of the positively sheared and stratified tongue.

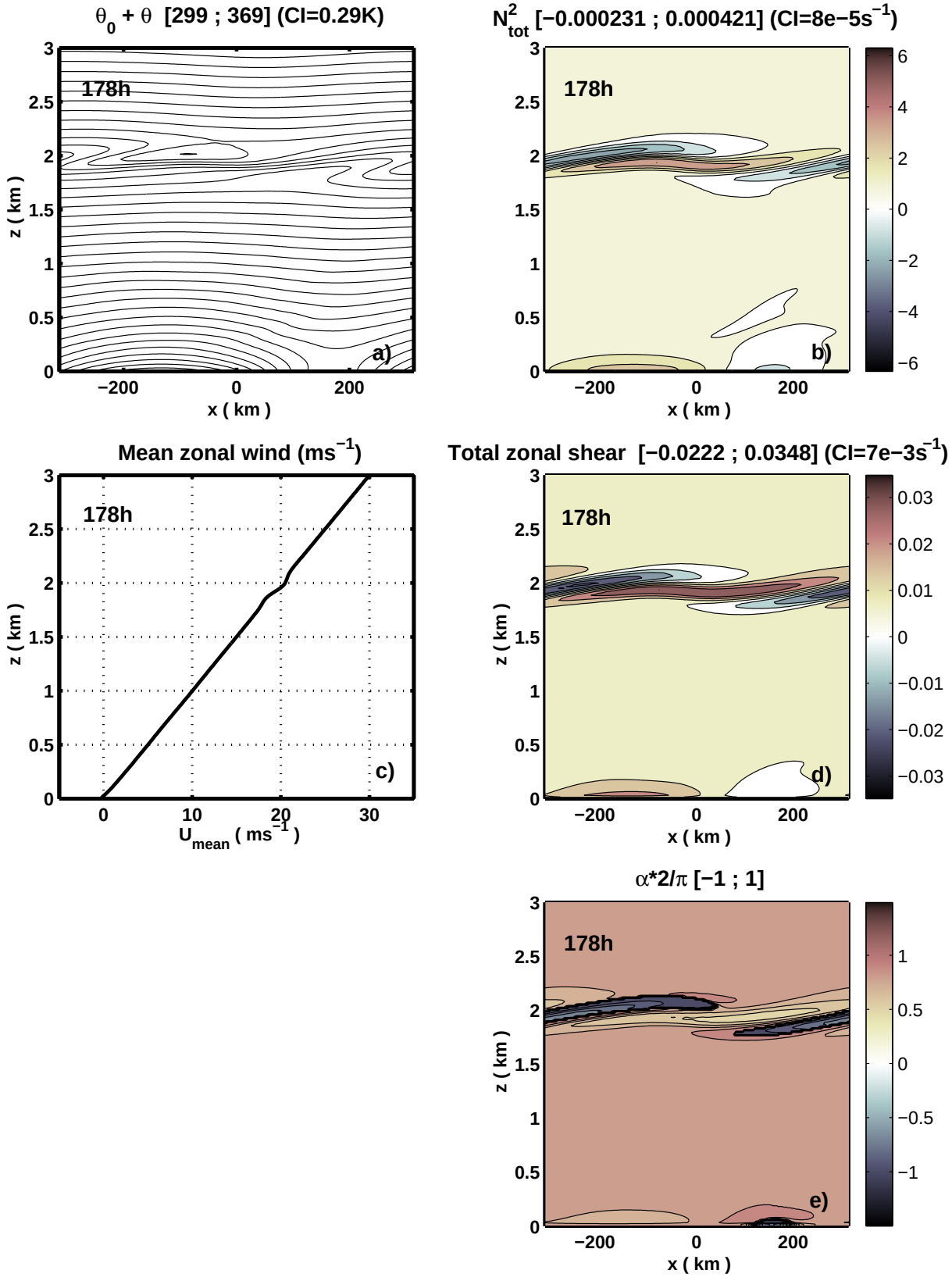

FIG. 3.14 – Stability diagnostics in experiment NL at t=178h : a) total potential temperature, b) total local Brunt-Vaïsalla constant, c) total horizontal mean zonal wind, d) total local zonal shear, and e) the image of the Richardson number $\frac{2}{\pi} * \alpha = \arctan(4\mathrm{Ri})$.

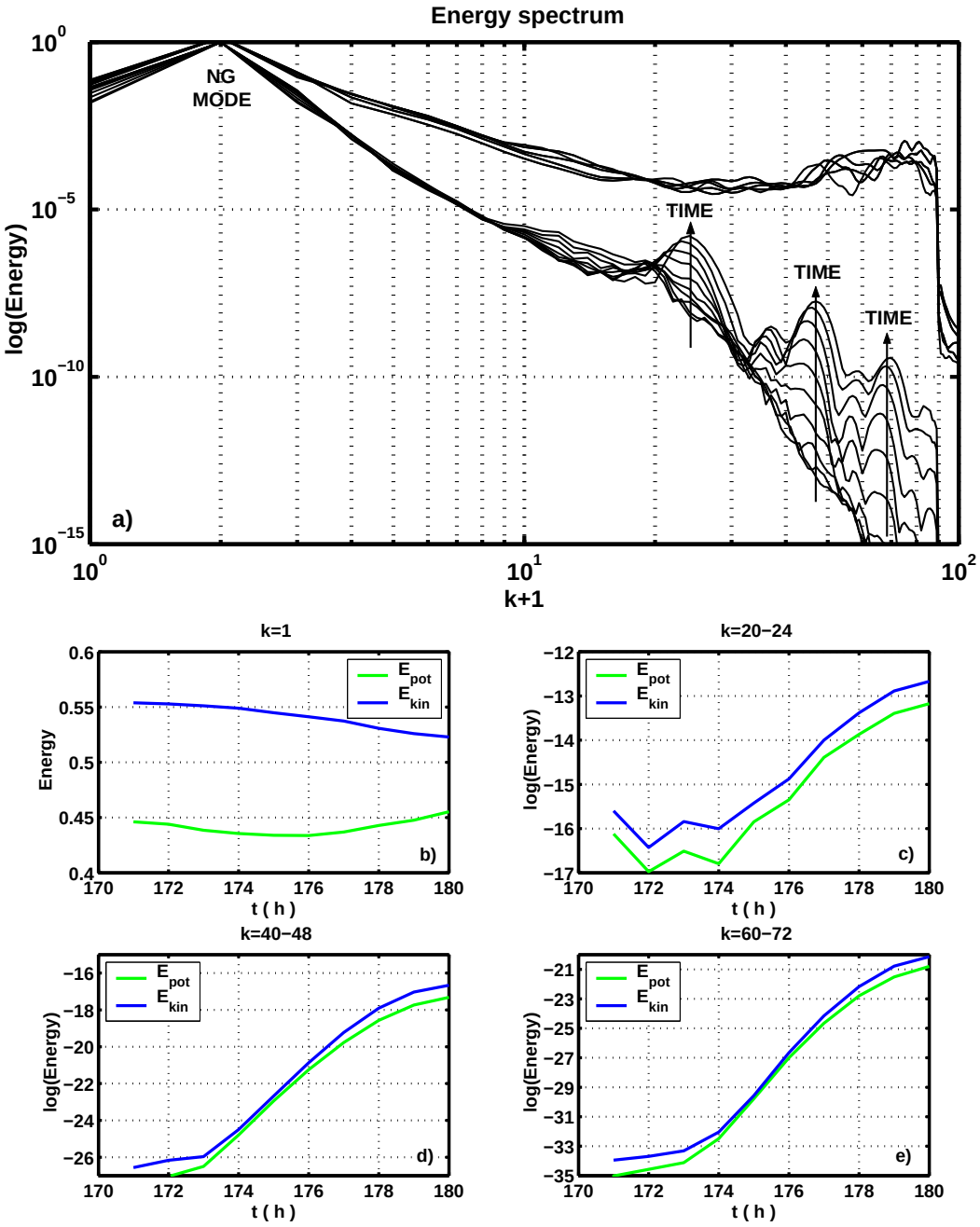

FIG. 3.15 – a) Evolution of the energy budget spectrum in experiment NL in log-log coordinates, for the periods t=171 to 180h, and t=216 to 220h. One curve for each hour. The evolution of the curves with time is indicated locally with arrows. The curves for t=216 to 220h are localized above. b,c,d,e) Evolution of the partition between potential energy E_{pot} and kinetic energy E_{kin} for the spectral bands k=1 (b), k=20-24 (c), k=40-48 (d) and k=60-72 (e).

In the Fig. 3.17, we have superimposed only the contours $[0,2]*10^{-4}$ of N^2_{tot} in red, and the contours $[0,2]*10^{-2}\mathrm{m.s}^{-1}$ of $\Lambda+u_z$ in green. The fields u, v and θ are also essentially embedded in the inertial critical layer. Only in the vertical velocity (Fig. 3.17c), the small scale unstable modes manage to escape from this layer, propagating outside as GWs of the same wavelength. Their phase velocity is nearly horizontal because of the intense background shear (Λ=0.01s^{-1}), corresponding to nearly vertical group

velocity. Propagating upward, the GWs have an increasing vertical velocity because of the decrease of the density. On the contrary, the absence of convectively unstable layer under the critical layer near x=0 makes the GWs generation towards the ground more efficient. For this reason, and because of the reflection at the surface, the GWs are more intense under the critical layer than above.

The small-scale instabilities depicted by the Figs. 3.16 and 3.17 are actually modulated in time because of the variations of the large scale flow structure itself. Indeed, as shown in the next section, the large scale flow in the inertial critical layer is significantly modulated by the inertial oscillation described in the Fig. 3.12c, which affects notably the fields u, v and θ. Because of that, not only the magnitude but also the structure and localization of the present small-scale unstable mode, are changing with a time scale of order the inertial period.

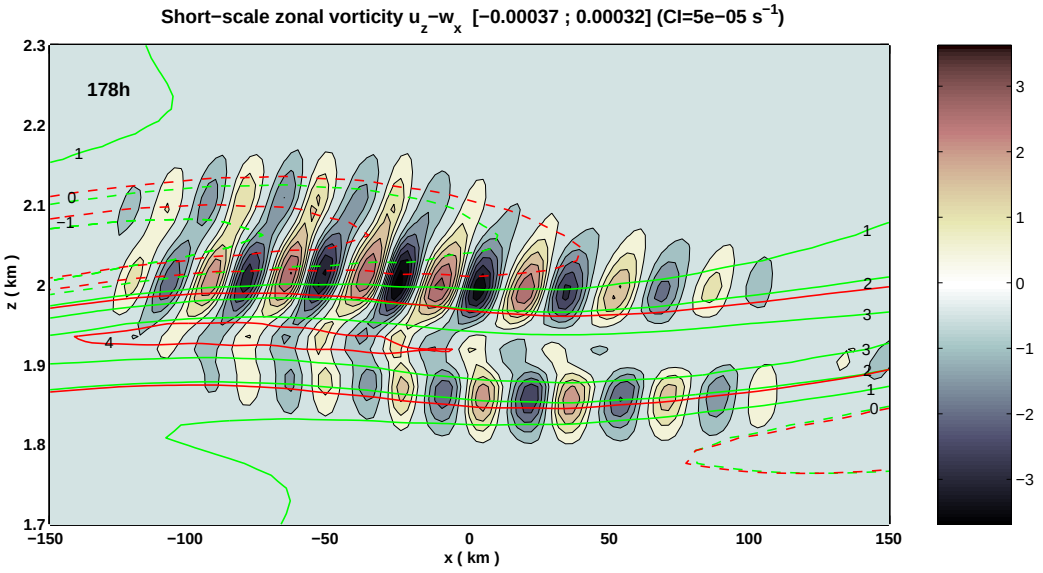

FIG. 3.16 – Small scale meridional vorticity $u_z - w_x$ in experiment NL at $t = 178$h. Wavenumbers $k < 15$ have been removed. The contours $[-1, 0, 2, 4] * 10^{-4}$ of N^2_{tot} are added in red, and the contours $[-1, 0, 1, 2, 3] * 10^{-2}$m.s^{-1} of the total zonal shear are added in green.

c. Discussion

These observations are in agreement with those of Lelong and Dunkerton (1998a and b). They found that in the case of convectively stable or unstable very large scale background IGWs (very low intrinsic frequencies), the most unstable wavenumbers lie in the horizontal Fourier plane on a typical isotropic "halo" structure of nondimensional radius k=20-25, and the instability mechanism is predominantly linked to shear instability. More rigorous comparison of the present instabilities and GWs generation with the earlier studies of breaking shear layers (see the references in the introduction) is out of the scope of this study, for at least three reasons. First, the size of the global domain prevents us from using a very high horizontal resolution. Note that Lelong and Dunkerton (1998) have the same horizontal resolution nevertheless, but in 3D. Second, and more seriously, the complex and unstationary structure of the large-scale flow of the NG mode in the critical layer, makes it difficult to compare in great details the nature and growth rates of the small scale unstable modes obtained here with those of more idealized studies. Moreover, Lelong and Dunkerton did not use a realistic ratio

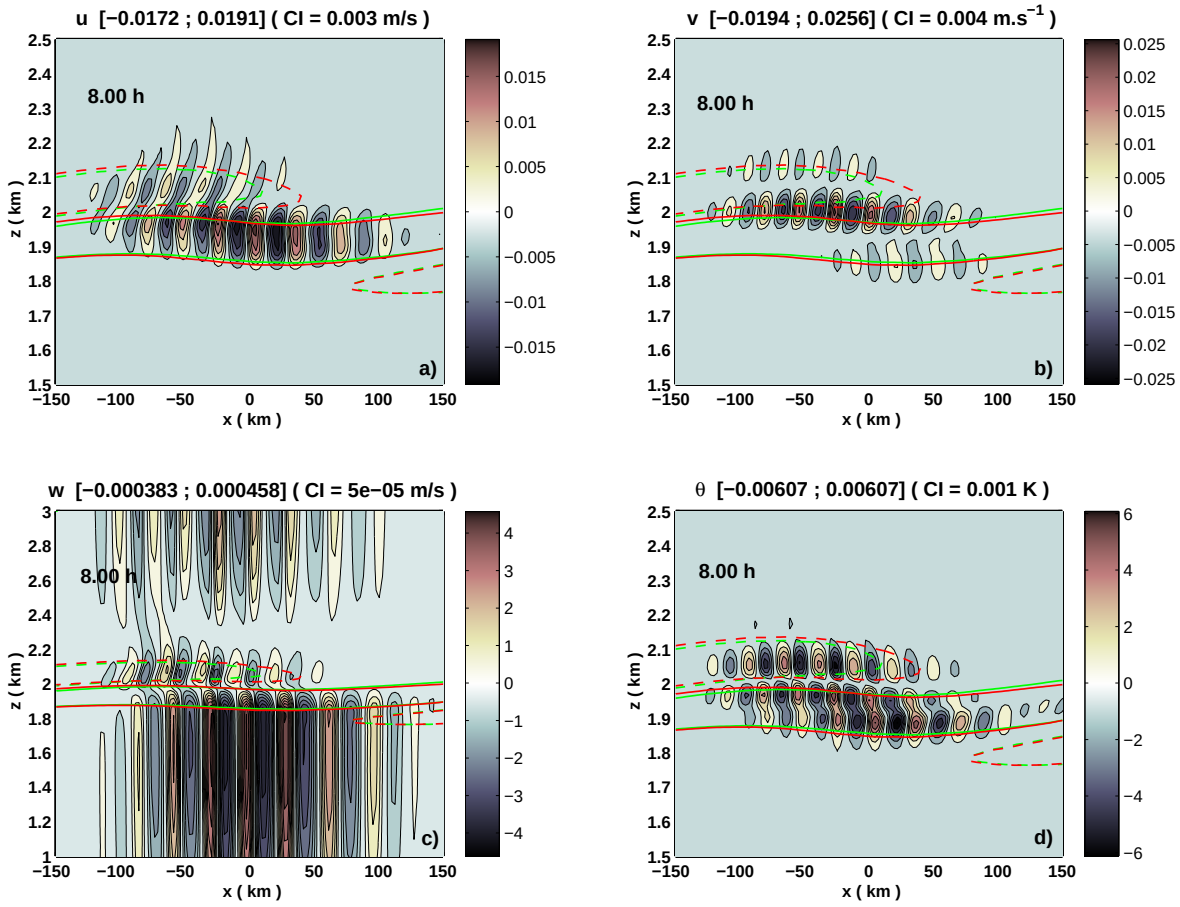

FIG. 3.17 – Small scale velocity and potential temperature fields in experiment NL at $t = 178$h. Wavenumbers $k < 15$ have been removed. The contours $[0, 2] * 10^{-4}$ of N^2_{tot} are added in red, and the contours $[0, 2] * 10^{-2}$m.s^{-1} of $\Lambda + u_z$ are added in green.

between horizontal and vertical scales, compensating with a modified ratio of time scales N/f in order to save CPU time. Third, the present 2D simulation prevents the transverse (meridional) shear instability from developping. As shown by Lelong and Dunkerton (1998b) for the present domain of scales, the rise of unstable modes is isotropic in the Fourier space. For this reason, our 2D simulation certainly over-estimates the lifetime of the large scale flow structure in the inertial critical layer. Hence, our measurement of the saturation level of the NG mode by a 2D simulation may give only an upper bound.

(ii) Feedback by the mean flow

As shown by the Fig. 3.14c, the background zonal wind is now slightly but significantly modified by the nonlinear NG mode, which induces a zonal mean perturbation in the inertial critical layer. This is consistent with the fact that the linear NG mode was shown to provide kinetic energy to the mean flow essentially in the inertial critical layer (Fig. 3.7a, blue line). More precisely, to understand the effect of the nonlinear NG mode on the mean flow, we use the residual mean meridional velocity

$$v^* = \bar{v} - \rho_0 \, f \, \overline{v\theta}/\theta_{0z} \tag{3.48}$$

and the TEM formulation of wave-mean interaction (see appendix C), which asserts that :

$$\partial_t \overline{u} - f\,\overline{v^*} = -\frac{1}{\rho_0}\,\partial_z\left(\rho_0\,\overline{uw} - \rho_0\,\frac{f\,\overline{v\theta}}{\theta_{0z}}\right) \tag{3.49}$$

$$\partial_t \overline{v^*} + f\,\overline{u} = -\frac{1}{\rho_0}\,\partial_z\left(\rho_0\,\overline{vw} + \partial_t\left(\rho_0\,\frac{\overline{v\theta}}{\theta_{0z}}\right)\right)\,. \tag{3.50}$$

In Eqs. (3.49)-(3.50), we neglect the influence of the viscous terms for the following discussion. These two equations represent the forcing of the mean flow by the NG mode as a forced oscillator resonating at the inertial frequency. Consistently, the evolution with time of the zonal mean zonal wind perturbation $\overline{u}$ shows oscillations at the inertial frequency. This is illustrated in the Fig. 3.18a, by the evolution of the vertical profiles of $\overline{u}(z)$ during one inertial period (one profile each third hour from t=171h to t=186h). This figure shows that the mean zonal wind perturbation freely oscillates at the inertial frequency around a mean profile. And this mean profile ressembles the profile of $-\partial_z\overline{uw}$ (see Fig. 3.7a, blue line). Note that the situation is different at the surface : the westward mean zonal wind in Fig. 3.18a is not forced by $-\frac{1}{\rho_0}\,\partial_z(\rho_0\,\overline{uw})$ but rather corresponds to $\frac{1}{\rho_0}\,\partial_z(\rho_0\,f\,\overline{v\theta}/\theta_{0z})$ (Fig. 3.7a, green).

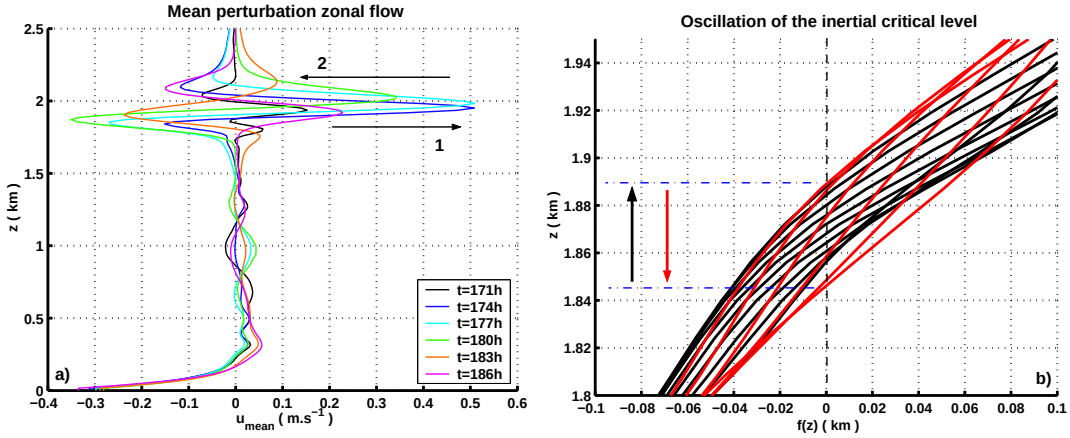

FIG. 3.18 – a) Evolution with time of the vertical profile of the horizontal mean zonal wind perturbation $\overline{u}$, between t=171h and 186h in experiment NL. The arrows 1 and 2 indicate the movement of the maximum. b) Evolution with time of the vertical profile of the function $f(z) = z - z_{CI} + \frac{\overline{u}-fL}{\Lambda}$, whose zero is approximately z_{IL}. The black curves move upward from t=171h to 181h, and then the red curves move down from t=182h to 186h.

As the NG mode was not perfectly initialized in our numerical setup, according to the Eq. (3.49), any perturbation from the pure exponential growth must unavoidably lead to the excitation of free inertial oscillations in the mean horizontal wind. That is why we observed an inertial oscillation in the total energy and energy tendencies in Fig. 3.12. Nevertheless, as discussed from Fig. 3.12c, this oscillation grows more rapidly than the average energy during the second stage of NL. The oscillation amplifies rapidly until the breakdown occurs. This indicates that in this period (say t=150h to 200h), the mean flow is not only oscillating freely but rather resonating at the inertial frequency.

To understand this process, we need to consider the feedback of the mean flow on the unstable NG mode. Particularly, the modification of the mean zonal wind near the

singularities of the NG mode, must modify the theoretical height of these singularities. This is illustrated in the Fig. 3.18b, in which the time evolution of the profile of the function $f(z) = z - z_{CL} + \frac{\overline{u}-fL}{\Lambda}$ is plotted for each hour, in the same lapse of time as in Fig. 3.18b (t=171h to 186h). To compute f at each time, we make the approximation that the CL stays stationary at the height measured in L, that is $z_{CL} = 855$m [7]. Thus, the level at which $f(z)$ vanishes is appproximately z_{IL}. The Fig. 3.18b shows that the inertial oscillation of the mean zonal wind in the inertial critical layer induces a slight oscillation of z_{IL} over a range of 45m, and hence an modulation of the NG mode structure in the inertial critical layer. In return, this introduces an inertial oscillation in the forcing by the NG mode upon the background flow. This closes a resonant feedback loop, which might be responsible for the rapid amplification of the inertial oscillation, leading to the final breakdown. A similar feedback loop was identified by Lott (2003) in the presence of a forcing by a sinusoidal orography.

Finally, we have also observed the nonlinear impact of the NG mode on the other background parameters that determine its linear behaviour. In particular, the background Richardson number was shown to determine the growth rate in the linear analysis. The total zonal mean shear, the total zonal mean stratification and the resulting mean Richardson number are indeed strongly perturbed especially inside of the inertial layer (see Fig. 3.19 at t=178h), but in such a way that it is difficult to draw any clear conclusion from the linear theory about the influence upon the growth rate. Nevertheless, it is likely that these abrupt variations of the background parameters disturb the unstable coupling that takes place near the IL, by creating a barrier between the propagating IGW and the surface Eady wave. But in our case, this effect is dominated by the destabilization by the amplifying inertial oscillation.

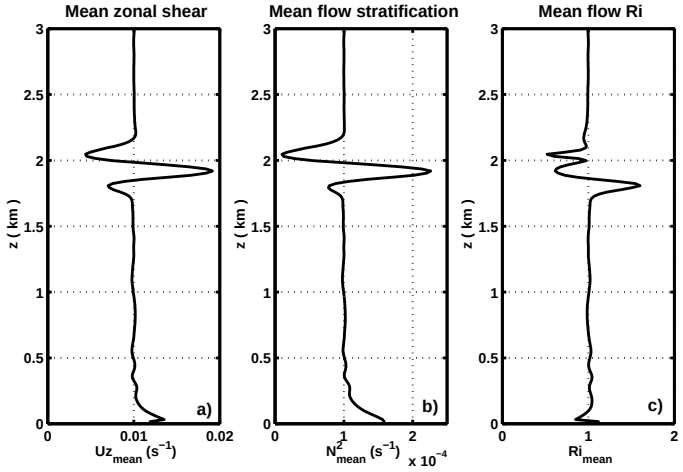

FIG. 3.19 – Vertical profile of the zonal mean of the zonal shear $\overline{\Lambda + u_z}$ (a), the total mean flow stratification $\overline{N^2} = \frac{g}{\overline{\theta}}\partial_z\overline{\overline{\theta}}$ (b), and the total mean flow Richardson number $\mathrm{Ri} = \frac{\overline{N^2}}{(\overline{\Lambda+u_z})^2}$, in experiment NL at $t = 178$h.

[7] This is not exactly true, as we can see in Fig. 3.18a that the inertial oscillation propagates along the vertical profile of $\overline{u}$ and is also significant near the critical level ($z \sim 1$km). Hence the height of the CL must also oscillate a little.

(iii) Nonlinear equilibration

Nakamura and Held (1989) proposed the nonlinear equilibration as a saturation mechanism for large scale 2D Eady waves. In this mechanism, the vertical stratification is locally increased by the creation of positive PV anomalies, out of the dissipation occuring in the frontal collapse at the surface and tropopause. As the stratification increases, the vertical coupling between the two boundary Eady waves at the surface and tropopause is reduced. It is a priori conceivable that the same mechanism enters into account in the saturation of the present subsynoptic scale NG mode, by reducing the vertical coupling between the surface Eady wave and the inertial critical layer.

Nakamura and Held (1989) evaluated the amplitude of the unstable baroclinic disturbance at the point of frontal collapse, and found that the balanced meridional wind satisfies $v_g \sim NH$. In our context, this gives a saturation near $v_g \sim 10$ m.s^{-1}. However, as shown in the Fig. 3.13, during the second stage the order of magnitude of the horizontal winds stays around 2-3 m.s^{-1}, the vertical velocity less than 0.01 m.s^{-1} and the potential temperature around 1K. In addition, observing the total potential temperature over the entire experiment (Fig. 3.14a for t=178h) confirms that the point of frontal collapse is never reached, and the warm front keeps rather smooth. Moreover, the stratification anomaly is negative above the warm front (Fig. 3.14b), and the same is true for the PV anomaly (not shown). Consequently, we can state that a the nonlinear equilibration mechanism does not enter into account in the present saturation. Notably, the slow oscillations observed by Nakamura because of periodical equilibration have nothing to do with the present oscillation, which is due to the feedback loop amplifying the inertial oscillation. Incidentally, we shall suggest that the latter is the counterpart of the former for subsynoptic scale unstable NG modes. Nevertheless this does not mean that the role of stratification near the surface is negligeable here, as explained in the next subsection.

3.5.4 Instability and breakdown of the inertial critical layer

During the last hours of the second stage of experiment NL (t=190 to 197h, not shown), the behaviour is similar to the one described in sections 3.5.3i) and 3.5.3ii). But the magnitude of the NG mode is so high that the local instabilities amplify and propagate along the entire critical layer, leading to a global instability of the inertial critical layer. In this process, the possible influence of the convectively unstable surface lobe (localized near x=150km at t=178hrs in Figs. 3.14d,f) is not clear to us. But it might help to destabilize the critical layer above, and to propagate the global instability.

The complete breakdown of the critical layer starts after t=197h, when the small scale instabilities are so intense that they become dominant in all the fields. We show a picture of this state at t=203h in Fig. 3.20, which was obtained after filtering out the very small and ill resolved wavelengthes that invade the fields at this stage (k>34). The Figs. 3.20a,b,d show that the large scale flow structure of the NG mode in the inertial critical layer is nearly destroyed, and the surface Eady wave is largely perturbed. We also see in the vertical velocity that the whole critical layer is destabilized and generates GWs (Fig. 3.20c). The total potential temperature (Fig. 3.20e) testifies that the magnitude of the generated GWs becomes very substantial, disturbing the background stratification in a large domain above and under the inertial layer. The energy and tendency spectra at the dates t=210 to 215h were added in the Fig. 3.15.

They show that the energy is now uniformly distributed, after a rather brutal cascade and inverse cascade by mixed convective and shear instabilities.

Note nevertheless that this 2D simulation ceases to be realistic, at least quantitatively, from t∼200h and until the end, because the process is fundamentally 3D. In addition, at this stage the magnitude of the GWs generated depends not only on the 2D constraint, but also considerably on the dissipation parameters (diffusivity constant, cutoff wavenumbers and power law). Nevertheless, the amount of potential energy stored in the inertial critical layer before the final collapse can be reasonnably thought as an important source of GWs, even through a 3D breakdown.

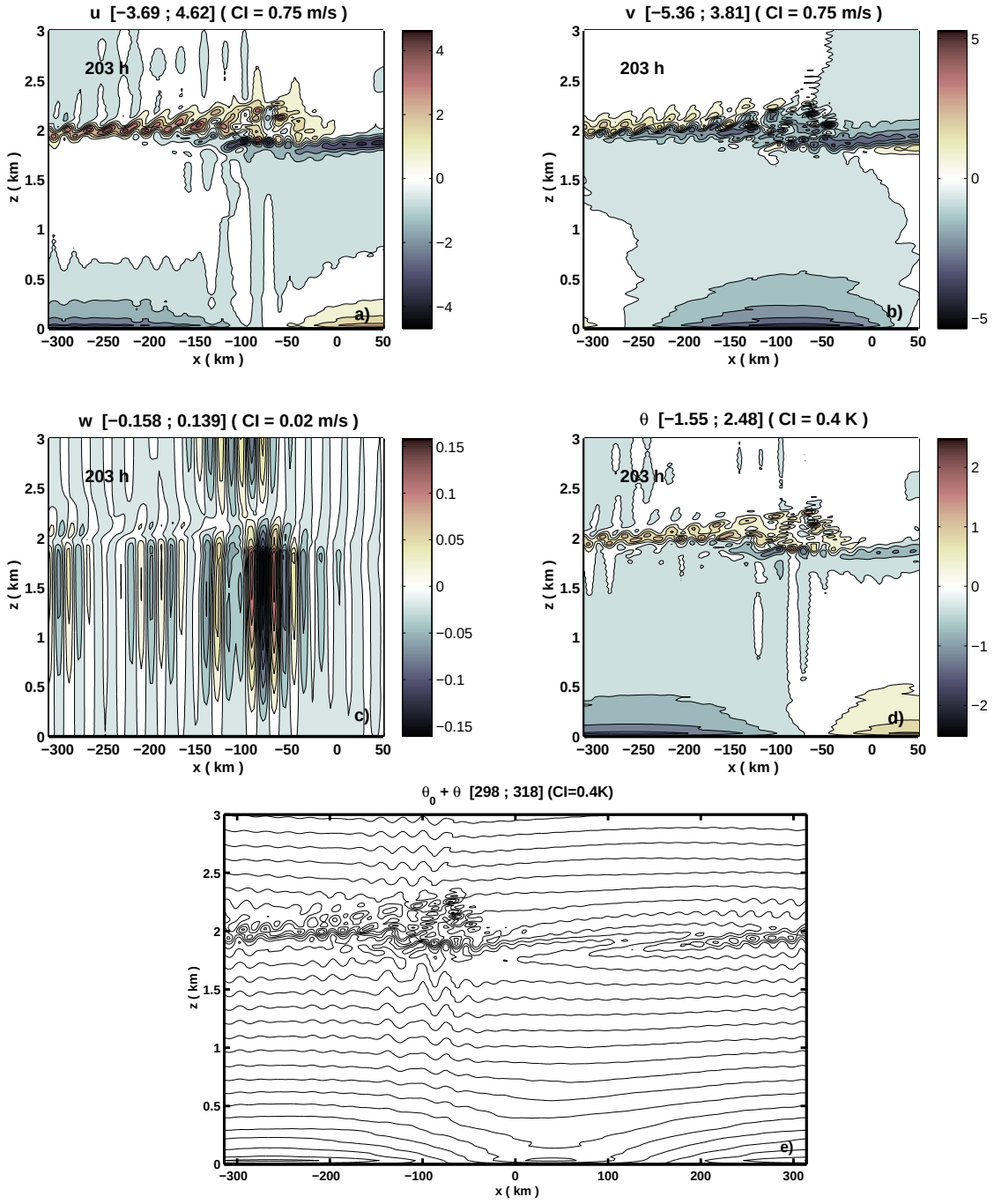

FIG. 3.20 – Velocity and potential temperature fields of the NG mode of experiment NL at t=203h. Total potential temperature in e).

Effect of the diffusivity

The experiment NL was repeated with increased values of the diffusivity. In the second stage the larger diffusivity offers a stronger dissipation of the small scale instabilities in the inertial layer. This tends to stabilize the latter, and increase its lifetime before the final breakdown. This also allows the large scale perturbation flow to reach slightly higher amplitudes in the inertial layer.

More generally, as the nonlinear evolution of a sheared layer is rather sensitive to the dissipation, we have repeated the experiment NL with different configurations. Actually, the behaviour in 3 stages described previously was first observed for a twice lower resolution (128 harmonics) and conventional laplacian diffusive terms. Increasing the viscosity μ, from 0.004 to $0.16\mathrm{m}^2.\mathrm{s}^{-1}$, did not change qualitatively the process. Thus, we found relevant to measure the saturation level with a diffusivity small enough to fairly reproduce the linear dynamics of the unstable mode, and notably the growth rate.

Moreover, the experiment NL was also repeated with different viscosity parameters (changing the power law and the cutoff wavenumber), and for different values of the Richardson number. We also tested another kind of diffusive parameterization, used by Fritts et al. (1994). In all these simulations, the behaviour was always found to be qualitatively the same as the one described above, except slight differences of the wavenumber and date at which the breaking instability begins.

3.6 Conclusion and discussion

In this chapter, we study the growth of the subsynoptic scale unstable NG modes of the 2D Eady problem, in the linear and nonlinear, anelastic, non hydrostatic, and viscous framework.

In the first part, we present the linear theoretical framework for subsynoptic scale Eady modes. The method is adapted from Tai (1983) to take into account the anelastic compressibility and non hydrostasy of the flow in the IGWs over-reflection process. In this linear approach, the existence of unstable modes is associated to the over-reflection criterium, relating assymptotically the growth rates to the amplitude of the jumps of the angular momentum / EP vertical flux at the critical levels. As shown by Tai (1983), the over-reflection of large scale IGWs is essentially related to the existence of a positive jump of angular momentum flux at the IL, to which we must add the smaller influence of a secondary jump at the CL. We find that the effect of anelastic compressibility is determined through the Richardson number, which is found to modulate the jump of angular momentum flux at the CL. For Ri=1, no difference appears with the inviscid Boussinesq model in which the CL is an apparent singularity, except very far above the singular levels where an essential singularity appears. For Ri$\neq$1, the CL increases or decreases the total absolute jump of angular momentum flux when respectively Ri>1 or Ri<1.

In the second part, an ensemble of linear numerical simulations is presented and analysed and systematically compared to the inviscid Boussinesq results of Plougonven et al. 2005. First, these linear results validate the model and its ability to resolve correctly the weakly unstable coupling between an IGW and an Eady edge wave through an IL. The instability is analyzed in terms of the interaction between a surface Eady wave and an inertial critical layer, as done previously by Nakamura (1988). Particularly, the vertical structure of the fields allows the unstable mode to extract some potential energy from the background flow in the evanescence layer, that is between the surface and the IL. Even if the mode also looses some kinetic energy in favor of the background flow, it receives a net gain of energy which is predominantly localized near the IL.

Second, the effect of the Richardson number expected from the previous analytical calculations is retrieved qualitatively in the EP flux profiles and in the growth rate sensitivity to Ri. For Ri=1, the anelastic growth rates converge towards the inviscid Boussinesq values for reasonably low heights of the upper boundary (z_{top} <20km), for which the essential singularity in $z \rightarrow \infty$ is negligeable (Fig. 3.10). For Ri$\neq$1, over-reflection can still occur, and the anelastic growth rates are larger than the Boussinesq ones if Ri>1, and smaller if Ri<1 (Fig. 3.8b). Noteworthy, we observe that our anelastic and viscous growth rates obtained for Ri>1 are significantly larger than the Boussinesq ones (PMS), even if they are rather small as regards to the typical geostrophic baroclinic growth rates. This might suggest that the Boussinesq framework under-estimates these unstable modes for Richardson numbers larger than 1.

In a third part, we present the nonlinear growth, saturation and breakdown of the most unstable NG mode (Ri=1), with a rather low diffusivity tuned consistently with the previous linear experiments. The mode is found to saturate at a level of magnitude physically measurable, but rather low compared to the case of large scale baroclinic waves. The horizontal and vertical wind reach about 2-3m.s^{-1} and 0.01m.s^{-1} respec-

tively. The essential saturation mechanism is found to result from the combination of two processes.
(i) First, in the inertial layer the flow is constituted of nearly horizontal elongated tongues overlying partly with each other, whose shear and stratification is of alternate sign : the positively stratified is positively sheared, and the negatively stratified is negatively sheared (Figs. 3.13-3.14). This highly overturned and sheared structure gives rise to a loss of energy of the large scales towards the short scales, through local Shear Instabilities (SI) mixed to the Convective Instabilities (CI) (Figs. 3.15-3.17). But the fact that the Richardson number falls under 0.25 in these areas is by no mean a sufficient condition for short scale instabilities to develop unboundedly. It is only a necessary condition for instabilities to exist. And the rate of large scale energy loss through these instabilities is actually modulated by the following second saturation process.
(ii) A natural positive feedback loop settles between the NG mode and the mean flow, localized essentially in the inertial critical layer, because the mean flow is increasingly distorted there (Fig. 3.18). It leads to the amplification of an inertial oscillation that destabilizes increasingly the inertial critical layer, leading finally to its abrupt global breakdown (Fig. 3.12). At this stage, the short scale instabilities are accompanied by the generation of intense gravity waves outside of the inertial critical layer, in agreement with earlier studies of critical layer breakdown (Sutherland et al. 1994, Scinocca and Ford, 2000). The intense background shear makes that these GWs have nearly horizontal phase velocity and vertical group velocities (Fig. 3.20).

We have restrained our study to 2D unstable modes, in order to increase the vertical resolution of the model and to resolve correctly the interaction at the IL. Concerning the linear results, it must be reminded that for such small Richardson numbers, the most unstable NG modes are non purely zonal and can have growth rates comparable to the geostrophic ones (Stone, 1970). Also, studying a 2D problem implies that the balanced background wind must be vertically sheared on the entire vertical domain (see appendix A), which is not realistic. This generates large scale IGWs with a horizontal phase velocity, whereas they usually have rather vertical phase velocities in the stratosphere. The same argument holds for the short GWs generated in the breakdown process.

As regards to the nonlinear saturation, the use of 2D dynamics can seem to be a strong limitation, since it was shown that the breaking of a sheared and overturned layer is intrinsically 3D. Particularly, it is likely that the lifetime of the inertial critical layer will be shorter in the presence of symmetric instabilities and transverse unstable modes, as well as the final breakdown might be more gentle. Nevertheless, even if the lifetime of our 2D NG modes is certainly unrealistic, the level of saturation measured here should be only slightly over-estimated. This experiment provides us with an upper bound for the magnitude of the unstable NG modes, which was never evaluated before to our knowledge. Notably, the fact that the level of saturation is physically measurable let us think that this unstable coupling between partly balanced Rossby waves and IGWs can be observed in the atmosphere, and hence constitutes a source of IGWs to consider. In that respect, we show in the following chapter that the PV deposit induced by short mountain GWs in the presence of critical levels, can force such weakly unstable modes in the large scale flow. In this situation, the force exerted by the mountain on the large scale flow can indirectly generate secondary IGWs.

Appendix

A. Model Equations

We choose the 2D rotating anelastic system in the f-plane, in which we divide the total flow $\tilde{\mathbf{u}}$ into (i) a linear background wind $\mathbf{U}(z) = U(z)\,\mathbf{e}_x + V_0\,\mathbf{e}_y$ where $U(z) = U_0 + \Lambda z$, and (ii) a perturbation $\mathbf{u}(x,z,t)$:

$$\tilde{\mathbf{u}} = \mathbf{U}(z) + \mathbf{u}(x,z,t) \text{ where } \mathbf{u} = (u,v,w). \tag{3.51}$$

The total potential temperature field can be defined as the sum of (i) a hydrostatic reference state profile $\theta_0(z)$, (ii) a background state $\Theta(y,z)$ in thermal wind balance with $\mathbf{U}(z)$, (iii) a local drift $\theta_d(y,z,t) = -V_0\,\Theta_y\,.\,t$ caused by advection by the meridional background wind V_0, and (iv) a perturbation $\theta(x,z,t)$ corresponding to the flow perturbation $\mathbf{u}(x,z,t)$:

$$\tilde{\theta} = \theta_0(z) + \Theta(y,z) + \theta_d(y,z,t) + \theta(x,z,t). \tag{3.52}$$

We use the approximation of Lipps and Hemler (1982) to write the pressure force with the use of a geopotential $\tilde{\phi}$ in the form $-\boldsymbol{\nabla}\tilde{\phi}$. This approximation allows the anelastic system to conserve total energy. As for $\tilde{\theta}$ we separate $\tilde{\phi}$ into the corresponding three parts :

$$\tilde{\phi} = \phi_0(z) + \Phi(y,z) + \phi(x,z,t). \tag{3.53}$$

The 2D incompressibility is written for the perturbation, considering a hydrostatic reference state density $\rho_0(z)$:

$$\nabla\cdot(\rho_0\mathbf{u}) = \partial_x(\rho_0 u) + \partial_z(\rho_0 w) = 0, \tag{3.54}$$

which allows to define a streamfunction $\psi(x,z,t)$ associated to (u,w) by

$$\rho_0(u\,\mathbf{e}_x + w\,\mathbf{e}_z) = \mathbf{e}_y \times \nabla\psi \text{ , that is } u = \frac{1}{\rho_0}\frac{\partial\psi}{\partial z} \text{ and } w = -\frac{1}{\rho_0}\frac{\partial\psi}{\partial x}. \tag{3.55}$$

The hydrostatic reference state $(\theta_0(z), \phi_0(z), \rho_0(z))$ is determined by imposing a constant Brunt-Vaisalla frequency N, where $N^2 = -\frac{g}{\theta_0(z)}\frac{d\theta_0}{dz}$, which is equivalent to consider an isothermal atmosphere at rest[8].
The background wind is required to be geostrophic, $f\mathbf{e}_z \wedge \mathbf{U} + \nabla\Phi = 0$, therefore the background thermal-wind balance can be integrated into :

$$\Theta(y,z) = -\frac{f\theta_0(z)\Lambda}{g}\,.y \tag{3.56}$$

In Eq. (4.33), g and f are respectively the gravity constant and Coriolis parameter. In this framework, the momentum equation and the thermodynamic equation that govern the evolution of the perturbation can be written respectively in the following way[9], separating the linear (left hand) and nonlinear (right hand) terms :

$$(\partial_t + U\partial_x)\mathbf{u} + \Lambda w\mathbf{e}_x + f\mathbf{e}_z \times \mathbf{u} + \nabla\phi - g\frac{\theta}{\theta_0}\mathbf{e}_z = -(\mathbf{u}\nabla)\mathbf{u} + \frac{1}{\rho_0}\nabla(\mu\nabla\mathbf{u}) \tag{3.57}$$

$$(\partial_t + U\partial_x)\theta + v\,\Theta_y + w\,\theta_{0z} = -(\mathbf{u}\nabla)\theta + \frac{1}{\rho_0}\nabla(\kappa\nabla\theta) \tag{3.58}$$

[8] Actually, under this strong approximation, the anelastic system is equivalent to the non hydrostatic primitive equations system in log-pressure coordinates.

[9] Anywhere in the paper, subscripts $_x$, $_y$ and $_z$ denote the corresponding spatial derivative.

In Eq. (4.35) we have neglected the term $w\Theta_z$ as regards to $w\theta_{0z}$ in order not to break the two-dimensionality of the system. Indeed, this way there is no dependence on y in Eqs. (4.34)-(4.35), whereas $\Theta_z = -\frac{f}{g}\frac{d\theta_0(z)}{dz}\Lambda.y$ introduces a small dependence in y. This approximation is valid if $\theta_{0z} \gg |\Theta_z|$, that is if $y \ll \frac{g}{f\Lambda} \sim 10000$km taking $f \sim 10^{-4}$ s^{-1} and $\Lambda \sim 10^{-2}$ s^{-1}, which is largely verified for any kind of 2D mountain on Earth. Note that this approximation can be avoided by choosing a shear that satisfies $\theta_0(z).\Lambda(z) =$ constant, which differs only by 10% from the constant shear for a domain 20km high. We did not do that choice in order to compare strictly to the other studies of constant shear unstable NG modes.

Note also that in Eq. (4.35), θ_d does not appear by definition. Indeed, this term only represent a horizontally uniform potential temperature advection, which essentially modifies the stratification. Therefore, it is possible to neglect this modification within a time satisfying the approximate condition $t \ll t_d = \frac{\theta_{0z}}{V_0\Theta_{yz}} = \frac{g}{fV_0\Lambda} \sim 280$ hours taking $V_0 \sim 10$ms^{-1}. The advantage of this formulation is that we can state that within a time $t < t_d$, the evolution of the flow perturbation will be qualitatively the same for any kind of veering background wind with uniform shear as for the unidirectionnal case $V_0 = 0$, which is not very realistic.

Finally, the upper and lower boundary conditions imposed are free slip and rigid.

B. Energy budget

The energy budget associated to this model is obtained from the combination $\rho_0(z)(\mathbf{u}*$ (4.34) $+\frac{g^2}{\theta_0^2(z)N^2}\theta*$ (4.35)) and using the continuity Eq. (4.31), to form what can be seen as the the local perturbation energy[10]

$$e = \frac{\rho_0}{2}\left(u^2 + v^2 + w^2 + \frac{g^2}{\theta_0^2 N^2}\,\theta^2\right). \tag{3.59}$$

After integrating over the entire domain and removing the vanishing terms because of periodicity and vanishing vertical velocity at the boundaries, it remains a tendency budget of the form :

$$\begin{aligned}\frac{\mathrm{d}}{\mathrm{d}t}\int_0^{Z_T}\!\!\int_{-L}^{L} e\,\mathrm{d}z\mathrm{d}x \;=\; &\int_0^{Z_T}\!\!\int_{-L}^{L}\rho_0\left[\frac{\Lambda f}{\theta_{0z}}\,v\theta - \Lambda\,uw - \mathbf{u}(\mathbf{u}\nabla)\mathbf{u} - \frac{g^2}{\theta_0^2N^2}\,\theta(\mathbf{u}\nabla)\theta\right. \\ &\left.+\frac{1}{\rho_0}\,\mathbf{u}\nabla(\mu\nabla\mathbf{u}) + \frac{g^2}{\rho_0\theta_0^2N^2}\,\theta\nabla(\kappa\nabla\theta) + \mathbf{u}.\boldsymbol{\mathcal{F}} + \frac{g^2}{\theta_0^2N^2}\,\theta\dot{\mathrm{H}}\right]\mathrm{d}z\mathrm{d}x\end{aligned} \tag{3.60}$$

Note that the divergence of the vertical flux of energy $\boldsymbol{\nabla}\phi\mathbf{u}$ does not enter into account in this global budget. Considering the total perturbation energy makes also disappear the vertical buoyancy flux $\rho_0\frac{g}{\theta_{0z}}\,\theta w$, which represents the exchange between potential energy and kinetic energy.

C. Transformed Eulerian Mean equations and Eliassen-Palm flux

To study the forcing of the large scales by the small scale waves, it is generally more adapted to use a transformed Eulerian Mean (TEM) of the equations of the large scale

[10] More precisely, this quadratic quantity is a usefull norm that represents the leading order approximation of the perturbation pseudoenergy relative to the background state (Scinocca and Shepherd, 1992). For very large perturbations, this cannot be strictly taken as the energy of the perturbation.

flow (Andrews and McIntyre, 1976). By applying a zonal mean operator ($\bar{x}$) to the Eqs. (4.34)-(4.35), and introducing the continuity Eq. (4.31), we get the large scale flow equations. Then, we introduce the residual mean circulation for this 2D problem

$$(v^*; w^*) = \left(\overline{v} - \frac{1}{\rho_0} \partial_z \left(\rho_0 \, \overline{v\theta} / \theta_{0z} \right) ; \overline{w} \right), \tag{3.61}$$

and obtain the TEM momentum equations

$$\partial_t \, \overline{u} - f \, \overline{v^*} = -\frac{1}{\rho_0} \partial_z \left(\rho_0 \, \overline{uw} - \rho_0 \, \frac{f \, \overline{v\theta}}{\theta_{0z}} \right) + \frac{1}{\rho_0} \partial_z \mu \partial_z \overline{u} \tag{3.62}$$

$$\partial_t \, \overline{v^*} + f \, \overline{u} = -\frac{1}{\rho_0} \partial_z \left(\rho_0 \, \overline{vw} + \partial_t \left(\rho_0 \, \frac{\overline{v\theta}}{\theta_{0z}} \right) \right) + \frac{1}{\rho_0} \partial_z \mu \partial_z \overline{v} \tag{3.63}$$

$$\partial_t \, \overline{\theta} + \overline{v^*} \, \Theta_y = -\frac{1}{\rho_0} \partial_z \left(\rho_0 \, \overline{\theta w} + \Theta_y \, \rho_0 \, \frac{\overline{v\theta}}{\theta_{0z}} \right) + \frac{1}{\rho_0} \partial_z \kappa \partial_z \overline{\theta} \, . \tag{3.64}$$

Note that usually, only the departures x' from the zonal mean flow variables $\bar{x}$ are used in the right hand quadratic terms of Eqs.(4.39)-(4.42), because the contribution of the mean is negligeable. But we prefer this formulation here because the vertical Eliassen-Palm (EP) flux

$$F^z = \rho_0 \left[\frac{f}{\theta_{0z}} \, \overline{v\theta} - \overline{uw} \right] \tag{3.65}$$

appears directly in the perturbation energy budget. Indeed, the first two terms in the right hand of Eq. (4.38) are exactly proportional to the vertical integral of F^z because the shear is constant. Therefore, in our context F^z represents not only the EP flux, the vertical divergence of whom is the zonal force exerted by the waves on the zonal mean flow, but also the vertical distribution of the lowest order non diffusive energy tendency terms, which describe respectively the exchange of potential ($\overline{v\theta}$) and kinetic ($\overline{uw}$) energy with the background flow. Indeed, the divergence of the vertical energy flux $\boldsymbol{\nabla} \phi \mathbf{u}$ does not enter into account in the global energy budget after integration, and only describes locally an internal vertical redistribution of the perturbation energy inside of itself. Hence it does not inform us about the place where the energy is exchanged with the background flow, even if it is usefull for a discussion in terms of over-reflection.

Finally, the EP flux F^z can also be used as an action flux. But we do not use the wave action budget in this study, because in our context the action cannot be defined as a one-signed quantity (Andrews, 1987), which limits the potential benefits in terms of wave generation interpretation. Another reason for not using it is given in section 3.4.1.

D. Numerical computation

The problem is considered to be horizontally periodic, on a domain of size $2\pi \times L$ where L =100km. The numerical scheme is spectral on the horizontal, with 64 harmonics in the linear case. On the vertical, we use a second order finite difference scheme. A typical configuration is a domain height of 20km, with a resolution of Δz =10m, which corresponds to 2000 levels. The lower and upper boundary conditions are free slip.

The dynamical core of the model consists in computing and adding the tendencies of the horizontal vorticity R, of the meridional velocity v and of the potential temperature

θ, through a leap-frog temporal scheme with Asselin filter. The tendencies are separated between linear and nonlinear contributions, which allows to switch off the nonlinear terms. At each time step, the streamfunction ψ is computed by inverting the vorticity R. The zonal and vertical velocities u and w are computed from ψ only at each storage, and also to compute the energy budget by trapezoïdal integrals. The model solution converges for a time step of 10s for the linear growth, or 5s for the nonlinear growth, that is about one hundredth of the buyancy period.

The diffusive terms are computed implicitely in the vertical, by inversion of a laplacian by gaussian elimination, and explicitly in the horizontal. The diffusivities μ and κ are constant in linear simulations, and can vary with the wave number in nonlinear simulations (see secttion 3.5). The Prandtl number is always set to 1.

References

Andrews, D. G. and McIntyre, M. E., 1976 : Planetary waves in horizontal and vertical shear : The generalized Eliassen-Palm relation and the mean zonal acceleration. *J. Atmos. Sci.*, **33**, 2031–2048.

Andrews, D. G., 1987 : On the interpretation of the Eliassen-Palm flux divergence. *Quart. J. Roy. Meteor. Soc.*, **113**, 323–338.

Bender, C. M. and Orszag, S. A., 1978 : *Advanced mathematical methods for scientists and engineers.* International series in pure and applied mathematics, McGraw-Hill, 593 pp.

Bretherton, F. P., 1966 : Baroclinic instability and the short wave cut-off in terms of potential vorticity. *Quart. J. Roy. Meteor. Soc.*, **92**, 335–345.

Booker, J. R., and F. P. Bretherton, 1967 : The critical layer for internal gravity waves in a shear flow. *J. Fluid Mech.*, **27(3)**, 513–539.

Bühler, O., McIntyre, M. E. and Scinocca, J. F., 1999 : On shear-generated gravity waves that reach the Mesosphere. Part I : Wave generation. *J. Atmos. Sci.*, **56**, 3749–3763.

Charney, J. G., 1947 : The dynamics of long waves in a baroclinic westerly current. *J. Meteor.*, **4**, 135–162.

Fritts, D. C. and Alexander, J., 2003 : Gravity wave dynamics and effects in the middle atmosphere. *Rev. Geoph.*, **41(1)**, 1003.

Fritts, D. C., Isler, J. R., and Andreassen, O., 1994 : Gravity wave breaking in two and three dimensions 2. Three-dimensional evolution and instability structure. *J. of Geoph. Res.*, **99(D4)**, 8109–8123.

Fritts, D. C., Garten, J. F., and Andreassen, Ø., 1996 : Wave breaking and transition to turbulence in stratified shear flows. *J. Atmos. Sci.*, **53(8)**, 1057–1085.

Fritts, D. C., Palmer, T. L., Andreassen, Ø. and Lie, I., 1996 : Evolution and breakdown of Kelvin-Helmholtz billows in stratified compressible flows. Part I : Comparison of two and three-dimensional flows. *J. Atmos. Sci.*, **53(22)**, 3173–3191.

Hazel, P., 1967 : The effect of viscosity and heat conduction on internal gravity waves at a critical level. *J. Atmos. Sci.*, **30**, 775–783.

Harnik, N. and Heifetz, E., 2007 : Relating overreflection and wave geometry to the counterpropagating Rossby wave perspective : toward a deeper mechanistic understanding of shear instability. *J. Atmos. Sci.*, **64**, 2238–2261.

Harnik, N., Heifetz, E., Umurhann, O. M. and Lott, F., 2008 : A buoyancy-vorticity wave interaction approach to stratified shear flow. *submitted to J. Atmos. Sci.*

Hoskins, B. J., 1975 : The geostrophic momentum approximation and the semi-geostrophic equations. *J. Atmos. Sci.*, **32(2)**, 233–242.

Jones, W. L., 1967 : Propagation of internal gravity waves in fluids with shear flow ond rotation. *J. Fluid Mech.*, **30**, 439–448.

Kim, Y.-J., Eckermann, S. D. and Chun, H.-Y., 2003 : An overview of the past, present and future of gravity-wave drag parametrization for numerical climate and weather prediction models. *Atm.-Oc.*, **41(1)**, 65–98.

Lelong, M.-P. and Dunkerton, T. J., 1998a : Inertia-gravity wave breaking in three dimensions. Part I : convectively stable waves. *J. Atmos. Sci.*, **55(15)**, 2473–2488.

Lelong, M.-P. and Dunkerton, T. J., 1998b : Inertia-gravity wave breaking in three dimensions. Part II : convectively unstable waves. *J. Atmos. Sci.*, **55(15)**, 2489–2501.

Lindzen, R., and Rosenthal, A., 1976 : On the instability of Helmholtz velocity profiles in stably stratified fluids when a lower boundary is present. *J. Geoph. Res.*, **81**, 1561–1571.

Lindzen, R., and Tung, K-K., 1978 : Wave overreflection and shear instability. *J. Atmos. Sci.*, **35**, 1626–1632.

Lindzen, R., B. Farrell and K.-K. Tung, 1980 : The concept of overreflection and its application to baroclinic instability. *J. Atmos. Sci.*, **37**, 44–63.

Lott, F. and Teitelbaum, H., 1992 : Nonlinear dissipative critical level interaction in a stratified shear flow : Instabilities and gravity waves. *Geophys. Astrophys. Fluid Dynamics*, **66**, 133–167.

Lott, F., 2003 Large scale flow response to short gravity waves breaking in a rotating shear flow. *J. Atmos. Sci.*, **60**, 1691–1704.

McLandress, C. M. and Scinocca, J. F., 2005 : The GCM response to current parameterizations of nonorographic gravity wave drag. *J. Atmos. Sci.*, **62**, 2394–2413.

Nakamura, N., 1988 : Scale selection of baroclinic instability - Effects of stratification and nongeostrophy. *J. Atmos. Sci.*, **45(21)**, 3253–3267.

Nakamura, N. and Held, I. M., 1989 : Nonlinear equilibration of two-dimensional Eady waves. *J. Atmos. Sci.*, **46(19)**, 3055–3064.

Olver, F. W., 1974 : *Asymptotic and special functions.* Computer science and applied mathematics, Academic Press, 574pp.

Plougonven, R., D. J., Muraki and C. Snyder, 2005 : A baroclinic instability that couples balanced motions and gravity waves. *J. Atmos. Sci.*, **62**, 1545–1559.

Plougonven, R. and Snyder, C., 2007 : Inertia-gravity waves spontanously generated by jets and fronts. Part I : Different baroclinic life cycles. *J. Atmos. Sci.*, **64**, 2502–2520.

Rosenthal, A. J. and Lindzen, R., 1983 : Instabilities in a stratified fluid having one critical level. Part II : Explaination of gravity wave instabilities using the concept of over-reflection. *J. Atmos. Sci.*, **40**, 521–529.

Scinocca, J. F. and Shepherd, T. G., 1992 : Nonlinear wave-activity conservation laws and hamiltonian structure for the two-dimensional anelastic equations. *J. Atmos. Sci.*, **49**, 5–27.

Scinocca, J. F. and Ford, R., 2000 : The nonlinear forcing of large-scale internal gravity waves by stratified shear instability. *J. Atmos. Sci.*, **57**, 653–672.

Shutts, G. J., 2001 : A linear model of back-sheared flow over an isolated hill in the presence of rotation. *J. Atmos. Sci.*, **58**, 3293–3310.

Stone, P. H., 1970 : On non-geostrophic baroclinic stability : Part II. *J. Atmos. Sci.*, **27**, 721–726.

Sutherland, B. R., Caulfield C. P. and Peltier, W. R., 1994 : Internal gravity wave generation and hydrodynamic instability. *J. Atmos. Sci.*, **51**, 3261–3280.

Tai, C.-K., 1983 : Over-reflection and instability. *Dyn. Atm. Oc.*, **7**, 147–165.

Teitelbaum, H., H. Kelder and C. A. Van Duin, 1987 : Propagation of internal gravity waves in a rotating fluid with shear flow. *J. Atm. Terr. Phys.*, **49(5)**, 413–420.

Tokioka, T., 1970 : Non-geostrophic and non-hydrostatic stability of a baroclinic fluid. *J. Meteor. Soc. Japan*, **48**, 503–520.

Umurhan, O. M., E. Heifetz, N. Harnick and F. Lott, 2008 : The instability of counter-propagating kernel gravity waves in a constant shear flow. *submitted to Physics of Fluids*.

Vadas, S. L., D. C. Fritts, and M. J. Alexander, 2003 : Mechanism for the generation of secondary waves in wave breaking regions. *J. Atmos. Sci.*, **60**, 194–214.

Winters, K. B. and D'Asaro, E. A., 1989 : Two-dimensional instability of finite amplitude internal gravity wave packets near a critical level. *J. Geoph. Res.*, **94(C9)**, 12709–12719.

Winters, K. B. and Riley, J. J., 1992 : Instability of internal waves near a critical level. *Dyn. Atm. Oc.*, **16**, 249–278.

Winters, K. B. and D'Asaro, E. A., 1994 : Three-dimensional wave instability near a critical level. *J. Fluid. Mech.*, **272**, 255–284.

Wurtele, M. G., Datta, A. and Sharman, R. D., 1996 : The propagation of gravity-inertia waves and lee waves under a critical level. *J. Atmos. Sci.*, **53(11)**, 1505–1523.

Yamanaka, M. D. and Tanaka, H., 1984 : Propagation and breakdown of internal inertia-gravity waves near critical levels in the middle atmosphere. *J. Meteor. Soc. Japan*, **62**, 1–17.

Yamazaki, Y. H. and Peltier, W. R., 2001 : Baroclinic instability in an Euler equations-based column model : The coexistence of a deep synoptic-scale mode and shallow subsynoptic-scale modes. *J. Atmos. Sci.*, **58**, 780–792.

Chapitre 4

Secondary generation of non-geostrophic unstable modes and inertia-gravity waves by breaking mountain gravity waves

Résumé

Dans ce chapitre, nous étudions à l'aide du même modèle 2D que dans le chapitre précédent, la réponse d'une atmosphère barocline de type Eady à la force exercée par les ondes de gravité de montagne courtes lorsqu'elles déferlent à un niveau critique. Comme précédemment, on s'intéresse à l'effet d'un relief isolé, dont l'échelle horizontale globale est maintenant de taille *s*ous-synoptique. On impose donc une force localisée dans l'espace et le temps. Cette force est d'abord paramétrisée, ce qui permet d'étudier extensivement la réponse de l'atmosphère dans différentes configurations avec une résolution horizontale relativement limitée. Puis la force est résolue directement par le modèle en imposant une orographie idéalisée, ce qui permet de vérifier la pertinence de la précédente paramétrisation, ainsi que son domaine de validité. Dans chaque cas, on étudie le/les mécanisme(s) de saturation non linéaire du forçage.

Naturellement, la réponse observée est polychromatique, mélangeant des échelles relativement longues à des échelles courtes comparables à celle du forçage. La force produit un dipole de vorticité potentielle, qui se déforme progessivement par advection différentielle dans l'écoulement de base cisaillé. Aux échelles longues, la réponse prend la forme de modes de Eady instables non géostrophiques ressemblant à ceux observés dans le chapitre précédent. Cette composante est favorisée par un forçage proche de la surface, l'interaction entre le dipole de vorticité potentielle et l'onde de surface étant le moteur de l'amplification. Aux échelles courtes, le signal est dominé par des trains d'ondes d'inertie-gravité qui se propagent vers le haut et le bas du dipole de vorticité potentielle, et lui sont directement connectés. Leur origine est diagnostiquée comme une génération spontannée par la partie équilibrée de l'écoulement directement associée au dipole de vorticité potentielle, qui de ce fait devient une source mobile d'ondes d'inertie-gravité.

Pour une force peu intense, la réponse est linéaire, et l'onde de Eady de surface domine sous la vorticité potentielle si celle ci est assez basse, alors que les ondes d'inertie-gravité dominent au dessus. En particulier, le mécanisme équilibré de production de l'onde de surface est naturellement cyclolytique, bien que la partie non équilibrée de l'écoulement en réduise l'amplitude. Pour une force intense, la zone forcée se déstabilise et émet alors des ondes d'inertie-gravité supplémentaires encore plus courtes, qui compliquent notamment la réponse au sol. Dans le cas d'un forçage orographique idéalisé, les réflexions non linéaires au niveau critique font saturer la force pour des montagnes trop hautes.

4.1 Introduction

The fact that mountains influence meteorology and climate is well known. In particular, the lee cyclogenesis accounts for the ability of mountains to modify and constrain cyclogenesis, and even to trigger it. This question has given rise to a number of theories, mixing the dynamics of fronts and baroclinic instability (e.g. Smith 1984, Pierrehumbert 1985, Speranza et al. 1985, Schär 1990). Thanks to the advance of numerical simulations and observations, the access to mesoscale dynamics has progressively become possible. In this context, the dynamics of Potential Vorticity (PV) (Haynes et McIntyre 1987) has emerged as a kee concept to understand lee cyclogenesis, by considering the orographic generation of PV anomalies (Schär and Smith 1993, Schär and Durran 1997, Aebischer and Schär 1998). For example, short mountain Gravity Waves (GWs) can be absorpted and break near critical levels (Booker and Bretherton, 1967), as illustrated in Fig. 4.1. By this process they can yield the momentum they transport to the large scale flow, and the resulting localized force induces PV anomalies. Note that in the absence of critical levels, mountain GWs can also deposit momentum if they have a strong amplitude, by overturning and breaking. Other orographic process can generate a non advective PV flux locally. In this respect, the combination of observational data from the MAP campaign (Mesoscale Alpine Program, Bougeault et al. 2001) with meso-scale numerical simulations have considerably improved our knowledge of the fine scale PV field in mountain wakes (Schär et al. 2003, Flammant et al. 2004).

This recent advance provides us now with new theoretical questions, concerning the effects of the meso-scale dynamics onto the synoptic and subsynopticscale dynamics, while there is still a need to improve the parameterization of subgrig-scale orography in the General Circulation and Numerical Weather Prediction Models. In this context, Martin and Lott (2007) have studied theoretically, in the linear semi-geostrophic framework, the large scale effects of the subgrid scale orography of isolated mountains in the presence of directional critical levels (Shutts, 1995). Indeed, these effects rely on a non evident 3D dynamical process involving the PV. This mechanism is still poorly represented in the current GW drag parameterization schemes, in spite of the recent advance (Lott and Miller 97, Gregory et al. 1998, Scinocca and McFarlane 2000). Thus, Martin and Lott (2007) have shown that the PV dipole, generated by the mountain GWs within a directional wind shear, influences lee cyclogenesis by forcing Eady edge waves at the surface and the tropopause. The effect was found to be significant though rather weak, and qualitatively predictible by a simple geometrical law of thumbs. In particular, it was found to be cyclolytic in the cold front cases. The aim of the present study is to extend this analysis, by computing the complete subsynoptic scale response to a mountain GWs' force localized in space and time.

In our context, the focus on PV is not usefull only to study the balanced part of the flow. It can also be a starting point to analyse the coupling mechanisms between the balanced and unbalanced flow components. And the unbalanced one is important for two reasons : (i) it enters into account in lee cyclogenesis at subsynoptic scales, and (ii) it contains Inertia-Gravity Waves (IGWs).

GWs and IGWs are relatively ubiquitous in the atmosphere. They influence the large scale circulation, and their effect is very significant in the middle atmosphere (Fritts and Alexander, 2003). Nevertheless, their parameterization in the General Circulation Models is today limited by our lack of knowledge about their sources (Kim et

al 2003, McLandress and Scinocca 2005). Notably, the mechanisms that link balanced flow to IGWs are still poorly understood (see for example Plougonven and Snyder 2007, and ref therein).

The idea that a body force applied to the flow can generate IGWs is not new. By a linear process, that we will call here *radiation*, a body force localized in time and space will generate perturbations in the flow, which will propagate by the oscillatory mechanism which is dominant at the scales induced by the force. Thus, in our context the force will radiate IGWs if the horizontal and temporal scales are such that the Rossby number is near 1 or larger. This mechanism was already described as a *secondary generation of IGWs* by the short mountain GWs breaking (Scavuzzo et al. 1998, Lott 2003, Vadas et al 2003). Actually, other mechanisms of secondary generation of GWs or IGWs have been proposed, that do not require the presence of a force, but which also rely on the nonlinear saturation and breaking of pre-existing GWs or IGWs (e.g. Satomura and Sato, 1999). More precisely, all of them rely on the existence of instabilities in a strongly sheared and overturned or mixed layer, that will result in the secondary generation of GWs or IGWs because of the linear (e.g. Sutherland et al. 1994) or nonlinear (Scinocca and Ford, 2000) growth of local unstable normal modes, or because of the global mixed-layer collapse (Bhüler et al., 1999). These mechanisms account for the generation of waves at different scales, which can be gathered under the general category of *shear generated GWs or IGWs*.

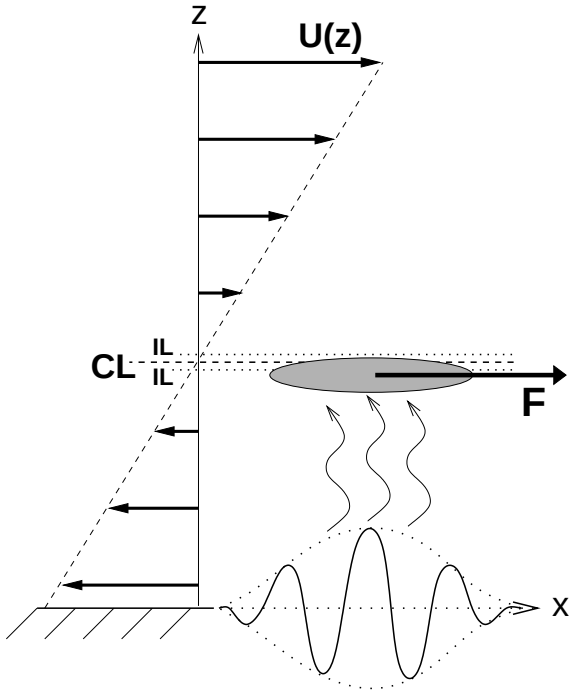

FIG. 4.1 – Schematic view of the problem. The background wind $\mathbf{U}(z)$, linearly sheared, is submitted to the short scale orographic variance of an isolated mountain. The short mountain gravity-waves have their inertial critical levels (IL) very close to their critical level (CL). They are absorpted in the critical layer and exert a force $\boldsymbol{\mathcal{F}}$ on the large-scale flow, which is localized slightly under the critical level.

In the present study, the force applied upon the background wind within limited time and area will obligatory generate IGWs by radiation. If the force varies slowly enough, these IGWs will behave as *inertial oscillations*, which stay embeded in the vi-

cinity of the force. Nevertheless, to explain completely the following linear responses, we need to introduce two new mechanisms of IGWs secondary generation. These are intrinsically different in that they are not directly linked to the force, but more specifically to the existence of a dipolar PV anomaly.

Namely, the first of these mechanisms is the forcing of the *unstable non-geostrophic normal Eady modes* of the subsynoptic scale Eady problem. These modes are the result of a coupling, near a critical level, between a partially balanced surface Eady wave and an IGW of the same wavelength (Plougonven et al, 2005). They were studied in the previous chapter. In that respect, Shutts (2001, 2003) has already shown, by means of linear analytical calculations, that a single mesoscale mountain ridge is able to force flow responses coupling Eady edge wave trains to IGW trains in the presence of a back-sheared or directionally sheared flows. Note that previously, Wurtele et al. (1996, 1999, 2000) and Shen and Lin (1999) had also identified similar responses for the back-sheared flow, using 2D numerical simulations forced by a sinusoidal surface or by an isolated mesoscale mountain. Our present analysis, based on the PV diagnosis, may help to further understand these responses in the subsynoptic scale context.

The second of these mechanisms is the *spontaneous generation of IGWs* by the balanced flow associated to the dipolar PV anomaly. Indeed, in certain situations the balanced flow can spontaneously generate IGWs, because short lagrangian time-scales arise locally in the flow. For example, this can happen because of the background shear flow (Vanneste and Yavneh 2004, Olafsdóttir et al. 2008), like in jets and fronts baroclinic life-cycles (Plougonven and Snyder 2007, and ref therein). To diagnose this situation in general, Plougonven and Zhang (2007) have recently proposed a calculation of the forcing of IGWs by the balanced flow. More particularly, spontaneous IGWs generation was described recently by Snyder et al. (2007) in the evolution of a dipole of couner-rotating balanced surface vortices. In our case, the dipole of vortices created by the force is in the midtroposphere, in the vertical plane, and not totally balanced. But we will show that it can also generate IGWs by an analogous mechanism. Note that this mechanism must be distinguished from another process of spontaneous IGWs generation by balanced vortices, which is refered to as analogous to Lighthill's radiation of sound waves (Ford et al. 2000, Plougonven and Zeitlin 2002). In this last process the IGWs wavelength is larger than the scale of the balanced vortex, which is not the case here.

Thus, in the following simulations, we will measure the relative importance of the three mechanisms of IGWs secondary generation described previously : (i) radiation, (ii) subsynoptic scale non geostrophic baroclinic instability, and (iii) spontaneous generation by the PV dipole. We will essentially concentrate on the last two ones, which have been less studied. In particular, (ii) and (iii) are actually closely related as they both rely directly on the PV anomaly. But we can distinguish them by the domain of horizontal scales they affect. As the forcing induces a continuous spectrum of wavelengths, both parts of the signal will be present in the total response, with a partition depending on the experimental conditions. Finally, note that in the context of nonlinear regimes, the response will be even more complicated, by the rise of smaller scale shear generated IGWs.

To interpret correctly the following numerical simulations, it is usefull to recall some results obtained in the previous chapter, concerning the subsynoptic non-geostrophic unstable Eady modes. Indeed, they were studied within the same theoretical and nu-

merical framework as here, that is the nonhydrostatic, anelastic 2D Eady model. These modes are made of an Eady edge wave and an IGW coupled near an inertial critical level, where an irreversible meridional heat flux extracts some potential energy from the background flow to the perturbation. Therefore, the growth rate of this instability is very sensitive to the dynamics of the flow near the inertial critical level, which depends notably on the effective turbulent diffusivities (viscous and thermal) and on the vertical resolution of the numerical simulation. Accordingly, the accurate simulation of the structures and growth rates required a high vertical resolution and a low diffusivity constant. By concern of consistency with these results and those concerning the nonlinear saturation, we will take care that the present numerical experimental conditions are close to those used previously, notably by using rather low diffusivities and a high vertical resolution.

For this last reason, we restrain to 2D simulations to reduce the numerical cost. In that respect, the fact that we will always assume a linearly backsheared background flow that vanishes in the mid-troposphere,

$$\mathbf{U}(z) = (U_0 + \Lambda\, z)\, \mathbf{e}_x = U(z)\, \mathbf{e}_x \ \text{, with } \ \Lambda\, U_0 < 0\,, \tag{4.1}$$

is not a strong restriction actually. Indeed, it is shown in the appendix A that if the orography can reasonably be considered 2D as regards to the scales considered, then the inclusion of a constant meridional background wind to the Eq. (4.1) will give a directional wind, but will change almost nothing to the physics of the problem. By contrast, in the case of a 3D mountain, the presence of a directional wind shear induces a thicker and smoother vertical distribution of the momentum deposit than for a 2D wind (Shutts 1995).

The outline of the chapter is as follows. In order to increase progressively the complexity of the problem, in section 2 we begin , by analysing the linear response of the background shear flow to a parameterized body force. This force mimics the action of short scale mountain GWs breaking at their critical level in the mid-troposphere, where the background flow vanishes. Then, the sensitivity of the response to the magnitude of the force, and to the height of the force is analysed. In section 3, we present the large scale response to an idealized orographic profile which represents the short scale orographic variance of an isolated mountain range. The mesoscale ridges of this mountain generate short scale GWs that break at their critical level, which is directly resolved by the model. The results are compared with the previous parameterized simulations of section 2. The sensitivity of the response to the height of the mountain is then presented. Finally, in section 4 we summarize and discuss the significance of our results in the context of IGWs secondary generation, and lee cyclogenesis. The details of the equations and the numerical model used are described in the appendices.

4.2 Response to a parameterized force

In this section, the background wind is submitted to a parameterized force designed to mimick the momentum deposit from short mountain GWs breaking at their critical level. The stationary mountain GWs propagating in the wind of Eq. (4.1) will reach their critical level at z^*, where the wind vanishes ($U(z^*) = 0$), and will be absorpted there. Anticipating the numerical results presented in section 4.3, we assume that the absorption induces a zonal force whose maximum is localized slightly under z^*, at a distance δz, and which is idealized by a gaussian profile of horizontal width L and vertical depth d (see the Fig. 4.1) :

$$\boldsymbol{\mathcal{F}}(x,z,t) = s(t)\, F_0\, e^{\{-2\frac{x^2}{L^2} - \frac{(z-z^*+\delta z)^2}{d^2}\}}\, \mathbf{e}_x. \tag{4.2}$$

This definition of L in the horizontal profile of the force is consistent with a gaussian orographic profile as defined in section 4.3 in Eq. (4.20). The force $\boldsymbol{\mathcal{F}}$ is modulated by a function of time $s(t)$, which allows to raise the force smoothly and also to cut it smoothly after a while if needed :

$$s(t) = \begin{cases} \frac{1}{2}\,(1-\cos(\pi\frac{t}{\tau_1})) & \text{, if} \quad 0 \le t < \tau_1 \\ 1 & \text{, if} \quad \tau_1 \le t < \tau_1 + T \\ \frac{1}{2}\,(1+\cos(\pi\frac{t-\tau_1-T}{\tau_2})) & \text{, if} \quad \tau_1 + T \le t < \tau_1 + T + \tau_2 \\ 0 & \text{, if} \quad t \ge \tau_1 + T + \tau_2. \end{cases} \tag{4.3}$$

Raising the force smoothly, within a time longer than half the inertial period, allows to minimize the generation inertial oscillations by radiation. But these oscillations will be present nevertheless, because the finite CPU time prevents us from using a very long spin-up time τ_1. Making the force vanish smoothly after a time T will allow us to study the influence of the PV anomaly alone, that is without any remaining body force, after the time t=τ_1+T+τ_2. Nevertheless, simulations with constant forcing after τ_1 will also be presented in the non parameterized problem of section 3, in relation with previous works by Lott (2003).

In the following, we start in section 4.2.1 by studying the response to a weak force localized in the mid-troposphere (experiment P1). As the force is weak, the response of the atmosphere will be essentially linear. And as the height of the force is rather close to the surface, it will be able to force non-geostrophic unstable Eady modes of the kind studied in chapter 3. Then, in section 4.2.2 the magnitude of the force is increased to observe the nonlinear saturation of the same problem (experiment P2). Finally, in section 4.2.3 the height of the force is raised in the high troposphere (experiment P3), in order not to generate unstable Eady modes. This allows to distinguish more clearly the two mechanisms of IGWs secondary generation forced by the PV, which take place together in P1.

4.2.1 Linear response to a weak force in the low-troposphere (P1)

i) Experimental setup

We define a reference experiment called P ("Parameterized"), from which we will start a series of sensitivity tests. The background flow parameters are

$$f = 10^{-4}\,\mathrm{s}^{-1},\ N = 10^{-2}\,\mathrm{s}^{-1},\ U_0 = -14\,\mathrm{ms}^{-1},\ \Lambda = 4.10^{-3}\,\mathrm{s}^{-1}\,, \tag{4.4}$$

which gives a wind vanishing at $z^* = 3.5$km. In Eq. (4.4), N is the Brunt-Vaisälla frequency and f the Coriolis constant. The force profile is defined by[1]

$$F_0 = \pi.10^{-5}\mathrm{m^2s^{-2}},\ L = 100\mathrm{km},\ d = 300\mathrm{m},\ \delta z = 200\mathrm{m},\ \tau_1 = \tau_2 = 15\mathrm{h},\ \text{and}\ T = 10\mathrm{h}. \tag{4.5}$$

The numerical scheme and parameters are described in Appendix F. Note that the diffusivity is set to $\mu = 0.01$ m^{2}s^{-1} for this experiment. This low value is necessary for accounting correctly for the unstable coupling that takes place near the inertial critical levels (see Chapter 3). The horizontal width of the domain is $2L_D$=2π*600km, and contains two lateral sponge layers of thickness L_s=π*200km. The physical and numerical parameters that will change in the following experiments are summarized in the Table 4.1.

Exp	z* (km)	L (km)	F_0 (m^2.s^{-2})	H_0 (m)	τ_1 (h)	T (h)	τ_2 (h)	μ (m^2.s^{-1})	L_D (km)	L_s (km)
P1	3.5	100	$\pi.10^{-5}$	_	15	10	15	0.05	π*600	π*200
P2	3.5	100	$\pi.10^{-4}$	_	15	10	15	0.05	π*400	π*200
P3	10	100	$\pi.10^{-5}$	_	15	10	15	0.05	π*600	π*200
M1	3.5	100	_	15	15	10	15	0.15	π*170	0
M2	5	75	_	15-250	10	∞	∞	0.5	π*187	π*37

TAB. 4.1 – Physical and numerical parameter settings of the different experiments.

ii) Total response, balanced part and unbalanced part

a. The method

In the following, we always study the perturbation flow in response to the forcing, and in reference to the background flow $\mathbf{U}(z)$ (see Appendix A). This perturbation flow is called the *total response*, and is analysed in terms of its *balanced* part (subscript $_b$), and its residual the *unbalanced* part (subscript $_{ub}$) :

$$(u, v, w, \theta, \phi) = (u_b, v_b, w_b, \theta_b, \phi_b) + (u_{ub}, v_{ub}, w_{ub}, \theta_{ub}, \phi_{ub})\,. \tag{4.6}$$

To describe the balanced part, we follow Martin and Lott 2007, and use a 2D linear semi-geostrophic balance set of equations (see Appendix C). At each storage time, the inflow PV anomaly q associated to this balance is evaluated out of the total flow by

$$\rho_0 q = (1 - \mathrm{Ri}^{-1})\,\theta_{0z}\,v_x + f\,\theta_z\,. \tag{4.7}$$

Then, it is used to extract the balanced fields, under the assumptions of geostrophy for v_b and ϕ_b, and hydrostasy for θ_b and ϕ_b. Therefore the geostrophic flow (v_b, θ_b, ϕ_b) is directly inverted from the inflow PV, and using the rigid boundary conditions in the balanced thermodynamic equation to include the Eady edge waves. The other balanced fields u_b and w_b are not geostrophic but purely *ageostrophic*[2]. For this reason, (u_b, w_b) is deduced from the Omega equation and the continuity equation. The unbalanced fields are then obtained by substraction of the balanced part to the total response, following Eq. (4.6). Thus, the *non-geostrophic* part of the flow is the sum of the balanced ageostrophic flow (u_b, w_b) and the unbalanced flow $(u_{ub}, v_{ub}, w_{ub}, \theta_{ub}, \phi_{ub})$. Nevertheless, internal waves can only be found in the unbalanced flow, because the

[1]The symbol h is used for the hour time unit.

[2]In 3D, u_b would be geostrophically equilibrated.

relation between the PV and the balanced flow is elliptic. In the following, according to this analysis we first describe the PV anomaly, then the balanced flow, the unbalanced flow and finally the total flow.

b. PV anomaly - Fig. 4.2

To understand qualitatively the PV pattern shown in Fig.4.2, we consider in a first approximation the PV budget in the 2D linear semi-geostrophic context (see Appendix C) :

$$(\partial_t + U\partial_x)\,\rho_0\, q + \boldsymbol{\nabla} \boldsymbol{J}_N = 0, \tag{4.8}$$

where the non-advective PV flux is given by

$$\mathbf{J}_N = (1 - \mathrm{Ri})\,\theta_{0z}\,\mathcal{F}\,\mathbf{e}_y - \Theta_y\,\mathcal{F}\,\mathbf{e}_z. \tag{4.9}$$

As there is no possible divergence in the meridional direction in the 2D context, the PV pattern can only be explained in terms of the vertical non-advective PV flux $\mathbf{J}_{Nz} = -\Theta_y\,\mathcal{F}\,\mathbf{e}_z$, and the advection by the background windshear $\mathbf{U}(z)$. As the wind is positively sheared ($\Lambda > 0$), hence $\Theta_y < 0$ in virtue of the thermal wind equilibrium, and $\mathbf{J}_{Nz}$ points upward. In the first stage, this induces a vertically oriented PV dipole in the vicinity of the force, made of a positive PV lobe above a negative one. This is illustrated in the Fig.4.2a for t=τ_1, that is at the end of the spin-up of the force. The PV lobes have roughly the same elongated and gaussian profile as the force $\boldsymbol{\mathcal{F}}$. Thereafter, the PV anomaly goes on intensifying as long as the force stops. In the same time, this structure is submitted to the differential advection by the background windshear. As the force is localized slightly under the level of vanishing wind, the negative PV lobe is substantially advected westward, whereas the positive one stays more or less centered around ($x = 0, z = z^*$) and is steered by the background shear (Fig.4.2b for t=45h). This process goes on until the end of the experiment, which increases progressively the global length of the PV pattern (Fig.4.2c for t=75h). The drift velocity of the negative anomaly is around 1.7m.s^{-1} between t=15h and 75h, which roughly correspond to $U(z = 3\mathrm{km})$.

Note that to account more precisely for this PV pattern, we must consider (i) the effect of the vertical advection of the background PV[3] which explains that the positive lobe is slightly more intense than the negative one, and (ii) the nonlinear term of vertical advection of the PV anomaly which explains the slight tilt of the positive lobe (see the subsequent description of the vertical velocity field in Fig. 4.3c and Fig. 4.6c).

c. Balanced flow - Fig. 4.3

The PV anomaly of the Fig.4.2b is added in Fig. 4.3f as a constant reference in space for the discussion. We first describe the flow directly induced in the vicinity of the PV anomalies.

As illustrated by the Eq. (4.7), a definite sign PV anomaly is generally associated to a vorticity anomaly v_x and a stratification anomaly $g\theta_z/\theta_{0z}$ of definite signs. Particularly, a positive (negative) PV anomaly induces a cyclonic (anticyclonic) circulation extending outside of itself. As in our case the two PV anomalies of opposite sign are approximately side by side, with the positive one on the right of the negative one, they combine to create a central dominant southward jet, surrounded by two weaker northward jets (v_b in Fig. 4.3b, near z=3km). This system is slightly tilted, as is the

[3]In the anelastic context, the background PV $P = \rho_0^{-1}\,(f\theta_{0z} + \Theta_y\Lambda)$ is not uniform in the vertical.

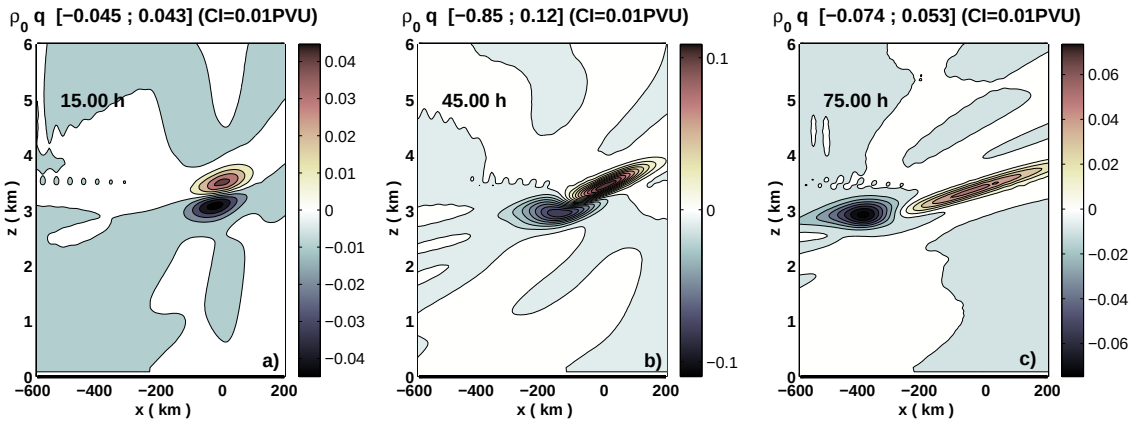

FIG. 4.2 – PV anomaly at the dates t=15h (a), 45h (b) and 75h (c), for experiment P1. The minimum and maximum values of the PV field at each time is indicated above each map, with the value of the Contour Interval (CI) in PV units (PVU).

PV dipole. The positive (negative) PV anomaly is also associated to a local increase (decrease) of the stratification, hence a negative potential temperature anomaly θ_b appears under it (above) and a positive one above it (under) (Fig. 4.3d). By a vertical integration of the hydrostatic relation starting from $z = z_{top}$, one can deduce from the Fig. 4.3d that the positive (negative) PV anomaly is associated to a negative (positive) geopotential anomaly (Fig. 4.3e). To explain the pattern of the vertical velocity w_b in Fig. 4.3c, we must remind that for the balanced flow, a positive (negative) meridional wind must induce an ascent (descent) to equilibrate partially the northward heat transport $-\Theta_y\, v_b$ by an adiabatic cooling (warming) $-\theta_{0z}\, w_b$ (see Eq. 4.44d in Appendix D). Finally, to respect the mass conservation, the Fig. 4.3c implies that the zonal velocity u_b must be convergent above the PV dipole, and divergent under, which is observed in Fig. 4.3a. An overview of this balanced mechanism is schematized in the Fig. 4.4.

This interpretation of the balanced circulation is essentially valid inside the flow, near the PV anomaly. But near the surface, as in Martin and Lott (2007), there is no vertical motion to balance the heat transport induced by the meridional wind associated with the PV. This triggers a surface Eady wave. Note that the same occurs at the upper boundary, but this can be neglected here since the PV is very far from it (z_{top}=40km). On the contrary, the magnitude of the surface anomalies of v_b and θ_b are comparable with those near the PV (Figs. 4.3b, and d). These surface anomalies are submitted to the Eady edge wave dynamics, with a anticyclonic circulation (Fig. 4.3b) centered on a cold anomaly (Fig. 4.3d) and a high pressure (Fig. 4.3e). Consistently, the vertical velocity follows the sign of the meridional velocity near the surface, for the same reason as near z^* (Fig. 4.3a). And the zonal velocity is in quadrature with v_b and in advance of phase (Fig. 4.3a). At this stage, the observed wavelength is rather short, between 600km (v_b and θ_b) and 1200km (ϕ_b), with an intermediate value of 800km for u_b. The westward propagation of this surface Eady wave packet is not clear in the Fig. 4.3, but will appear later in the simulation, as will be confirmed in section 4.2.1. It is important to notice that the horizontal position of the surface anomalies is slightly shifted as regards to the corresponding anomalies near the PV (z^*). The resulting tilt of the phase lines is upshear for u_b, v_b, w and ϕ_b, and downshear for θ_b, which allows the disturbance to extract energy from the background flow. This point

will be discussed further and quantified in the next paragraphs.

d. Unbalanced flow - Fig. 4.5

The first thing to note is that the magnitude of the unbalanced flow is globally a little weaker than the magnitude of the balanced flow (Fig. 4.3), but comparable with it (pay attention to the different vertical domains of the different maps). The ratio is approximately from 2 to 5 times smaller, except for u_{ub} which is comparable with its balanced ageostrophic counterpart u_b.
The second thing to note is that the unbalanced response can globally be divided into two distinct components out of the horizontal scales appearing in the fields. A rather short horizontal wavelength of around 500km dominates the signal, essentially in the range $x = [-400; 200]$km, that is above the PV and under it near the surface. But a secondary wavelength, larger and weaker in amplitude, is clearly visible near the surface in θ_{ub} and ϕ_{ub} (around 1200km) and in u_{ub} (around 1000km). The latter is also slightly visible in the background of w_{ub}, in the left part of the panel.
The third important feature is that at the surface, all the unbalanced fields are in phase opposition with the balanced ones over almost the whole domain. This is notably very clear under the PV ($x = [-300; 100]km$). This is a main result, which means that the unbalanced flow tends to reduce the effect of the balanced flow at the surface. The reason will be explained with P3 in section 4.2.3.

To understand the rather complex structure of these unbalanced fields, we must remind that it is made of two contributions : namely the IGWs of the total response, which are the essential part, but also the residual of the balanced fields which was not captured by our linear semi-geostrophic balance system. Indeed, for such subsynoptic scales our balance system is limited, since it is more adapted for synoptic scales. In other words, this means that our extraction of the IGWs part of the response is slightly corrupted by the imperfection of our balance system. Particularly, this means that near the surface, the unbalanced response is a mix between IGWs and the residual of the balanced surface Eady waves. This probably explains partially the presence of a large scale component in the surface signals. Note that the use of a higher order balance could reduce even more this residual contribution.

Hence, it is easier to first analyse the signals above the PV, where the dominant feature is at $\lambda \sim 500$km. The latter appears rather clearly in the w_{ub} and ϕ_{ub} (Figs. 4.5c and e), between z=5km to 30km, as an IGW packet linked to the PV. It is also slightly visible in u_{ub} and θ_{ub} (Figs. 4.5a and d). The associated generation mechanism will be diagnosed in a clearer context in section 4.2.3. In the vertical velocity the IGWs reach a magnitude of 5.10^{-4}m.s^{-1}, comparable with the global amplitude of w_{ub}. And in the pressure perturbation they reach 0.6 Pa, that is about 20% of the global amplitude of ϕ_{ub}. The phase lines are tilted upshear, indicating an upward group velocity, and they are less tilted in their lower part since the intrinsic frequency approaches the inertial frequency (Fig. 4.5c). The wave packet is damped by the sponge layer above 20km. Finally, the presence of the second component at $\lambda \sim 1000$km is perceivable in the background, as a large negative lobe 500km wide ($x = [-1000; -500]$km), and a slight assymetry between the two main small scale lobes described above ($x = [-400; 0]$km, the positive lobe is stronger).

This IGW packet is connected to the surface flow through the region of the PV anomaly, near $z = 3 - 4$km and $x = [-300; 100]$km (Fig. 4.5c). In this region, the inertial oscillation generated locally by radiation by the force is clearly visible in u_{ub}, v_{ub}, and w_{ub}. It takes the form of a main tongue very sheared and elongated, thin and

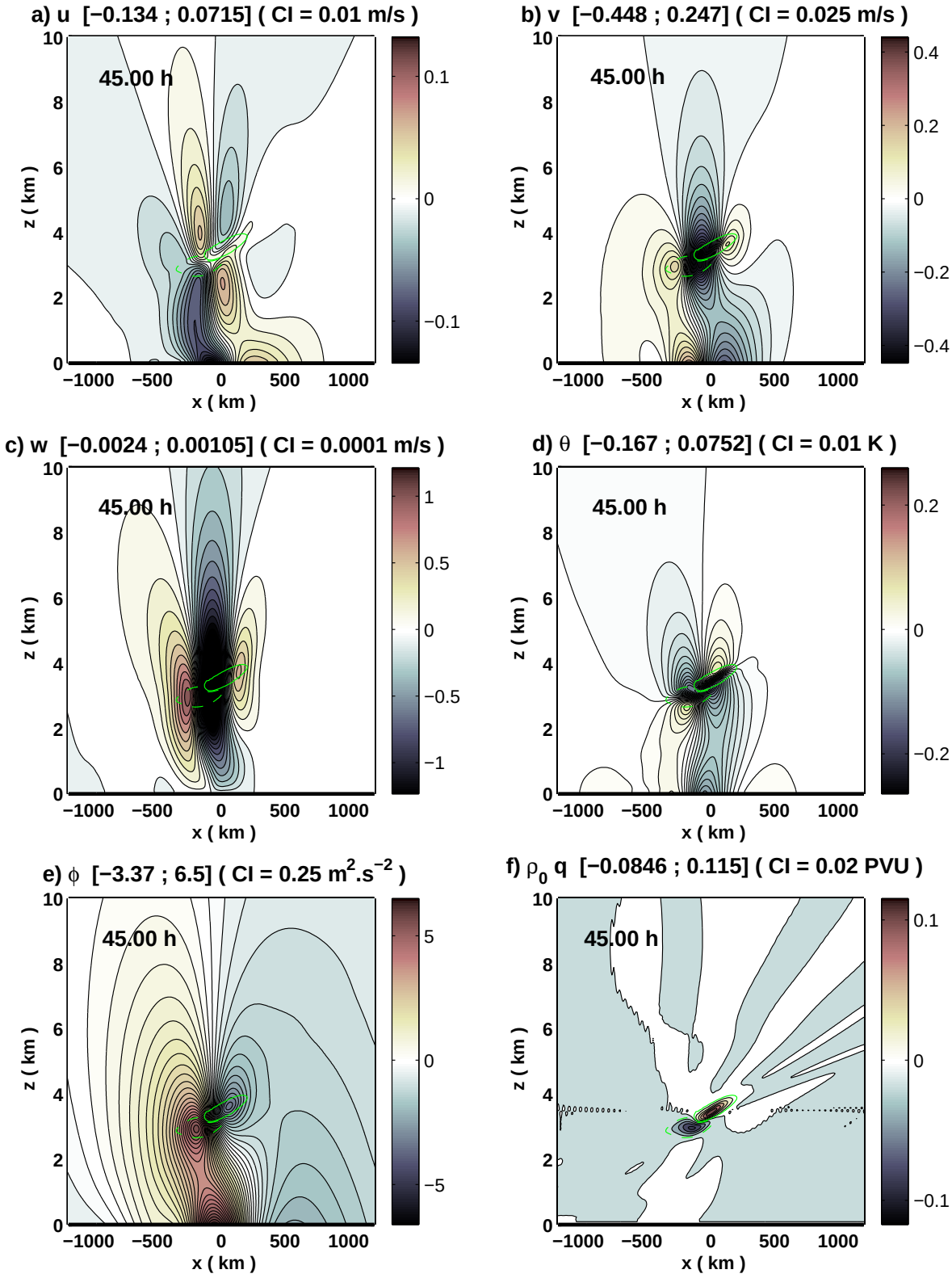

FIG. 4.3 – Balanced part of the response to the forcing at t=45h for experiment P1 : a) zonal velocity, b) meridional velocity, c) vertical velocity, d) potential temperature, e) geopotential perturbation (or pressure) and f) PV anomaly. The minimum and maximum values of each field at this time is indicated above each map, with the value of the Contour Interval (CI). The PV anomaly is added as a reference (±1PVU in green), but is identical to Fig. 4.2b.

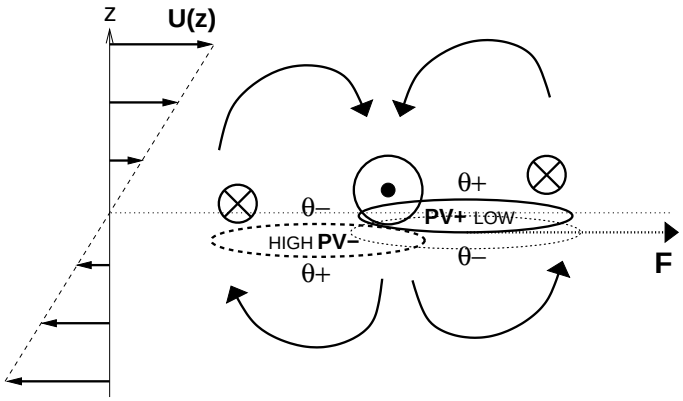

FIG. 4.4 – Schematic view of the the balanced mechanism. The PV anomalies created by the force $\boldsymbol{\mathcal{F}}$ are shifted horizontally by the background shear $\mathbf{U}(z)$. This induces a circulation indicated by the arrows (the meridional component is represented slightly above the PV lobes for clarity), and a positive (negative) geopotential anomaly on the negative (positive) PV lobe (HIGH and LOW). The potential temperature anomalies are also indicated, which account for the local change of the stratification associated to the PV anomalies.

nearly horizontal, but slightly tilted as the PV pattern. At this moment, this tongue is moderate and negative in v_{ub}, and intense and positive in u_{ub}. Actually, this pattern propagates a little vertically, very slowly.

As will be explained in section 4.2.3, another short scale IGW packet is also generated downward by the PV ($\lambda \sim 500$km). It is clearly visible between the PV and the surface in v_{ub}, w_{ub}, θ_{ub} and ϕ_{ub}. The signal is more complex in u_{ub} but this IGW is also largely present at the surface. The phase relationships are correct : u_{ub} and θ_{ub} are in quadrature with v_{ub}, and in advance of phase. The same is true for ϕ_{ub} by hydrostasy. It is striking that this IGW packet is largely more intense at the surface than above when approaching the PV. This can be explained as follows. Further examination of the surface response by a Hovmuller diagram shows that this lower IGW is propagating very slowly and following the advection of the PV (not shown, see section 4.2.1 for the method). This means that its critical level is localized near z^*. And its lower inertial critical level can be deduced from the wavelength and the shear Λ by $z_{IL} - z_{CL} = \frac{f\lambda}{2\pi\Lambda} \sim 2$km, that is near z=1.5km. Thus, this IGW packet is trapped between the ground and its lower inertial critical level in the first two kilometers, and is evanescent above.

e. Total flow - Fig. 4.6

Superimposed to the balanced part, the unbalanced contributions result globally in (i) a reduction of the amplitude of the total surface Eady wave (Figs. 4.6b,d,e), (ii) a reduction of the vertical tilt of the phase lines for u, v and ϕ (Figs. 4.6a,b,e) and an increase of this tilt for θ (Fig. 4.6d), and (iii) an increase of the wavelength of the total Eady wave, which is about 1200 km (Figs. 4.6b,d,e). The magnitude of the total response is rather weak, which ensures the linearity of the process, and must be related to the weakness of the force amplitude F_0 in this experiment. The perturbation horizontal velocities and potential temperature are of order 10^{-1}m.s^{-1} and 10^{-1}K, the perturbation geopotential (pressure) is about 5 m^2.s^{-2} (or Pa), and the vertical velocity is of order 10^{-3}m.s^{-1}. The propagation properties will be described further in section

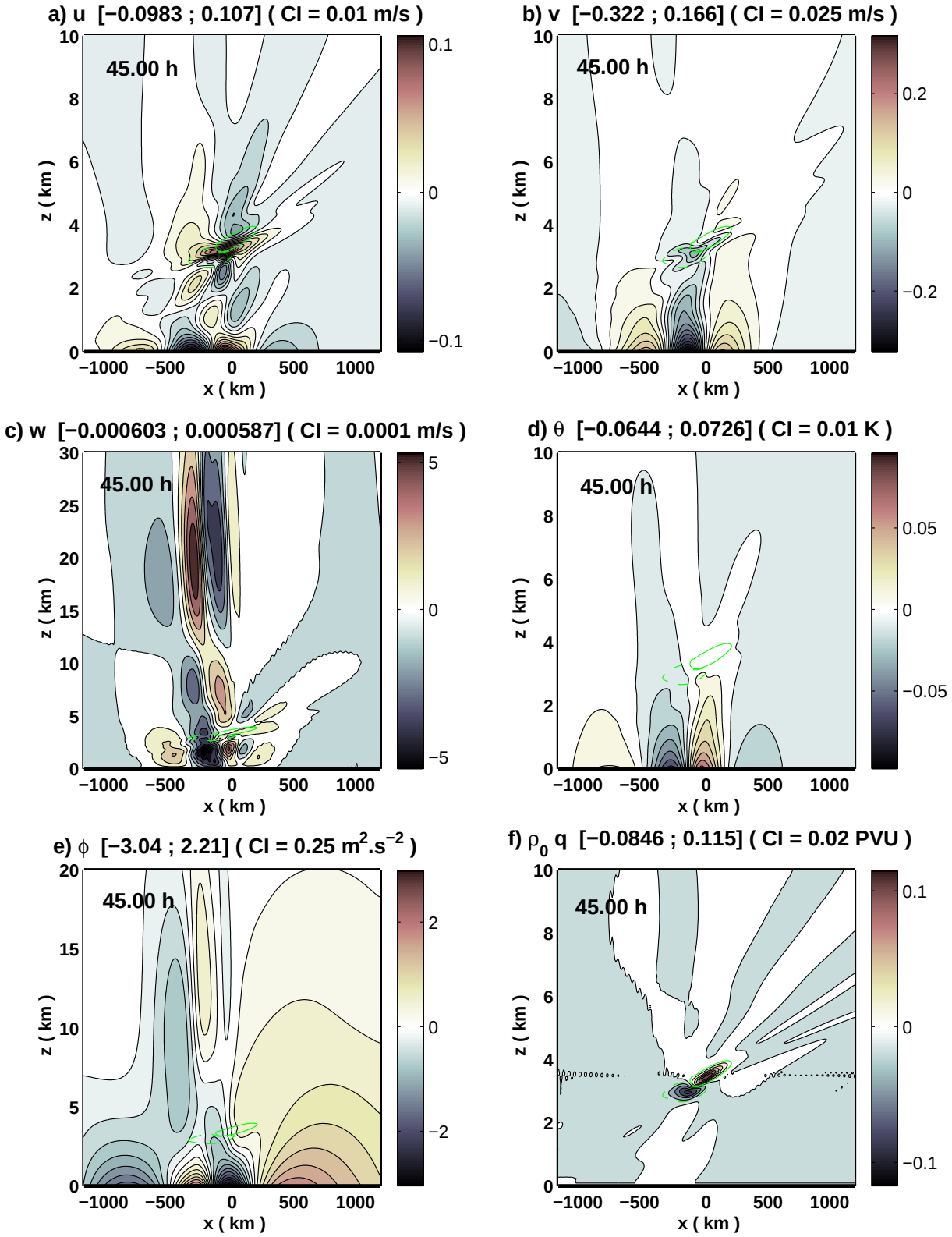

FIG. 4.5 – Unbalanced part of the response to the forcing at t=45h for experiment P1 : a) zonal velocity, b) meridional velocity, c) vertical velocity, d) potential temperature, e) geopotential perturbation (or pressure) and f) PV anomaly. The PV anomaly is added as a reference (±1PVU in green), but is identical to Fig. 4.2b.

4.2.1.

Noteworthy, it is now very clear, notably in Fig. 4.6c, that the total response can be divided essentially into two contributions : (i) a short scale upper IGW packet ($\lambda \sim 500$km) and (ii) a larger scale non geostrophic Eady mode ($\lambda \sim 1000$km) which couples a surface Eady wave with an IGW of the same scale.

At the surface, the horizontal extension of the total Eady wave is larger than for the balanced Eady wave. This is consistent with the general idea that the unbalanced flow is faster than the balanced one by definition. And it was verified previously in the Fig. 4.5. In particular, at the surface the two components tend to destroy each other upstream, whereas the Eady wave is extended downstream. Hence, the unbalanced flow accelerates the building up of the lee wave generated by the PV, though it reduces its amplitude under the PV.

Another way to understand that the horizontal scale of the balanced surface Eady wave is increased by the unbalanced flow contribution, is to refer to the previous observations of Nakamura (1988). For this discussion, we need to introduce a characteristic vertical scale H, and a characteristic horizontal scale L_E, to describe the surface Eady wave. We define the Burger, Richardson, and Rossby numbers respectively by :

$$\mathrm{Bu} = \frac{NH}{fL_E} \quad , \ \mathrm{Ri} = \frac{N^2}{\Lambda^2} \quad , \text{and} \quad \mathrm{Ro} = \frac{\Lambda H}{fL_E} = \frac{\mathrm{Bu}}{\sqrt{\mathrm{Ri}}}, \tag{4.10}$$

In order to keep consistent with the conventions defined in Chapter 3 about non-geostrophic unstable modes, we impose arbitrarily that the height H corresponds to the quasi-geostrophic regime in which

$$\mathrm{Bu} = \frac{NH}{fL_E} = 1. \tag{4.11}$$

This way, the corresponding Rossby and Richardson numbers are designed to describe the surface dynamics in comparison with the results of Chapter 3. Hence, we find $\mathrm{Ro} \sim 0.4$, and $\mathrm{Ri} \sim 6.25$. The observed surface wavelength λ_E is between 600km and 1200km in the balanced and unbalanced responses, which corresponds to a scale $L_E = \lambda_E/2\pi$ between L and $2L$ (we remind that L refers to the force profile). This yields H=1km to 2km, which is reasonable in comparison with the surface signals observed in the Figs. 4.3, 4.5 and 4.6. Hence, the Rossby number is between $\mathrm{Ro} \sim 0.2$ and 0.4, while $\mathrm{Ri} \sim 6.25$.

According to Nakamura (1988) we know that for increasing shears or Rossby numbers, the ageostrophic flow tends to stabilize the unstable Eady modes by decreasing the vertical height of penetration of the edge waves. This increases the horizontal scale of the most unstable mode as regards to the quasi-geostrophic value, and can be summarized by the modified deformation radius relation :

$$L_R = \frac{h\sqrt{N^2 + \Lambda^2}}{f}. \tag{4.12}$$

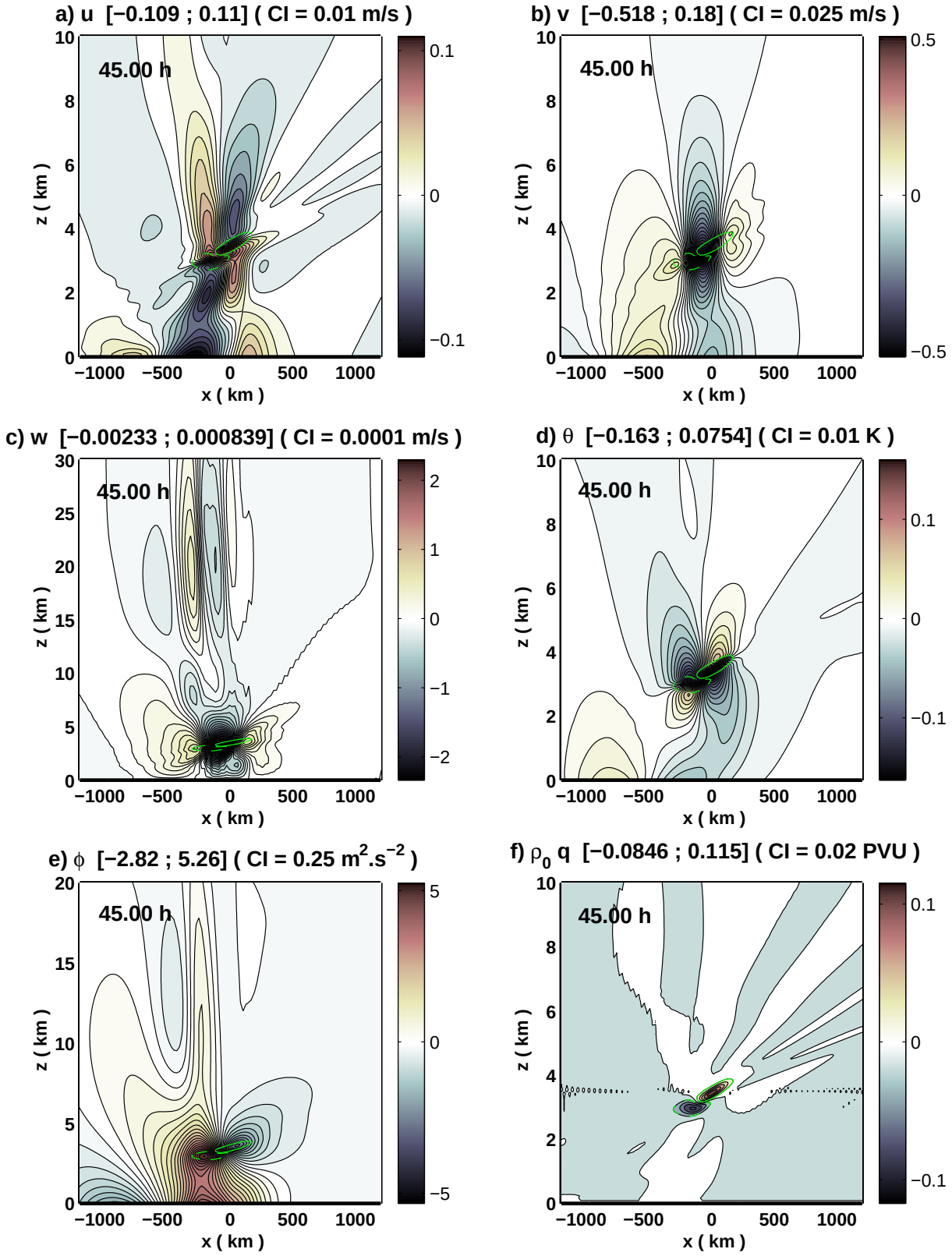

FIG. 4.6 – Total response to the forcing at t=45h for experiment P1 : a) zonal velocity, b) meridional velocity, c) vertical velocity, d) potential temperature, e) geopotential perturbation (or pressure) and f) PV anomaly. The PV anomaly is added as a reference (±1PVU in green), but is identical to Fig. 4.2b.

iii) Energy budget and Eliassen-Palm flux

The energy budget of the experiment P1 is presented until t=50h in Fig. 4.7 in relation with the equations given in Appendix B and Appendix D : energy of the perturbation in a), energy tendency terms in b), and geostrophic meridional heat flux in c). In particular, the total energy and its geostrophic and non geostrophic components are computed respectively by space integrals of

$$\begin{aligned} e &= \frac{\rho_0}{2}\left(u^2+v^2+w^2+\frac{g^2}{\theta_0^2 N^2}\,\theta^2\right)\,, \\ e_g &= \frac{\rho_0}{2}\left(v_b^2+\frac{g^2}{\theta_0^2 N^2}\,\theta_b^2\right)\,, \text{ and} \\ e_{ng} &= \frac{\rho_0}{2}\left(u^2+v_{ub}^2+w^2+\frac{g^2}{\theta_0^2 N^2}\,\theta_{ub}^2\right)\,, \end{aligned} \tag{4.13}$$

over the entire domain. Note that the non geostrophic balanced fields u_b and w_b take part of e_{ng}, not e_g.

The tendency curves in Figs. 4.7b and c show that the perturbation energy growth is essentially due to the transfer of potential energy from the baroclinic background flow to the perturbation via the meridional heat flux (green curves). This process is predominantly balanced, and linear. But it is strongly modulated by the inertial oscillation radiated by the force, as testified by the difference between both green curves. We do not concentrate especially on this inertial oscillation in this study, since it can be substantially reduced by keeping the force constant over the whole experiment after the spin-up time τ_1. Actually, this inertial oscillation is essentially localized near the PV but also partially contained by the global mean flow, because of the finite size of the space domain. This latter contribution can also be reduced by increasing even more the width of the domain.

A closer examination of the energy curves in Fig. 4.7a indicates that the process can be divided into three stages. During the first 15h, the force settles and the perturbation starts to grow, essentially through an unbalanced process because the balanced dynamics is slower. A southward meridional jet starts to develop, equilibrating the force by the coriolis torque. In the next 20h, the force is building up the PV anomaly which is continuously steered by the shear, increasing the southward meridional jet by the mechanism described in Fig. 4.4. This jet intensifies the energy growth by carrying a positive heat flux, feeding essentially the balanced part of the flow. The third stage starts a little before 40h, when the force becomes neglectable. It is characterized by a simultanous exponential growth of the balanced and unbalanced components of the flow until the end of the experiment at t=80hrs (not shown), by a spontaneous mechanism in the absence of the force. We argue that this mechanism is essentially the growth of a non-geostrophic unstable Eady mode of the kind studied in Chapter 3, forced by the advected dipolar PV anomaly. We show it in the following. Incidentally, we note also that the fact that the unbalanced flow reduces the amplitude of the surface Eady wave is now visible in the total energy (black), which is smaller than the balanced energy (red) for t>45h.

As explained in the appendix C, in our model the vertical distribution of the perturbation energy tendency is well represented by the two components of the horizontal

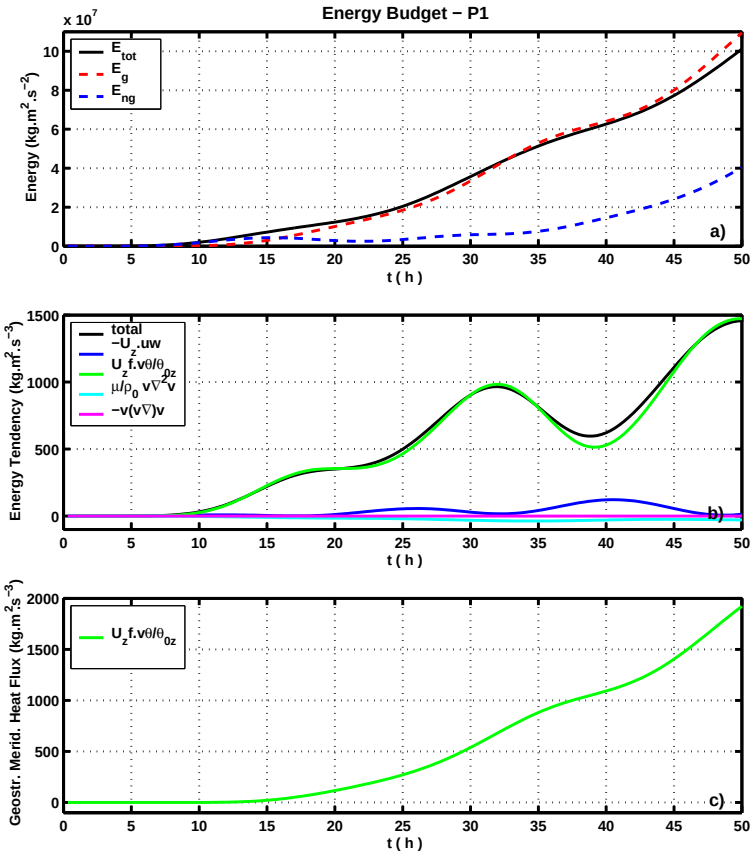

FIG. 4.7 – Time evolution of the perturbation energy budget, for experiment P1 of section 4.2.1 : a) total perturbation energy, and its geostrophic and non geostrophic contributions (Appendix B and Appendix D), b) tendency terms of the energy budget, and c) geostrophic meridional heat flux.

mean vertical Eliassen-Palm (EP) flux

$$F^z = \rho_0 \left[\frac{f}{\theta_{0z}} \overline{v\theta} - \overline{uw} \right], \tag{4.14}$$

provided that the other energy tendency terms, diffusive or nonlinear, are neglectable. This profile can help to characterize the dominant energy growth process and the vertical structure of the perturbation, as was done in Chapter 3. The result is shown in Fig. 4.8. The flux profiles were averaged in time for the period t=40h to 57h, which represents one inertial period starting when the force vanishes (thick lines). To represent the influence of the inertial oscillation which modulates the fluxes, we also display the profiles at two dates separated by one half inertial period and representative of the amplitude of the modulation, that is t=45h and 53h (thin lines).

In many respects, these profiles are strongly reminiscent of the profiles observed in Chapter 3 for the non-geostrophic unstable Eady modes (Fig. 7). Under z=3km, the meridional heat flux (green) is positive, nearly constant except a slight decrease with height. On the contrary, the kinetic energy flux profile (blue) is approximately zero. These profiles are typical of a 2D baroclinic Eady wave, in which the phase lines of v are tilted upshear and the phase lines of θ are tilted downshear, as it is the case here (Figs. 4.6b and d, it is less clear for v than for θ, and Figs. 4.3b,d for the balanced part which is dominant in the energy budget). Note that, as said before, the fields u

and w are totally non-geostrophic because the wave is 2D, hence the kinetic energy flux $-\overline{uw}$ is substantially smaller than the meridional heat flux $\frac{f}{\theta_{0z}}\,\overline{v\theta}$.

Between z=3km and 3.5km, that is in the area where the force was acting before t=40h, the meridional heat flux is positive and peaks typically as it does in Chapter 3. This can be interpreted as the presence of an inertial critical level for the global perturbation. The term $-\overline{uw}$ averaged in time does not peak in this zone but the instantanous values do, as indicated by the profiles for t=45h and 53h, testifying of a critical behaviour as for $\frac{f}{\theta_{0z}}\,\overline{v\theta}$. We see that the inertial oscillation modulates the signal essentially in the critical zone, that is where the force was applied before, and makes the two peaks oscillate around their mean value. On the contrary, under this critical zone, the profile has an positive value increasing with time, because of the growth of the unstable mode.

To check that the mechanism of the perturbation energy growth (after the force cut-off) is essentially the one of an unstable non-geostrophic Eady mode of the kind studied in Chapter 3, we note that the observed position of the inertial critical layer, between z=3km and 3.5km, is consistent with the lower estimate of the balanced surface Eady wave wavelength λ_E, which is around 600-700km and corresponds to the geostrophic fields v_b and θ_b (Fig. 4.3b and d). Refering to the analysis in Chapter 3 (and Plougonven et al 2005), this corresponds to a characteristic horizontal scale $L_E = \lambda_E/(2\pi) \sim L = 100$km, giving a critical level localized near $z_{CL} \approx \frac{fL}{N} \sim 1000$m, which corresponds to the characteristic height $H = 1$km and the Rossby number Ro=0.4. The inertial critical level z_{IL} then satisfies $z_{IL} - z_{CL} = \frac{fL}{\Lambda} \sim 2500$m, which indicates a critical layer centered around $z_{IL} \sim 3.5$km. This is consistent with the EP profiles in Fig. 4.8. The discussion of the phase velocity of these unstable modes in respect to the wind speed at the critical level is adressed in the next paragraph.

Finally, to make the comparison complete, the perturbation growth rate σ is measured from the total energy curve between t=40h to 80h (not shown), and its non-dimensionalized value in found to be

$$\sigma \frac{N}{f\Lambda} = 0.156 \pm 3\%. \tag{4.15}$$

This is about 10 times larger than the growth rates obtained for free unstable growth of non-geostrophic modes in Plougonven et al. (2005) (growth rates were not measured in Chapter 3 for such a small shear). Nevertheless, we should not be mistaken by the fact that this value is closer to the usual geostrophic baroclinic growth rates (0.3 for the most unstable quasi-geostrophic mode, Gill 1982). Indeed, as the height of the top of the model is 40km, accounting for this growth rate by a quasi-geostrophic baroclinic unstable mode requires a horizontal wavelength of around 80000km, which is far larger than the model domain. This underlines the crucial effect of the PV dipole in forcing the disturbance observed here. This is not totally surprising nevertheless, since De vries and Opsteegh (2005, 2007) have shown recently in the linear quasi-geostrophic context, that tropospheric PV anomalies can force optimal Eady waves with strongly enhanced growth rates in the first days. This happens notably when the PV anomalies are localized near the steering level of the disturbance, and relies essentially on two mechanisms that are very efficient in the first two days, namely the PV unshielding, and the resonance between the PV and the surface Eady wave.

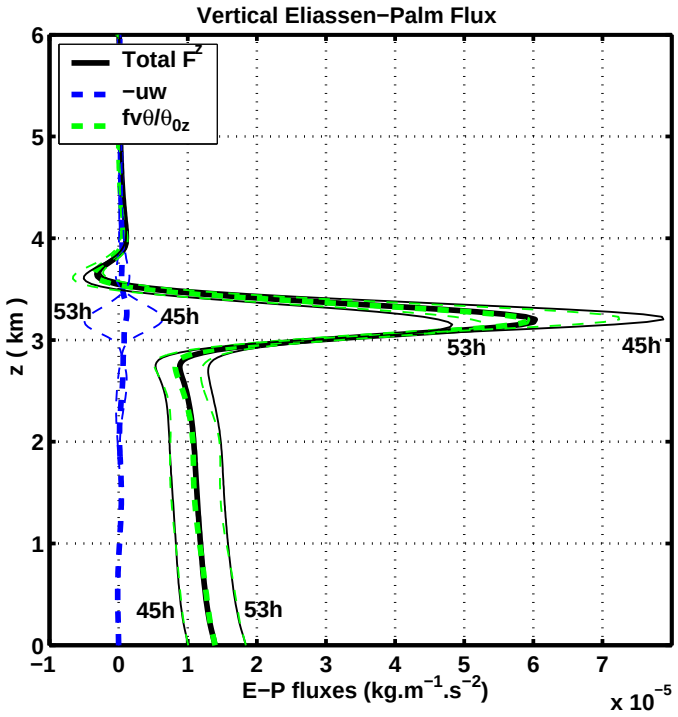

FIG. 4.8 – Horizontal mean of the vertical EP flux contributions averaged in time between t=40h and t=57h (thick lines), within one inertial oscillation period, for experiment P1. The thin lines are the same profiles at t=45h and 53h.

iv) Generation of an Eady wave train and an intermittent IGW train

To characterize the waves generated in the whole experiment, we need their phase and group velocities. We also need to observe the IGW generation process during the whole experiment. We present the Hovmuller diagrams of horizontal sections of the flow fields in Fig. 4.9.

The surface sections of u, v and θ are shown in Figs. 4.9d,e and f. They account for the westward propagation of a surface Eady wave packet, whose wavelength is increasing with time. The measurement of its phase velocity is not univocal because this wave is not purely monochromatic neither steady, but can be estimated between -1.3 and -4,0m.s^{-1}. This "local" phase speed is faster far the PV anomalies than close to them. These values are significantly slower than the surface wind (-14 m.s^{-1}), and indicates critical levels localized near z=3km.

The upper IGWs generation process also appears more clearly in the Figs. 4.9a,b, and c, which present the horizontal sections of u, w and θ near z=20km. Note that the phase relationships corresponding to westward propagating IGWs are respected, with w in advance of phase relative to θ and u. The overall process can be described from the field w (Figs. 4.9b), as the generation of an intermittent IGW train, originated from the dipolar PV anomaly. This generation lasts very steadily until the end of the simulation, that is for several inertial periods after the end of the forcing. The group velocity of the IGW train is measured from the position of the last three subsequent maxima in w, which gives 1.7m.s^{-1}. This value corresponds to the drift velocity of the negative PV lobe evaluated before (Fig. 4.2). This ensures that the IGW train is continuously linked to the PV. The local maximum vertical velocity varies between

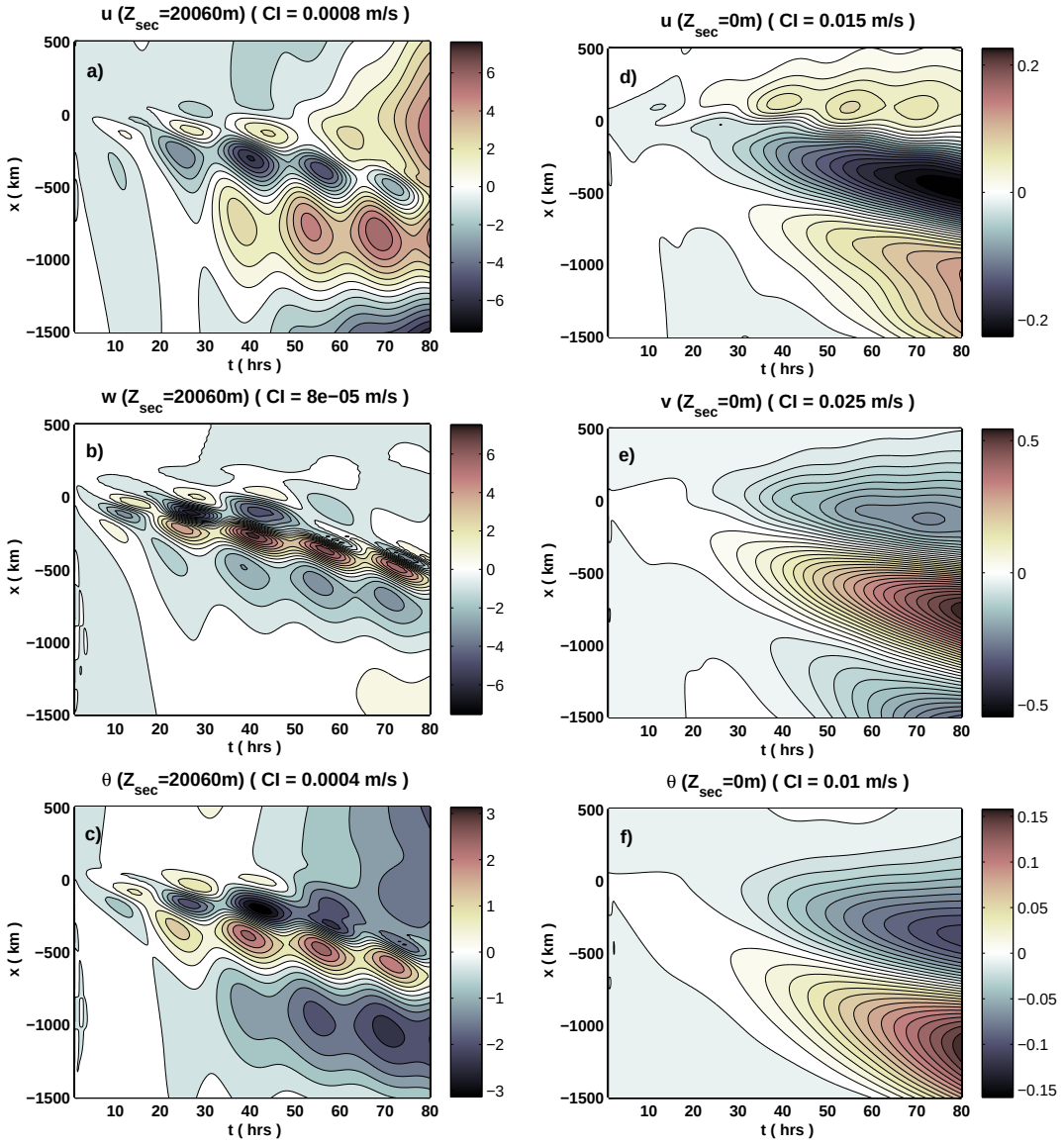

FIG. 4.9 – Hovmuller diagrams for experiment P1, of horizontal sections at the level Z_s=20060m in a), b), c) and Z_s=0m in d), e) and f). a) and d) zonal velocity, b) vertical velocity, c) and f) potential temperature, e) meridional velocity.

3.10^{-4} and 6.10^{-4}m.s^{-1}, with a peak at nearly 10^{-3}m.s^{-1} reached at t=40h. In the first stage, the initial growth and slow drift of the negative PV lobe induces an increase of the wavelength of the IGW packet during the forcing phase, from around 200km at the begining, to 400-500km at t=40h and until the end. For t<40, it also increases the lifetime of each IGW packet between the extinctions. In the last 40h, these IGWs are progressively invaded by growing larger scale patterns. These patterns are linked to the larger scale components of the response, which have two different contributions. The first is the growing balanced flow directly induced by the PV dipole (Figs. 4.3a,c,d). The second contribution is the large scale non-geostrophic unstable Eady mode that couples the surface Eady wave with large scale upper IGWs (lower part of the Figs. 4.9a,b,c, negative x positions).

It is striking from t∼30h that the intermittency settles as a modulation at the inertial frequency (period of 17h). The inertial oscillation described earlier, which mo-

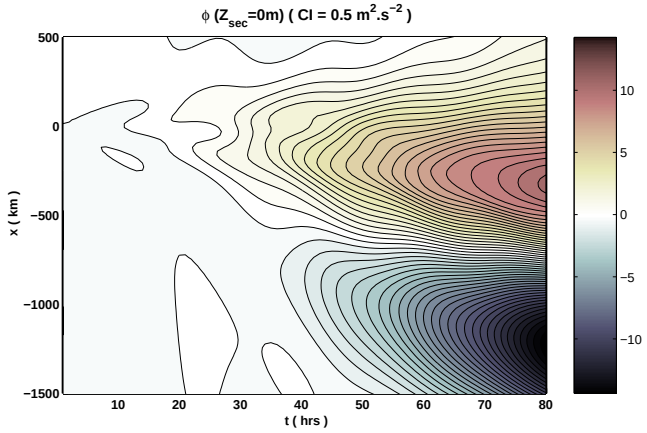

FIG. 4.10 – Hovmuller diagram for experiment P1, of the surface geopotential perturbation (Z_s=0m).

dulates the total response essentially near the PV anomaly, is actually also responsible for this modulation. This can be verified by plotting the Hovmuller diagrams of horizontal sections of the two PV anomalies, which reveals that they are submitted to the same horizontal oscillation (not shown).

The fact that these IGWs do not propagate very far from the PV anomalies indicates that their own phase velocity is close to the one of the moving PV lobe, giving a critical level close to z^*. This implies an upper inertial critical levels near z=z^*+1.6km=5.1km, that is above the PV anomalies but close to them. This indicates that these small scale IGWs are coupled with the balanced flow directly associated to the PV anomalies rather than to the surface Eady edge wave, whose wavelength is around twice larger. This is a central point concerning this IGW generation mechanism, and we will discuss it further in the section 4.2.3.

v) Lee Cyclogenesis

The influence of the force $\boldsymbol{\mathcal{F}}$ in terms of lee cyclogenesis, in this 2D situation, can be evaluated by looking at the surface perturbation fields in the downwind side of the force, that is for $x < 0$. The examination of the Figs. 4.6b,d,e, of the Hovmuller diagrams of v and θ (Figs. 4.9e,f) and of the surface pressure perturbation ϕ (Fig. 4.10), confirms the qualitative conclusions that were deduced from the balanced mechanism schematized in Fig. 4.4. Namely, over the first 500km downwind of $x < 0$, the surface Eady wave produced by the force starts to grow with an anticyclonic pattern centered around a high pressure perturbation, which is associated to a cold potential temperature anomaly. Noteworthy, as shown previously the global influence of the unbalanced contributions is to reduce the amplitude of the balanced lee wave. Even if the amplitude of the signal is very weak in this experiment, we can draw a general qualitative conclusion. In this 2D backsheared background wind, the influence of the force exerted by the GWs breaking at their critical level is cyclolytic. This confirms the linear semi-geostrophic results of Martin and Lott (2007), in the 2D non-balanced subsynoptic scale context.

4.2.2 Nonlinear response to a strong force in the low-troposphere (P2)

The experiment P2 is the same as P1, except that the force is intensified by a factor 10 : $F_0 = \pi.10^{-4}\mathrm{m.s}^{-2}$. We also increase the horizontal resolution by reducing the length of the domain to $2L_D$=2π*400km.

The Fig. 4.11 shows the PV anomaly generated at t=25h when the force starts to decrease (a), and the impact in terms of total stratification (total potential temperature in b) and total Brunt Vaïsalla frequency in c)). The PV anomalies are more intense than in P1 by one order of magnitude, but the negative anomaly seems substantially destabilized and less pronounced than the positive one (-0.7PVU versus 1.12PVU). The effect on the stratification is substantial, since it is doubled in the positive PV anomaly, whereas the negative PV anomaly is negatively stratified. Moreover, these intense PV anomalies of opposite signs are close to each other, and induce a strong shear of the flow in this area. Hence, this area near the negative PV anomaly is destabilized by shear and convective instabilities which appears in the total flow as very small scale instabilities (not shown). For this reason, the maps shown in the Fig. 4.11 only present the large scale part of the flow, after filtering all the fields to remove the scales smaller than 80km (wavenumbers larger than 30). To do this, we use a low-pass filter with a Kaiser window and sidelobe attenuation of 40dB (Kaiser, 1974).

The large scale flow perturbation generated here, after filtering, is very close to the response of P1, as shown in Fig. 4.12 at t=45h (be careful to the different hozizontal domains). Nevertheless, several important differences must be noted. The response is now substantial, with u and v around 1m.s^{-1}, θ around 1K, w around 0.05m.s^{-1}, and ϕ reaches almost 40Pa. Noteworthy, the large scale balanced component of the response is approximately 5 to 10 times larger than in P1, but the

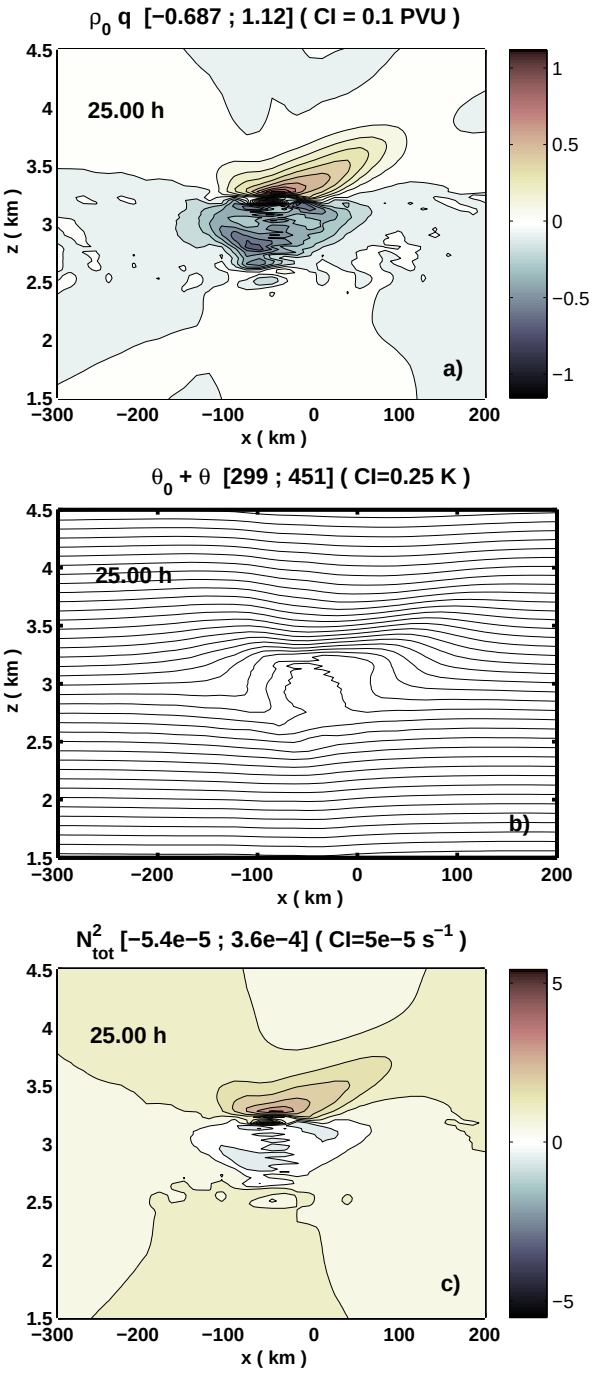

FIG. 4.11 – Stability diagnosis for experiment P2 (with $F_0 = \pi.10^{-4}$ m^{2}s^{-2}), when the force starts to decrease at t=25h : a) PV anomaly, b) total potential temperature, and c) total local stratification $N^2_{tot} = \frac{g}{\tilde{\theta}}\partial_z\tilde{\theta}$.

magnitude of the IGW packet is increased roughly by a factor 100. The PV anomaly is much more distorted by the flow, and the negative lobe is largely destabilized and reduced because of the small scale instabilities. This explains why the balanced flow amplitude does not completely increases linearly with F_0, but saturates a little. In the same time, this destabilization also implies the arising of shear generated IGWs forced in the vicinity of the negative PV anomaly, which are much more intense and have smaller horizontal scales than in P1 (Fig. 4.12c). Indeed, at the surface the large scale Eady wave is now modulated by smaller scale IGWs whose wavelength is of order 60km, as shown clearly by the Figs. 4.12a,c,d,e. And above the PV, the upper IGWs have also a smaller wavelength than in P1, of order 70-80km, and a much stronger magnitude (Figs. 4.12c,e). These observations are confirmed in the Hovmuller diagrams of the Fig. 4.13 for the whole experiment.

To summarize, if the force is sufficiently strong, the mechanism described in experiment P1 becomes nonlinear. The strongly disturbed area of the negative PV anomaly induces a saturation of the large scale balanced process. On the contrary, it can enhance the generation of short IGWs because of arising shear and convective instabilities, consistently with Sutherland et al. (1994), and Scinocca and Ford (2000).

4.2.3 Linear response to a weak force in the high-troposphere (P3)

i) Analysis

The Experiment P3 is the same as P1, except that we change the level z^* where the wind vanishes, and hence the level where the force applies. This level is raised in the high-troposphère, at $z^* = 10$km. The total response is shown in the Fig. 4.14 at t=45h, and the Hovmuller diagrams in Fig. 4.15.

The responses ressemble those of experiment P1 (see Fig. 4.6 and Fig. 4.9), except an important difference. The surface Eady wave is neglectable, and makes a very small contribution to the balanced part of the signal. The reason is that the PV is now quite far from the surface. Actually, for the horizontal scales of the IGWs excited here (Fig. 4.14c), there is a second inertial critical level under z^*, which allows IGWs to propagate under the PV. That is why the response between the PV and the surface is dominated in w by an IGWs packet propagating eastward (Fig. 4.15c,d), which is submitted to multiple reflexion at the surface and at z^*. This lower secondary IGWs packet was already described in Lott (2003) in the case of the Rayleigh-Drazin background flow. Note nevertheless, that Lott (2003) did not observe the upper IGWs observed here above z^*.

The Fig. 4.15 suggests that the generation process of the upper and lower IGW trains is the same as in experiment P1, and the waves have comparable amplitudes. Nevertheless, the vertical EP flux averaged in time between t=41 to 57h are shown in Fig. 4.16. It confirms that the surface Eady wave is not a prerequisite to produce a large transfer of energy toward the disturbance, localized near the altitude z^*. It means that in the present configuration, such that z^* is in the high-troposphere, the meridional flow resulting essentially from the balanced mechanism described in Fig. 4.4 is alone responsible for the transfer of potential energy from the background flow to the perturbation. Consistently, the energy budget shows absence of energy growth after the spin-up time τ_1, since the surface is too far for the PV to excite a substantial Eady

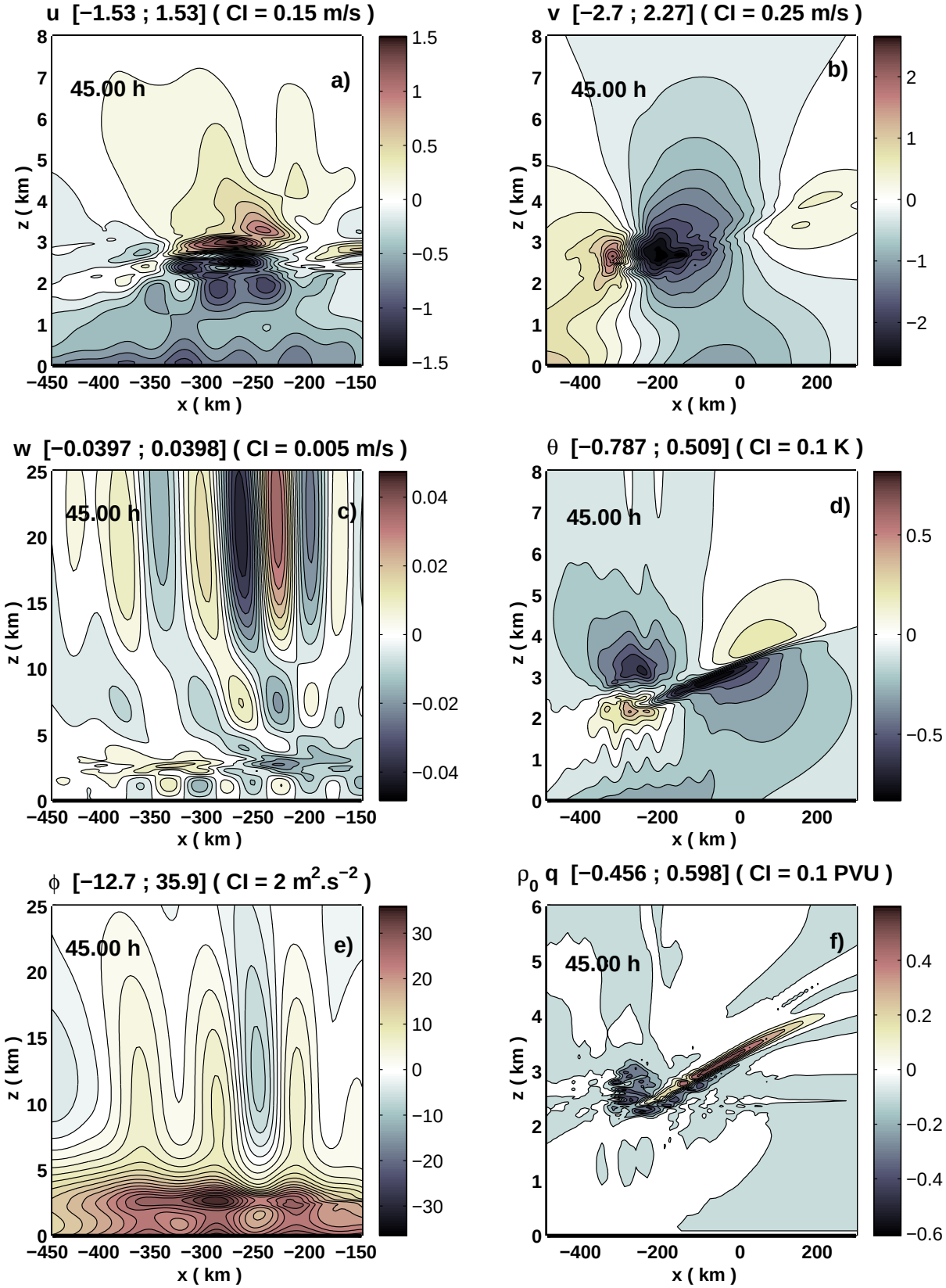

FIG. 4.12 – Total large scale response to the forcing at t=45h for experiment P2 (with $F_0 = \pi.10^{-4}$ m^{2}s^{-2}) : a) zonal velocity, b) meridional velocity, c) vertical velocity, d) potential temperature, e) geopotential perturbation (or pressure) and f) PV anomaly.

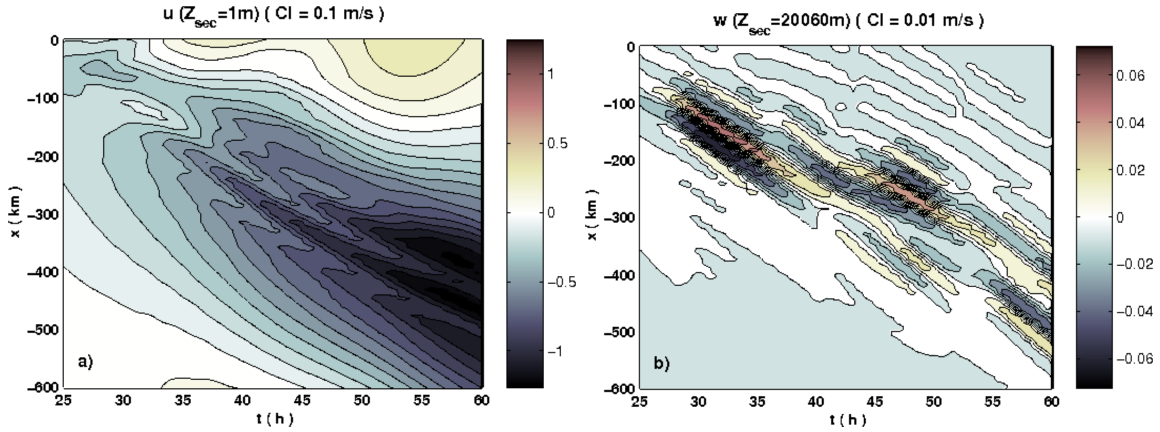

FIG. 4.13 – Hovmuller diagrams for horizontal sections at the level Z_s for experiment P2 (with $F_0 = \pi.10^{-4}$ m^{2}s^{-2}) : a) large scale zonal velocity (Z_s=293m), b) large scale vertical velocity (Z_s=20060m).

wave and resonate with it (not shown).

ii) Diagnosis of a mechanism for IGW secondary generation

In other words, the forcing of a non-geostrophic unstable Eady mode of the type observed in Chapter 3 is not necessary to generate spontaneously upper and lower IGWs packets of the same horizontal scale than the force. The force itself is not necessary neither since the generation lasts almost steadily several inertial periods after its extinction (Fig. 4.9a,b,c and Fig. 4.15). This will be confirmed below with a second experiment called P3b, a variant of P3. The local mechanism described in Fig. 4.4 can help us to understand this secondary generation process. The balanced flow above and under the PV dipole is such that it contains small horizontal scales and fast lagrangian timescales comparable with the inertial period. So that IGWs might be generated with a wavelength of comparable scale, and through a mechanism that might be essentially linear, in response to the pattern of vertical velocity induced by the balanced flow.

In the litterature about spontaneous IGWs generation by jets, some imbalance diagnoses were proposed based on the lagrangian Rossby number (O'Sullivan and Dunkerton, 1995), or on the residual of the Nonlinear Balance Equation (NBE, see Zhang et al. 2001). These are only qualitative nevertheless and do not provide any quantitative mechanism. Moreover, in our context the measure of the lagrangian Rossby number by the ratio of the non-geostrophic wind to the total wind,

$$\mathrm{Ro}^L = \frac{|\mathbf{u}_{ng}|}{|\tilde{\mathbf{u}}|}, \tag{4.16}$$

did not reveal fruitful, because the background wind vanishes in z^*.

More recently, Plougonven and Zhang (2007) have proposed a method to calculate the forcing of IGWs by the synoptic scale flow, by splitting the flow in two components and using scaling arguments. Within the framework of the Boussinesq hydrostatic primitive equations without external forcing, they obtain a wave equation for the short scale and fast part of the vertical velocity w_w, forced by the large scale and slow part of the flow. In Appendix E, we present the adaptation of this method to our anelastic 2D Eady problem, under the hydrostatic approximation. In our context, the forcing

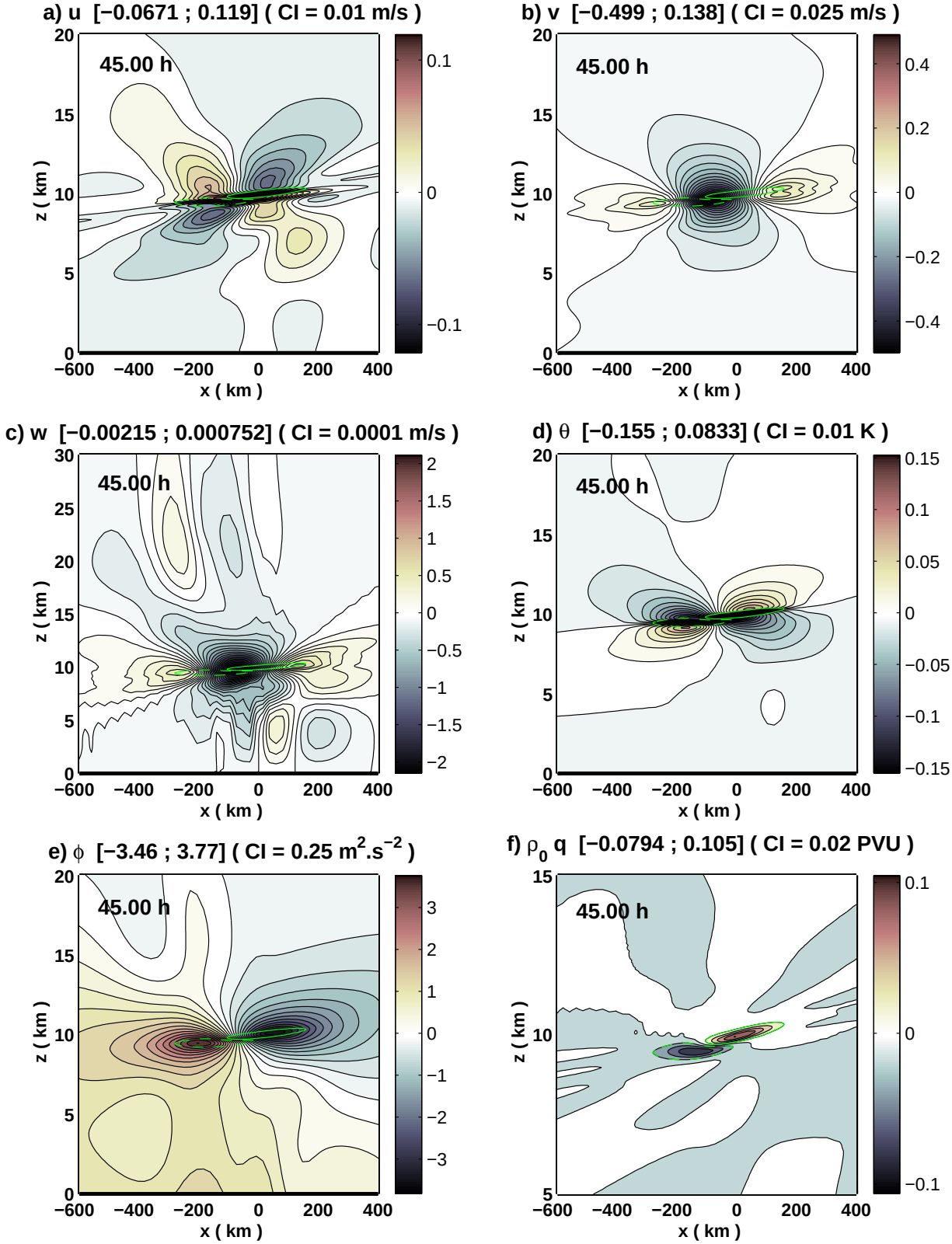

FIG. 4.14 – Total response to the forcing at t=45h for experiment P3 : a) zonal velocity, b) meridional velocity, c) vertical velocity, d) potential temperature, e) geopotential perturbation (or pressure) and f) PV anomaly.

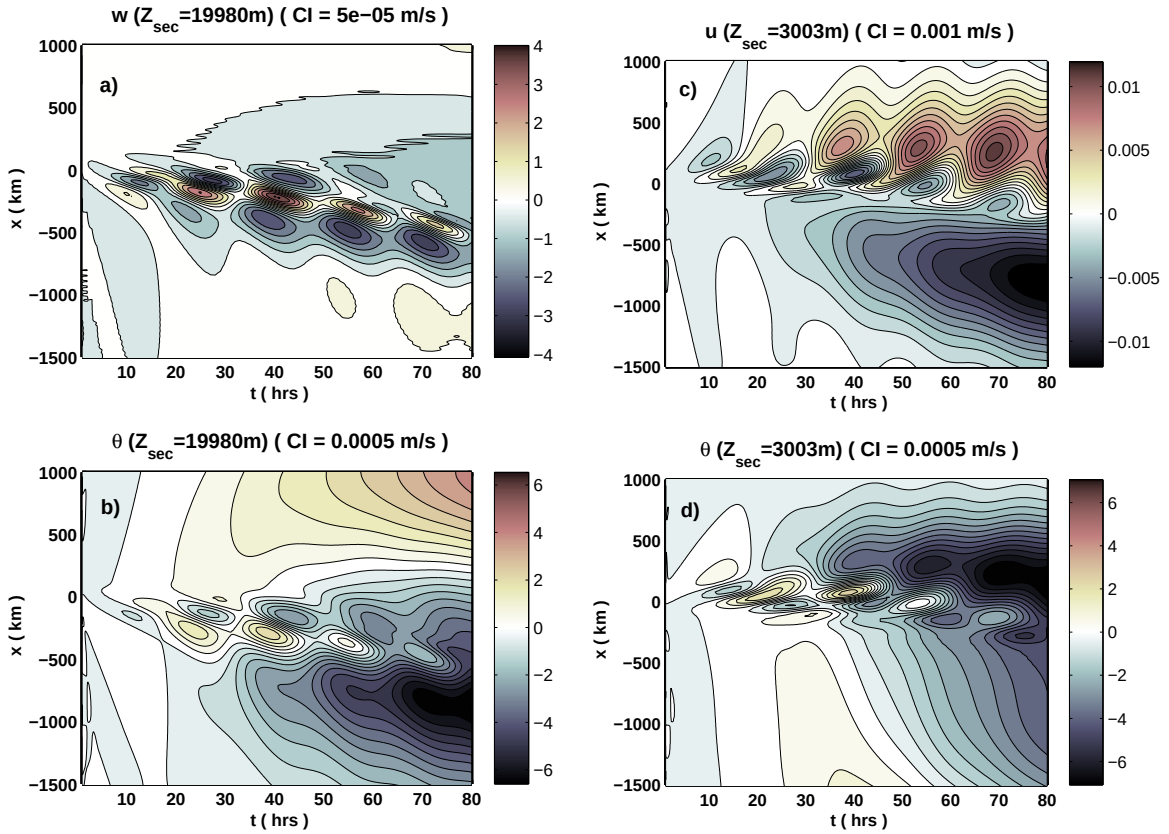

FIG. 4.15 – Hovmuller diagrams for experiment P3, for horizontal sections at the level Z_s=19980m in a) and b), and Z_s=3003m in c) and d). a) vertical velocity, b) and d) potential temperature, and c) zonal velocity.

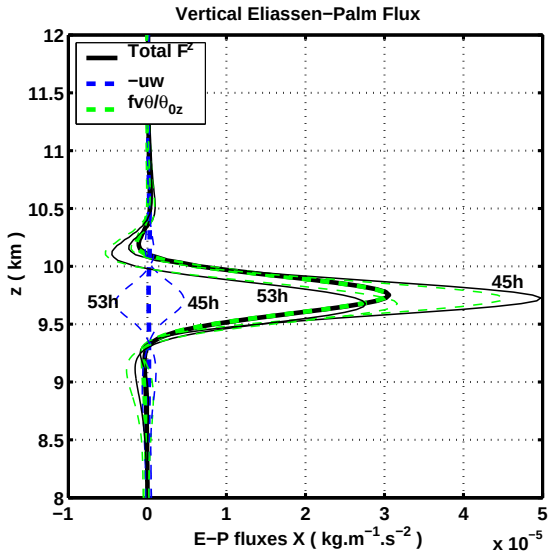

FIG. 4.16 – Horizontal mean of the vertical Eliassen-Palm (EP) fluxes averaged in time between t=40h and t=57h (thick lines), within one inertial oscillation period, for experiment P3. The thin lines are the same profiles at t=45h and 53h.

flow is the balanced flow $\mathbf{U}(z) + \mathbf{u}_b$ and the wave flow is the unbalanced flow $\mathbf{u}_{ub}$. In particular, we add the contribution of a general body force $\boldsymbol{\mathcal{F}} = \mathcal{F}\,\mathbf{e}_x + \mathcal{G}\,\mathbf{e}_y$, and we assume that the horizontal scales of the balanced and unbalanced flow perturbations are equal, consistently with observations. We obtain the following wave equation

$$[D^2 + f^2]\,(\frac{1}{\rho_0}(\rho_0 w_{ub})_z)_z + N^2\,w_{ub_{xx}} \approx \mathcal{S}_{IGW}\,, \tag{4.17}$$

where $D = \partial_t + U\partial_x$, and where $\mathcal{S}_{IGW}$ is a forcing function of $\mathbf{U}(z) + \mathbf{u}_b$. To the first order, the forcing is found to reduce to

$$\mathcal{S}_{IGW} = -\Lambda^2\,w_{b_{xx}} - D\mathcal{F}_{xz} + \Lambda\mathcal{F}_{xx}\,. \tag{4.18}$$

This forcing was computed for experiment P3 at t=45h, and is shown after normalization by $\frac{N^2}{L^2}$ in Fig. 4.17. At this time, the terms linked to the force $\boldsymbol{\mathcal{F}}$ in Eq. (4.18) are null. Hence the IGWs are only forced by the balanced flow through the term $-\Lambda^2\,w_{b_{xx}}$, which has a shape of butterfly centered around the steered PV dipole (in green). This pattern is forcing a horizontal wave-vector component above and below the PV deposit, which corresponds to the small scale IGW packets observed above and under the PV in experiments P1 and P3. Moreover, in a qualitative purpose the Eq. (4.17) can be approximated crudely above and under the PV anomaly, by neglecting the vertical derivative term. This gives

$$w_{ub} \approx -\frac{L^2}{N^2}\,\mathcal{S}_{IGW} \approx \frac{L^2}{\mathrm{Ri}}\,w_{b_{xx}} \sim -\frac{1}{\mathrm{Ri}}\,w_b = -\mathrm{Ro}^2\,w_b\,. \tag{4.19}$$

This indicates that the IGW part of w, that is approximately w_{ub}, must be in phase opposition with $\mathcal{S}_{IGW}$ or w_b in these two areas. This property is indeed observed in the Fig. 4.17 (violet contours for w_{ub}). More generally, it is the reason why the unbalanced surface flow is in phase opposition with the balance one in experiment P1. In addition, the order of magnitude of the IGW response suggested by Eq. (4.19) corresponds to $w_{ub} \sim -w_b/6$. This is in agreement with the ratio of magnitudes observed in Figs. 4.14c and 4.15a, with w_b approximately in the range $[-0.002, 0.0008]\mathrm{m.s}^{-1}$ and w_{ub} approximately in the range $[-0.0002, 0.0003]\mathrm{m.s}^{-1}$.

It is remarkable that the dominant forcing term, $-\Lambda^2\,w_{b_{xx}}$, is the semi-geostrophic residual of the quasi-geostrophic Omega equation (see appendix D). This means that the quasi-geostrophic balance cannot capture this forcing term, and underlines the necessity of using a semi-geostrophic balance for this diagnosis.

Finally, the computation of the additional forcing term linked to the maximum body force $\mathcal{F}$ applied beetween $t = \tau_1$ and $t = \tau_1 + T$, that is $-U\,\mathcal{F}_{xxz} + \Lambda\,\mathcal{F}_{xx}$, gives a strong contribution ($[-0.008; 0.0036]\mathrm{m.s}^{-1}$) with a tripolar pattern, but which is only concentrated near $(x = 0; z = z^*)$. When following the time evolution, the picture of $\mathcal{S}_{IGW}$ described in Fig. 4.17 is very steady during the whole experiment, except that the magnitude decreases slightly in the second half of the experiment. Also, the butterfly pattern is progressively distorted in the end of the experiment, and advected with the negative PV anomaly. During the whole experiment, the unbalanced vertical velocity w_{ub} keeps very steadily connected to the forcing term $\mathcal{S}_{IGW}$ near z^*, respecting very well the relation $w_{ub} * \mathcal{S}_{IGW} < 0$ in this area (except the very localized modulation by the inertial oscillation).

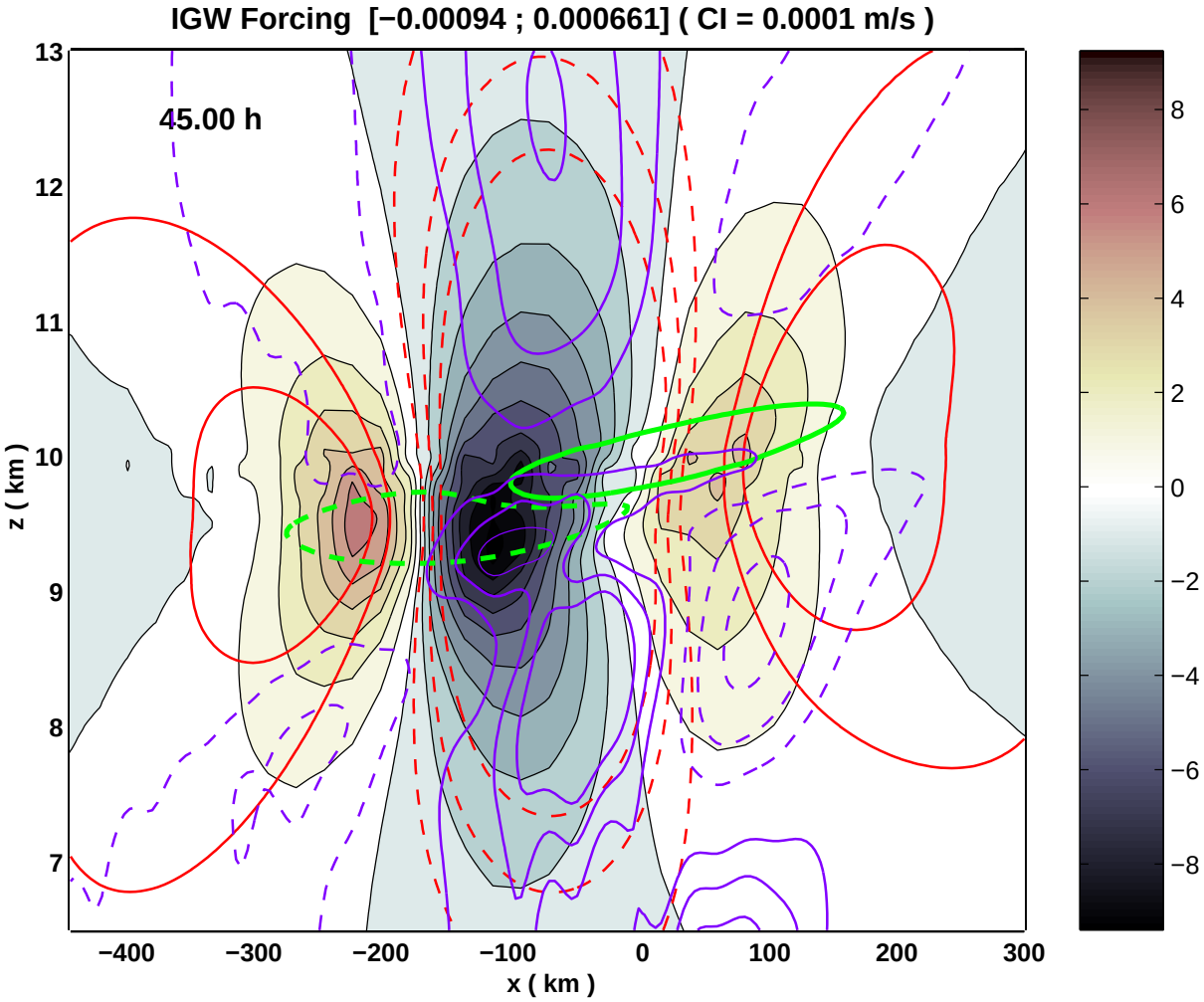

FIG. 4.17 – First order term of the IGW forcing function $\mathcal{S}_{IGW}$ at t=45h for experiment P3, normalized by $\frac{N^2}{L^2}$. The balanced vertical velocity (w_b) contours $[-8,-6,-4,2,4]*10^{-4}$m.s^{-1} are superimposed in red (negative values dashed). The unbalanced vertical velocity (w_{ub}) contours $[-3,-2,-1,1,2,3]*10^{-4}$m.s^{-1} are superimposed in violet. The PV anomaly contours $\pm$0.02PVU are superimposed in green.

iii) Spontaneous generation of IGW by the balanced flow (P3b)

Note that at this stage, the separation summarized in Eq. (4.18) between the direct forcing by the force and the undirect forcing through the balanced flow, does not appear clearly in the Fig. 4.15. A way to better illustrate this conceptual separation is to make the IGW generation longer after the explicit forcing by $\mathcal{F}$. That is why we now modify slightly P3 by reducing the shear to $\Lambda = 2.10^{-3}$s^{-1}, and describe this new experiment called P3b in the rest of this section. Because of this modification, the two PV anomalies will take a longer time to get far from each other, which will increase the duration of the generation.

The Fig. 4.18a and b present respectively the total and unbalanced vertical velocity at t=45h. Comparison with the Fig. 4.14c shows two differences. The first difference is that the phase lines of the upper IGWs are clearly less vertically tilted than in P3, which was naturally expected for IGWs propagating in a smaller shear. The second difference is that the magnitude of the IGWs, and more generally the global magnitude,

is weaker than in P3. The reasons can be listed this way : (i) the vertical non advective PV flux is proportional to Λ, and hence the PV anomaly and the geostrophic fields are also proportional to Λ while the ageostrophic fields w_b and u_b are proportional to Λ^2 (see appendix D, and notably the Omega equation), (ii) the position of the two PV anomalies one relative to the other is different in P3 and P3b for the same date because the advection is different, and (iii) $\mathcal{S}_{IGW}$ is proportional to Λ^2 and to w_b.

The Fig. 4.19a presents the Hovmuller diagram of the vertical velocity in P3b, for a horizontal section at 20km, and should be compared to the Fig. 4.15a. This diagram corroborate the two differences described previously. In addition, the generation continues very steadily more than 80hrs, as expected. Furthermore, we see that at this level the IGWs are not modulated any more by the inertial oscillation, contrary to what is observed in P3.

Finally, to leave no ambiguity about the fact that the IGWs are generated by the balanced flow, we proceed with a last experiment. The force is removed such that there is no forcing in the problem. But now the flow is initialized by the balanced perturbation flow obtained in P3b at t=40h. The Hovmuller diagram of the vertical velocity at z=20km is shown in the Fig. 4.19b for comparison. It can be seen that after a short adjustment stage in the first hours, the IGWs generation settles again, with approximately the same magnitude.

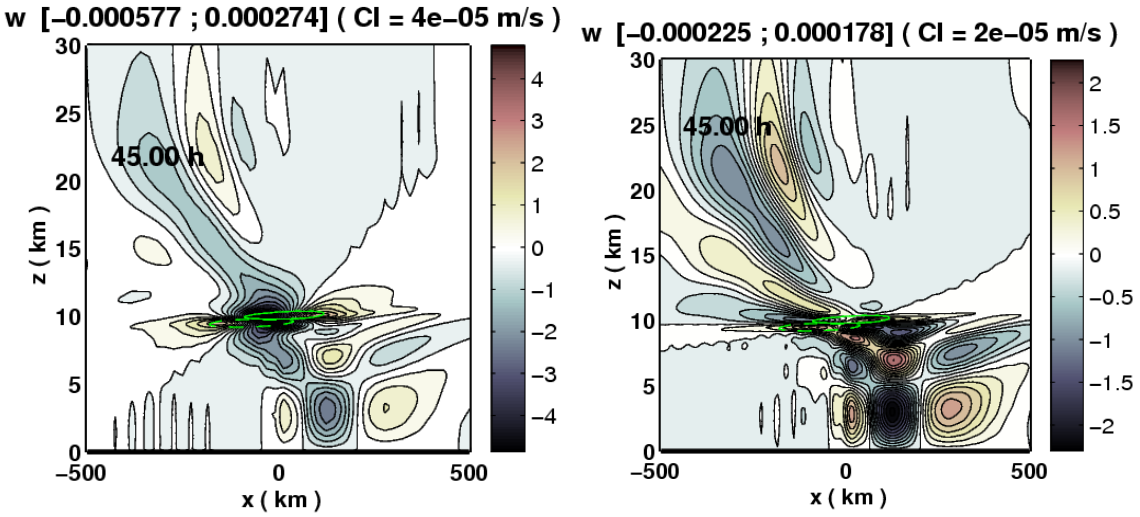

FIG. 4.18 – Response to the force at t=45h for experiment P3b : a) total vertical velocity, b) unbalanced vertical velocity. The PV dipole is localized by its contours ±0.02PVU.

Consequently, we conclude that the forcing term $-\Lambda^2 w_{b_{xx}}$ given in Eq. (4.18) can be considered as the essential cause of generation of the small scale upper and lower IGWs packets observed in Figs. 4.14c and 4.15 for the overall experiment, as well as more generally in all the experiments of this chapter. We note that the process is more efficient in a strongly sheared background wind. The fact that the forcing is simply proportional to $-w_{b_{xx}}$ confirms that the mechanism is linked to the production of rather small horizontal scales by the juxtaposition of PV anomalies of opposite signs. This results in small lagrangian time scales in the vertical motion above and below the PV dipole, where the background flow is large enough. Thus, the perturbation flow linked to the PV is connected to IGWs near their inertial critical level, that is where the inertial frequency of the waves is of order f.

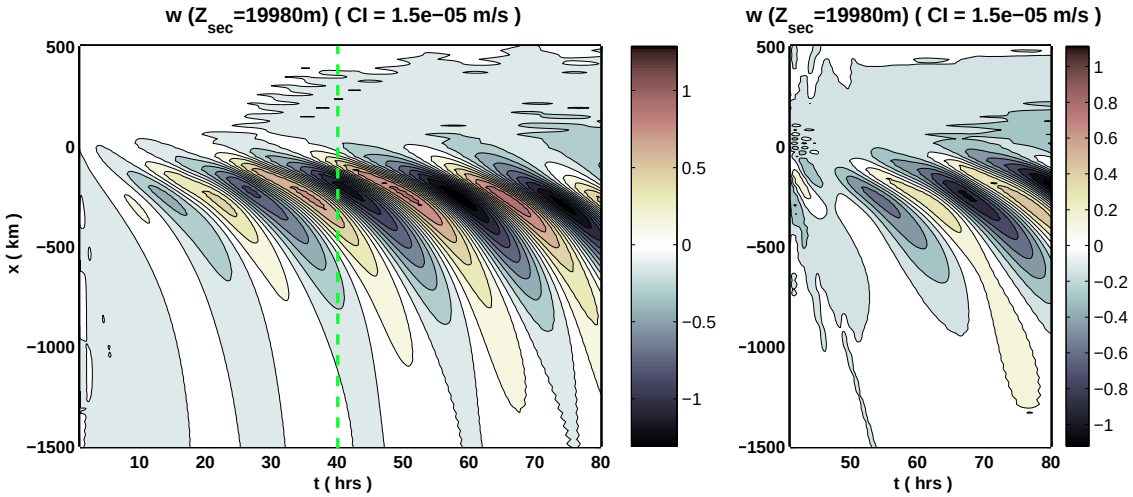

FIG. 4.19 – Hovmuller diagram of the vertical velocity for a horizontal section at the level Z_s=19980m : a) experiment P3b, b) experiment initialized by the balanced flow of P3b at t=40h, that is the date of the end of the force.

4.3 Large scale response to short scale orography

In this section, the background wind of Eq. (4.1) is submitted to an idealized orographic profile h that represents the small scale orographic variance of an isolated gaussian mountain. This profile is made of around 10 parallel ridges of width λ_w and maximum height $2H_0$,

$$h(x,t) = s(t)\, H_0\, e^{\{-\frac{x^2}{L^2}\}}\, \cos\left(\frac{2\pi x}{\lambda_w}\right), \tag{4.20}$$

and is modulated by the same function $s(t)$ defined in Eq. (4.3). The surface boundary condition is linear :

$$w(x, z=0, t) = U_0.\partial_x h(x,t) \tag{4.21}$$

In this context, we do not have to prescribe any parameterized force. By filtering the equations of motion given in appendix A (Eqs. (4.34)-(4.35)) with the same low-pass filter as in section 4.2.3 (symbol $< >$)[4], we obtain a system governing the large scale flow $(\mathbf{u}_L, \theta_L) = (< \mathbf{u} >, < \theta >)$. In this system, the short scale flow $\mathbf{u}_S = \mathbf{u} - \mathbf{u}_L$ enters into account by the large scale mean of the nonlinear short scale advective terms, which gives rise to a force upon the large scales :

$$\boldsymbol{\mathcal{F}} = < -(\mathbf{u}_S \boldsymbol{\nabla})\mathbf{u}_S > . \tag{4.22}$$

We neglect the heating term $< -(\mathbf{u}_S \boldsymbol{\nabla})\, \theta_S >$ since it is weak for short GWs. Note that by introducing also the large scale nonlinear advective term $-(\mathbf{u}_L \boldsymbol{\nabla})\mathbf{u}_L$ in the definition $\boldsymbol{\mathcal{F}}$, our problem can now be thought in terms of the linear response to a given dynamical large scale forcing. Actually, in our case this choice will not be crucial because the large scale flow is generally weak enough to be neglectable in $\boldsymbol{\mathcal{F}}$.

4.3.1 Large scale response to a tiny mountain (M1)

Now we define a reference experiment called M1, from which we will start a series of sensitivity tests and comparisons with experiment P1. All the physical parameters of M1 are the same as in P1, except that the force is replaced by the mountain of Eq. (4.20) where

$$H_0 = 15\,\text{m},\;\; L = 100\,\text{km, and}\;\; \lambda_w = 25\,\text{km}. \tag{4.23}$$

The experimental setup is identical to the one of experiment P1, except for some parameters summarized in table 4.1. Notably, because we need now to resolve the short mountain GWs dynamics with the same CPU time constraint, we reduce the total domain length to $2L_D = 2\pi * 170$km and remove the lateral sponge layers. Consequently, we must reduce the duration of the experiment in order to limit the effects of the periodical horizontal boundary conditions. Note that raising and then lowering smoothly the mountain is not realistic, but in the context of our model, it is a simple way to take into account that in reality the baroclinic front impinging on the mountain has a limited extent.

To damp correctly the short scale mountain GWs where they reach their critical level, we need to increase slightly the diffusivity as regard to the experiments P. It

[4]We use the same wavenumber cut-off $k = 30$, now keeping wavelengths larger than 40km.

is set to $\mu = 0.15$ m^{2}s^{-1}. In such conditions, the viscous scale l_μ of the critical level interaction, defined by Hazel (1967), is

$$l_\mu = \left[\frac{\mu\lambda_w}{\rho_0\, 2\pi\Lambda}\right]^{1/3} \sim 56\text{m}. \tag{4.24}$$

This gives an indication for the vertical resolution needed to resolve the critical level interaction of the short scale mountain GWs near z^* (see appendix E).

i) Short scale flow

The total perturbation flow response is shown in Fig. 4.20 at t=22h, with the profile of the mountain as a reference (which was artificially elevated to 1000m for visibility). We also show in Fig. 4.21a the small scale contribution F^z_S to the total vertical EP flux F^z at t=22h, computed by

$$F^z_S = \rho_0 \left[\frac{f}{\theta_{0z}}\,\overline{v_S\theta_S} - \overline{u_S w_S}\right], \tag{4.25}$$

and carried by the wavelengths smaller than 80km.

The flow is dominated by the small scale GWs generated by the small scale orography, with an amplitude reaching nearly 0.5-1m.s^{-1} for u and v, 0.2K for θ and 0.05m.s^{-1} for w. The phase lines are tilted upwind, and tend to become more and more horizontal when approaching the critical level $z^* = 3.5$km, since the ratio between vertical and horizontal group velocity must vanish at the critical level. The amplitude of w decreases with height, whereas on the contrary the amplitudes of u, v, and θ increase with height, to maintain a vertical EP flux constant with height under the critical level. Note that the latter is not rigorously constant (Fig. 4.21a). Before the decrease in amplitude near the critical level, there is a rapid increase because of the existence of an inertial critical level slightly underneath. This could be eliminated by taking shorter mountain GWs. Above the critical level, the mountain waves and the flux are almost null. We also notice that at the date t=22h, the meridional velocity has a blatant negative horizontal mean (Fig. 4.20b), which is the large scale southward jet in response to the GWs.

As reminded in Appendix C, the vertical divergence of the EP flux F^z can be in general interpreted as a force acting upon the transform eulerian mean of the zonal flow $\overline{u}$. Similarly, here $\partial_z F^z_S$ can be related to the force acting upon the large scale zonal flow u_L, that is $\mathcal{F}$. This zonal force $\mathcal{F}$ is computed from Eq. (4.22), and shown in Fig. 4.21b at t=22h, which is the date when it is maximum. Both pictures in Fig. 4.21 agree to indicate a positive force localized just under the critical level, approximately between z=3.2 to 3.4km. The amplitude of the force is $2.8.10^{-5}$ m^{-1}.s^{-2} (Fig. 4.21b), which is of the same order as in experiment P1 ($\pi.10^{-5}$). And the force is embeded over the mountain, with a horizontal width shorter than the mountain width because the relation between $\mathcal{F}$ and h is quadratic. This point was taken into account in Eq. (4.2). Actually, the profile of F^z_S also agrees quantitatively with $\mathcal{F}$. The maximum vertical derivative of F^z_S is evaluated to $3.0.10^{-4}$kg.m^{-1}.s^{-2} To compare $\partial_z F^z_S$ to $\mathcal{F}$, the flux must be renormalized to take into account that the effective area occupied by the short mountain GWs is not the entire domain but a horizontal column of approximate width $\mathrm{L}_F \sim L \sim$100km, as illustrated by $\mathcal{F}$ in Fig. 4.21b. This yields

$$\frac{1}{\rho_0(z^*)}\,\partial_z \tilde{F}^z_S = \frac{1}{\rho_0(z^*)}\,\frac{2\mathrm{L}_D}{\mathrm{L}_F}\,\partial_z F^z_S \approx 3.6.10^{-5}\,\text{m}^{-1}.\text{s}^{-2}. \tag{4.26}$$

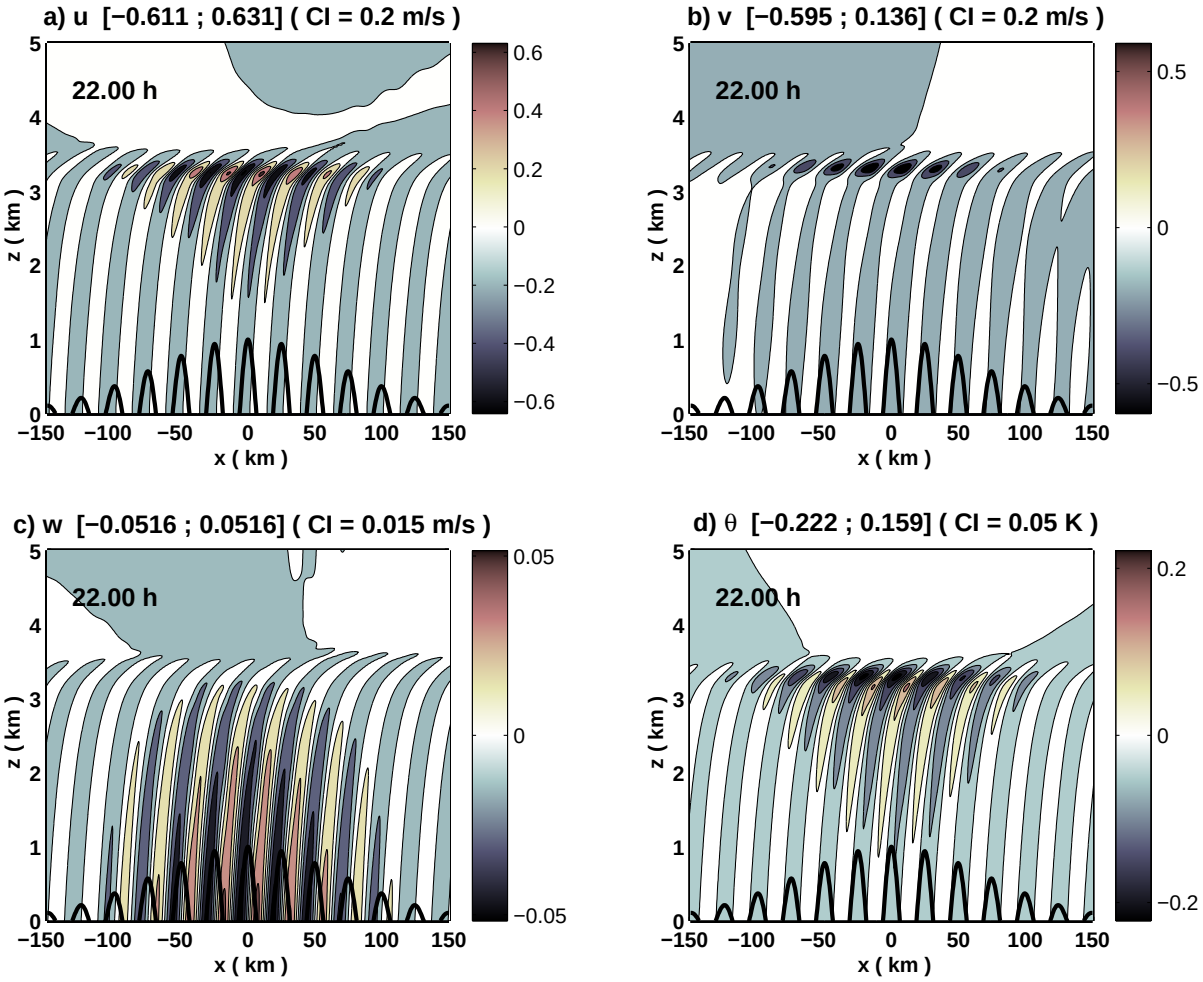

FIG. 4.20 – Total response to the orography at t=22h for experiment M1 : a) zonal velocity, b) meridional velocity, c) vertical velocity and d) potential temperature. The mountain height is not true but artificially elevated to 1000m for visibility.

Note that this last comparison can be used as a method to tune the value of L_F, and more generally to build the profile of the parameterized force in P1 (Chen et al. 2007).

Noteworthy, the forcing zone is thinner than in the parameterized form of experiment P1 (Eq. (4.5)). In particular, it is not significant higher than z^*. This is a consequence of using a 2D mountain. This generates only zonally propagating mountain waves which must all break near and under z^*. Note that the thickness of this force can be increased by increasing artificially the diffusivity. In the more realistic case of a 3D isolated mountain and a background wind turning with height, there exist an ensemble of directional critical levels that distribute vertically the force more smoothly (Shutts 1995, Martin and Lott 2007). That is the reason why the parameterized force was chosen slightly thicker in the experiments P. Notably, in experiments P the force is significant at the height z^*, which gives a higher positive PV anomaly. Because of that, the form of the PV dipole will evoluate slightly differently in M than in P.

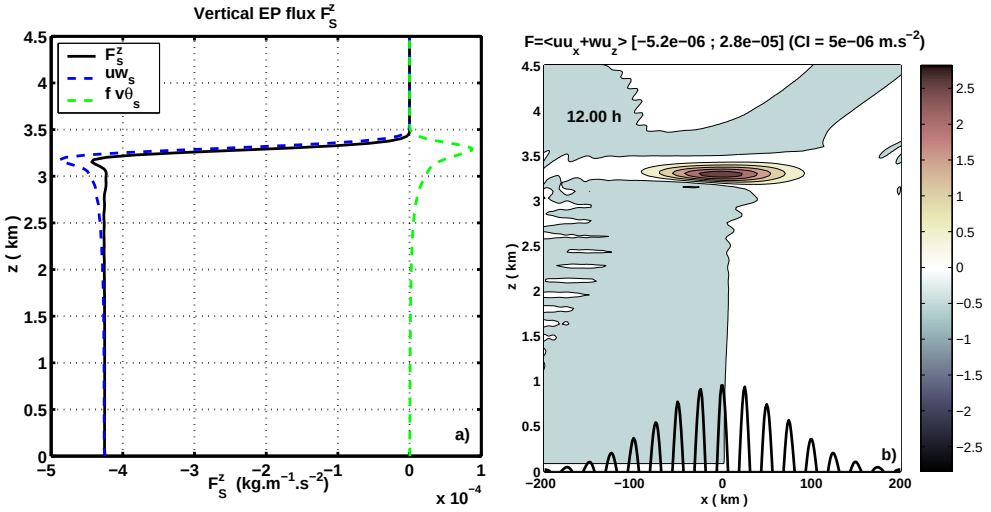

FIG. 4.21 – a) Horizontal mean of the vertical EP flux carried by the small scales F_S^z ($\lambda < 80$km), at t=22h, for experiment M1. The two contributions are shown in green and blue (Eq. (4.25)). b) Zonal forcing term of the large scale dynamics, $\mathcal{F} = - < \mathbf{u_S}.\boldsymbol{\nabla} u_S >$, for experiment M1 at t=22h.

ii) Large scale flow

Now that we have shown that the force upon the large scales was very close to the parameterized force in experiment P1, we analyse and compare the large scale response. The total large scale flow is shown at t=45h in Fig. 4.22, 5h after the complete end of the forcing, and Hovmuller diagrams are given in Fig. 4.23. Comparison with the Figs. 4.6 and 4.9 shows that the process was rather correctly parameterized in experiment P1. Not only the main qualitative features observed in P1 are recovered in M1, but also the magnitudes are of the same order., though smaller by a factor near 2.

We note nevertheless several important differences. First, all the fields are globally smaller than in P1 by a factor 2. Second, the positive PV anomaly is more horizontal (pay attention nevertheless to the horizontal domain which is smaller), because the advection by the vertical velocity is weaker. And the PV lobes are slightly shorter in the horizontal, and thinner in the vertical. Third, the surface Eady wave is proportionally less developped compared to the whole response, and the near geostrophic fields v and θ are embedded in a horizontal layer that is thinner than in P1.

Essentially two reasons can account for these differences. The first is physical : the actual force $\mathcal{F}$ has a thinner vertical profile than the parameterized force in P1. The second is numerical : the computional horizontal domain is highly reduced in M1 compared to P1 and the lateral damping layers have been removed. This second reason is believed to have the greatest impact. Indeed, by preventing the larger scales to arise in the signal, it reduces the magnitude of the whole response, and especially the surface Eady wave which is a very large scale feature. In addition, the periodical lateral boundaries have now a visible impact on the Eady wave, which is also developped in the upslope side of the mountain.

The weakness of the Eady wave is also clearly visible in the surface Hovmuller diagram of u in Fig. 4.23b (and ϕ, not shown), where it appears mixed with an IGW packet generated by the same process than above the PV, propagating eastward like

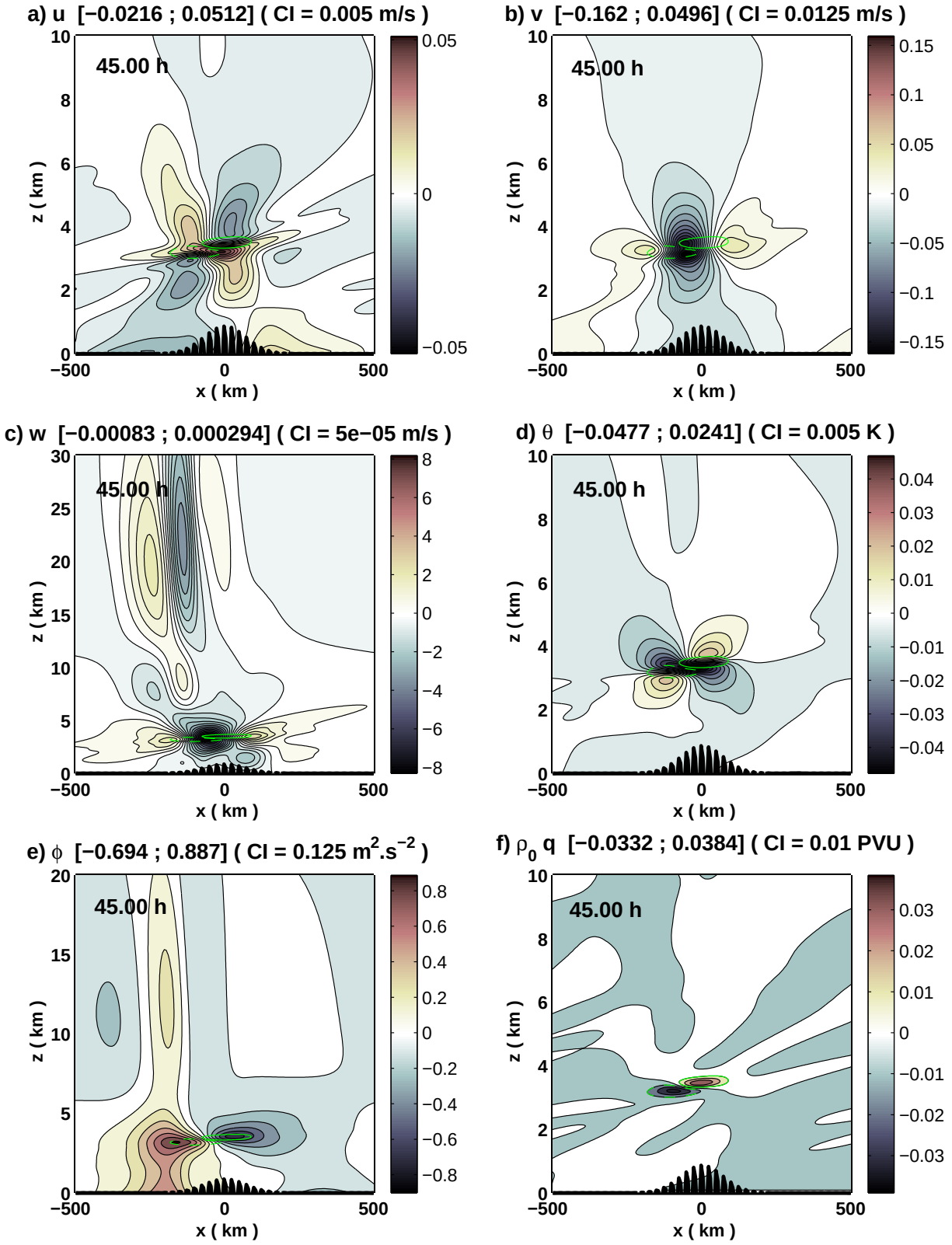

FIG. 4.22 – Total large scale response to the orography at t=45h for experiment M1 : a) zonal velocity, b) meridional velocity, c) vertical velocity, d) potential temperature, e) geopotential perturbation (or pressure) and f) PV anomaly.

in experiments P. These lower IGW packets are less so visible at the end of the experiment, when the balanced response becomes substantial.

To complete the comparison with experiment P1, we present the energy budget diagnoses for M1. The vertical EP flux carried by the large scales ($\lambda < 80$km), averaged over an inertial period from t=37 to 50h, that is essentially after the end of the mountain forcing, is shown in Fig. 4.24. Note that from t=40hHence, there is no more EP flux carried by the short scales, because there are no more short scale mountain GWs in the flow. The flux is only significant near the PV, but it almost vanishes below. This confirms that the mechanism is the same as in P1, but that the surface Eady wave is largely weaker in M1.
The time evolution of the perturbation energy and its components is shown in Fig. 4.25a. The energy curves ressemble very much those of P1 in Fig. 4.7, for the corresponding domain of time, except a delay of about 5h which is due to the spin-up of the force. Notably, the unbalanced flow is naturally faster than the balanced flow to settle in response to the forcing. This was not the case in Lott (2003) because the forcing was taking part to the balance (his Fig. 10). Nevertheless, the orders of magnitude of the energy is around 5 times smaller here than in P1, which is notably due to the weakness of the surface Eady wave.

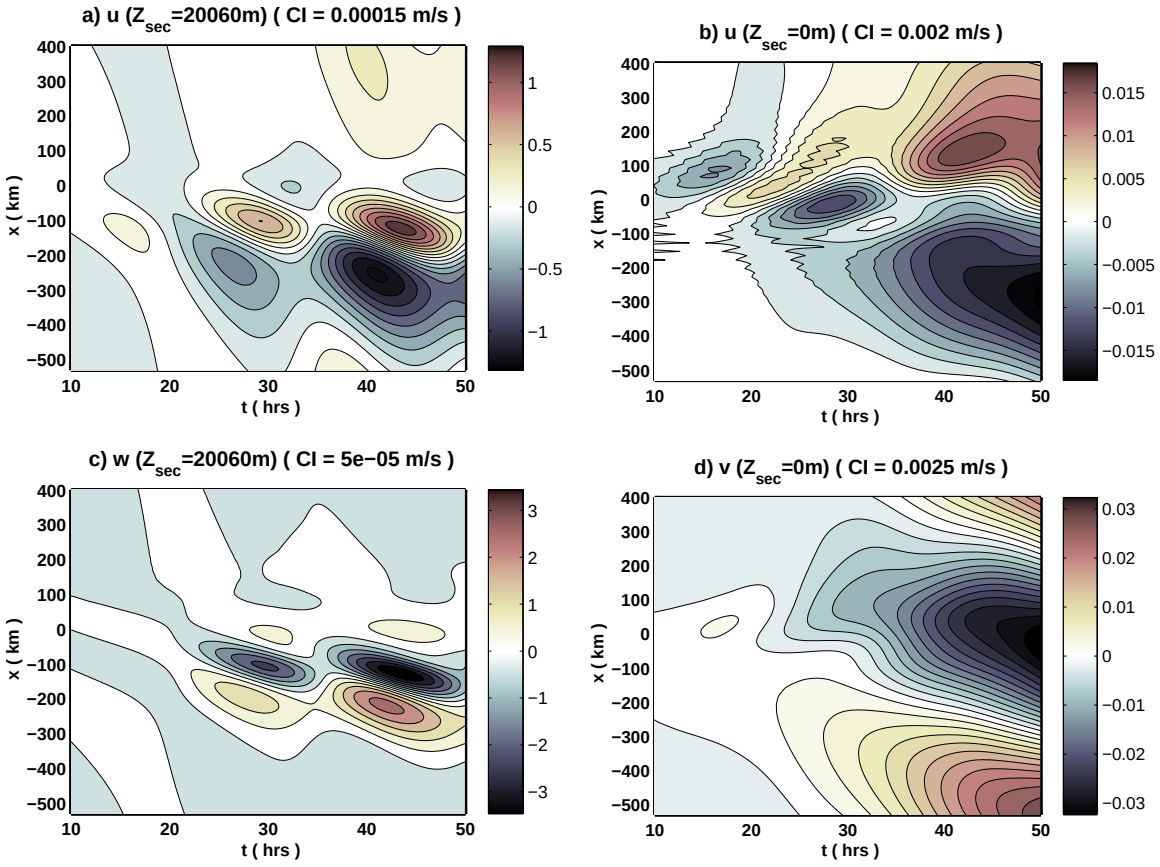

FIG. 4.23 – Hovmuller diagrams for experiment M1, for horizontal sections of the large scale flow at the level Z_s=20060m in a), c) and Z_s=0m in b), d) : a) and b) zonal velocity, c) vertical velocity and d) meridional velocity.

Increasing the height of the critical level for the mountain GWs was also found to give results ressembling those of P3. But the question remains to study the relationship between the height of the mountain and the resulting force applied to the large scale flow by the GWs. The next section is dedicated to this question.

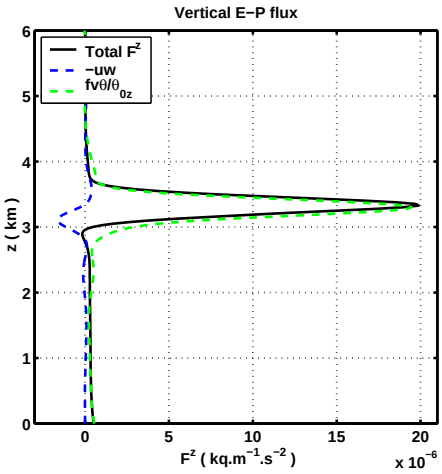

FIG. 4.24 – Vertical EP fluxes carried by the large scales ($\lambda < 80$km), and averaged in time within one inertial period, between t=37h and t=50h (thick lines), for experiment M1.

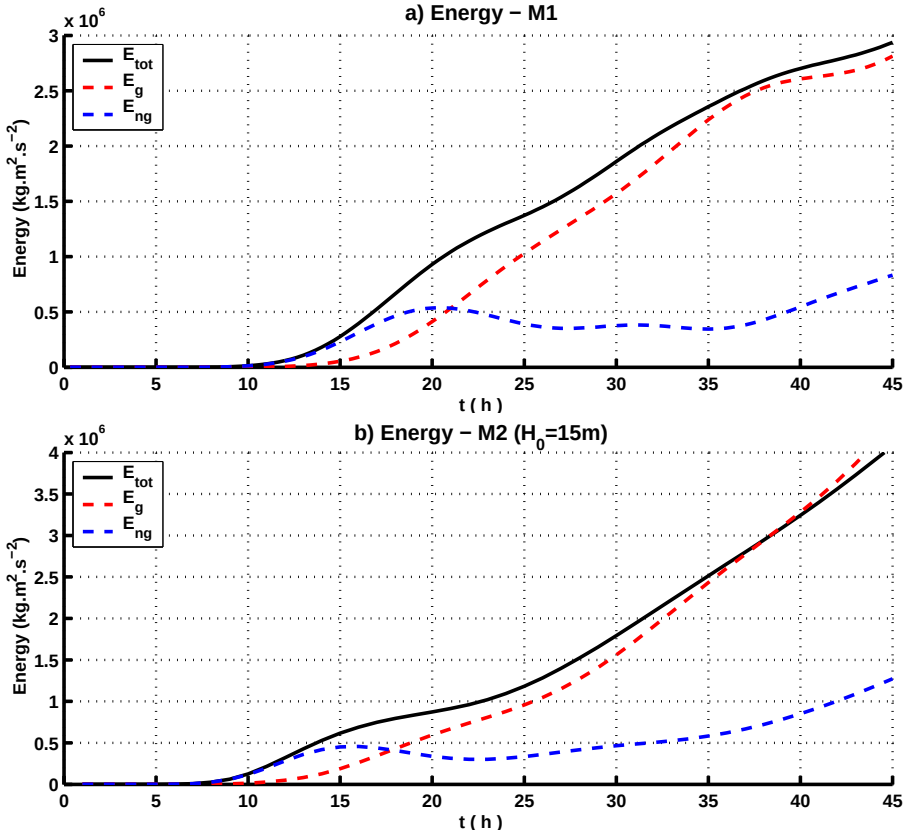

FIG. 4.25 – Large scale energy budget versus time, for experiment M1 (a) and M2 (H_0=15m) (b).

4.3.2 Nonlinear saturation for higher mountains

In this section, we study the sensitivity of the problem to the height of the mountain H_0, looking for the level at which nonlinear behaviour starts to modify the behaviour of experiment M1. We define an experiment called M2, which is the same experiment as M1 except : (i) the short wave critical level is raised to $z^* = 5$km by imposing the surface wind $U_0 = -20\text{m.s}^{-1}$, (ii) the characteristic half width of the mountain is slightly reduced to $L = 75$km, and (iii) the spin-up parameters are $\tau_1 = 15$h, $T = \infty$ (the orography is never removed). M2 is repeated for increasing values of H_0, from 15m to 250m, high mountains being prohibited by the loss of numerical stability.

The energy budget for H_0=15m is given in Fig. 4.25b for comparison with M1, in which the time evolution of the forcing was more complex. Here, the mountain is raised more slowly and remains until the end. The energies reached are then globally smaller than in M1 during the start-up stage. But they are comparable at the end, because the mountain is continously forcing the atmosphere until the end in M1. Notably, the growth of the balanced energy is linear in the last 15 hours, which likely indicates a resonance between the PV and a surface Eady wave.

The Fig. 4.26 presents the evolution of the drag exerted by the mountain GWs (a), and the associated inflow zonal force (b and c), versus H_0. To measure the drag, we average in time the short scale EP flux $|F_S^z|$ between t=8h and t=30h, and take minus the minimum value of the profile, after smoothing over a window of 75m, and renormalizing by $\frac{L}{2L_D}\frac{4NU_0H_0^2}{\lambda_w}$. The force is measured as the maximum vertical divergence of the smoothed F_S^z, and after smoothing once again over a window of 75m. The Fig. 4.26a shows that the normalized drag seems to be optimal for an intermediate half-height of H_0=50. After this value the normalized drag starts to decrease because of the nonlinear saturation of the critical level interaction. Meanwhile, the corresponding normalized force also decreases. Note that the force does not increase when the drag increases. The reason is that the critical layer, where the EP is absorpted, is becoming thicker and thicker, which increases the vertical depth of the momentum deposit, but reduces the maximum magnitude of the force. We notice incidentally in Fig. 4.26c that the normalized force seems to follow a law in $1/H_0$.

These results can be better understood by introducing the nonlinear scale l_N (Lott and Teitelbaum 1992), which caracterizes the distance from z^* under which the critical level dynamics is nonlinear :

$$l_N = \left[\frac{NU_0H_0^2}{\Lambda^2}\right]^{1/3} . \tag{4.27}$$

This length should be compared to the viscous scale l_μ defined in Eq. (4.24), which amounts to $l_\mu \sim 89$m for M2. For $H_0 = 50$m (respectively 75m), we obtain $l_N = 85$m (respectively 98m). This explains that the nonlinear behaviour starts to be efficient for half-heights larger than $H_0 = 50$m, that is for mountains higher than 100m.

To better understand the nonlinear behaviour, we describe briefly what happens for $H_0 = 150$m. The time average of the small scale vertical EP flux is shown in Fig. 4.27 (thick lines), together with the profiles at each hour of the simulation (thin lines). In the first hours, the profile is smooth and regular, and tend to settle as the expected nearly monotonous profile found in Fig. 4.21. But it never reaches this expected profile, and from t=6h it starts to oscillate in a way that seems rather chaotic, changing drastically

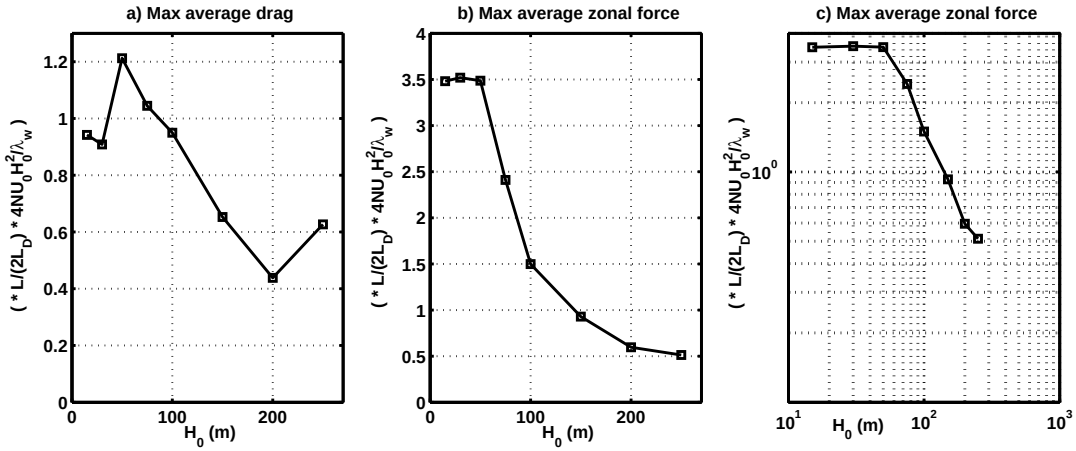

FIG. 4.26 – Evolution of the maximum absolute vertical zonal mean EP flux F_S^z (small scales) averaged between t=8h and t=30h (a) and its maximum vertical divergence (b, and c in loglog) with increasing heights H_0 (15m to 250m), for experiments M2. Both quantities are normalized by $\frac{L}{2L_D}\frac{4NU_0H_0^2}{\lambda_w}$.

its shape at each hour. Noteworthy, the global time average EP flux seems correct because monotonous and nearly constant under z=3km. But its magnitude is around -0.025 kg.m^{-1}.s^{-2} near the surface, that is only 60 times larger than in M1 (Fig. 4.21), whereas the height was multiplied by 10 and the EP flux should be quadratic in H_0. Therefore, the process is loosing its efficiency for such a small mountain ($2H_0$=300m). This behaviour of the small scale EP flux follows that the GWs experience strong and repeated reflections at the critical level z^* and at the surface (Lott 2003).

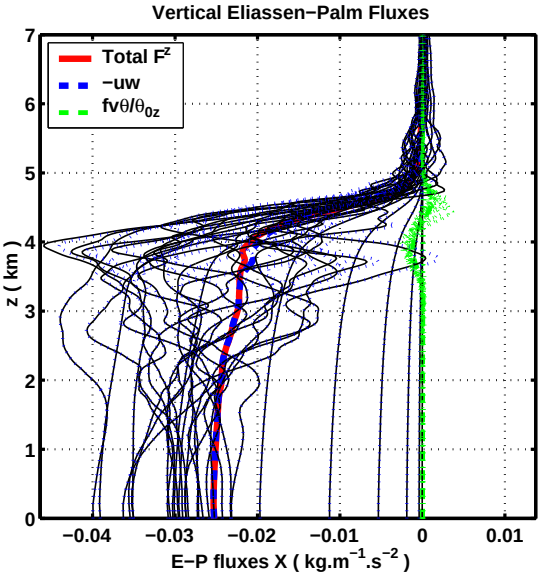

FIG. 4.27 – Horizontal mean of the vertical EP fluxes carried by the small scales ($\lambda < 80$km) at each hour (thin lines), and averaged in time between t=1h and t=30h (thick lines), for experiment M2 ($H_0 = 150$m). Note that the total EP flux is always in black, except in the mean profile where it is red for clarity.

Nevertheless, we know from the section 4.2.2 that, if the force is increased by a

factor 60 from the value in Fig. 4.21b ($2.8.10^{-5}$), the effect of the PV deposit should be nonlinear as in P2. This is confirmed by the Figs. 4.28 and 4.29, which show respectively the total large scale response at t=20h, and the Hovmuller diagrams of its sections at z≈20km. The PV anomalies are seriously disturbed by local instabilities (Fig. 4.28f), while the IGWs generated are significantly more intense ($w \sim 0.05\text{m.s}^{-1}$) and shorter (100 to 200km) than in M1. Their phase velocity is also larger, around 6-7m.s^{-1}, corresponding to a critical level around z=3250-3500m. Because of this fast velocity, the IGWs tend to escape from the mountain and travel a significant distance. Finally, the surface pressure perturbation reaches around 25Pa, which is now significant but still weak.

4.4 Conclusion

In this chapter, we have applied the same 2D model as in the previous chapter, to study the subsynoptic scale response of an Eady background shear flow to an horizontal body force localized in space and time. In the first part, the force is parameterized and designed to represent the effect of the short scale orographic variance of an isolated mountain, when the short mountain GWs break at a critical level. In the second part, the force is directly resolved by the model in the presence of an idealized mountain.

For both forcing methods, we obtain similar polychromatic linear responses, in which we identify three components. The first component is an inertial oscillation which stays embeded in the forcing area, and does not influence neither the surface nor the upper atmosphere. It is due to the temporal spectrum of the force applied, which always contains some energy near the inertial frequency. The two other components are directly related to the PV dipole induced by the force and steered by the background shear. In this 2D problem, only the vertical component of the non advective PV flux is relevant, and it points upward. This induces a positive PV anomaly above a negative one, the latter moving faster away from the mountain (Fig. 4.2). Therefore, from the standpoint of the surface or the tropopause, the PV dipole is approximately seen as a horizontal juxtaposition of opposite anomalies.

The second component of the linear response is observed in the larger scales, and was diagnosed as a non-geostrophic unstable Eady mode ressembling those studied in the previous chapter. We show that if the PV dipole is close enough to the surface, it induces a surface Eady wave which propagates, starting with a cold high pressure anomaly in the lee of the mountain (Figs. 4.3, 4.4 and 4.9d,e,f). In terms of lee cyclogenesis, this means that in this 2D context the primary effect of the force is cyclolytic. Nevertheless, this effect is weak, notably because it is reduced by the unbalanced component of the response. Also, the development of the lee wave is accelerated by the unbalanced flow. And the surface wave goes on interacting with the flow near the forcing area even after that the force is removed. An unstable coupling settles, analogous to the one observed in the non geostrophic unstable Eady modes, dominated by the meridional heat flux (Figs. 4.7-4.8). But the associated growth is rather rapid, accelerated by the presence of the advected PV near the steering level of the surface wave. Above the PV, a weak IGW of the same scale as the surface wave develops, with the correct phase lag (Fig. 4.6c).

The third component of the linear response dominates the small scales of the signal. It was diagnosed as a spontaneous secondary generation by the PV dipole, above and

below itself, of IGW packets having approximately the same horizontal scale than the force (Figs. 4.6c and 4.9a,b,c). These IGWs are substantially more intense than the previous very large scale IGW associated to the non-geostrophic unstable modes. And their horizontal scale and phase velocity indicate that they are directly coupled with the PV rather than with the surface Eady wave. This was confirmed by raising the force in the high troposphere, such that the surface Eady wave is neglectable in front of these IGW packets (Figs. 4.14c and 4.15). Moreover, they are in phase opposition with the local balanced flow near the PV. Because of that, they reduce the amplitude of the balance surface Eady wave, and hence the cyclolytic impact.

This latter mechanism of IGW secondary generation relies on the production of a PV dipole. The fact that the PV anomalies are localized approximately side by side rather than one above the other, because they have been shifted by the background shear, seems to be favorable. The peculiar associated balanced circulation is far from geostrophy, because rather small horizontal scales exist near the dipole. Thus, this balanced flow is naturally coupled to IGWs which have a horizontal scale comparable to the scale of the PV anomalies. This interpretation is supported by the diagnosis of the IGWs forcing function (Fig. 4.17), adapting the method proposed by Plougonven and Zhang (2007). This diagnosis allowed to account aproximately for the observed magnitude ratio between the IGWs and the balanced flow, which was found to satisfy approximately $w_w \sim \frac{L^2}{\mathrm{Ri}}\, w_{b_{xx}} \sim -\frac{1}{\mathrm{Ri}}\, w_b \sim -\mathrm{Ro}^2\, w_b$. In this regard, there is a similarity between this generation process and the large scale IGWs generation by nearly balanced jets and fronts, when small spatial scales and small lagrangian timescales are produced by the natural breakdown of balance (Snyder et al. 1993, O'Sullivan and Dunkerton 1995, Zhang 2004, Plougonven and Snyder 2007). Of course, the process that builds the PV dipole in our problem is not completely balanced before the begining of the IGWs generation process. But the generation is sustained steadily for several inertial periods, and well after the extinction of the body force. Moreover, these IGWs are also generated when initializing the perturbation flow with the balanced flow associated to the PV dipole. Snyder et al. (2007) have studied a problem that has some similarity, in which IGWs are generated by a dipole of 3D vortices initially totally balanced, which moves slowly at the surface. We have also carried on a somewhat similar experiment, initializing the flow with the balanced flow inverted from an idealized PV dipole ressembling the one of Fig. 4.2. The IGWs generation was also observed.

Noteworthy, the PV dipole is advected and can behave as a moving source of IGWs thanks to this mechanism. Therefore, it is a way for mountains to generate IGWs at a long distance. Moreover, this generation process does not seem to be exclusively owing to the presence of critical level absorption of mountain GWs. It should appear more generally as soon as a local body force is exerted upon a background shear flow, producing PV anomalies which are shifted one as regards to the other. In particular, the force can be owing to overturning breaking mountain GWs. More generally, it might also work in case of weak background shear, if any kind of low level orographic process produces dipolar PV banners so elongated that they are quasi 2D. In this regard, the small scale of the primary PV banners observed during the MAP campaign (Schär et al 2003, Flammant et al 2004) might produce intense IGWs. Finally, another efficient process to produce two side by side PV anomalies of opposite signs, is to apply a body force perpendicular to the background wind, $\boldsymbol{\mathcal{F}} = \mathcal{G}\, \mathbf{e}_y$, because in this case the horizontal non advective PV flux $\mathbf{J}_{Nx} = -\mathcal{G}\theta_{0z}\, \mathbf{e}_x$ dominates the PV budget. This happens notably when mountain GWs are absorpted by directional critical levels

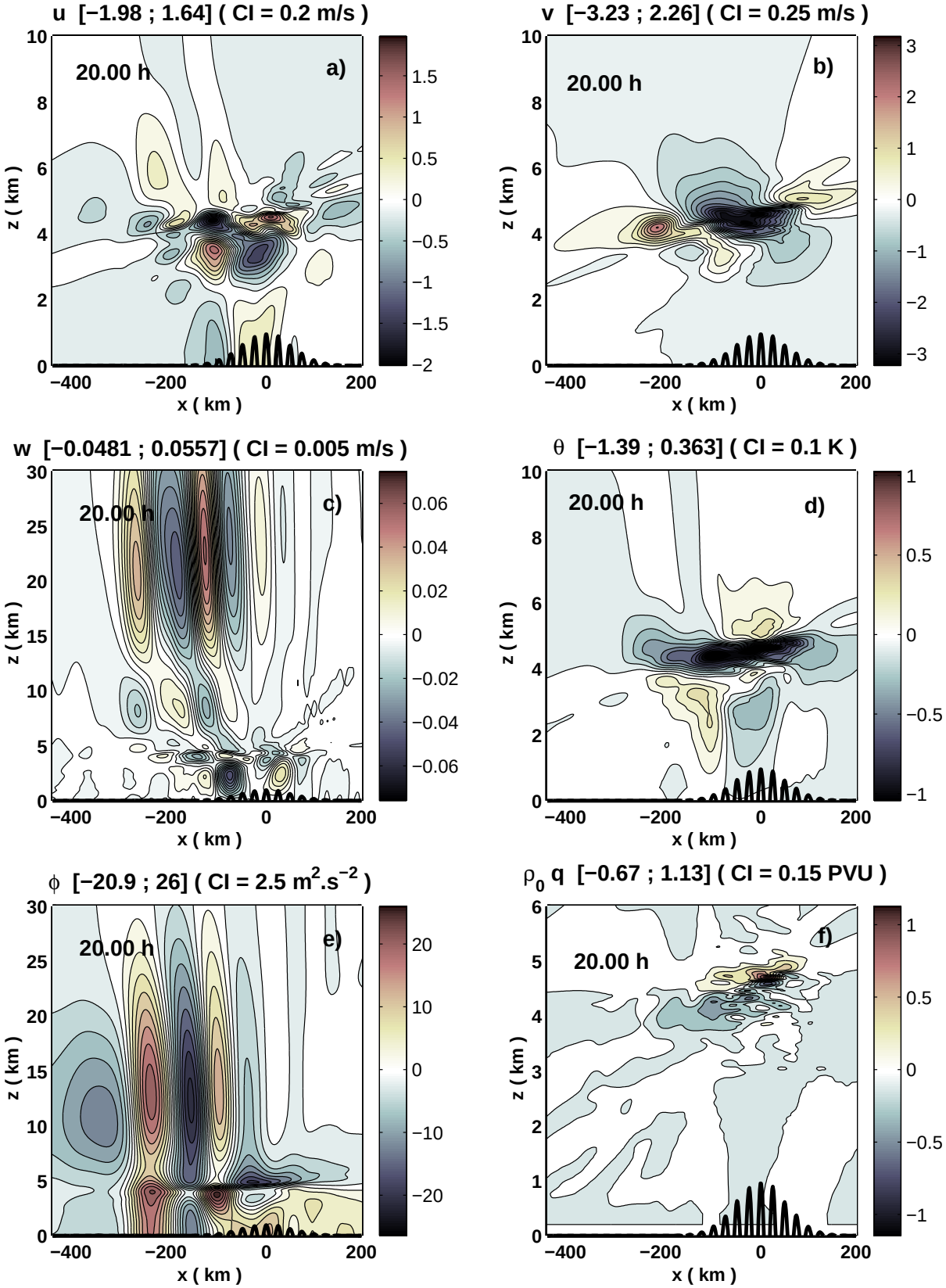

FIG. 4.28 – Total large scale response to the orography at t=20h for experiment M2 (H_0 = 150m) : a) zonal velocity, b) meridional velocity, c) vertical velocity, d) potential temperature, e) geopotential perturbation and f) PV anomaly.

(Shutts 1995, Martin and Lott 2007). Some of these different situations can be studied easily within the present 2D model. Such experiments might also help to elucidate further the intermitency observed here in the IGWs generation.

Because of the peculiarity of the Eady model which requires a uniform shear over the entire domain, the IGWs observed here have almost vertical phase lines, which is not really realistic given the large horizontal scale of these waves. The use of a Rayleigh-Drazin type wind profile might help to obtain more horizontal group velocities, by chosing a shear layer of moderate depth. For such a background wind nevertheless, the hypothesis of a 2D flow is not sustainable any more in the presence of rotation, because of the existence of a non uniform meridional potential temperature gradient (Appendix A). Note that the inclusion of a stratosphere should also force the energy to propagate vertically, by refracting the waves.

When the response is nonlinear, that is for a stronger body force or for higher mountains, intense shear-generated IGWs appear and dominate the signal, because of the small scale instabilities of the layer distorted by the strong PV anomalies (Fig. 4.11). These short IGWs can almost dominate the surface Eady wave in amplitude (Figs. 4.12, 4.13, 4.28 and 4.29). In this context, the surface signal can be increased locally, but it is difficult to draw a general rule of thumbs concerning the impact in terms of lee cyclogenesis. This highly depends on the structure of these IGWs. Nevertheless, for the same reason, that is the breakdown of the negative PV anomaly, the magnitudes found for the surface Eady wave as well as for the IGWs do not increase linearly with the magnitude of the force. This is a first saturation process for the forcing of the surface Eady wave. Note that it is for the same physical reason that non-geostrophic unstable Eady modes cannot reach very large magnitudes, that is because of the breakdown of their critical layer, as shown in the previous chapter.

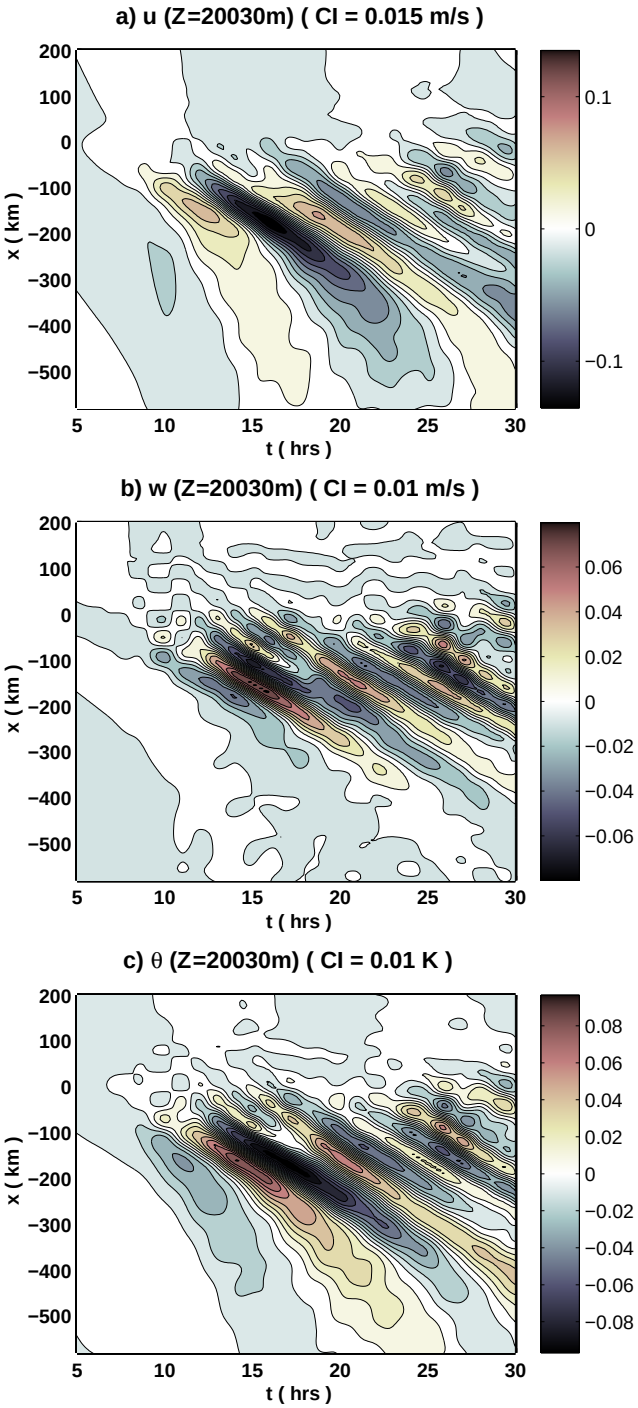

FIG. 4.29 – Hovmuller diagrams for experiment M2 (H_0 = 150m), for horizontal sections of the large scale flow at the level Z_s=20060m : a) zonal velocity, b) vertical velocity and c) potential temperature.

Finally, the direct simulation of the short mountain GWs has shown that the nonlinearity of the critical level interaction, in the presence of a complex orography with several ridges, implies a saturation of the body force itself even for relatively small mountains. This is a second saturation process for the surface response. Nevertheless, it is likely that this saturation mechanism appears for higher mountains in the case of a 3D orographic profile, because the GWs can radiate in the meridional direction. More generally, the orographic spectrum chosen here is rather sharp. Real orographic spectra and directional windshear result in a smoothing of the singularity at the critical levels. This might allow forces stronger than in our simulations, and within deeper layers. High resolution 3D simulations are necessary to assess these points. Nevertheless, combining both of the nonlinear saturation mechanisms described here, namely the critical level interaction and the small scale shear and convective instabilities, we find unlikely to get responses of magnitude larger than $w \sim 0.1\text{m.s}^{-1}$ and $p \sim 1\text{mb}$.

Appendix

A. Model Equations

We choose the 2D rotating anelastic system in the f-plane, in which we divide the total flow $\tilde{\mathbf{u}}$ into (i) a linear background wind $\mathbf{U}(z) = U(z)\,\mathbf{e}_x + V_0\,\mathbf{e}_y$ where $U(z) = U_0 + \Lambda z$, and (ii) a perturbation $\mathbf{u}(x,z,t)$:

$$\tilde{\mathbf{u}} = \mathbf{U}(z) + \mathbf{u}(x,z,t) \text{ where } \mathbf{u} = (u,v,w). \tag{4.28}$$

The total potential temperature field can be defined as the sum of (i) a hydrostatic reference state profile $\theta_0(z)$, (ii) a background state $\Theta(y,z)$ in thermal wind balance with $\mathbf{U}(z)$, (iii) a local drift $\theta_d(y,z,t) = -V_0\,\Theta_y\,.\,t$ caused by advection by the meridional background wind V_0, and (iv) a perturbation $\theta(x,z,t)$ corresponding to the flow perturbation $\mathbf{u}(x,z,t)$:

$$\tilde{\theta} = \theta_0(z) + \Theta(y,z) + \theta_d(y,z,t) + \theta(x,z,t). \tag{4.29}$$

We use the approximation of Lipps and Hemler (1982) to write the pressure force with the use of a geopotential $\tilde{\phi}$ in the form $-\boldsymbol{\nabla}\tilde{\phi}$. This approximation allows the anelastic system to conserve total energy. As for $\tilde{\theta}$ we separate $\tilde{\phi}$ into the corresponding three parts :

$$\tilde{\phi} = \phi_0(z) + \Phi(y,z) + \phi(x,z,t). \tag{4.30}$$

Anywhere in the paper, the subscripts $_x$, $_y$ and $_z$ denote the corresponding spatial derivative. The 2D incompressibility is written for the perturbation, considering a hydrostatic reference state density $\rho_0(z)$:

$$\nabla\cdot(\rho_0\mathbf{u}) = \partial_x(\rho_0 u) + \partial_z(\rho_0 w) = 0, \tag{4.31}$$

which allows to define a streamfunction $\psi(x,z,t)$ associated to (u,w) by

$$\rho_0(u\,\mathbf{e}_x + w\,\mathbf{e}_z) = \mathbf{e}_y \times \nabla\psi \text{ , that is } u = \frac{1}{\rho_0}\frac{\partial\psi}{\partial z} \text{ and } w = -\frac{1}{\rho_0}\frac{\partial\psi}{\partial x}. \tag{4.32}$$

The hydrostatic reference state $(\theta_0(z), \phi_0(z), \rho_0(z))$ is determined by imposing a constant Brunt-Vaisalla frequency N, where $N^2 = \frac{g}{\theta_0(z)}\frac{d\theta_0}{dz}$, which is equivalent to consider an isothermal atmosphere at rest[5].
The background wind is required to be geostrophic, $f\mathbf{e}_z \wedge \mathbf{U} + \nabla\Phi = 0$, therefore the background thermal-wind balance can be integrated into :

$$\Theta(y,z) = -\frac{f\theta_0(z)\Lambda}{g}\,.y \tag{4.33}$$

In Eq. (4.33), g and f are respectively the gravity constant and Coriolis parameter. In this framework, the momentum equation and the thermodynamic equation that govern the evolution of the perturbation can be written respectively in the following way, separating the linear (left hand) and nonlinear (right hand) terms, and adding diffusion terms and arbitrary forcings $\boldsymbol{\mathcal{F}}$ and H :

$$(\partial_t + U\partial_x)\mathbf{u} + \Lambda w\mathbf{e}_x + f\mathbf{e}_z \times \mathbf{u} + \nabla\phi - g\frac{\theta}{\theta_0}\mathbf{e}_z = -(\mathbf{u}\nabla)\mathbf{u} + \frac{1}{\rho_0}\nabla(\mu\nabla\mathbf{u}) + \boldsymbol{\mathcal{F}} \tag{4.34}$$

$$(\partial_t + U\partial_x)\theta + v\,\Theta_y + w\,\theta_{0z} = -(\mathbf{u}\nabla)\theta + \frac{1}{\rho_0}\nabla(\kappa\nabla\theta) + \dot{\mathrm{H}} \tag{4.35}$$

[5]Actually, under this strong approximation, the anelastic system is equivalent to the non hydrostatic primitive equations system in log-pressure coordinates.

In Eq. (4.35) we have neglected the term $w\Theta_z$ as regards to $w\theta_{0z}$ in order not to break the two-dimensionality of the system. Indeed, this way there is no dependence on y in Eqs. (4.34)-(4.35), whereas $\Theta_z = -\frac{f}{g}\frac{d\theta_0(z)}{dz}\Lambda.y$ introduces a small dependence in y. This approximation is valid if $\theta_{0z} \gg |\Theta_z|$, that is if $y \ll \frac{g}{f\Lambda} \sim 10000$km taking $f \sim 10^{-4}$ s^{-1} and $\Lambda \sim 10^{-2}$ s^{-1}, which is largely verified for any kind of 2D mountain on Earth. Note that this approximation can be avoided by choosing a shear that satisfies $\theta_0(z).\Lambda(z) =$ constant, which differs only by 10% from the constant shear for a domain 20km high. We did not do that choice in order to compare strictly to the other studies of constant shear unstable NG modes.

Note also that in Eq. (4.35), θ_d does not appear by definition. Indeed, this term only represent a horizontally uniform potential temperature advection, which essentially modifies the stratification. Therefore, it is possible to neglect this modification within a time satisfying the approximate condition $t \ll t_d = \frac{\theta_{0z}}{V_0\Theta_{yz}} = \frac{g}{fV_0\Lambda} \sim 280$ hours taking $V_0 \sim 10$ms^{-1}. The advantage of this formulation is that we can state that within a time $t < t_d$, the evolution of the flow perturbation will be qualitatively the same for any kind of veering background wind with uniform shear as for the unidirectionnal case $V_0 = 0$, which is not very realistic.

Finally, the upper and lower boundary conditions imposed are free slip and rigid. Notably, we apply a linear lower boundary condition if there is a topography $h(x)$:

$$w(x, z = 0) = \mathbf{U}(z = 0).\boldsymbol{\nabla} h(x). \tag{4.36}$$

B. Energy budget

The energy budget associated to this model is obtained from the combination $\rho_0(z)(\mathbf{u}*$ (4.34) $+\frac{g^2}{\theta_0^2(z)N^2}\theta*$ (4.35)) and using the continuity Eq. (4.31), to form what can be seen as the the local perturbation energy[6]

$$e = \frac{\rho_0}{2}\left(u^2 + v^2 + w^2 + \frac{1}{2}\frac{g^2}{\theta_0^2 N^2}\,\theta^2\right). \tag{4.37}$$

After integrating over the entire domain and removing the vanishing terms because of periodicity, it remains a tendency budget of the form :

$$\begin{aligned}\frac{\mathrm{d}}{\mathrm{dt}}\int_0^{Z_T}\!\!\int_{-L_D}^{L_D} e\,\mathrm{d}z\mathrm{d}x \;=\; & \int_0^{Z_T}\!\!\int_{-L_D}^{L_D}\rho_0\left[\frac{\Lambda f}{\theta_{0z}}\,v\theta - \Lambda\,uw - \mathbf{u}(\mathbf{u}\nabla)\mathbf{u} - \frac{g^2}{\theta_0^2N^2}\,\theta(\mathbf{u}\nabla)\theta\right. \\ & \left. + \frac{1}{\rho_0}\,\mathbf{u}\nabla(\mu\nabla\mathbf{u}) + \frac{g^2}{\rho_0\theta_0^2N^2}\,\theta\nabla(\kappa\nabla\theta) + \mathbf{u}.\boldsymbol{\mathcal{F}} + \frac{g^2}{\theta_0^2N^2}\,\theta\dot{\mathrm{H}}\right]\mathrm{d}z\mathrm{d}x\end{aligned} \tag{4.38}$$

When studying the large scale energy budget, we replace in Eqs. (4.37)-(4.38) the fields $(\mathbf{u}, \theta)$ by their large scale part after filtering ($<\mathbf{u}>, <\theta>$), except in the advective tendencies where $(\mathbf{u}\nabla)\mathbf{u}$ and $(\mathbf{u}\nabla)\theta$ are replaced by $<(\mathbf{u}\nabla)\mathbf{u}>$ and $<(\mathbf{u}\nabla)\theta>$. Accordingly, for the large scales these averadge advective terms act as forcing terms similar to the last two terms of Eq. (4.38).

[6]More precisely, this quadratic quantity is a usefull norm that represents the leading order approximation of the perturbation pseudoenergy relative to the background state (Scinocca and Shepherd, 1992). For very large perturbations, this cannot be strictly taken as the energy of the perturbation.

C. Transformed Eulerian Mean equations and Eliassen-Palm flux

To study the forcing of the large scales by the small scale waves, it is generally more adapted to use a transformed Eulerian Mean (TEM) of the equations of the large scale flow (Andrews and McIntyre, 1976). By applying a zonal mean operator ($\bar{x}$) to the Eqs. (4.34)-(4.35), and introducing the continuity Eq. (4.31), we get the large scale flow equations. Then, we introduce the residual mean circulation for this 2D problem

$$(v^*; w^*) = \left(\overline{v} - \frac{1}{\rho_0} \partial_z \left(\rho_0 \, \overline{v\theta}/\theta_{0z} \right) ; \overline{w} \right), \tag{4.39}$$

and obtain the TEM momentum equations

$$\partial_t \, \overline{u} - f \, \overline{v^*} = -\frac{1}{\rho_0} \partial_z \left(\rho_0 \, \overline{uw} - \rho_0 \, \frac{f \, \overline{v\theta}}{\theta_{0z}} \right) + \frac{1}{\rho_0} \partial_z \mu \partial_z \overline{u} \tag{4.40}$$

$$\partial_t \, \overline{v^*} + f \, \overline{u} = -\frac{1}{\rho_0} \partial_z \left(\rho_0 \, \overline{vw} + \partial_t \left(\rho_0 \, \frac{\overline{v\theta}}{\theta_{0z}} \right) \right) + \frac{1}{\rho_0} \partial_z \mu \partial_z \overline{v} \tag{4.41}$$

$$\partial_t \, \overline{\theta} + \Theta_y \, \overline{v^*} = -\frac{1}{\rho_0} \partial_z \left(\rho_0 \, \overline{\theta w} + \Theta_y \, \rho_0 \, \frac{\overline{v\theta}}{\theta_{0z}} \right) + \frac{1}{\rho_0} \partial_z \kappa \partial_z \overline{\theta} \, . \tag{4.42}$$

Note that usually, only the departures x' from the zonal mean flow variables $\bar{x}$ are used in the right hand quadratic terms of Eqs.(4.39)-(4.42), because the contribution of the mean is negligeable. But we prefer this formulation here because the vertical Eliassen-Palm (EP) flux

$$F^z = \rho_0 \left[\frac{f}{\theta_{0z}} \, \overline{v\theta} - \overline{uw} \right] \tag{4.43}$$

appears directly in the perturbation energy budget. Indeed, the first two terms in the right hand of Eq. (4.38) are exactly proportional to the vertical integral of F^z because the shear is constant. Therefore, in our context F^z represents not only the EP flux the vertical divergence of whom is the zonal force exerted by the waves on the zonal mean flow, but also the vertical distribution of the lowest order non diffusive energy tendency terms, which describe respectively the exchange of potential ($\overline{v\theta}$) and kinetic ($\overline{uw}$) energy with the background flow. Finally, the EP flux F^z can also be used as an action flux. But we do not do so in this study, because in our context the action cannot be defined as a one-signed quantity (Andrews, 1987), which limits the potential benefits in terms of wave generation interpretation.

D. Balanced equations system

We use a linear semi-geostrophic balance adapted from Martin and Lott (2007) for the anelastic context. In the 2D context, the only geostrophic component of the wind perturbation is $v_b \equiv \partial_x \phi_b / f$ ($-\partial_y \phi_b / f = 0$), and the forced balanced equations reduce to

$$\begin{aligned}
\Lambda \, w_b - f v + \partial_x \phi_b &= \mathcal{F} && \text{(a)} \\
(\partial_t + \mathbf{U}\nabla) \, v_b + f u_b &= \mathcal{G} && \text{(b)} \\
\partial_z \phi_b &= g\theta_b/\theta_0 && \text{(c)} \\
(\partial_t + \mathbf{U}\nabla) \, \theta_b + \Theta_y \, v + \theta_{0z} \, w_b &= \dot{\mathrm{H}} && \text{(d)} \\
\partial_x(\rho_0 u_b) + \partial_z(\rho_0 w_b) &= 0 && \text{(e)} \, ,
\end{aligned} \tag{4.44}$$

in which we have introduced a meridional force G and a heating term H for generality. From the system of Eqs. (4.44), we form the linearized budget of the PV disturbance q. For this, we calculate $\boldsymbol{\nabla} \wedge ((4.44a),(4.44b),(4.44c)) .(0, \Theta_y, \theta_{0z}) - \theta_{0z} R_i^{-1} \partial_x (4.44b) + f \partial_z (4.44d)$, and use Eq. (4.33), which yields after neglecting the small terms :

$$(\partial_t + \mathbf{U}\nabla)\ \rho_0 q + \nabla . \mathbf{J}_N = 0 \ , \text{ where} \tag{4.45}$$

$$\rho_0\, q \ = \ \theta_{0z}(1 - Ri^{-1})\, v_{bx} + f\theta_{bz} \ , \text{ and} \tag{4.46}$$

$$\mathbf{J}_N \ = \ -\,\theta_{0z}\,(1 - Ri^{-1})\,\mathcal{G}\,\mathbf{e}_x - \Theta_y\,\mathcal{F}\,\mathbf{e}_z \ . \tag{4.47}$$

In Eqs. (4.45) and (4.47), $\mathbf{J}_N$ is the non-advective PV flux.

Using the geostrophic equilibrium for v_b and the hydrostasy, we obtain the link between the PV perturbation and the geopotential perturbation,

$$\frac{\rho_0 g}{f\theta_0}\, q = \phi_{b_{zz}} + \frac{N^2}{f^2}(1 - Ri^{-1})\, \phi_{b_{xx}} \tag{4.48}$$

which can be inverted to find a particular solution ϕ_p that vanishes at the lower and upper boundaries. The total geopotential perturbation is then found by adding two Eady edge waves for the surface and the top of the model (this one is neglectable here because the top is very high, z_{top}=40km),

$$\phi_b(x,z,t) = \phi_p(x,z,t) + \phi_{0s}(x,t)e^{-\lambda z} + \phi_{0t}(x,t)e^{+\lambda(z - z_{top})} \ , \tag{4.49}$$

and applying the thermodynamic Eq. (4.44d) at the two boundaries. The use of these boundary conditions to compute the evolution of the edge waves is described in more details in Martin and Lott (2007).

Using the same method as for the total perturbation, we derive a balanced energy budget similar to the previous one for the balanced perturbation, whose energy is now reduced to the geostrophically and hydrostatically balanced fields :

$$e_g = \frac{\rho_0}{2}\left(v_b^2 + \frac{g^2}{\theta_0^2 N^2}\,\theta_b^2\right). \tag{4.50}$$

Note that in Eq. (4.50), e_g is only the energy of the geostrophic flow, but not of the complete balanced flow. To be consistent with this, we do not define an unbalanced energy, but a non geostrophic energy, by :

$$e_{ng} = \frac{\rho_0}{2}\left(u^2 + v_{ub}^2 + w^2 + \frac{g^2}{\theta_0^2 N^2}\,\theta_{ub}^2\right). \tag{4.51}$$

We then form the Omega equation by $\frac{g}{f\theta_0}\partial_x(4.44d)$ -$\partial_z(4.44b)$+(4.44e), which yields

$$\left(\frac{1}{\rho_0}(\rho_0 w_b)_z\right)_z + \frac{N^2}{f^2}(1 - \mathrm{Ri}^{-1})\, w_{b_{xx}} = 2\frac{\Lambda}{f}\, v_{b_{xx}} - \frac{\Lambda}{f^2}\,\mathcal{F}_{xx} - \frac{1}{f}\,\mathcal{G}_{xz} + \frac{g}{f^2\theta_0}\dot{\mathrm{H}}_{xx}. \tag{4.52}$$

Finally, the ageostrophic fields w_b and u_b are obtained by inversion of the Omega equation and using the continuity Eq. (4.44e).

E. Spontaneous IGW generation forced by the balanced flow

In the following, we adapt the method of Plougonven and Zhang (2007) to our anelastic 2D Eady problem in the presence of external forcing, in order to obtain an IGW equation forced by the balanced flow. First, out of the Eq. (4.34) we form equations for the horizontal divergence and vertical vorticity of the flow, respectively $\delta = u_x$ and $\zeta = v_x$:

$$\partial_t \delta + (U\partial_x + \mathbf{u}\boldsymbol{\nabla})\,\delta + \delta^2 + w_x\, u_z - f\zeta + \phi_{xx} = \mathcal{F}_x\,, \tag{4.53}$$

$$\partial_t \zeta + (U\partial_x + \mathbf{u}\boldsymbol{\nabla})\,\zeta + \zeta\delta + w_x v_z + f\delta = \mathcal{G}_x\,. \tag{4.54}$$

Now, the method consists in splitting the flow variables into the balanced part $_b$ and the unbalanced part $_{ub}$, inside of the Eqs.(4.53), (4.54) and (4.35). In each of these three equations, it is then possible to gather the terms only involving the balanced flow in $\mathcal{A}$, the terms linearly depending on the unbalanced flow in $\mathcal{L}$, and the terms nonlinear in the unbalanced flow in $\mathcal{Q}$. This gives a system of three equations of the form

$$\boldsymbol{\mathcal{A}} + \boldsymbol{\mathcal{L}} + \boldsymbol{\mathcal{Q}} = (\mathcal{F}_x, \mathcal{G}_x, \dot{\mathrm{H}})\,. \tag{4.55}$$

By the use of the following scaling arguments, we can organize all the terms appearing in $\boldsymbol{\mathcal{A}}$, $\boldsymbol{\mathcal{L}}$ and $\boldsymbol{\mathcal{Q}}$ by order of magnitude. In our problem, the background wind U is of order ΛH and the meridonal response v_b is of order[7] $\Lambda H/10$. In particular, because of the two-dimensionality, $u_b \sim \mathrm{Ro}\, v_b$. For the unbalanced flow we assume that $u_{ub} \sim v_{ub} \sim \alpha\, v_b$, where α is a small parameter[8]. The components u and w are linked by the balanced and unbalanced continuity equations. And the geopotential perturbation is scaled as fv. The time scale associated to the balanced flow is $L/(\Lambda H)$ whereas the unbalanced flow is assumed to change at the inertial frequency f. Finally, observations lead us to consider horizontal and vertical scales equal for the balanced and unbalanced flows. Using these scaling hypotheses, we approximate the Eq. (4.55) by keeping only the first order term of each component,

$$\mathcal{L}_{1,\delta} \approx -\mathcal{A}_{1,\delta} + \mathcal{F}_x \tag{4.56}$$

$$\mathcal{L}_{1,\zeta} \approx -\mathcal{A}_{1,\zeta} + \mathcal{G}_x \tag{4.57}$$

$$\mathcal{L}_{1,\theta} \approx -\mathcal{A}_{1,\theta} + \dot{\mathrm{H}} \tag{4.58}$$

where

$$\mathcal{L}_{1,\delta} = (\partial_t + U\partial_x)\,\delta_{ub} - f\zeta_{ub} + \phi_{ub_{xx}} \sim 1 \tag{4.59}$$

$$\mathcal{L}_{1,\zeta} = (\partial_t + U\partial_x)\,\zeta_{ub} + f\delta_{ub} \sim 1 \tag{4.60}$$

$$\mathcal{L}_{1,\theta} = (\partial_t + U\partial_x)\,\theta_{ub} + \theta_{0z} w_{ub} \sim 1 \tag{4.61}$$

$$\mathcal{A}_{1,\delta} = -f\zeta_b + \phi_{b_{xx}} \sim \frac{1}{\alpha} \tag{4.62}$$

$$\mathcal{A}_{1,\zeta} = (\partial_t + U\partial_x)\,\zeta_b + f\delta_b \sim \frac{\mathrm{Ro}}{\alpha} \tag{4.63}$$

$$\mathcal{A}_{1,\theta} = (\partial_t + U\partial_x)\,\theta_b + \Theta_y v_b + \theta_{0z} w_b \sim \frac{\mathrm{Ro}}{\alpha}\,. \tag{4.64}$$

[7]This scaling for v_b is based on observation of the linear experiments P1 and P3, in which the background wind largely dominates the flow response.

[8]Observations in P3 give $\alpha \sim \mathrm{Ro}^4$.

Note that in the previous equations, the order of magnitude after nondimensionalization is indicated at the right. The hydrostatic IGW equation is then formed by calculating $D\partial_z(4.56) + f\partial_z(4.57) - \frac{g}{\theta_0}\partial_{xx}(4.58)$, where $D = (\partial_t + U\partial_x)$, and using hydrostasy and continuity. Keeping only the first order terms in the left hand, it yields

$$[D^2 + f^2]\,(\frac{1}{\rho_0}(\rho_0 w_{ub})_z)_z + N^2\, w_{ub_{xx}} \approx \mathcal{S}_{IGW}\,, \tag{4.65}$$

$$\mathcal{S}_{IGW} = D\partial_z(\mathcal{A}_{1,\delta} - \mathcal{F}_x) + f\partial_z(\mathcal{A}_{1,\zeta} - \mathcal{G}_x) - \frac{g}{\theta_0}\,\partial_{xx}(\mathcal{A}_{1,\theta} - \dot{\mathrm{H}}). \tag{4.66}$$

Since the balanced flow was computed using the linear semi-geostrophic Eqs. (4.44) (Appendix D), we can use them again to simplify the Eq. (4.66). We obtain

$$\mathcal{A}_{1,\delta} = 0 \quad , \quad \mathcal{A}_{1,\zeta} = \mathcal{G}_x \quad \text{, and} \quad \mathcal{A}_{1,\theta} = \frac{\Lambda\theta_0}{g}\,(\Lambda w_b - \mathcal{F}). \tag{4.67}$$

This yields

$$\mathcal{S}_{IGW} = -\Lambda^2\, w_{b_{xx}} - D\mathcal{F}_{xz} + \Lambda\mathcal{F}_{xx} + \frac{g}{\theta_0}\,\partial_{xx}\dot{\mathrm{H}}\,. \tag{4.68}$$

Note that the largest contribution of the terms neglected in $\mathcal{S}_{IGW}$ is $D\partial_z(w_{b_x}u_{b_z})$. This term is of order Ro/10 smaller than $-\Lambda^2\, w_{b_{xx}}$, that is about 4% of the first order forcing by the balanced flow (since Ro=0.4 in this whole study). Finally, the heating rate $\dot{\mathrm{H}}$ is null in experiments P, and neglectable in experiments M.

F. Numerical scheme

The problem is considered to be horizontally periodic, and the numerical scheme is spectral on the horizontal, with 512 harmonics. On the vertical, we use a second order finite difference scheme. We use a horizontal domain of length $2\mathrm{L}_D$, with two lateral Rayleigh damping sponge layers of thickness L_s. A rigid and free slip boundary condition is applied at the top ($z_{top} = 40$km) and at the surface, and an upper sponge layer with Rayleigh damping is introduced from $z = 20$km to z_{top}. To save some CPU time we use a vertical grid with variable mesh size, stretched far from the area where the model must resolve precisely the dynamics, that is near critical levels. The mesh size is $\Delta z = 25$m around the level z^* and over a layer 5km deap. Outside of this layer and symmetrically, it increases smoothly over a depth of 2.5km to reach $\Delta z = 200$m, constant for the rest of the domain.

The dynamical core consists in computing and adding the tendencies of the horizontal vorticity R, of the meridional velocity v and of the potential temperature θ, through a leap-frog temporal scheme with Asselin filter. The tendencies are separated between linear and nonlinear contributions, which allows to switch off the nonlinear terms. At each time step, the streamfunction ψ is computed by inverting the vorticity R. The zonal and vertical velocities u and w are computed from ψ only at each storage, and also to compute the energy budget by trapezoïdal integrals. The model solution converges for a time step of 5 to 10 seconds, that is about one hundredth of the buoyancy period.

The diffusive terms are computed implicitely in the vertical, by inversion of a laplacian by gaussian elimination, and explicitly in the horizontal. The diffusivities μ and κ are constant, and the Prandtl number is always set to 1 ($\mu = \kappa$).

References

Aebischer, U. and C. Schär, 1998 : Low-level potential vorticity and cyclogenesis to the lee of the alps. *J. Atmos. Sci.*, **55(2)**, 186–207.

Andrews, D. G. and McIntyre, M. E., 1976a : Planetary waves in horizontal and vertical shear : The generalized Eliassen-Palm relation and the mean zonal acceleration. *J. Atmos. Sci.*, **33**, 2031–2048.

Andrews, D. G., 1987 : On the interpretation of the Eliassen-Palm flux divergence. *Quart. J. Roy. Meteor. Soc.*, **113**, 323–338.

Booker, J. R., and F. P. Bretherton, 1967 : The critical layer for internal gravity waves in a shear flow. *J. Fluid Mech.*, **27(3)**, 513–539.

Bougeault, P., P. Binder, A. Buzzi, R. Dirks, R. Houze, J. Kuettner, R. B. Smith, R. Steinacker, and H. Volkert, 2001 : The map special observing period. *Bull. Amer. Meteor. Soc.*, **82**, 433–462.

Bühler, O., McIntyre, M. E. and Scinocca, J. F., 1999 : On shear-generated gravity waves that reach the Mesosphere. Part I : Wave generation. *J. Atmos. Sci.*, **56**, 3749–3763.

Chen, C.-C., Hakim, G. J. and Durran, D. R., 2007 : Transient mountain waves and their interaction with large scales. *J. Atmos. Sci.*, **64**, 2378–2400.

De Vries, H. and Opsteegh, J. D., 2005 : Optimal perturbations in the Eady model : resonnance versus PV unshielding. *J. Atmos. Sci.*, **62**, 492-505.

De Vries, H. and Opsteegh, J. D., 2007 : Resonance in optimal perturbation evolution. Part I : Two-layer Eady model. *J. Atmos. Sci.*, **64**, 673–694.

Flamant, C., E. Richard, C. Schär, R. Rotunno, L. Nance, M. Sprenger, and R. Benoit, 2004 : The wake south of the alps : Dynamics and structure of the lee-side flow and secondary potential vorticity banners. *Quart. J. Royal Meteor. Soc.*, **130**, 1275–1303.

Ford, R., McIntyre, M. E. and Norton, W. A., 2000 : Balance and the slow quasimanifold : some explicit results. *J. Atmos. Sci.*, **57**, 1236–1254.

Fritts, D. C. and Alexander, J., 2003 : Gravity wave dynamics and effects in the middle atmosphere. *Rev. Geoph.*, **41(1)**, 1003.

Gregory, D., G. J. Shutts, and J. R. Mitchell, 1998 : A new gravity-wave-drag scheme incorporating anisotropic orography and low-level wave-breaking : Impact upon the climate of the uk meteorological office unified model. *Quart. J. Royal Meteor. Soc.*, **124**, 463–493.

Haynes, P. H. and M. E. McIntyre, 1987 : On the evolution of vorticity and potential vorticity in the presence of diabatic heating and frictional or other forces. *J. Atmos. Sci.*, **44(5)**, 828–841.

Hazel, P., 1967 : The effect of viscosity and heat conduction on internal gravity waves at a critical level. *J. Atmos. Sci.*, **30**, 775–783.

Kaiser, J. F., 1974 : Nonrecursive Digital Filter Design Using the I0-sinh Window Function *Proc. 1974 IEEE Symp. Circuits and Systems*, April, 20–23.

Kim, Y.-J., Eckermann, S. D. and Chun, H.-Y., 2003 : An overview of the past, present and future of gravity-wave drag parametrization for numerical climate and weather prediction models. *Atm.-Oc.*, **41(1)**, 65–98.

Lott, F. and M. J. Miller, 1997 : A new subrig-scale orographic parametrization : Its formulation and testing. *Quart. J. Royal Meteor. Soc.*, **123**, 101–127.

Lott, F., 2003 Large scale flow response to short gravity waves breaking in a rotating shear flow. *J. Atmos. Sci.*, **60**, 1691–1704.

Martin, A. and Lott, F., 2007 : Synoptic responses to mountain gravity waves encountering directional critical levels. *J. Atmos. Sci.*, **64**, 828–848.

McLandress, C. M. and Scinocca, J. F., 2005 : The GCM response to current parameterizations of nonorographic gravity wave drag. *J. Atmos. Sci.*, **62**, 2394–2413.

Olafsdóttir, E. I., Olde Daalhuis, A. B. and Vanneste, J., 2008 : Inertia-gravity wave radiation by a sheared vortex. *J. Fluid Mech.*, **596**, 169–189.

O'Sullivan, D. and Dunkerton, T. J.", 1995 : Generation of inertia-gravity waves in a simulated life cycle of baroclinic instability. *J. Atmos. Sci.*, **52(21)**, 3696–3716.

Pierrehumbert, R. T., 1985 : A theoretical model of orographically modified cyclogenesis. *J. Atmos. Sci.*, **42(12)**, 1244–1258.

Plougonven, R. and Zeitlin, V., 2002 : Internal gravity wave emission from a pancake vortex : An example of wave-vortex interaction in strongly stratified flows. *Phys. Fluids*, **14(3)**, 1259–1268.

Plougonven, R., D. J. Muraki and C. Snyder, 2005 : A baroclinic instability that couples balanced motions and gravity waves. *J. Atmos. Sci.*, **62**, 1545–1559.

Plougonven, R. and Snyder, C., 2007 : Inertia-gravity waves spontaneously generated by jets and fronts. Part I : Different baroclinic life cycles. *J. Atmos. Sci.*, **64**, 2502–2520.

Plougonven, R. and F., Zhang, 2007 : On the forcing of inertia-gravity waves by synoptic-scale flows. *J. Atmos. Sci.*, **64**, 1737–1742.

Satomura, T. and K., Sato, 1999 : Secondary generation of gravity waves associated with the breaking of mountain waves. *J. Atmos. Sci.*, **56**, 3847–3858.

Scavuzzo, C. M., M. A. Lamfri, H. Teitelbaum, and F. Lott, 1998 : A study of the low frequency inertio-gravity waves observed during PYREX. *J. of Geophysical Research*, **103(D2)**, 1747–1758.

Schär., C., 1990 : Quasi-geostrophic lee cyclogenesis. *J. Atmos. Sci.*, **47(24)**, 3044–3066.

Schär, C. and Smith, R. B., 1993 : Shallow-Water Flow past Isolated Topography. Part I : Vorticity Production and Wake Formation. *J. Atmos. Sci.*, **50(10)**, 1373–1400.

Schär, C. and D. R. Durran, 1997 : Vortex formation and vortex shedding in continuously stratified flows past isolated topography. *J. Atmos. Sci.*, **54(4)**, 533–554.

Schär, C., M. Sprenger, D. Lüthi, Q. Jiang, R. B. Smith, and R. Benoit, 2003 : Structure and dynamics of an alpine potential-vorticity banner. *Quart. J. Royal Meteor. Soc.*, **129**, 825–855.

Scinocca, J. F. and Shepherd, T. G., 1992 : Nonlinear wave-activity conservation laws and hamiltonian structure for the two-dimensional anelastic equations. *J. Atmos. Sci.*, **49**, 5–27.

Scinocca, J. F., and N. A. McFarlane, 2000 : The parametrization of drag induced by stratitified flow over anisotropic orography. *Quart. J. Royal Meteor. Soc.*, **126(568)**, 2353–2393.

Scinocca, J. F. and Ford, R., 2000 : The nonlinear forcing of large-scale internal gravity waves by stratified shear instability. *J. Atmos. Sci.*, **57**, 653–672.

Shen, B.-W. and Lin, Y.-L., 1999 : Effects of critical levels on two-dimensionnal back-sheared flow over an isolated mountain ridge on an f-plane. *J. Atmos. Sci.*, **56**, 3286–3302.

Shutts, G. J., 1995 : Gravity-wave drag parametrization over complex terrain : the effect of critical-level absorption in directional wind-shear. *Quart. J. Royal Meteor. Soc.*, **121**, 1005–1021.

Shutts, G. J., 2001 : A linear model of back-sheared flow over an isolated hill in the presence of rotation. *J. Atmos. Sci.*, **58**, 3293–3310.

Shutts, G. J., 2003 : Inertia-gravity wave and neutral eady wave trains forced by directionnally sheared flow over isolated hills. *J. Atmos. Sci.*, **60(4)**, 593–606.

Smith, R. B., 1984 : A theory of lee cyclogenesis. *J. Atmos. Sci.*, **41(7)**, 1159–1168.

Snyder, C., Skamarock, W. C. and Rotunno, R., 1993 : Frontal dynamics near and following frontal collapse. *J. Atmos. Sci.*, **50(18)**, 3194–3211.

Snyder, C., Muraki, D. J., Plougonven, R. and Zhang, F., 2007 : Inertia-gravity waves generated within a dipole-vortex. *J. Atmos. Sci.*, *64*, 4417–4431.

Speranza, A., A. Buzzi, A. Trevisan, and P. Malguzzi, 1985 : A theory of deep cyclogenesis in the lee of the alps. part i : Modifications of baroclinic instability by localized topography. *J. Atmos. Sci.*, **42**, 1521–1535.

Sutherland, B. R., Caulfield C. P. and Peltier, W. R., 1994 : Internal gravity wave generation and hydrodynamic instability. *J. Atmos. Sci.*, **51**, 3261–3280.

Umurhan, O. M., Heifetz, E., N. Harnick and F. Lott, 2008 : The instability of counter-propagating kernel gravity waves in a constant shear flow. *Submitted to Physics of Fluids.*

Vadas, S. L., D. C. Fritts, and M. J. Alexander, 2003 : Mechanism for the generation of secondary waves in wave breaking regions. *J. Atmos. Sci.*, **60**, 194–214.

Vanneste, J. and Yavneh, I., 2004 : Exponentially small inertia-gravity waves and the breakdown of quasigeostrophic balance. *J. Atmos. Sci.*, **61**, 211–223.

Viudez, A. and Dritschel D. G., 2006 : Spontanous generation of inertia-gravity wave paquets by balanced geophysical flows. *J. Fluid Mech.*, **553**, 107–117.

Viudez, A., 2008 : The stationary frontal wave packet spontaneously generated in mesoscale dipoles. *J. Phys. Ocean.*, **38**, 243-256.

Wurtele, M. G., Datta, A. and Sharman, R. D., 1996 : The propagation of gravity-inertia waves and lee waves under a critical level. *J. Atmos. Sci.*, **53(11)**, 1505–1523.

Wurtele, M. G., Datta, A. and Sharman, R. D., 1999 : Unsteadyness and periodicity in gravity waves and lee waves forced by a fixed rigid boundary. *J. Atmos. Sci.*, **56**, 2269–2276.

Wurtele, M. G., Datta, A. and Sharman, R. D., 2000 : The propagation of a gravity-inertia wave in a positively sheared flow. *J. Atmos. Sci.*, **57**, 3703–3715.

Zhang, F., S. E. Koch, C. A. Davis, and M. L. Kaplan, 2001 : Wavelet analysis and the governing dynamics of a large amplitude mesoscale gravity wave event along the east coast of the United States. *Quart. J. Royal Meteor. Soc.*, **127**, 2209–2245.

Chapitre 5

Conclusion

Dans cette thèse, nous avons tenté de décrire et mesurer l'impact des Ondes de Gravité (OG) de montagne sur l'écoulement de grande échelle en présence de niveaux critiques. Cette étude s'incrit dans le cadre de la recherche pour une meilleure paramétrisation des effets des OG courtes, qui sont actuellement non résolues par les modèles de circulation générale et de prévision du temps. En particulier, notre attention a porté sur la description qualitative et quantitative des contributions équilibrée et non équilibrée de l'écoulement. Nous avons privilégié une approche conceptuelle, basée sur l'idée que l'interaction entre les ondes courtes et les grandes échelles peut être décrite par la production et l'évolution d'anomalies de Vorticité Potentielle (VP). Toutes nos études ont été réalisées dans le cadre du problème idéalisé de Eady. Cela nous a permis de dégager des résultats généraux, sur la base de mécanismes simplifiés liés à la dynamique de la VP dans un environnement atmosphérique barocline. En particulier, nous avons interprété l'effet sur la cyclogénèse à ces différentes échelles, mais aussi analysé comment les montagnes peuvent participer de façon indirecte à la production d'Ondes d'Inertie-Gravité (OIG) relativement longues. Nous avons aussi toujours pris soin de garder un lien quantitatif avec la réalité de la météorologie de montagne.

Nous avons ainsi pu étudier d'abord (chapitre 2), l'effet de la force des OG sur les échelles synoptiques équilibrées, dans un cadre semi-géostrophique linéaire. Pour cela, nous avons d'abord évalué la force exercée par les échelles sous-maille de l'orographie, dans le cas d'un front advecté sur un massif montagneux isolé, c'est-à-dire en présence de niveaux critiques directionnels. Puis nous avons introduit cette force paramétrisée dans le problème de Eady tri-dimensionnel (3D) classique. Prolongeant la démarche de Smith (1984) pour l'étude de la cyclogénèse de montagne, nous avons alors étudié l'impact de la VP créée par la force en termes d'ondes de Eady de surface. Or la force crée par les niveaux critiques directionnels a la particularité d'être perpendiculaire au vent, ce qui donne lieu à un flux de VP parallèle au vent. Le dipole de VP ainsi créé est advecté par le front, ce qui donne lieu à deux bannières de VP superposées et légèrement décalées. Cette structure de VP particulière se traduit à court terme et en surface, dans le cas du front froid, par une perturbation anticyclonique dans le sillage direct de la montagne. Autrement dit, la force est cyclolytique dans le cas d'un front froid. Le résultat est inversé dans le cas d'un front chaud. Nous avons ensuite appliqué cette paramétrisation au cas du massif Alpin, et trouvé une influence d'amplitude faible mais significative, en deçà du millibar.

Puis nous avons abordé les effets à des échelles intermédiaires (chapitres 3 et 4), dont la dynamique est plus complexe qu'aux échelles synoptiques, et ce à l'aide de simulations aux équations primitives bi-dimensionnelles (2D). De façon générale, cela nous a permis de caractériser et quantifier la partie non-équilibrée des ondes de Eady de surface pour de telles échelles, ainsi que les OIG générées dans ce problème.

En particulier, parmi les modes instables normaux du problème de Eady non-géostrophique, nous avons étudié la structure de ceux qui couplent une onde de Eady de surface avec une OIG (chapitre 3). Ce fut l'occasion d'analyser leur mécanisme de croissance ainsi que celui de leur saturation non-linéaire. Les deux mécanismes sont liés essentiellement à la structure de l'écoulement près du niveau critique inertiel. C'est en effet au voisinage de cette singularité que les modes instables extraient leur énergie de l'écoulement de base. Mais c'est aussi dans cette zone qu'ils perdent ensuite leur énergie lorsqu'ils deviennent non-linéaires, via des instabilités de petite échelle et un couplage rétro-actif déstabilisant avec l'écoulement moyen. Cette étude a donné une limite supérieure au temps de vie de la couche inertielle cisaillée (largement sur-estimée à cause de la bidimensionnalité imposée à l'écoulement), ainsi qu'à son amplitude avant rupture. Elle a aussi permit de mettre en évidence la génération d'OIG courtes générées lors de cette rupture.

Ensuite, nous avons étudié dans ce même modèle de Eady, la réponse polychromatique forcée par une force paramétrisée ou directement par une orographie de petite échelle (chapitre 4).

Dans ce contexte 2D, la force des OG de montagne est parallèle au vent, contrairement au cas 3D des niveaux critiques directionnels (chapitre 2). En termes de cyclogénèse de montagne, nous avons trouvé que dans le cas où cette force est suffisamment faible pour que la réponse soit linéaire, et suffisamment basse pour que la VP excite ensuite des ondes de Eady à la surface, l'influence des OGs de montagne a toutes les chances d'être cyclolytique. L'amplitude de la perturbation reste faible cependant, comparable ou inférieure à celles obtenues dans le chapitre 2. Cependant, la réponse contient aussi des OIG, que l'on attribue à trois mécanismes de génération certes physiquement reliés mais conceptuellement distincts. Le premier, relativement connu, consiste en la génération par la force variable dans le temps, d'une OIG localisée au voisinage de cette force. Le deuxième mécanisme est lié à l'existence des modes instables non-géostrophiques étudiés dans le chapitre 3, et donne lieu à une OIG de même échelle que l'onde de Eady de surface, et qui lui est couplée. Le troisième mécanisme est plus spécifiquement lié à la structure du dipole de VP, qui grâce à l'existence d'échelles sous-synoptiques dans l'écoulement équilibré, génère spontanément des OIG de plus petite échelle horizontale que précédemment. Cette émission spontannée se fait au dessus et en dessous du dipole de VP, sous la forme de trains d'OIG qui peuvent s'éloigner de la VP. En amplitude, elle domine largement l'OIG associée au mode non-géostrophique dominant. Par conséquent, en terme de cyclogénèse la réponse en surface peut être modifiée par l'existence d'un paquet d'OIG inférieur de ce type.

Nous avons ensuite mesuré le niveau de saturation nonlinéaire de l'atmosphère vis-à-vis d'une force donnée (paramétrisée ou non) de taille sous-synoptique. De même que dans l'étude des modes non-géostrophiques purs (chapitre 3), nous avons observé que l'instabilité de la couche critique se traduit par la génération d'OIG courtes, qui amplifient d'autant plus la part des OIG dans la réponse totale. Néanmoins, les amplitudes obtenues pour les OIG restent plus faibles que dans le cas monochromatique (chapitre 3), car dans ce cas polychromatique la couche critique a une structure moins singulière (la superposition des nombres d'onde lisse la singularité), et elle est rapide-

ment perturbée par l'oscillation inertielle.

Enfin, dans le cas non paramétrisé, ces simulations ont permis de quantifier l'intensité de la force exercée par le profil orographique idéalisé choisi, ainsi que le niveau de saturation nonlinéaire de la dynamique au niveau critique. Ces résultats 2D appellent d'ailleurs un élargissement au cas de spectres orographiques 3D plus fournis, voire ajustés sur des spectres réels, dans un vent de base lui aussi 3D, comme dans le chapitre 2.

Ces études quantitatives mériteraient d'être élargies dans le cadre des équations primitives 3D, pour plusieurs raisons. Nous avons vu en effet que les équations primitives nous apportaient la description précieuse de la dynamique non géostrophique, en particulier des ondes d'inertie-gravité, ainsi que la mesure de la limite nonlinéaire des phénomènes étudiés et leurs mécanismes de saturation. Cependant, nous avons aussi remarqué que la possibilité d'une dynamique 3D doit certainement modifier les résultats obtenus en 2D, concernant les niveaux de saturation, les amplitudes des OIG émises, ainsi que celles des forces exercées. Nous avons vu aussi que l'existence d'un vent de base tournant donne lieu à une distribution plus lisse et plus réaliste du dépôt de quantité de mouvement par les OG si la montagne est elle-même 3D, ainsi qu'une dynamique des ondes de Eady de surface particulière liée au comportement de la VP dans ce contexte. Il serait donc naturel de rassembler ces différents aspects dans le cadre d'une étude plus générale, qui serait cependant toujours axée sur la question de la paramétrisation des niveaux critiques. C'est dans ce but que j'ai commencé à me familiariser avec le modèle méso-échelles WRF développé par le NCAR. Ce modèle performant est de plus en plus utilisé par une large communauté pour des questions fondamentales ou appliquées. En prenant exemple sur le travail réalisé par Chen et al. (2007) pour représenter l'effet des ondes de montagne courtes transitoires sur les grandes échelles, on pourrait développer une mesure systématique des phénomènes sous-maille à paramétriser à l'aide de simulations méso-échelles, puis réintroduire les contraintes mesurées sous forme de paramétrisations "parfaites". Remarquons qu'un autre intérêt de WRF est la possibilité d'étudier des cas réels. C'est évidemment un point essentiel dans le cadre de la recherche d'une meilleure paramétrisation. Par exemple, Doyle et Jiang (2006) ont mis en évidence, dans les observations issues de la campagne MAP pour le 13 Novembre 1999, un cas de déferlement d'OGs de montagne dans un vent cisaillé tournant. Plus récemment, Eckermann et al (2007) ont mis en évidence un cas similaire sur la Scandinavie en 2003. Bien que j'aie commencé à me servir de WRF pour mes enseignements, je n'ai malheureusement pas encore eu le temps de mettre en place ces expériences.

L'un des intérêts de cette approche plutôt conceptuelle et mécaniste, reposant sur la dynamique de la VP, est qu'elle est probablement transposable à d'autres phénomènes sources de VP dans des écoulements atmosphériques cisaillés. En particulier, pour rester dans le cadre de la météorologie de montagne, les OG de montagne qui déferlent par nonlinéarité propre (en l'absence de niveaux critiques) influent aussi sur la dynamique de grande échelle au sol, et représentent aussi certainement une source secondaire d'OIG. D'autre part, la production de VP par le chauffage diabatique associé aux précipitations orographiques mériterait aussi d'être abordée, les effets étant certainement assez différents et quantitativement non négligeables. Mais avant d'appliquer cette approche à ces autres problèmes, notons que les études réalisées ici demandent à être approfondies et complétées pour répondre en particulier à deux questions qui se

sont imposées dans ces travaux.

D'une part, nous avons vu que pour mieux comprendre l'effet d'un dipole de vorticité potentielle en terme de cyclogénèse (de montagne), il serait utile de se placer dans le cadre de la recherche de modes optimaux et non normaux, et de discerner et quantifier les mécanismes de croissance qui entrent en jeu. Cela a été fait récemment dans le cadre du modèle de Eady quasi-géostrophique linéaire 2D par De Vries et Opsteegh (2005, 2007). Cette approche pourrait au moins être étendue au cadre semi-géostrophique linéaire 3D du chapitre 2, en s'attachant à construire des modes optimaux pertinents par rapport au problème des OG de montagne en présence de niveaux critiques directionnels. Plus généralement, les concepts développés dans ce cadre très simplifié pourraient certainement être transposables dans le cadre des simulations aux équations primitives, au moins pour la partie équilibrée de l'écoulement. Notamment, les concepts de résonance entre une anomalies de VP et un mode de surface, et de "démarquage" d'anomalies de VP[1] (ou mécanisme de Orr généralisé), semblent être tout à fait pertinents pour raffiner notre étude.

D'autre part, le mécanisme de génération spontanée d'OIG par un dipole de VP, proposé au chapitre 4 (section 2.3.2), mériterait d'être exploré de façon approfondie. Ceci pourrait d'abord se faire à l'aide d'un modèle linéaire simple de propagation des ondes d'inertie-gravité, forcé par un dipole de VP dont on pourrait prescrire librement la configuration spatiale. Cela permettrait notamment d'identifier les termes de forçages dominants selon les configurations choisies. Puis on pourrait compléter cela en introduisant l'effet de l'écoulement de base sur la propagation des ondes. Cela permettrait de quantifier de façon générale l'amplitude des ondes attendues de ce mécanisme, et ainsi en déduire quelle configuration de météorologie de montagne est susceptible d'en émettre le plus. Enfin, et comme indiqué en conclusion au chapitre 4, d'autres expériences de sensibilité peuvent être réalisées l'aide du modèle 2D aux équations primitives utilisé dans cette thèse. Notamment, les premiers résultats indiquent que le phénomène est relativement sensible à l'amplitude du cisaillement, ainsi qu'à la position et à la direction de la force par rapport au vent de base cisaillé.

[1]Proposition de traduction pour l'expression "PV unshielding".

Bibliographie

Aebischer, U., and Schär, C., 1998 : Low-level potential vorticity and cyclogenesis to the lee of the alps. *J. Atmos. Sci.*, **55(2)**, 186–207.

Andrews, D. G., 1987a : The influence of atmospheric waves on the general circulation of the middle atmosphere. *Phil. Trans. R. Soc. Lond. Ser. A*, **323**, 693–705.

Andrews, D. G., 1987b : On the interpretation of the eliassen-palm flux divergence. *Quart. J. Roy. Meteor. Soc.*, **113**, 323–338.

Andrews, D. G., Holton, J. R., and Leovy, C. B., 1987 : *Middle Atmosphere Dynamics*. Academic Press.

Andrews, D. G., and McIntyre, M. E., 1976a : Planetary waves in horizontal and vertical shear : The generalized eliassen-palm relation and the mean zonal acceleration. *J. Atmos. Sci.*, **33**, 2031–2048.

Andrews, D. G., and McIntyre, M. E., 1976b : Planetary waves in horizontal and vertical shear : Asymptotic theory for equatorial waves in weak shear. *J. Atmos. Sci.*, **33**, 2049–2053.

Andrews, D. G., and McIntyre, M. E., 1978a : Generalized eliassen-palm and charney-drazin theorems for waves on axisymmetric mean flowsin compressible atmospheres. *J. Atmos. Sci.*, **35**, 175–185.

Andrews, D. G., and McIntyre, M. E., 1978b : An exact theory of nonlinear waves on a lagrangian-mean flow. *J. Fluid Mech.*, **89**, 609–646.

Andrews, D. G., and McIntyre, M. E., 1978c : On wave-action and its relatives. *J. Fluid Mech.*, **89**, 647–664.

Bacmeister, J. T., 1993 : Mountain-wave drag in the stratosphere and mesosphere inferred from observed winds and a simple mountain-wave parameterization scheme. *J. Atmos. Sci.*, **50**, 377–399.

Bacmeister, J. T., and Pierrehumbert, R. T., 1988 : On high-drag states of nonlinear stratified flow over an obstacle. *J. Atmos. Sci.*, **45(1)**, 63–80.

Baines, P. G., 1995 : *Topographic effects in stratified flows*. Cambridge University Press.

Baines, P. G., and Palmer, T. N., 1990 : Rationale for a new physically based parametrization of sub-grid scale orographic effects. *ECMWF Tech, Memo*, **169**.

Bannon, P. R., 1992 : A model of rocky mountain lee cyclogenesis. *J. Atmos. Sci.*, **49(16)**, 1510–1522.

Beljaars, A. C. M., Brown, A. R., and Wood, N., 2004 : A new parametrization of turbulent orographic form drag. *Quart. J. Roy. Meteor. Soc.*, **130**, 1327–1347.

Bender, C. M., and Orszag, S. A., 1978 : *Advanced mathematical methods for scientists and engineers*. International series in pure and applied mathematics, McGraw-Hill.

Bergeron, T., 1928 : Überdie dreidimensionalverknüpfende wetteranalyse, teil i. *Geophys. Publ.*, **5**, 1–111.

Binder, P., and Schär, C., 1996 : The mesoscale alpine program map : Design proposal. 77p, available from http ://www.map.ethz.ch/proposal.html.

Bishop, C. H., and Heifetz, E., 2000 : Apparent absolute instability and the continuous spectrum. *J. Atmos. Sci.*, **57**, 3592–3608.

Bleck, R., and Mattocks, C., 1984 : Preliminary analysis of the role of potential vorticity in alpine lee cyclogenesis. *Contrib. Atmos. Phys.*, **57**, 357–368.

Blumen, W., 1972 : Geostrophic adjustment. *Rev. Geophys.*, **10**, 485–528.

Blumen, W., 1992 : Propagation of fronts and frontogenesis versus frontolysis over orography. *Meteor. Atmos. Phys.*, **48**, 37–50.

Boer, G. J., McFarlane, N. A., Laprise, R., Henderson, J. D., and Blanchet, J.-P., 1984 : The canadian climate center spectral atmospheric general circulation model. *Atmos.-Ocean.*, **22**, 397–429.

Bolin, B., 1950 : On the influence of earth orography on the general character of the westerlies. *Tellus*, **2**, 184–195.

Booker, J. R., and Bretherton, F. P., 1967 : The critical layer for internal gravity waves in a shear flow. *J. Fluid Mech.*, **27(3)**, 513–539.

Bougeault, P., Benech, B., Bessemoulin, R., Carissimo, B. Jansa Clar, A., Pelon, J., Petitdidier, M., and Richard, E., 1997 : Pyrex : A summary of the findings. *Bull. Amer. Meteor. Soc.*, **78(4)**, 637–650.

Bougeault, P., Binder, P., Buzzi, A., Dirks, R., Houze, R., Kuettner, J., Smith, R. B., Steinacker, R., and Volkert, H., 2001 : The map special observing period. *Bull. Amer. Meteor. Soc.*, **82**, 433–462.

Boyd, J. P., 1976 : The noninteraction of waves with the zonally averadge flow on a spherical earth and the interrelationships of eddy fluxes of energy, heat and momentum. *J. Atmos. Sci.*, **33**, 2285–2291.

Bretherton, F. P., 1966 : Baroclinic instability and the short wave cut-off in terms of potential vorticity. *Quart. J. Roy. Meteor. Soc.*, **92**, 335–345.

Bretherton, F. P., 1969 : Momentum transport by gravity waves. *Quart. J. Roy. Meteor. Soc.*, **95(404)**, 213–243.

Broad, A. S., 1995 : Linear theory of momentum fluxes in 3-d flows with turning of the wind with height. *Quart. J. Roy. Meteor. Soc.*, **121**, 1891–1902.

Broad, A. S., 1999 : Do orographic gravity waves break in flows with uniform wind direction turning with height ? *Quart. J. Roy. Meteor. Soc.*, **125**, 1695–1714.

Broutman, D., Rottman, J. W., and Eckermann, S., 2001 : A hybrid method for wave propagation from a localized source, with application to mountain waves. *Quart. J. Roy. Meteor. Soc.*, **127**, 129–146.

Bühler, O., and McIntyre, M. E., 2005 : Wave capture and wave-vortex duality. *J. Fluid Mech.*, **534**, 67–95.

Bühler, O., McIntyre, M. E., and Scinocca, J. F., 1999 : On shear-generated gravity waves that reach the mesosphere. part i : Wave generation. *J. Atmos. Sci.*, **56**, 3749–3763.

Buzzi, A., D'Isidoro, M., and Davolio, S., 2003 : A case-study of an orographic cyclone south of the alps during the map sop. *Quart. J. Roy. Meteor. Soc.*, **129**, 1795–1818.

Buzzi, A., Speranza, A., Tibaldi, S., and Tosi, E., 1987 : A unified theory of orographic influences upon cyclogenesis. *Meteor. Atmos. Phys.*, **40**, 91–107.

Buzzi, A., and Tibaldi, S., 1978 : Cyclogenesis in the lee of the alps : A case study. *Quart. J. Roy. Meteor. Soc.*, **104**, 271–287.

Buzzi, A., and Tosi, E., 1989 : Statistical behavior of transient eddies near mountains and implications for theories of lee cyclogenesis. *J. Atmos. Sci.*, **46(9)**, 1233–1249.

Charney, J. G., 1947 : The dynamics of long waves in a baroclinic westerly current. *J. Meteor.*, **4**, 135–162.

Charney, J. G., 1948 : On the scale of atmospheric motion. *Geofys. Publ. Oslo*, **17(2)**, 1–17.

Charney, J. G., and De Vore, J. G., 1979 : Multiple flow equilibria in the atmosphere and blocking. *J. Atmos. Sci.*, **36**, 1205–1216.

Charney, J. G., and Eliassen, A., 1949 : A numerical method for predicting the perturbations of the middle latitude westerlies. *Tellus*, **1(2)**, 38–54.

Chen, C.-C., Hakim, G. J., and Durran, D. R., 2007 : Transient mountain waves and their interaction with large scales. *J. Atmos. Sci.*, **64**, 2378–2400.

Chopra, K. P., 1973 : Atmospheric and oceanic flow problems introduced by islands. *Adv. Geophys.*, **16**, 297–421.

Clark, T. L., and Miller, M. J., 1991 : Pressure drag and momentum fluxes due to the alps. ii : Representation in large-scale atmospheric models. *Quart. J. Roy. Meteor. Soc.*, **117**, 527–552.

Clark, T. L., and Peltier, W. R., 1984 : Critical level reflexion and the resonant growth of nonlinear mountain waves. *J. Atmos. Sci.*, **41**, 3122–3134.

Davies, H. C., 1984 : On the orographic retardation of a cold front. *Contrib. Atmos. Phys.*, **57(3)**, 409–418.

Davies, H. C., and Schär, C., 1991 : Orographic destabilisation of a laterally sheared flow. *Tellus*, **43A**, 321–333.

Davis, C. A., 1997 : The modification of baroclinic waves by the rocky mountains. *J. Atmos. Sci.*, **54**, 848–868.

Davis, C. A., and Stoelinga, M. T., 1999 : Interpretation of the effect of mountains on synoptic-scale baroclinic waves. *J. Atmos. Sci.*, **56**, 3303–3320.

De Vries, H., and Opsteegh, J. D., 2005 : Optimal perturbations in the eady model : resonnance versus pv unshielding. *J. Atmos. Sci.*, **62**, 492–505.

De Vries, H., and Opsteegh, J. D., 2007a : Resonance in optimal perturbation evolution. part i : Two-layer eady model. *J. Atmos. Sci.*, **64**, 673–694.

Doyle, J. D., Durran, D. R., Chen, C., Colle, B. A., Georgelin, M., Grubisic, V., Hsu, W. R., Huang, C. Y., Landau, D., L. Y. L. P. G. S., Sun, W. Y., Weber, D. B., Wurtele, M. G., and Xue, M., 2000 : An intercomparison of model-predicted wave breaking for the 11 january 1972 boulder windstorm. *Mon. Wea. Rev.*, **128**, 901–914.

Doyle, J. D., and Jiang, Q., 2006 : Observations and numerical simulations of mountain waves in the presence of directional wind shear. *Quart. J. Roy. Meteor. Soc.*, **132**, 1877–1905.

Drazin, P. G., and Reid, W. H., 1981 : *Hydrodynamic stability*. Cambridge University Press.

Dunkerton, T. J., 1982 : Theory of the mesopause semiannual oscillation. *J. Atmos. Sci.*, **39**, 2681–2690.

Durran, D. R., 1986a : Another look at downslope winds. part i : The development of analogs to supercritical flow in an infinitely deep, continuously stratified fluid. *J. Atmos. Sci.*, **43**, 2527–2543.

Durran, D. R., 1986b : Mountain waves. P. S. Ray, Ed., *Mesoscale meteorology and forecasting*, Boston : American Meteorological Society.

Durran, D. R., 1990 : Mountain waves and downslope winds. B. W., Ed., *Atmospheric process over complex terrain*, Boston : American Meteorological Society.

Durran, D. R., 1995b : Do breaking mountain waves decelerate the local mean flow. *J. Atmos. Sci.*, **52**, 4010–4032.

Durran, D. R., and Klemp, J. B., 1987 : Another look at downslope winds. part ii : Nonlinear amplification beneath wave-overturning layers. *J. Atmos. Sci.*, **44**, 3402–3412.

Eady, E. T., 1949 : Long waves and cyclone waves. *Tellus*, **1**, 33–52.

Eckermann, S. D., Ma, J., Wu, D. L., and Broutman, D., 2007 : A three-dimensional mountain wave imaged in satellite radiance throughout the stratosphere : Evidence of the effects of directional wind shear. *Quart. J. Roy. Meteor. Soc.*, **133**, 1959–1975.

Egger, J., 1988 : Alpine lee cyclogenesis : verification of theories. *J. Atmos. Sci.*, **45(15)**, 2187–2203.

Egger, J., and Hoinka, K. P., 1992 : Fronts and orography. *Meteor. Atmos. Phys.*, **48**, 3–36.

Eliassen, A., and Palm, E., 1961 : On the transfer of energy in the stationnary mountain waves. *Geophys. Publ.*, **22(3)**, 1–23.

Epifanio, C. C., and Durran, D. R., 2002a : Lee-vortex formation in free-slip stratified flow over ridges. part i : Comparison of weakly nonlinear inviscid theory and fully nonlinear viscous simulations. *J. Atmos. Sci.*, **59**, 1153–1165.

Epifanio, C. C., and Durran, D. R., 2002b : Lee-vortex formation in free-slip stratified flow over ridges. part ii : Mechanisms of vorticity and pv production in nonlinear viscous wakes. *J. Atmos. Sci.*, **59**, 1166–1181.

Fantini, M., and Davolio, S., 2001 : Instability of neutral eady waves and orography. *J. Atmos. Sci.*, **58**, 1146–1154.

Farrell, B. F., 1982 : The initial growth of disturbances in a baroclinic flow. *J. Atmos. Sci.*, **39**, 1663–1686.

Ficker, H., 1920 : Der einfluss der alpenauf fallgebiete des luftdrucks und die entwicklung von depressionen über dem mittelmeer. *Meteor. Zeitschr.*, **37**, 350–363.

Flamant, C., Richard, E., C., S., Rotunno, R., Nance, L., Sprenger, M., and Benoit, R., 2004 : The wake south of the alps : Dynamics and structure of the lee-side flow and secondary potential vorticity banners. *Quart. J. Roy. Meteor. Soc.*, **130**, 1275–1303.

Ford, R., McIntyre, M. E., and Norton, W. A., 2000 : Balance and the slow quasimanifold : some explicit results. *J. Atmos. Sci.*, **57**, 1236–1254.

Fritts, D. C., and Alexander, J., 2003 : Gravity wave dynamics and effects in the middle atmosphere. *Rev. Geophys.*, **41(1)**, 1003.

Fritts, D. C., Garten, J. F., and Andreassen, Ø., 1996a : Wave breaking and transition to turbulence in stratified shear flows. *J. Atmos. Sci.*, **53(8)**, 1057–1085.

Fritts, D. C., Isler, J. R., and Andreassen, O., 1994 : Gravity wave breaking in two and three dimensions 2. three-dimensional evolution and instability structure. *J. Geophys. Res.*, **99(D4)**, 8109–8123.

Fritts, D. C., and Luo, Z., 1992 : Gravity wave excitation by geostrophic adjustment of the jet stream. part i : two-dimensional forcing. *J. Atmos. Sci.*, **49(8)**, 681–697.

Fritts, D. C., Palmer, T. L., Andreassen, Ø., and Lie, I., 1996b : Evolution and breakdown of kelvin-helmholtz billows in stratified compressible flows. part i : Comparison of two and three-dimensional flows. *J. Atmos. Sci.*, **53(22)**, 3173–3191.

Georgelin, M., and Lott, F., 2001 : On the transfer of momentum by trapped lee waves : case of the iop 3 of pyrex. *J. Atmos. Sci.*, **58**, 3563–3580.

Gill, A. E., 1982 : *Atmosphere-Ocean Dynamics*. International Geophysics series, Academic Press.

Gregory, D., Shutts, G. J., and Mitchell, J. R., 1998 : A new gravity-wave-drag scheme incorporating anisotropic orography and low-level wave-breaking : Impact upon the climate of the uk meteorological office unified model. *Quart. J. Roy. Meteor. Soc.*, **124**, 463–493.

Gross, B. D., 1994 : Frontal interaction with isolated orography. *J. Atmos. Sci.*, **51(11)**, 1480–1496.

Hamilton, K., 1999 : Dynamical coupling of the lower and middle atmosphere : history background to current research. *J. Atmos. Sol.-Terr. Phys.*, **61**, 73–84.

Harnik, N., and Heifetz, E., 2007 : Relating overreflection and wave geometry to the counterpropagating rossby wave perspective : toward a deeper mechanistic understanding of shear instability. *J. Atmos. Sci.*, **64**, 2238–2261.

Harnik, N., Heifetz, E., Umurhann, O. M., and Lott, F., 2008 : A buoyancy-vorticity wave interaction approach to stratified shear flow. *J. Atmos. Sci., in press*.

Haynes, P. H., Marks, C. J., McIntyre, M. E., Shepherd, T. G., and Shine, K. P., 1991 : On the 'downward control' of extratropical diabatic circulations by eddy-induced mean zonal forces. *J. Atmos. Sci.*, **48**, 651–678.

Haynes, P. H., and McIntyre, M. E., 1987 : On the evolution of vorticity and potential vorticity in the presence of diabatic heating and frictional or other forces. *J. Atmos. Sci.*, **44(5)**, 828–841.

Haynes, P. H., and McIntyre, M. E., 1990 : On the conservation and impermeability theorems for potential vorticity. *J. Atmos. Sci.*, **47(16)**, 2021–2031.

Hazel, P., 1967 : The effect of viscosity and heat conduction on internal gravity waves at a critical level. *J. Fluid Mech.*, **30**, 775–783.

Heifetz, E., and Methven, J., 2005 : Relating optimal growth to counterpropagating rossby waves in shear instability. *Physics of Fluids*, **17(6)**, 064107.

Hines, C., 1988 : A modelling of atmospheric gravity waves and wave drag generated by isotropic and anisotropic terrain. *J. Atmos. Sci.*, **45**, 309–322.

Hines, C., 1997a : Doppler-spread parameterization of gravity wave momentum deposition in the middle atmosphere. 1, basic formulation. *J. Atmos. Sol. Terr. Phys.*, **59**, 371–386.

Hines, C., 1997b : Doppler-spread parameterization of gravity wave momentum deposition in the middle atmosphere. 2, broad and quasi-monochromatic spectra and implementation. *J. Atmos. Sol. Terr. Phys.*, **59**, 387–400.

Hoinka, K. P., 1985 : Observations of the air flow over the alps during a foehn event. *Quart. J. Roy. Meteor. Soc.*, **111**, 199–224.

Hoinka, K. P., and Davies, H. C., 2007 : Upper-tropospheric flow features and the alps : an overview. *Quart. J. Roy. Meteor. Soc.*, **133**, 847–865.

Hoinka, K. P., Hagen, M., Volkert, H., and Heimann, D., 1990 : On the influence of the alps on a cold front. *Tellus*, **42A**, 140–164.

Hoinka, K. P., Richard, E., Poberaj, G., Busen, R., Caccia, J.-L., Fix, A., and Mannstein, H., 2003 : Analysis of a potential-vorticity streamer crossing the alps during map iop 15 on 6 november 1999. *Quart. J. Roy. Meteor. Soc.*, **129**, 609–632.

Hoinka, K. P., Schwierz, C., and Martius, O., 2006 : Synoptic-scale weather patterns during alpine heavy rain events. *Quart. J. Roy. Meteor. Soc.*, **132**, 2853–2860.

Hoinka, K. P., and Volkert, H., 1987 : The german front experiment 1987. *Bull. Amer. Meteor. Soc.*, **68**, 1424–1427.

Hoinka, K. P., and Volkert, H., 1992 : Fronts and the alps : findings from the front experiment 1987. *Meteorol. Atmos. Phys.*, **48**, 51–75.

Holton, J. R., 1982 : The role of gravity wave induced drag and diffusion in the momentum budget of the mesosphere. *J. Atmos. Sci.*, **39**, 791–799.

Holton, J. R., 1992 : *An introduction to Dynamic Meteorology*. International Geophysics series, Academic Press, 3rd edn.

Hoskins, B. J., 1975 : The geostrophic momentum approximation and the semi-geostrophic equations. *J. Atmos. Sci.*, **32(2)**, 233–242.

Hoskins, B. J., and Karoly, D. J., 1981 : The steady linear response of a spherical atmosphere to thermal and orographice forcing. *J. Atmos. Sci.*, **38**, 1179–1196.

Hoskins, B. J., McIntyre, M. E., and Robertson, A. W., 1985 : On the use and significance of isentropic potential vorticity maps. *Quart. J. Roy. Meteor. Soc.*, **111**, 877–946.

Jones, W. L., 1967 : Propagation of internal gravity waves in fluids with shear flow ond rotation. *J. Fluid Mech.*, **30**, 439–448.

Kaiser, J. F., 1974 : Nonrecursive digital filter design using the i0-sinh window function. *Proc. 1974 IEEE Symp. Circuits and System*, 20–23.

Kim, Y., 1996 : Representation of subgrid-scale effects in a general circulation model : Part i. impact on the dynamics of a simulated january climate. *J. Climate*, **9**, 2698–2717.

Kim, Y., and Arakawa, A., 1995 : Improvement of orographic gravity wave parameterization using a mesoscale gravity wave model. *J. Atmos. Sci.*, **52**, 1875–1902.

Kim, Y.-J., Eckermann, S. D., and Chun, H.-Y., 2003 : An overview of the past, present and future of gravity-wave drag parametrization for numerical climate and weather prediction models. *Atm.-Oc.*, **41(1)**, 65–98.

Kljun, N., Sprenger, M., and C., S., 2001 : Frontal modification and lee cyclogenesis in the alps : A case study using the alpex reanalysis data set. *Meteor. Atmos. Phys.*, **78**, 89–105.

Landau, D. M., 1992 : *Eddy vortices produced by nonlinear reflection of a gravity wave by a critical level*. Ph.d. dissertation, University of California, Los Angeles, 268 pp.

Legras, B., and Ghil, M., 1985 : Persistent anomalies, blocking and variations in atmospheric predictibility. *J. Atmos. Sci.*, **42**, 433–471.

Lejenäs, H., and Madden, R. A., 2000 : Mountain torques caused by normal-mode global rossby waves, and the impact on atmospheric angular momentum. *J. Atmos. Sci.*, **57**, 1045–1051.

Lelong, M.-P., and Dunkerton, T. J., 1998a : Inertia-gravity wave breaking in three dimensions. part i : convectively stable waves. *J. Atmos. Sci.*, **55(15)**, 2473–2488.

Lelong, M.-P., and Dunkerton, T. J., 1998b : Inertia-gravity wave breaking in three dimensions. part ii : convectively unstable waves. *J. Atmos. Sci.*, **55(15)**, 2489–2501.

Lighthill, J., 1978 : *Waves in fluids*. Cambridge University Press.

Lilly, D. K., 1972 : Wave momentum flux - a garp problem. *Bull. Amer. Meteor. Soc.*, **53**, 17–23.

Lilly, D. K., 1978 : A severe downslope windstorm and aircraft turbulence event induced by a mountain wave. *J. Atmos. Sci.*, **35**, 59–77.

Lindzen, R., 1981 : Turbulence and stress owing to gravity wave and tidal breakdown. *J. Geophys. Res.*, **86**, 9707–9714.

Lindzen, R., Farrell, B., and Tung, K.-K., 1980 : The concept of overreflection and its application to baroclinic instability. *J. Atmos. Sci.*, **37**, 44–63.

Lindzen, R., and Holton, ., 1968 : A theory of the quasi-biennial oscillation. *J. Atmos. Sci.*, **25**, 1095–1107.

Lindzen, R., and Rosenthal, A., 1976 : On the instability of helmholtz velocity profiles in stably stratified fluids when a lower boundary is present. *J. Geophys. Res.*, **81**, 1561–1571.

Lindzen, R., and Tung, K.-K., 1978 : Wave overreflection and shear instability. *J. Atmos. Sci.*, **35**, 1626–1632.

Liniger, M. A., and C., D. H., 2003 : Substructure of a map streamer. *Quart. J. Roy. Meteor. Soc.*, **129**, 633–651.

Lott, F., 1999 : Alleviation of stationary biases in a gcm through a mountain drag parametrization scheme and a simple representation of mountain lift forces. *Mon. Wea. Rev.*, **127**, 788–801.

Lott, F., 2003 : Large scale flow response to short gravity waves breaking in a rotating shear flow. *J. Atmos. Sci.*, **60**, 1691–1704.

Lott, F., and D'Andrea, F., 2005 : Mass and wind axial angular momentum responses to mountain torques in the 1-25 day band : links with the arctic oscillation. *Quart. J. Roy. Meteor. Soc.*, **131**, 1483–1500.

Lott, F., de Viron, O., Viterbo, P., and Vial, F., 2007 : Axial atmospheric angular momentum budget at diurnal and subdiurnal periodicities. *J. Atmos. Sci.*, **in press**.

Lott, F., and Miller, M. J., 1997 : A new subrig-scale orographic parametrization : Its formulation and testing. *Quart. J. Roy. Meteor. Soc.*, **123**, 101–127.

Lott, F., and Miller, M. J., 1997b : The representation of sub-grid scale orography in gcms. K. Hamilton, Ed., *Gravity-wave processes and their parameterization in global climate models*, Springer-Verlag.

Lott, F., Robertson, A. W., and Ghil, M., 2004a : Mountain torques and northern-hemisphere low-frequency variability. part i : Hemispheric aspects. *J. Atmos. Sci.*, **61**, 1259–1271.

Lott, F., and Teitelbaum, H., 1992 : Nonlinear dissipative critical level interaction in a stratified shear flow : Instabilities and gravity waves. *Geophys. Astrophys. Fluid Dynamics*, **66**, 133–167.

Lott, F., and Teitelbaum, H., 1993 : Linear unsteady mountain waves. *Tellus*, **45A**, 201–220.

Madden, R. A., 2007 : Large scale, free rossby waves in the atmosphere - an update. *Tellus*, **59(5)**, in press.

Martin, A., and Lott, F., 2007 : Synoptic responses to mountain gravity waves encountering directional critical levels. *J. Atmos. Sci.*, **64**, 828–848.

Martius, O., Zenklusen, E., Schwierz, C., and Davies, H. C., 2006 : Episodes of alpine heavy precipitation with an overlying elongated stratospheric intrusion : a climatology. *Int. J. Climatol.*, **26**, 1149–1164.

McFarlane, N. A., 1987 : The effect of orographically excited gravity wave drag on the general circulation of the lower stratosphere and troposphere. *J. Atmos. Sci.*, **44**, 1775–1800.

McIntyre, M. E., 2001 : Global effects of gravity waves in the middle atmosphere : A theoretical perspective. *Adv. Space Res.*, **27(10)**, 1723–1736.

McLandress, C. M., 1998 : On the importance of gravity waves in the middle atmosphere and their parameterization in general circulation models. *J. Atmos. Terr. Phys.*, **60**, 1357–1383.

McLandress, C. M., and Scinocca, J. F., 2005 : The gcm response to current parameterizations of nonorographic gravity wave drag. *J. Atmos. Sci.*, **62**, 2394–2413.

Medvedev, A. S., and Klaassen, G. P., 2000 : Parameterization of gravity wave momentum deposition based on nonlinear interactions : Basic formulation and sensitivity tests. *J. Atmos. Sol. Terr. Phys.*, **62**, 1015–1033.

Messinger, F., and Pierrehumbert, R. T., 1986 : Alpine lee cyclogenesis : numerical simulation and theory. *Scient. Results. Alpine Exp.*, no. 27 in Vol 1, GARP Publications Series, 141–165.

Miller, M. J., and Palmer, T. N., 1986 : Orographic gravity-wave drag : Its parameterization and influence in general circulation and numerical weather prediction models. *Proc. Seminar/Workshop on observation, theory, and modeling of orographic effects*, Vol 1, Shinfield Park, Reading, United Kingdom, ECMWF, 283–333.

Miller, M. J., Palmer, T. N., and Swinbank, R., 1989 : Parametrization and influence of subgridscale orography in general circulation and numerical weather prediction models. *Meteor. Atmos. Phys.*, **40**, 84–109.

Miranda, P. M. A., and James, I. A., 1992 : Nonlinear three dimensional effects on gravity-wave drag : Splitting flow and breaking waves. *Quart. J. Roy. Meteor. Soc.*, **118**, 1057–1081.

Morgenstern, O., and Davies, H. C., 1999 : Disruption of an upper-level pv-streamer by orographic and cloud-diabatic effects. *Contrib. Atmos. Phys.*, **72**, 173–186.

Nakamura, N., 1988 : Scale selection of baroclinic instability - effects of stratification and nongeostrophy. *J. Atmos. Sci.*, **45(21)**, 3253–3267.

Nakamura, N., and Held, I. M., 1989 : Nonlinear equilibration of two-dimensional eady waves. *J. Atmos. Sci.*, **46(19)**, 3055–3064.

Olafsdóttir, E. I., Olde Daalhuis, A. B., and Vanneste, J., 2008 : Inertia-gravity wave radiation by a sheared vortex. *J. Fluid Mech.*, **596**, 169–189.

Olafsson, H., and Bougeault, P., 1996 : Nonlinear flow past an elliptic mountain ridge. *J. Atmos. Sci.*, **53**, 2465–2489.

Olafsson, H., and Bougeault, P., 1997 : The effect of rotation and surface friction on orographic drag. *J. Atmos. Sci.*, **54**, 193–210.

Olver, F. W., 1974 : *Asymptotic and special functions*. Computer science and applied mathematics, Academic Press.

Orlanski, I., and Gross, B. D., 1994 : Orographic modification of cyclone development. *J. Atmos. Sci.*, **51**, 589–611.

Orr, W., 1907 : Stability or instability of the steady-motions of a perfect liquid. *Proc. Roy. Irish Acad. B*, **27**, 9–138.

O'Sullivan, D., and Dunkerton, T. J., 1995 : Generation of inertia-gravity waves in a simulated life cycle of baroclinic instability. *J. Atmos. Sci.*, **52(21)**, 3696–3716.

Palmén, E., and Newton, C. W., 1969 : *Atmospheric circulation systems*. Academic Press, London.

Palmer, T., Shutts, G. J., and Swinbank, R., 1986 : Alleviation of a systematic westerly bias in general circulation and numerical weather prediction models through an orographic gravity wave drag parametrization. *Quart. J. Roy. Meteor. Soc.*, **112**, 1001–1039.

Peltier, W. R., and Clark, T. L., 1979 : The evolution and stability of finite-amplitude mountain waves. part ii : Surface wave drag and severe downslope windstorms. *J. Atmos. Sci.*, **36**, 1498–1529.

Peltier, W. R., and Clark, T. L., 1984 : Nonlinear mountain waves in two and three spatial dimensions. *Quart. J. Roy. Meteor. Soc.*, **109**, 527–548.

Pettersen, S., 1956 : *Weather analysis and forecasting*. McGraw-Hill, New York.

Phillips, D. S., 1984 : Analytical surface pressure and drag for linear hydrostatic flow over three-dimensional elliptical mountains. *J. Atmos. Sci.*, **41**, 1073–1084.

Pichler, H., and Steinacker, R., 1987 : On the synoptics and dynamics of orographically induced cyclones in the mediterranean. *Meteor. Atmos. Phys.*, **36**, 108–117.

Pierrehumbert, R. T., 1985 : A theoretical model of orographically modified cyclogenesis. *J. Atmos. Sci.*, **42(12)**, 1244–1258.

Pierrehumbert, R. T., 1986 : Lee cyclogenesis. P. S. Ray, Ed., *Mesoscale Meteorology and Forecasting*, Amer. Meteor. Soc.

Pierrehumbert, R. T., and Wyman, B., 1985 : Upstream effect on mesoscale mountains. *J. Atmos. Sci.*, **42**, 977–1003.

Plougonven, R., Muraki, D. J., and Snyder, C., 2005 : A baroclinic instability that couples balanced motions and gravity waves. *J. Atmos. Sci.*, **62**, 1545–1559.

Plougonven, R., and Snyder, C., 2007 : Inertia-gravity waves spontanously generated by jets and fronts. part i : Different baroclinic life cycles. *J. Atmos. Sci.*, **64**, 2502–2520.

Plougonven, R., and Zeitlin, V., 2002 : Internal gravity wave emission from a pancake vortex : An example of wave-vortex interaction in strongly stratified flows. *Physics of Fluids*, **14(3)**, 1259–1268.

Pratt, L. J., 1983 : On inertial flow over topography. part i. semi-geostrophic adjustment to an obstacle. *J. Fluid Mech.*, **131**, 195–218.

Queney, P., 1948 : The problem of airflow over mountains : a summary of theoretical studies. *Bull. Amer. Meteor. Soc.*, **29**, 16–26.

Radinović, D., 1986 : On the development of orographic cyclones. *Quart. J. Roy. Meteor. Soc.*, **112**, 927–951.

Rosenthal, A. J., and Lindzen, R., 1983 : Instabilities in a stratified fluid having one critical level. part ii : Explaination of gravity wave instabilities using the concept of overreflexion. *J. Atmos. Sci.*, **40**, 521–529.

Rossby, C. G., 1937 : On the mutual adjustment of pressure and velocity distributions in certain simple current systems. *J. Mar. Res.*, **1**, 15–28.

Rossby, C. G., 1940 : Planetary flow patterns in the atmosphere. *Quart. J. Roy. Meteor. Soc.*, **66**, suppl, 68–87.

Rossby, C. G., 1949 : On the dispersion of planetary waves in a barotropic atmosphere. *Tellus*, **1**, 54–58.

Rossby, C. G. *et al.*., 1939 : Relations between variations in the intensity of the zonal circulation of the atmosphere and the displacements of the semipermanent centers of action. *J. Mar. Res.*, **2**, 38–55.

Rotunno, R., Grubisic, V., and Smolarkiewicz, P. K., 1999 : Vorticity and potential vorticity in mountain wakes. *J. Atmos. Sci.*, **56**, 2796–2810.

Rotunno, R., and Houze, R. A., 2007 : Lessons on orographic precipitation from the mesoscale alpine programme. *Quart. J. Roy. Meteor. Soc.*, **133**, 811–830.

Salby, M. L., 1984 : Survey of planetary-scale traveling waves : the theory and observations. *Rev. Geophys. Space Phys.*, **22**, 209–236.

Satomura, T., and Sato, K., 1999 : Secondary generation of gravity waves associated with the breaking of mountain waves. *J. Atmos. Sci.*, **56**, 3847–3858.

Sawyer, J. S., 1959 : The introduction of the effects of topography into methods of numerical forecasting. *Quart. J. Roy. Meteor. Soc.*, **85**, 31–43.

Scavuzzo, C., M.A., L., Teitelbaum, H., and Lott, F., 1998 : A study of the low frequency inertio-gravity waves observed during pyrex. *J. Geophys. Res.*, **103(D2)**, 1747–1758.

Schär, C., 1990 : Quasi-geostrophic lee cyclogenesis. *J. Atmos. Sci.*, **47(24)**, 3044–3066.

Schär, C., 1993 : A generalization of bernoulli's theorem. *J. Atmos. Sci.*, **50(10)**, 1437–1443.

Schär, C., 2003 : Lee cyclogenesis. J. R. Holton, J. A. Curry, and J. A. Pyle, Eds., *Encyclopedia of Atmospheric Sciences*, Academic Press - Elsevier Science.

Schär, C., and Davies, H. C., 1988 : Quasi-geostrophic stratified flow over isolated finite amplitude topography. *Dyn. Atmos. Oceans*, **11**, 287–306.

Schär, C., and Durran, D. R., 1997 : Vortex formation and vortex shedding in continuously stratified flows past isolated topography. *J. Atmos. Sci.*, **54(4)**, 533–554.

Schär, C., and Smith, R. B., 1993a : Shallow-water flow past isolated topography. part i : Vorticity production and wake formation. *J. Atmos. Sci.*, **50(10)**, 1373–1400.

Schär, C., and Smith, R. B., 1993b : Shallow-water flow past isolated topography. part ii : Transition to vortex shedding. *J. Atmos. Sci.*, **50(10)**, 1401–1412.

Schär, C., Sprenger, M., Lüthi, D., Jiang, Q., Smith, R. B., and Benoit, R., 2003 : Structure and dynamics of an alpine potential-vorticity banner. *Quart. J. Roy. Meteor. Soc.*, **129**, 825–855.

Scinocca, J. F., and Ford, R., 2000 : The nonlinear forcing of large-scale internal gravity waves by stratified shear instability. *J. Atmos. Sci.*, **57**, 653–672.

Scinocca, J. F., and McFarlane, N. A., 2000 : The parametrization of drag induced by stratitified flow over anisotropic orography. *Quart. J. Roy. Meteor. Soc.*, **126(568)**, 2353–2393.

Scinocca, J. F., and Shepherd, T. G., 1992 : Nonlinear wave-activity conservation laws and hamiltonian structure for the two-dimensional anelastic equations. *J. Atmos. Sci.*, **49(1)**, 5–27.

Scorer, R. S., 1949 : Theory of waves in the lee of mountains. *Quart. J. Roy. Meteor. Soc.*, **82**, 75–81.

Shen, B.-W., and Lin, Y.-L., 1999 : Effects of critical levels on two-dimensionnal back-sheared flow over an isolated mountain ridge on an f-plane. *J. Atmos. Sci.*, **56**, 3286–3302.

Shutts, G. J., 1995 : Gravity-wave drag parametrization over complex terrain : the effect of critical-level absorption in directional wind-shear. *Quart. J. Roy. Meteor. Soc.*, **121**, 1005–1021.

Shutts, G. J., 1998a : Stationary gravity-wave structure in flows with directional wind shear. *Quart. J. Roy. Meteor. Soc.*, **124**, 1421–1442.

Shutts, G. J., 1998b : Idealized models of the pressure drag force on mesoscale mountain ridges. *Contrib. Atmos. Phys.*, **71(3)**, 303–313.

Shutts, G. J., 2001 : A linear model of back-sheared flow over an isolated hill in the presence of rotation. *J. Atmos. Sci.*, **58**, 3293–3311.

Shutts, G. J., 2003 : Inertia-gravity wave and neutral eady wave trains forced by directionnally sheared flow over isolated hills. *J. Atmos. Sci.*, **60(4)**, 593–606.

Shutts, G. J., and Gadian, A., 1999 : Numerical simulations of orographic gravity waves in flows which back with height. *Quart. J. Roy. Meteor. Soc.*, **125**, 2743–2765.

Smith, R. B., 1979a : The influence of mountains on the atmosphere. *Adv. Geophys.*, **21**, 87–230.

Smith, R. B., 1979b : The influence of the earth rotation on mountain wave drag. *J. Atmos. Sci.*, **36**, 177–180.

Smith, R. B., 1979c : Some aspects of the quasi-geostrophic flow over mountains. *J. Atmos. Sci.*, **36**, 2385–2393.

Smith, R. B., 1984 : A theory of lee cyclogenesis. *J. Atmos. Sci.*, **41(7)**, 1159–1168.

Smith, R. B., 1986 : Further development of a theory of lee cyclogenesis. *J. Atmos. Sci.*, **43(15)**, 1582–1602.

Smith, R. B., 1989a : Hydrostatic airflow over mountains. *Adv. Geophys.*, **31**, 1–41.

Smith, R. B., 1989b : Comment on low froude number flow past three-dimensional obstacles. part i : Baroclinically generated lee vortices. *J. Atmos. Sci. - Notes and corr.*, **46**, 3611–3617.

Smith, R. B., 2003 : Mountain meteorology. J. R. Holton, J. A. Curry, and J. A. Pyle, Eds., *Encyclopedia of Atmospheric Sciences*, Academic Press - Elsevier Science.

Smith, R. B., Skubis, S., Doyle, J. D., S., B. A., Kiemle, C., and Volkert, H., 2002 : Mountain wave over mont blanc : Influence of a stagnant boundary layer. *J. Atmos. Sci.*, **59**, 2073–2092.

Smolarkiewicz, P. K., and Rotunno, R., 1989 : Low froude number flow past three-dimensional obstacles. part i : Baroclinically generated lee vortices. *J. Atmos. Sci.*, **46**, 1154–1164.

Smolarkiewicz, P. K., and Rotunno, R., 1990 : Low froude number flow past three-dimensional obstacles. part ii : Upwind flow reversal zone. *J. Atmos. Sci.*, **47**, 1498–1511.

Snyder, C., Muraki, D. J., Plougonven, R., and Zhang, F., 2007 : Inertia-gravity waves generated within a dipole-vortex. *J. Atmos. Sci.*, **64**, 4417–4431.

Snyder, C., Skamarock, W. C., and Rotunno, R., 1993 : Frontal dynamics near and following frontal collapse. *J. Atmos. Sci.*, **50(18)**, 3194–3211.

Speranza, A., Buzzi, A., Trevisan, A., and Malguzzi, P., 1985 : A theory of deep cyclogenesis in the lee of the alps. part i : Modifications of baroclinic instability by localized topography. *J. Atmos. Sci.*, **42**, 1521–1535.

Stone, P. H., 1970 : On non-geostrophic baroclinic stability : Part ii. *J. Atmos. Sci.*, **27**, 721–726.

Sutherland, B. R., Caulfield, C. P., and Peltier, W. R., 1994 : Internal gravity wave generation and hydrodynamic instability. *J. Atmos. Sci.*, **51(22)**, 3261–3280.

Tafferner, A., 1990 : Lee cyclogenesis resulting from combined outbreak of cold air and potential vorticity against the alps. *Meteor. Atmos. Phys.*, **43**, 31–47.

Tafferner, A., and Egger, J., 1990 : Test of theories of lee cyclogenesis : Alpex cases. *J. Atmos. Sci.*, **47**, 2417–2428.

Tai, C.-K., 1983 : Over-reflexion and instability. *Dyn. Atmos. Oceans*, **7**, 147–165.

Teitelbaum, H., Kelder, H., and Van Duin, C. A., 1987 : Propagation of internal gravity waves in a rotating fluid with shear flow. *J. Atmos. Terr. Phys.*, **49(5)**, 413–420.

Thorncroft, C. D., and Hoskins, B. J., 1990 : Frontal cyclogenesis. *J. Atmos. Sci.*, **47**, 2317–2336.

Tibaldi, S., 1986 : Enveloppe orography and maintenance of quasi-stationary waves in the ecmwf model. *Adv. Geophys.*, **29**, 339–374.

Tibaldi, S., and Geylin, J., 1981 : The production of a new orography, land-sea mask and associated climatoligical surface fields for operational purposes. *ECMWF Research Department, Technical Memorandum*, **40**.

Tokioka, T., 1970 : Non-geostrophic and non-hydrostatic stability of a baroclinic fluid. *J. Meteor. Soc. Japan*, **48**, 503–520.

Umurhan, O. M., Heifetz, E., Harnick, N., and Lott, F., 2008 : The instability of counter-propagating kernel gravity waves in a constant shear flow. *submitted to Physics of Fluids*.

Vadas, S. L., Fritts, D. C., and Alexander, M. J., 2003 : Mechanism for the generation of secondary waves in wave breaking regions. *J. Atmos. Sci.*, **60**, 194–214.

Vallis, G. K., 2006 : *Atmospheric and oceanic fluid dynamics*. Cambridge University Press, Cambridge.

Vanneste, J., and Yavneh, I., 2004 : Exponentially small inertia-gravity waves and the breakdown of quasigeostrophic balance. *J. Atmos. Sci.*, **61**, 211–223.

Viudez, A., 2008 : The stationary frontal wave packet spontaneously generated in mesoscale dipoles. *J. Phys. Ocean.*, **38**, 243–256.

Viudez, A., and G., D. D., 2006 : Spontanous generation of inertia-gravity wave paquets by balanced geophysical flows. *J. Fluid Mech.*, **553**, 107–117.

Volkert, H., Keil, C., Kiemle, C., Poberaj, G., J-P., C., and Richard, E., 2003 : Gravity waves over the eastern alps : A synopsis of the 25 october 1999 event (iop 10) combining in situ and remote-sensing measurements with a high-resolution simulation. *Quart. J. Roy. Meteor. Soc.*, **129**, 777–797.

Warner, C. D., and McIntyre, M. E., 2001 : An ultrasimple spectral parameterization for nonorographic gravity waves. *J. Atmos. Sci.*, **58**, 1837–1857.

Webster, S., Brown, A. R., Cameron, D. R., and Jones, C. P., 2003 : Improvements to the representation of orography in the met office unified model. *Quart. J. Roy. Meteor. Soc.*, **129**, 1989–2010.

Whiteman, C. D., 2000 : *Mountain meteorology : fundamentals and applications*. Oxford University Press.

Whitham, G. B., 1974 : *Linear and nonlinear waves*. Pure and Applied Mathematics, John Wiley & Sons, wiley-interscience edn.

Whittaker, L. M., and Horn, L. H., 1984 : Northern hemisphere extratropical cyclone activity for four mid-season months. *Int. J. Climatol.*, **4**, 297–310.

Winters, K. B., and D'Asaro, E. A., 1989 : Two-dimensional instability of finite amplitude internal gravity wave packets near a critical level. *J. Geophys. Res.*, **94(C9)**, 12709–12719.

Winters, K. B., and D'Asaro, E. A., 1994 : Three-dimensional wave instability near a critical level. *J. Fluid Mech.*, **272**, 255–284.

Winters, K. B., and Riley, J. J., 1992 : Instability of internal waves near a critical level. *Dyn. Atmos. Oceans*, **16**, 249–278.

Wurtele, M. G., 1996 : Atmospheric lee waves. *Ann. Rev. Fluid Mech.*, **28**, 429–476.

Wurtele, M. G., Datta, A., and Sharman, R. D., 1996 : The propagation of gravity-inertia waves and lee waves under a critical level. *J. Atmos. Sci.*, **53(11)**, 1505–1523.

Wurtele, M. G., Datta, A., and Sharman, R. D., 1999 : Unsteadyness and periodicity in gravity waves and lee waves forced by a fixed rigid boundary. *J. Atmos. Sci.*, **56**, 2269–2276.

Wurtele, M. G., Datta, A., and Sharman, R. D., 2000 : The propagation of a gravity-inertia wave in a positively sheared flow. *J. Atmos. Sci.*, **57**, 3703–3715.

Yamanaka, M. D., and Tanaka, H., 1984 : Propagation and breakdown of internal inertia-gravity waves near critical levels in the middle atmosphere. *J. Meteor. Soc. Japan*, **62**, 1–17.

Yamazaki, Y. H., and Peltier, W. R., 2001 : Baroclinic instability in an euler equations-based column model : The coexistence of a deep synoptic-scale mode and shallow subsynoptic-scale modes. *J. Atmos. Sci.*, **58**, 780–792.

Yoden, S., 1985 : Multiple stable states of quasi-geostrophic barotropic flow over sinusoidal topography. *J. Meteor. Soc. Japan*, **62**, 1–17.